

Dynamics of chaotic strings

Dissertation

zur Erlangung des Doktorgrades
der Naturwissenschaften

vorgelegt beim Fachbereich Physik
der Goethe Universität
Frankfurt am Main

von

Mirko Schäfer

aus Ehringshausen

Frankfurt, 2011

(D30)

vom Fachbereich Physik der

Goethe Universität als Dissertation angenommen.

Dekan: Prof. Dr. Michael Huth

Gutachter: Prof. Dr. Martin Greiner, Prof. Dr. Joachim Maruhn,
Prof. Dr. Christian Beck

Datum der Disputation: 13.07.2011

Contents

Zusammenfassung in deutscher Sprache	v
1 Introduction	1
2 Chaotic map networks	5
2.1 Chaotic Maps	5
2.1.1 One-dimensional maps	5
2.1.2 Examples of chaotic maps	7
2.1.3 Higher-dimensional maps	10
2.2 Complex networks	12
2.2.1 Properties of complex networks	12
2.2.2 Network structure models	14
2.3 Coupled map networks	16
2.3.1 Coupled map lattices	17
2.3.2 Globally coupled maps	19
2.3.3 Coupled map networks with complex topology	20
2.3.4 Dynamical network structures	21
3 Chaotic strings	23
3.1 Definition	23
3.2 Interaction energy and self energy	35
3.3 Chaotic strings and standard model couplings	37
3.4 Physical embedding	39
4 Discrete symmetries of chaotic strings	41
4.1 Symmetries for the coupled Tchebycheff map dynamics	41
4.2 Symmetries of the interaction energy and the self energy	48
5 Interaction energy of chaotic strings	51
5.1 Dependence of the interaction energy on initial values and node	51
5.2 Precise numerical determination of the zeros	62
6 Correlations and most-random behaviour in coupled Tchebycheff map networks	65
6.1 Interaction energy and most-random behaviour	65

6.2	Lyapunov exponents of chaotic strings	66
6.3	Spatial correlation measures	76
6.3.1	Higher order cumulants	76
6.3.2	Mutual information	82
7	Disordered chaotic strings	87
7.1	Coupling disorder	87
7.2	Network disorder	88
7.3	Discussion	89
8	Complete synchronization of networks	93
8.1	Synchronization in coupled map networks	93
8.2	Master stability functions for complete synchronization on complex networks	96
8.3	Complete synchronization of coupled Tchebycheff map networks . . .	102
8.3.1	$2A$ dynamics	104
8.3.2	$3A$ dynamics	105
8.3.3	$2B$ dynamics	105
8.3.4	$2A^-$ dynamics	108
8.3.5	$2B^-$ dynamics	111
8.3.6	$3B$ dynamics	113
9	Cluster synchronization	117
9.1	Master stability functions for two-cluster synchronization on bipartite networks	117
9.2	Two-cluster synchronization on bipartite Tchebycheff networks	122
9.2.1	Two-cluster synchronized fixed points and period-2 orbits . . .	123
9.2.2	Symmetries of two coupled maps	125
9.2.3	Numerical results	130
10	Conclusion	135
A	Publications	139
	Robustness of networks against fluctuation-induced cascading failures . . .	141
	Acknowledgments	155
	CV	157

Zusammenfassung in deutscher Sprache

Die vorliegende Arbeit behandelt dynamische Eigenschaften gekoppelter chaotischer Tchebycheff-Abbildungen auf Netzwerken. Besondere Beachtung findet dabei die Anwendung dieser dynamischen Systeme in dem von Beck in Ref. [17] im Zusammenhang mit stochastisch quantisierten Feldtheorien vorgeschlagenen Modell.

Gekoppelte chaotische Abbildungen auf Netzwerken sind zeitlich diskrete dynamische Systeme, die verschiedene interessante Eigenschaften aufweisen. An jedem Knoten ist die Dynamik durch die Iteration einer chaotischen Abbildung realisiert, wobei diese in der hier vorliegenden Arbeit durch Tchebycheff-Polynome gegeben ist. Diese speziellen Abbildungen sind konjugiert zu einer Bernoulli-Abbildung und zeigen geringstmögliche Korrelationen höherer Ordnung. Sie können dementsprechend als ‘maximal chaotisch’ bezeichnet werden [17]. Durch die Kopplung zwischen den verschiedenen Abbildungen entlang der Verbindungen eines Netzwerks wird eine Vielzahl komplexer dynamischer Muster erzeugt. Diese raum-zeitlichen globalen Dynamiken sind ein emergentes Phänomen des Systems, hervorgerufen durch das Zusammenspiel der gekoppelten Elemente, und können nicht durch die Betrachtung der einzelnen isolierten Bestandteile verstanden werden. In diesem Sinne repräsentieren gekoppelte chaotische Abbildungen auf Netzwerken ein prototypisches Modell zur Untersuchung des Zusammenhangs zwischen lokaler Dynamik, Netzwerkstruktur und emergenter globaler Dynamik. Entsprechende Systeme stellen ein intensiv studiertes Forschungsgebiet im Rahmen der Theorie dynamischer Systeme und der statistischen Physik komplexer Netzwerke dar. Es finden sich zahlreiche Anwendungen als phänomenologische Modelle, beispielsweise auf dem Gebiet der Turbulenz, der Musterbildung oder zur Untersuchung von Synchronisationsprozessen auf Netzwerken [7, 69, 70].

Eine neue als ‘Chaotic-Strings’ bezeichnete Anwendung gekoppelter chaotischer Abbildungen auf Ring-Netzwerken im Zusammenhang mit Quantenfeldtheorien wird in Ref. [17] vorgeschlagen. Das Standardmodell der Elementarteilchenphysik ist eine physikalische Theorie zur Beschreibung der bekannten Elementarteilchen und deren fundamentalen Wechselwirkungen, formuliert als relativistische Quantenfeldtheorie [49, 53, 63]. Es steht in exzellenter Übereinstimmung mit experimentellen Befunden. Nichtsdestotrotz kann es keine abschließende ‘Theory Of Everything’ darstellen. Beispielsweise ist die Beschreibung der Gravitation als fundamentale Wechselwirkung im Rahmen des Standardmodells nicht möglich [49]. Weiterhin enthält es ca. 20 freie Parameter, deren Werte nicht aus der Theorie selbst folgen und die demnach expe-

rimentell bestimmt werden müssen [110]. Das in Ref. [17] vorgestellte Modell liefert einen phänomenologischen Ansatz zur Erklärung der Werte dieser Parameter. Demnach werden diese mittels zusätzlicher Felder festgelegt und stabilisiert, welche durch gekoppelte Tchebycheff-Abbildungen auf Ring-Netzwerken beschrieben werden. Die raum-zeitlich chaotische Dynamik dient weiterhin als stochastisches Feld für die stochastische Quantisierung von Feldtheorien nach Parisi-Wu [82]. Bemerkenswerterweise zeichnen sich im Modell bestimmte numerische Werte der Kopplungsstärke der Dynamik aus, die mit Kopplungskonstanten des Standardmodells der Elementarteilchenphysik assoziiert werden können. Obwohl das in Ref. [17] vorgeschlagene Modell keine vollständige Theorie darstellt und die physikalische Einbettung der chaotischen Dynamik noch nicht abschließend geklärt ist, motivieren diese Resultate eine eingehendere Untersuchung.

Die vorliegende Arbeit untersucht das Chaotic-String-Modell im Hinblick auf die dynamischen Eigenschaften der zugrundeliegenden Systeme gekoppelter Tchebycheff-Abbildungen. Die Ergebnisse ermöglichen ein grundlegendes Verständnis der Dynamiken und liefern somit einen essentiellen Beitrag zu einer kritischen Diskussion der möglichen physikalischen Einbettung und Interpretation des Modells. Die Relevanz der untersuchten Aspekte, beispielsweise Synchronisationseigenschaften oder ein maximal stochastisches Verhalten des Systems, ist nicht auf das Chaotic-String-Modell beschränkt. Vielmehr sind diese Konzepte auch unabhängig von konkreten Anwendungen von Interesse in der Theorie dynamischer Systeme und komplexer Netzwerke [7, 70].

Auf eine allgemeine Einleitung der vorliegenden Arbeit in Kapitel 1 folgt in Kapitel 2 eine Einführung in die für die Behandlung gekoppelter chaotischer Abbildungen relevanten Konzepte aus der Theorie der dynamischen Systeme und komplexen Netzwerke. Chaotische Abbildungen sowie wichtige Maße zu deren Beschreibung werden charakterisiert und verschiedene Beispielabbildungen vorgestellt. Bedingt durch die besondere Relevanz für das Chaotic-String-Modell [17] liegt der Fokus auf Tchebycheff-Polynomen. Daran anschließend wird die Notation zur Beschreibung komplexer Netzwerke eingeführt und wichtige Netzwerkeigenschaften definiert. Weiterhin erfolgt eine kurze Übersicht verschiedener Netzwerkmodelle. Gekoppelte chaotische Abbildungen auf Netzwerken verbinden dann die zuvor vorgestellten Konzepte aus den Bereichen der dynamischen Systeme und komplexen Netzwerke. Die entsprechenden dynamischen Systeme werden definiert und der aktuelle Stand der Forschung in diesem Bereich übersichtsartig wiedergegeben.

Nach dieser allgemeinen Einführung in die Theorie gekoppelter chaotischer Abbildungen auf Netzwerken wird in Kapitel 3 das in Ref. [17] vorgeschlagene Chaotic-String-Modell vorgestellt. Es handelt sich dabei um gekoppelte Tchebycheff-Abbildungen auf Ring-Strukturen. Die zugehörigen Evolutionsgleichungen und Observablen werden definiert und qualitative Einblicke in die auftretenden Dynamiken gegeben. Von entscheidender Bedeutung in diesem Modell sind zwei formal aus den Evolutionsgleichungen abgeleitete Observablen, welche als Wechselwirkungsenergie und Selbstenergie der Dynamik bezeichnet werden. In Ref. [17] wird angegeben, dass bestimmte mit einer verschwindenden Wechselwirkungsenergie assoziierte Kopplungs-

konstanten des dynamischen Modells mit Kopplungskonstanten des Standardmodells der Elementarteilchenphysik identifiziert werden können. Die entsprechenden numerischen Beobachtungen aus Ref. [17] werden dargestellt und eine dort vorgestellte physikalische Einbettung des Modells skizziert.

Kapitel 4 behandelt diskrete Symmetrien gekoppelter Tchebycheff-Abbildungen auf Netzwerken. Die mathematische Herleitung des Chaotic-String-Modells führt zu insgesamt 16 scheinbar unterschiedlichen Dynamiken, basierend auf Tchebycheff-Abbildungen zweiter und dritter Ordnung [17]. In Ref. [17] wurde aufgrund von Symmetrieargumenten diese Anzahl auf lediglich sechs grundlegend unterschiedliche Dynamiken reduziert. Die Untersuchungen in Kapitel 4 bestätigen diese Argumente mit Hilfe einer vollständigen Analyse diskreter Symmetrietransformation der entsprechenden Dynamiken. Diese Transformationen sind allgemein für bipartite Netzwerkstrukturen formuliert. Ein bipartites Netzwerk besteht aus zwei disjunkten Teilmengen von Knoten mit Netzwerkverbindungen lediglich zwischen Knoten aus unterschiedlichen Teilmengen. Ein Ring-Netzwerk mit einer geraden Anzahl von Knoten ist eine spezielle Realisierung eines solchen bipartiten Netzwerks.

Eine der grundlegenden Observablen des Chaotic-String-Modells ist die Wechselwirkungsenergie. Von besonderem Interesse in Ref. [17] sind bestimmte zu einer verschwindenden Wechselwirkungsenergie führende Kopplungen der chaotischen Dynamik, da für diese eine numerische Übereinstimmung mit Kopplungskonstanten des Standardmodells beobachtet wird. Da die Wechselwirkungsenergie im Wesentlichen ein räumliches Korrelationsmaß für die Dynamik auf den Knoten des Rings darstellt, wird in Ref. [17, 21] eine Interpretation der entsprechenden dynamischen Zustände als ‘maximal chaotisch’ oder ‘maximal stochastisch’ nahegelegt. Solch eine Interpretation sollte jedoch ein allgemeineres dynamisches Prinzip zur Auszeichnung bestimmter Dynamiken und Kopplungswerte liefern und wäre demzufolge nicht nur an eine spezielle Observable gekoppelt.

Die Wechselwirkungsenergie ist ein solches spezielles räumliches Korrelationsmaß und gibt demzufolge nur in begrenztem Umfang Aufschluss über die Eigenschaften der Dynamik. Um bestimmte dynamische Zustände als maximal stochastisch zu beurteilen oder um ein vergleichbares dynamisches Prinzip aufzustellen, ist ein tiefergehendes Verständnis über diese Observable hinaus unverzichtbar.

Ein erster Schritt zu einem solchen besseren Verständnis wird in Kapitel 5 unternommen. Obwohl die Wechselwirkungsenergie jeweils separat für alle gekoppelten Knoten-Paare definiert ist, wird in Ref. [17] der räumliche Mittelwert dieser lokalen Observablen über das gesamte Ring-Netzwerk betrachtet. Die in Kapitel 5 vorgestellten Rechnungen zeigen, dass dieser räumliche Mittelungsprozess zu missverständlichen Ergebnissen führen kann. Für einen weiten Bereich von Kopplungen stellt sich die Dynamik als nicht-ergodisch heraus, was zu einer Abhängigkeit der Observablen vom jeweiligen Knoten des Netzwerks und den Anfangsbedingungen führt. Insbesondere wird gezeigt, dass zwei der in Ref. [17] mit Kopplungskonstanten des Standardmodells identifizierten Nullstellen der Wechselwirkungsenergie lediglich aus diesem globalen Mittelungsprozess resultieren, für die jeweiligen Dynamiken diese Observable aber lokal nicht verschwindet. Für die sechs weiteren interessanten Nullstellen der

Wechselwirkungsenergie wird ein ergodisches Verhalten der Dynamik beobachtet, und die Wechselwirkungsenergie verschwindet lokal. Diese Nullstellen werden im weiteren Verlauf von Kapitel 5 numerisch mit hoher Präzision berechnet und anhand dieser Rechnungen die entsprechenden Ergebnisse aus Ref. [17] bestätigt.

In Kapitel 6 wird ein eventuelles maximal chaotisches Verhalten der Chaotic-String-Dynamiken für die Nullstellen der Wechselwirkungsenergie überprüft. Um eine genauere Charakterisierung der Dynamik zu erreichen, werden zuerst verschiedene auf dem Lyapunov-Spektrum basierende Maße betrachtet. Die Lyapunov-Exponenten eines dynamischen Systems beschreiben die Separationsrate nahe aneinanderliegender Trajektorien im Phasenraum, wobei bereits ein positiver Exponent chaotisches Verhalten indiziert. Neben dem größten Lyapunov-Exponenten wird der Mittelwert über alle positiven Lyapunov-Exponenten und die Lyapunov-Dimension der Dynamiken berechnet. Diese drei Maße zeigen Maxima für ungekoppelte Tchebycheff-Abbildungen und Minima für synchronisierte Fixpunkte und stellen demnach Indikatoren für die Chaotizität der Dynamik dar. Die numerischen Rechnungen zeigen, dass für größere Kopplungswerte ein großer Teil oder sogar das gesamte Lyapunov-Spektrum nicht-positive Werte annimmt und dementsprechend zahlreiche Richtungen im Phasenraum existieren, in welchen die Dynamik nicht-chaotisches Verhalten zeigt. Für kleine Kopplungen wird ein vollständig positives Lyapunov-Spektrum beobachtet, was eine stark chaotische Dynamik indiziert. Jedoch zeigen sowohl der maximale Lyapunov-Exponent sowie der mittlere positive Lyapunov-Exponent ein mit steigender Kopplung monoton abfallendes Verhalten. Demzufolge ist hinsichtlich dieser Lyapunov-Maße kein maximal chaotisches oder maximal stochastisches Verhalten zu erkennen und die Existenz eines dementsprechenden dynamischen Prinzips zur Selektion von Kopplungswerten mit verschwindender Selbstenergie kann ausgeschlossen werden.

Das Lyapunov-Spektrum einer Dynamik hängt von der zeitlichen Evolution des Systems ab, während die Wechselwirkungsenergie lediglich räumliche Korrelationen berücksichtigt. Eine Möglichkeit, das dynamische Prinzip eines maximal stochastischen Verhaltens beizubehalten, ist eine Abschwächung dieses Prinzips auf räumliche Korrelationen. Zur Überprüfung dieses abgeschwächten Prinzips werden in Kapitel 6 neben den bereits genannten Lyapunov-Maßen auch Kumulanten höherer Ordnung und das Transinformationsmaß berechnet. Diese beiden letzteren Messgrößen verschwinden jeweils für statistisch unabhängige Zufallszahlen und dienen somit als Indikatoren für räumliche Korrelationen. Für Chaotic-String-Dynamiken basierend auf Tchebycheff-Polynomen zweiter Ordnung liefert bereits der Kumulant erster Ordnung andere Nullstellen als die Wechselwirkungsenergie, wodurch eine Identifikation mit Standard-Modell-Kopplungen nicht möglich ist. Die Nullstellen der Wechselwirkungsenergie für Chaotic-String-Dynamiken basierend auf Tchebycheff-Polynomen dritter Ordnung korrespondieren für kleine Kopplungen zwar mit den Nullstellen des Kumulanten erster Ordnung, Kumulanten höherer Ordnungen verschwinden für diese Kopplungen jedoch nicht. Auch die Transinformation zeigt für die Nullstellen der Wechselwirkungsenergie kein besonderes ausgezeichnetes Verhalten.

Die Untersuchungen in Kapitel 6 widersprechen demnach einer Interpretation der

Nullstellen der Wechselwirkungsenergie durch ein maximal chaotisches oder maximal stochastisches Verhalten der jeweiligen Dynamik. Dementsprechend sind diese Nullstellen lediglich anhand einer speziellen Observable, der Wechselwirkungsenergie, ausgezeichnet, jedoch nicht durch ein allgemeineres dynamisches Prinzip. Folglich sollte das in Ref. [17] vorgeschlagene Chaotic-String-Modell diese Observable mit starken physikalischen Argumenten begründen, da eine Motivation mittels eines allgemeinen dynamischen Prinzips nicht möglich ist.

Das Chaotic-String-Modell ist in Ref. [17] auf einem Ring-Netzwerk definiert. In Kapitel 7 wird eine Erweiterung des Modells basierend auf der Einführung einer regelbaren Unordnung des Systems untersucht. Zum einen wird eine inhomogene Verteilung der Kopplungsstärken betrachtet, zum anderen eine Perturbation der Netzwerkstruktur durch zusätzliche Netzwerkverbindungen, welche die Ring-Struktur in ein sogenanntes ‘Small-World’ Netzwerk überführen [88]. Es wird beobachtet, dass beide Arten von Unordnung zu einer Verschiebung der jeweiligen Nullstellen der Wechselwirkungsenergie führen, wodurch eine Interpretation als Standard-Modell-Kopplung erschwert wird. Es zeigt sich jedoch, dass durch eine passende Kombination von sowohl inhomogener Kopplungsverteilung als auch Perturbation der Netzwerkstruktur die Nullstellen erhalten bleiben. Eine Ausnahme stellt eine Nullstelle einer auf Tchebycheff-Polynomen dritter Ordnung basierenden Dynamik dar, welche als elektromagnetische Kopplung identifiziert wird und für die eine solche Kombination sich gegenseitig ausgleichender Arten von Unordnung nicht gefunden werden kann.

In Kapitel 8 und 9 werden Synchronisationseigenschaften gekoppelter Tchebycheff-Abbildungen auf Netzwerken untersucht. Die Rechnungen basieren auf dem sogenannten ‘Master-Stability-Formalismus’, mittels dessen die Stabilität des synchronisierten Zustands in allgemeiner Form zu den spektralen Eigenschaften des Netzwerks, ausgedrückt durch Eigenwerte einer die Netzwerkstruktur darstellenden Matrix, in Beziehung gesetzt werden kann [7, 96]. Kapitel 8 behandelt vollständige Synchronisation, das heißt, alle Knoten des Netzwerks zeigen exakt identisches Verhalten. Zwei-Gruppen-Synchronisation auf bipartiten Netzwerken wird in Kapitel 9 untersucht. Bei dieser zweiten Art von Synchronisation sind jeweils alle Knoten verschiedener Teilmengen der Knoten synchronisiert, das Verhalten der jeweiligen Gruppen unterscheidet sich jedoch. Es wird beobachtet, dass für gekoppelte Tchebycheff-Abbildungen die synchronisierte Dynamik für vollständige wie auch für Zwei-Gruppen-Synchronisation sowohl chaotisches, wie auch periodisches Verhalten oder sogar einen stabilen Fixpunkt aufweisen kann. Semi-analytische Berechnungen zeigen, dass für einen großen Bereich der Kopplungswerte die Synchronisation einen stabilen Zustand darstellt. Neben diesen semi-analytischen Berechnungen werden auch analytische Resultate für vollständig und zwei-Gruppen-synchronisierte Fixpunkte und Periode-2-Orbits hergeleitet. Aufgrund der Verwendung des Master-Stability-Formalismus können die Ergebnisse auf die im Rahmen des Chaotic-String-Modells betrachteten Ring-Netzwerke angewendet werden, sind aber allgemein für beliebige (für Zwei-Gruppen-Synchronisation bipartite) Netzwerkstrukturen gültig.

Zahlreiche weiterführende Fragestellungen können mit den in der vorliegenden Arbeit betrachteten Methoden und Konzepten behandelt werden. Eine logische Fort-

führung der in Kapitel 4 vorgestellten Analyse diskreter Symmetrien wäre eine Erweiterung auf r -partite Netzwerke, die aus insgesamt r disjunkten Teilmengen von Knoten bestehen. Gekoppelte chaotische Abbildungen auf solchen r -partiten Netzwerken werden kompliziertere Transformationseigenschaften aufweisen. Es wäre interessant, die daraus resultierenden allgemeineren diskreten Symmetrien sowie die Auswirkung einer Symmetriebrechung auf die Dynamik zu untersuchen.

In Kapitel 6 werden Lyapunov-Maße und Korrelationen höherer Ordnungen für das Chaotic-String-Modell berechnet. Es liegt nahe, diese Betrachtungen auf allgemeine Netzwerkstrukturen auszuweiten und so den Einfluss der Netzwerkstruktur auf die Chaotizität der Dynamik zu untersuchen. Ein weiterer interessanter Ansatz ist die Anwendung der in Kapitel 8 und 9 eingesetzten Methoden im Rahmen der in Kapitel 7 eingeführten Netzwerkkunordnung und inhomogenen Kopplungsverteilungen. Es stellt sich die Frage, ob Unordnungsphänomene die Synchronisierbarkeit von Netzwerken verringern oder steigern. Eine ähnliche Fragestellung betrifft die Gruppen-Synchronisation, wie sie in Kapitel 9 anhand von Zwei-Gruppen-Synchronisation auf bipartiten Netzwerken untersucht wird. Welche Auswirkung hat eine Perturbation der bipartiten Netzwerke auf die Dynamik? Es ist vorstellbar, dass die Zwei-Gruppen-Synchronisation in verminderter Form erhalten bleibt, aber auch die Ausbildung neuer raum-zeitlicher Muster ist denkbar. Mit Hinblick auf das Chaotic-String-Modell liefert die vorliegende Arbeit zahlreiche neue Erkenntnisse und tiefere Einsichten in die dem Modell zugrundeliegenden dynamischen Systeme. Der hier gewählte Ansatz ist eine Untersuchung unter dynamischen Gesichtspunkten. Es ist zwingend, dass zukünftige Untersuchungen einer physikalischen Einbettung und Interpretation dieses Modells die hier vorgestellten Ergebnisse berücksichtigen.

1 Introduction

Chaos is a nowadays well-known mathematical concept with applications in a multitude of disciplines, including physics, biology or economics [3, 94]. The most important characteristic for chaotic behaviour is its sensitivity on initial conditions: a small difference in the initial conditions grows exponentially in time. Since initial conditions in nature are always only known up to a certain restricted precision, the long-term behaviour of chaotic systems is in general unpredictable, although the dynamics is completely deterministic. This chaotic behaviour is not restricted to high-dimensional, evidently complex systems, but can already be observed in simple one-dimensional discrete-time systems, for which the logistic map is the archetypical example [36].

Although there is still ongoing research, many features of low-dimensional chaos are well understood today, and elaborate descriptions and methods, often inspired by concepts from statistical physics, have become standard techniques in this field [3, 94]. But what happens, when several chaotic systems are coupled? An approach to this question was proposed by Kaneko in the 80s by the introduction of the coupled map lattice model [64]. Such a dynamical system consists of a population of low-dimensional maps on a regular lattice structure, which interact by a diffusive next-neighbour coupling. Although it is a rather abstract model governed by a simple time-discrete evolution equation, the coupled map lattice dynamics exhibits a rich structure of complex dynamical phenomena. It has been used as a model to quantitatively study the dynamics of spatially extended systems, with applications ranging from hydrodynamical flows, turbulence, and chemical reactions to synchronization [29, 69, 70]. A straightforward modification of this model is the globally coupled map dynamics, where the next-neighbour coupling is replaced by an all-to-all coupling, leading to qualitatively new phenomena like cluster synchronization [68]. There are various studies on coupled map lattices and globally coupled map models, but up to now only a limited understanding of the dynamics has been achieved. Several rigorous analytical results are known for the small coupling limit, but for larger couplings most studies are based on numerical methods.

The coupled map lattices and globally coupled maps are two special cases of coupled map networks, which have recently been studied by scientists in the field of complex networks. In principle, every system consisting of a collection of objects which in some way relate to each other can be described by a network. The individual object is abstracted as a node, and the relation between objects is represented by a link of the network. One example is a power grid, where transmission stations are represented

by nodes, and transmission lines as links, another one the WWW, with the web pages corresponding to nodes and hyperlinks to links, respectively. Initiated by the seminal work of Watts and Strogatz in 1998 [114], in the last decade a science of complex networks has emerged. Initially, most research has been based on a static point of view, that is the description of the respective network structures by various measures, and the development of generic models which reproduce real world properties and thus provide insights into their structure and function. Only recently scientists have started to address dynamical properties of networks, and the focus has shifted to the interplay between network structure, local dynamics, and the emerging dynamics on a global level. A prototypical class of dynamical network models are coupled map networks, which are the natural generalization of the coupled map lattice using concepts from the science of complex networks. There have already been several studies on these systems, with the focus on synchronization properties [7], but the dynamical properties of coupled map networks are still far from being well-understood.

Apart from being of interest in the theory of dynamical systems, an interesting application in connection with quantum field theories in particle physics has been pointed out by Beck in Ref. [17] for a certain class of coupled map lattices. The standard model of particle physics is a coherent model, which characterizes particles and forces in nature [49, 53, 63]. It provides a unified description of the strong, weak and electromagnetic forces in the language of quantum field theory [51, 97]. Although it is in excellent accordance with experimental data, the standard model is not a complete theory. Besides failing to incorporate gravity, one major shortcoming is its dependence on about 20 parameters (coupling constants, masses, mixing angles [32, 56, 110]), which are not fixed by the standard model itself. In order to explain the observed values of these parameters, one has to apply anthropic arguments, or embed the standard model into a larger, more fundamental theory. A phenomenological approach to this problem, based on coupled Tchebycheff map lattices, has been proposed by Beck in Refs. [16, 17, 21]. In this model, called ‘chaotic strings’, the coupled map lattice dynamics generates the noise needed for the Parisi-Wu approach of stochastic quantization [82]. By considering two formal energies which depend on a global coupling parameter, in Ref. [17] the author reproduces a large number of standard model parameters to an accuracy of about four decimal digits.

Although the model introduced by Beck in Refs. [16, 17] is not a complete theory itself, but rather a preliminary model, due to its surprisingly exact numerical findings it deserves further attention. In this thesis I will study the chaotic string model and its network generalization from a dynamical point of view. The results are not only of importance for a better understanding of the specific chaotic string dynamics and the connections to a possible physical embedding, but are also relevant to the theory of coupled map network dynamics in general.

The second chapter of the present work starts in Sec. 2.1 with the definition of chaotic maps and some of their properties. Some examples of chaotic maps are given, with a focus on Tchebycheff polynomials, which are of relevance for the chaotic string model. The following Sec. 2.2 introduces the notation for describing complex networks, defines important network properties, and reviews selected network models.

The concepts of chaotic dynamical systems and complex networks are brought together in Sec. 2.3, thereby introducing coupled map networks. The respective dynamical models are defined, and results from the literature are reviewed.

Chapter 3 reviews Beck's chaotic string model. In Sec. 3.1 the dynamical model itself is introduced. Subsequently Sec. 3.2 defines two formal energies (self energy and interaction energy) for the chaotic string model. In Ref. [17] it is observed, that certain chaotic string couplings corresponding to a vanishing interaction energy correspond to running coupling constants of the standard model of particle physics. The respective numerical findings of Ref. [17] are displayed in Sec. 3.3. A possible physical embedding of the chaotic string model as proposed in Refs. [16, 17, 20, 21] is reviewed in Sec. 3.4.

Chapter 4 contains a detailed treatment of discrete symmetries of the chaotic string dynamics and its observables. Although in Ref. [17] some of these symmetries have already been listed, an complete formal analysis of the respective properties has been missing up to now.

In Chap. 5 the interaction energy of chaotic strings is studied. An important concept in Beck's model is the interpretation of the chaotic string dynamics as generating the noise of stochastic quantization [17]. Since the interaction energy is basically a correlation measure, in Refs. [17, 21] dynamical states corresponding to a vanishing interaction energy are interpreted in terms of a most random behaviour. For this interpretation to hold, according to a presumed ergodic behaviour of the dynamics the interaction energy should vanish locally at every lattice site, and not just due to spatial averaging only. In Sec. 5.1 this condition is checked for zeros of the interaction energy, which in Ref. [17] are associated with standard model couplings. Additionally, in Sec. 5.2 selected numerical results of the Beck theory are verified by extensive computations.

The interaction energy is only one specific spatial correlation measure. Chapter 6 studies the notion of a most random behaviour of distinguished chaotic string dynamics by means of other observables from dynamical system theory. In Sec. 6.2 several Lyapunov measures are numerically calculated, which provide estimations of the chaoticity of the chaotic strings dynamics. Sec. 6.3 analyzes spatial correlations by considering higher-order cumulants and the mutual information measure.

In Chap. 4-6 the original Beck model of coupled Tchebycheff map lattices is studied. This model is generalized in Chap. 7 by the introduction of a tunable disorder to the chaotic string dynamics. Inhomogeneous coupling weights as well as small-world perturbations of the ring-network structure are discussed.

Chapters 8 and 9 treat synchronization properties of coupled Tchebycheff networks. By application of master stability functions [96], the complete synchronization of these systems is studied semi-analytically. The stability of synchronized fixed points and period-2 orbits on general network structures is analytically determined. The notion of synchronization is expanded to two-cluster synchronization on bipartite networks in Chap. 9. Master stability functions for this kind of cluster synchronization are formulated, and subsequently applied to coupled Tchebycheff map networks.

In Chap. 10 the results are summarized and possible future studies are proposed.

2 Chaotic map networks

The main topic of this thesis are coupled Tchebycheff map networks, with the focus on the application in the chaotic string model proposed by Beck in Ref. [17]. In order to introduce the reader to this topic, in the following chapter I will review several concepts from dynamical system theory and the science of complex networks. After defining chaotic maps and explaining some of their properties, the relevant notation for complex networks is established and some network models are discussed. Subsequently, coupled map networks are defined and dynamical properties of these dynamical models are reviewed.

2.1 Chaotic Maps

2.1.1 One-dimensional maps

In this thesis I will mostly focus on one-dimensional chaotic maps as the individual units of the network dynamics [3, 94]. A one-dimensional map is a function $f : I \rightarrow I$ whose domain and range are the same interval $I \in \mathbb{R}$. For $x \in I$ the set of points $\{x, f(x), f^2(x), \dots\}$ is called the orbit or trajectory of x under f . One writes $x(0)$ for the initial value, and $x(t) = f^t[x(0)]$ for the value of x at time t .

A point p is a periodic point of period k , if $f^k(p) = p$, and k is the smallest such positive integer. Obviously, if a point p is periodic with period k , it is also periodic with period $2k, 3k, \dots$. For $k = 1$ the periodic point is called a fixed point. The stability of a periodic orbit $\{p(0), \dots, p(k-1)\}$ is accounted for the time evolution of a small perturbation, which is given by the derivatives along the orbit:

$$\begin{aligned} \left| \prod_{t=0}^{k-1} f'[p(t)] \right| < 1 & : \text{ stable orbit,} \\ \left| \prod_{t=0}^{k-1} f'[p(t)] \right| > 1 & : \text{ unstable orbit.} \end{aligned} \quad (2.1)$$

If the product in this equation is exactly equal to one, one has to consider higher-order derivatives to get information about the stability of the orbit.

A periodic point with a stable orbit is called a ‘sink’, whereas a periodic point with an unstable orbit is called a ‘source’. If an orbit converges to a periodic orbit, it is called asymptotically periodic.

2 Chaotic map networks

The average per-step divergence of nearby points along the orbits is quantified by the Lyapunov number $\Theta[x(0)]$ of the orbit $\{x(0), x(1), \dots\}$, which for a one-dimensional map f is given by

$$\Theta[x(0)] = \lim_{t \rightarrow \infty} \left(|f'[x(0)]| \cdot |f'[x(1)]| \cdot \dots \cdot |f'[x(t)]| \right)^{1/t}, \quad (2.2)$$

if this limit exists. The Lyapunov exponent $\mu[x(0)]$ of this orbit is defined as the natural logarithm of the Lyapunov number:

$$\mu[x(0)] = \lim_{t \rightarrow \infty} \frac{1}{t} \left(\ln |f'[x(0)]| + \dots + \ln |f'[x(t)]| \right). \quad (2.3)$$

Hence the stability of a periodic point corresponds to a negative Lyapunov exponent. Note that the concept of Lyapunov numbers and exponents also applies to nonperiodic orbits. A bounded orbit, which is not asymptotically periodic and has a positive Lyapunov exponent, is called chaotic. Such an orbit shows sensitive dependence on initial conditions, that means that even infinitesimally close points move after sufficiently large number of iterations at least some prescribed nonzero distance away.

The definitions in the last paragraph apply to specific orbits of a map, which often, depending on the initial value, can be either chaotic or periodic. In order to make more general statements about a map, it is useful to consider probability distributions of its iterates for various initial conditions [22, 94].

Consider an ensemble of different initial conditions $x(0)$. For a certain subset of the phase space $A \subseteq I$, the probability measure $\omega(A; 0)$ gives the probability of having $x(0) \in A$. The probability density $\rho(x; 0)$ is defined by

$$\omega(A; 0) = \int_A dx \rho(x; 0). \quad (2.4)$$

Consider the orbits of different initial values $x(0)$ under the map $f(x)$, which are initially distributed according to the probability density $\rho(x; 0)$. The probability measure $\omega(A; t)$ of these iterates after t iterations of the map is given by

$$\omega(A; t) = \int_A dx \rho(x; t). \quad (2.5)$$

It holds

$$\omega(A; t+1) = \omega(f^{-1}(A); t), \quad (2.6)$$

where $f^{-1}(A)$ denotes the preimage of A . This relation follows from the fact, that the probability of having iterates $x(t+1)$ in the subset A must be equal to the probability of having iterates $x(t)$ in the preimage $f^{-1}(A)$.

An invariant probability measure satisfies the condition

$$\omega(A; t+1) = \omega(A; t), \quad (2.7)$$

that is, it describes a stationary state of the probability measure. The corresponding probability density is called an invariant density.

Ensemble averages over an observable $O(x)$ are obtained by

$$\langle O \rangle_{\text{ensemble}} = \int_I dx \rho(x) O(x). \quad (2.8)$$

I assume an invariant density, so the index t in $\rho(x; t)$ has been omitted.

A time average of the observable $O(x)$ is defined by

$$\langle O \rangle_{\text{time}, x(0)} = \lim_{t \rightarrow \infty} \frac{1}{t} \sum_{\tau=0}^{t-1} O[x(\tau)], \quad (2.9)$$

which in general depends on the initial value $x(0)$.

A map $f(x)$ together with an invariant density ρ is called ‘ergodic’, if for every observable $O(x)$ the ensemble average with respect to ρ is equal to the time average for arbitrary initial conditions up to a set of measure zero. Consequently, for such an ergodic map one obtains the invariant measure by iterating an initial value and counting the relative number of iterates in a certain subset A of the phase space [22].

Usually there exist different invariant measures for a certain map [22]. For example, consider a map $f(x)$ with an unstable fixed point p_f . The Dirac delta function $\delta(x - p_f)$ is an invariant density of the map, but since the fixed point is unstable, this density is only relevant for the fixed point itself and its preimages. In contrast, a natural invariant measure is the invariant measure, which one obtains by iterating a randomly chosen point [22]. It is relevant for all values of the phase space up to a subset of measure zero.

By means of this probability concept one can apply a Lyapunov exponent to a map $f(x)$ rather than to a single orbit. If there exist a natural invariant measure for the map, it implies that the right-hand side of Eq. (2.3) is the same for all initial values $x(0)$ up to set of measure zero. In general this is then called the Lyapunov exponent of the map, without stating explicitly the reference to the respective natural invariant measure¹

2.1.2 Examples of chaotic maps

The circle map On the unit circle, denoted by S^1 , a point is determined by an angle $\phi \in [0, 2\pi)$ measured in radians. The circle map $C : S^1 \rightarrow S^1$ defined by

$$C_m(\phi) = m \cdot \phi \pmod{2\pi}, \quad (2.10)$$

where m denotes an integer larger one, is a simple example for a chaotic map [39]. One can write the angle $\phi(t)$ as

$$\phi(t) = 2\pi \left(\sum_{j=1}^{\infty} \frac{s_j(t)}{m^j} \right) \quad (2.11)$$

¹To be precise, this holds if the map has only one attractor. If there are several attractors in the system, one has to attribute natural invariant measures to each attractor, and in general obtains different Lyapunov exponents. See Ref. [94] for details)

2 Chaotic map networks

with $s_j(t) \in \{0, 1, \dots, m-1\}$. The most common case is $m = 2$, where Eq. (2.11) is just the binary representation of the angle ϕ .

In this representation Eq. (2.10) reads

$$\begin{aligned}
\phi(t+1) &= 2\pi \left(\sum_{j=1}^{\infty} \frac{s_j(t+1)}{m^j} \right) \\
&= C_m[\phi(t)] \\
&= m \cdot \phi(t) \pmod{2\pi} \\
&= m \cdot 2\pi \left(\sum_{j=1}^{\infty} \frac{s_j(t)}{m^j} \right) \pmod{2\pi} \\
&= 2\pi \left(\sum_{j=1}^{\infty} \frac{s_j(t)}{m^{j-1}} \right) \pmod{2\pi} \\
&= 2\pi \left(s_1(t) + \sum_{j=2}^{\infty} \frac{s_{j-1}(t)}{m^j} \right) \pmod{2\pi} \\
&= 2\pi \left(\sum_{j=2}^{\infty} \frac{s_{j-1}(t)}{m^j} \right) \tag{2.12}
\end{aligned}$$

By comparing the first and the last line of this set of equations, this leads to $s_j(t+1) = s_{j-1}(t)$. Thus, if one identifies ϕ with the sequence s_1, s_2, \dots , the action of the circle map $C_m(\phi)$ on ϕ corresponds to a shift of the sequence $s_2 \rightarrow s_1, s_3 \rightarrow s_2, \dots$, denoted as a Bernouilli shift. Accordingly the circle map $C_m(\phi)$ is equivalent to a Bernouilli shift of m symbols [39].

The baker map Consider the map $B(x) : [0, 1] \rightarrow [0, 1]$ (called baker map) defined by

$$B(x) = \begin{cases} 2x & 0 \leq x < \frac{1}{2}, \\ 2x - 1 & \frac{1}{2} \leq x \leq 1. \end{cases} \tag{2.13}$$

Obviously it holds that $|B'(x)| = 2$ for all $x \in [0, 1]$, so every orbit has Lyapunov exponent $\ln 2$. Consequently no stable periodic orbit exist, and this map is chaotic (see Ref. [39]).

The logistic map The logistic map $L(x) : [0, 1] \rightarrow [0, 1]$ is defined by

$$L(x) = ax(1-x). \tag{2.14}$$

This map is chaotic for $a = 4$, with Lyapunov exponent $\ln 2$ for all chaotic orbits [36, 39].

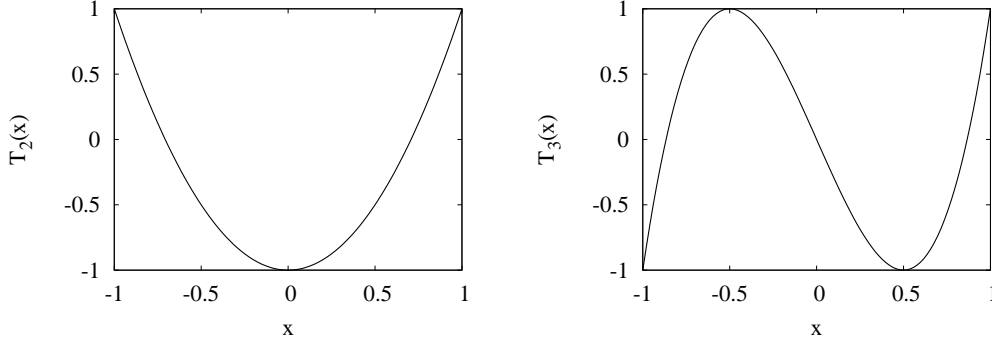


Figure 2.1: Tchebycheff polynomials of second order $T_2(x)$ (left) and third order $T_3(x)$ (right).

Tchebycheff polynomials Of special interest in this thesis is a class of maps denoted as Tchebycheff polynomials $T_m : \mathbb{R} \rightarrow \mathbb{R}$, defined as

$$\begin{aligned}
 T_0(x) &= 1, \\
 T_1(x) &= x, \\
 T_2(x) &= 2x^2 - 1, \\
 T_3(x) &= 4x^3 - 3x.
 \end{aligned} \tag{2.15}$$

Higher order polynomials can be determined by the following relation:

$$T_{m+1}(x) = 2xT_m(x) - T_{m-1}(x). \tag{2.16}$$

For $m \geq 2$ these polynomials are chaotic with Lyapunov exponent $\ln m$ for chaotic orbits. Fig. 2.1 shows $T_2(x)$ and $T_3(x)$. All Tchebyscheff polynomials map the interval $[-1, 1]$ to itself, so for an initial value $x(0)$ in this set, all future iterations also remain in this set. In the following I will always assume that the dynamics is restricted to this interval $[-1, 1]$.

For $T_m : [-1, 1] \rightarrow [-1, 1]$ holds

$$T_m = \cos[m \arccos x]. \tag{2.17}$$

To show the chaotic behaviour of Tchebycheff polynomials one uses the concept of topological conjugacy [39]. For this purpose define $h : S^1 \rightarrow [-1, 1]$ by $h(\phi) = \cos \phi$, and furthermore $C_m(\phi) = m\phi$ as the circle map. Note that the function $h(\phi)$ is just a projection from S^1 to the x -axis. It follows

$$\begin{aligned}
 h \circ C_m(\phi) &= \cos[m\phi] \\
 &= \cos[m \arccos[\cos[\phi]]] \\
 &= T_m(\cos \phi) \\
 &= T_m \circ h(\phi).
 \end{aligned} \tag{2.18}$$

By use of the fact that the circle map is chaotic, one can show via this relation that the Tchebycheff polynomials are also chaotic for $m \geq 2$. The circle map $C_m(\phi)$ and the m th order Tchebycheff polynomial are said to be semi-conjugated (instead of conjugated), since $h(\phi) = \cos \phi$ is not injective, but always maps two different points on the unit circle S^1 to the same point on the real axis. A consequence of this semi-conjugacy to the circle map is that the m th order Tchebycheff polynomial is also semi-conjugated to a Bernouilli shift of m symbols. By means of this semi-conjugacy it can also be shown that the Tchebycheff polynomials are ergodic with the natural invariant density of all Tchebycheff polynomials with $m \geq 2$ given by [17]

$$\rho(x) = \frac{1}{\pi\sqrt{1-x^2}}. \quad (2.19)$$

One can calculate time averages of observables $O(x)$ by

$$\langle O \rangle = \int_{-1}^1 dx \rho(x) O(x). \quad (2.20)$$

Higher-order correlation functions of iterates $x(t)$ of Tchebyscheff maps are given by

$$\begin{aligned} \langle x(t + \tau_1) \cdots x(t + \tau_r) \rangle_{\text{time}} &= \langle f^{\tau_1}[x(t)] \cdots f^{\tau_r}[x(t)] \rangle \\ &= \int_{-1}^1 dx \rho(x) f^{\tau_1}(x) \cdot f^{\tau_2}(x) \cdots f^{\tau_r}(x). \end{aligned} \quad (2.21)$$

In Ref. [55] it has been shown, that compared with other maps \tilde{T} conjugated to a Bernouilli shift, Tchebycheff maps have least non-vanishing higher-order correlations. In this sense the iterates of these maps are closest to uncorrelated Gaussian white noise, obtained by a smooth deterministic system [17]. This interpretation of Tchebycheff polynomials as being ‘most random’ will be of further relevance in later chapters of this thesis.

2.1.3 Higher-dimensional maps

The definition of orbits, fixed points and periodic points of higher-dimensional maps $\mathbf{f} : \mathbb{R}^N \rightarrow \mathbb{R}^N$ is analogous to the case of one-dimensional maps as given before [3, 94]. The stability of a fixed point $\mathbf{p} \in \mathbb{R}^N$ of \mathbf{f} depends on its Jacobian matrix $\mathbf{Df}(\mathbf{p})$, defined as

$$\mathbf{Df}(\mathbf{p}) = \begin{pmatrix} \frac{\partial f_1}{\partial x_1}(\mathbf{p}) & \cdots & \frac{\partial f_1}{\partial x_N}(\mathbf{p}) \\ \vdots & & \vdots \\ \frac{\partial f_N}{\partial x_1}(\mathbf{p}) & \cdots & \frac{\partial f_N}{\partial x_N}(\mathbf{p}) \end{pmatrix}. \quad (2.22)$$

The fixed point \mathbf{p} is a source, if all eigenvalues of $\mathbf{Df}^k(\mathbf{p})$ are greater 1. If there exist both some eigenvalues with magnitude larger 1 and some smaller 1, \mathbf{p} is called a saddle. Just like a source, a saddle point has an unstable orbit. In case all eigenvalues are smaller 1, the fixed point \mathbf{p} is a sink and has a stable orbit. The same principle

holds for periodic points \mathbf{p} with period k , where \mathbf{f} has to be replaced by \mathbf{f}^k . For a periodic orbit $\{\mathbf{p}(0), \mathbf{p}(1), \dots, \mathbf{p}(k-1)\}$ of period k one obtains by use of the chain rule

$$\mathbf{Df}^k[\mathbf{p}(0)] = \Pi_{t=0}^{k-1} \mathbf{Df}[\mathbf{p}(t)]. \quad (2.23)$$

Thus the stability of a periodic orbit of period k is determined by the eigenvalues of the product matrix of the k Jacobian matrices along the orbit.

The concept of Lyapunov exponents as a measure of the divergence or contraction of nearby orbits can also be applied to higher-dimensional maps. Different from the one-dimensional case, the Lyapunov exponent might not only depend on the initial condition, but in general will depend on the direction in which the orbits are initially separated. Consider an initial condition $\mathbf{x}(0)$ and an infinitesimal displacement in the direction of a tangent vector $\xi(0)$. The evolution equation of this tangent vector is given by

$$\xi(t) = \mathbf{Df}[\mathbf{x}(t-1)] \cdot \xi(t-1), \quad (2.24)$$

and consequently

$$\xi(t) = \left(\Pi_{\tau=0}^{t-1} \mathbf{Df}[\mathbf{x}(\tau)] \right) \cdot \xi(0). \quad (2.25)$$

The Lyapunov exponent for initial condition $\mathbf{x}(0)$ and initial displacement $\xi(0)$ is defined as

$$\begin{aligned} \mu[\mathbf{x}(0), \xi(0)] &= \lim_{t \rightarrow \infty} \frac{1}{t} \ln \left[\frac{|\xi(t)|}{|\xi(0)|} \right] \\ &= \lim_{t \rightarrow \infty} \frac{1}{t} \ln \left[\frac{|\mathbf{Df}^t[\mathbf{x}(0)] \cdot \xi(0)|}{|\xi(0)|} \right]. \end{aligned} \quad (2.26)$$

For an N -dimensional map \mathbf{f} and a given initial value $\mathbf{x}(0)$, there will be at most N different Lyapunov exponents, depending on the choice of the tangent vector $\xi(0)$. One can show [94] that the Lyapunov exponent is approximated by

$$\mu[\mathbf{x}(0), \xi(0)] = \lim_{t \rightarrow \infty} \frac{1}{2t} \ln \left[\frac{\xi^T(0) \cdot \mathbf{J}_t[\mathbf{x}(0)] \cdot \xi(0)}{|\xi(0)|^2} \right], \quad (2.27)$$

with

$$\mathbf{J}_t[\mathbf{x}(0)] = (\mathbf{Df}^t[\mathbf{x}(0)])^T \cdot \mathbf{Df}^t[\mathbf{x}(0)]. \quad (2.28)$$

By choosing eigenvectors \mathbf{u}_j of $\mathbf{J}_t[\mathbf{x}(0)]$ as the tangent vector $\xi(0)$, one obtains the N Lyapunov exponents $\mu_1[\mathbf{x}(0)] \geq \mu_2[\mathbf{x}(0)] \dots \geq \mu_N[\mathbf{x}(0)]$. For an arbitrary tangent vector $\xi(0)$, the corresponding Lyapunov exponent $\mu[\mathbf{x}(0), \xi(0)]$ will converge to the largest one of these exponents, that is $\mu_1[\mathbf{x}(0)]$. In order to let $\mu[\mathbf{x}(0), \xi(0)]$ converge to $\mu_2[\mathbf{x}(0)]$, the initial tangent vector $\xi(0)$ has to lie in the subspace orthogonal to the eigenvector \mathbf{u}_1 of $\mathbf{J}_t[\mathbf{x}(0)]$. Subsequent Lyapunov exponents are obtained by this principle of choosing the initial tangent vector orthogonal to the eigenvectors associated with the already calculated exponents.

A common way to visualize the different Lyapunov exponents of an N -dimensional map is to consider an N -dimensional ball with infinitesimal radius dr around the

initial value $\mathbf{x}(0)$. Under application of the map \mathbf{f} the shape of this ball will evolve into a ellipsoid centered around the respective iteration of the initial value $\mathbf{x}(0)$. For large times the rate of growth or shrinking of the principal axes of this ellipsoid is given by the Lyapunov exponents [3].

As for one-dimensional maps, a Lyapunov exponent larger zero indicates chaotic behaviour and sensitivity to initial conditions. For numerical techniques and further details on Lyapunov exponents of higher-dimensional maps see Refs [3, 94].

2.2 Complex networks

Many complex systems consisting of a collection of objects which in some way relate to each other can be described by complex networks. In such a description, the individual object is abstracted as a node and the relation between objects as links connecting these nodes. Examples vary from interconnected neurons in the brain over power plants connected by transmission lines to social systems, consisting of a multitude of interacting individuals. In the following sections the notation for the description of networks is defined, and basic network structure properties and structure models are introduced. For a more detailed account on complex networks see Refs. [2, 28, 42, 88].

2.2.1 Properties of complex networks

A network or graph $G = (\mathcal{V}, \mathcal{E})$ consists of the set of vertices (or nodes) $\mathcal{V} = \{v_1, v_2, \dots, v_N\}$ and the set of edges (or links) $\mathcal{E} = \{\hat{e}_1, \hat{e}_2, \dots, \hat{e}_K\}$, where the edge \hat{e}_k formally is given by the pair $\{i, j\}$ of vertices i and j which are connected by it. The size of the network is given by $N = |G| = |\mathcal{V}|$, the number of edges by $K = ||G|| = |\mathcal{E}|$. For a directed network the link \hat{e}_k is the ordered pair (i, j) , where the first node i is denoted as the target and the second node j as the source of the edge. The node v_i will usually be referred to by its label i , whereas the link (i, j) is sometimes also referred to by the notation e_{ij} . For an undirected network e_{ij} and e_{ji} relate to the same link. For convenience I will also use the notation (i, j) for a link in an undirected network.

It is often helpful to represent the network G by its adjacency matrix A , which is defined by

$$A_{ij} = \begin{cases} 1 & : \text{there is a link from node } j \text{ to node } i, \\ 0 & : \text{else.} \end{cases} \quad (2.29)$$

Obviously for an undirected network the adjacency matrix is symmetric.

If two nodes i and j are connected by a link (i, j) , they are called neighbouring or adjacent. The set of neighbouring nodes of a node i is denoted by the symbol \mathcal{N}_i , with the number of neighbors $|\mathcal{N}_i|$ called the degree k_i of the vertex. The degree distribution $p(k)$ gives the probability that a randomly picked vertex has degree k . It provides a first characterization of the network structure. Note that for directed

networks this notion has to be extended to the out-degree (in-degree) k_i^{out} (k_i^{in}) and the respective sets \mathcal{N}_i^{out} (\mathcal{N}_i^{in}) and degree distributions $p^{out}(k)$ ($p^{in}(k)$). It holds

$$\begin{aligned} k_i^{in} &= \sum_{j \in \mathcal{V}} A_{ij}, \\ k_i^{out} &= \sum_{j \in \mathcal{V}} A_{ji}. \end{aligned} \quad (2.30)$$

A graph $G' = (\mathcal{V}', \mathcal{E}')$ is called a subgraph of $G = (\mathcal{V}, \mathcal{E})$, if $\mathcal{V}' \subseteq \mathcal{V}$ and $\mathcal{E}' \subseteq \mathcal{E}$. If the subgraph G' contains all links of G that join nodes in $\mathcal{V}' \subseteq \mathcal{V}$, then $G' = G[\mathcal{V}']$ is called the subgraph of G induced by \mathcal{V}' .

A path $P[i \rightarrow j]$ in G is a subgraph consisting of a chain of neighbourings node and their connecting links, starting at node i and ending at node j , with no edge or node repeated. The path length $l(P[i \rightarrow j])$ is the number of links contained in this chain. The shortest path $P_s[i \rightarrow j]$ is a path from i to j with a minimal number of links in it. One calls the path length $l(P_s[i \rightarrow j])$ of such a shortest path from i to j the distance d_{ij} . If for every pair of distinct nodes i and j there exists a path $P[i \rightarrow j]$, the graph is said to be connected, otherwise it is called unconnected. For a connected graph the average distance

$$\langle d \rangle = \frac{1}{N(N-1)} \sum_{i,j \in \mathcal{V}} d_{ij} \quad (2.31)$$

is another basic characterization of the graph structure. If the graph consists of different unconnected subgraphs, the distance between nodes from different subgraphs and consequently the average distance is infinite. In this case one has to consider an alternative measure, called the network efficiency

$$E = \frac{1}{N(N-1)} \sum_{i,j \in \mathcal{V}} \frac{1}{d_{ij}}. \quad (2.32)$$

Note that a fully connected network, where every vertex has a direct edge to every other vertex, shows $E = \langle d \rangle = 1$.

Different from the degree distribution $p(k)$, which only contains information about the local properties of the network, the average distance incorporates global information about the network topology.

Another basic property of complex networks is the degree of clustering, that is the likelihood that two neighbours of some node are neighbours themselves. Such a structure of three mutually connected nodes is called a triangle or 3-cycle. In undirected networks this clustering property is formally accounted for by the clustering coefficient C_i of node i , defined by

$$C_i = \frac{2o_i}{k_i(k_i - 1)}, \quad (2.33)$$

where o_i denotes the number of edges between neighbors of i , and $k_i(k_i - 1)/2$ is the maximum possible number of such edges. The clustering coefficient $\langle C \rangle$ of the

network is then defined as the average of C_i over all vertices:

$$\langle C \rangle = \frac{1}{N} \sum_{i \in \mathcal{V}} C_i. \quad (2.34)$$

Symmetries of networks I call vertices or sets of vertices similar, if the network looks identical for them. For example in a ring structure, for any node the networks looks the same, thus all nodes are called similar. The same holds for all coupled pairs of nodes in a ring. However, if for instance node i is part of a triangle in the network, whereas node j is not, for these two nodes the networks obviously has to look different and hence i and j cannot be similar.

Weighted networks The binary structure of graphs, where a link is either present or absent, can be generalized by the concept of (link-) weights. A weighted network $G^W = (\mathcal{V}, \mathcal{E}, \mathcal{W})$ consists of the set of vertices and edges, and additionally a set of weights $\mathcal{W} = \{\tilde{w}_1, \tilde{w}_2, \dots, \tilde{w}_K\}$, which are real numbers associated with the respective links. The weights are usually represented by the matrix W , given by

$$W_{ij} = \begin{cases} \tilde{w}_l & : \text{weight of the link } \hat{e}_l = (i, j) \text{ from node } j \text{ to node } i, \\ 0 & : \text{node } j \text{ and node } i \text{ are not connected by a link.} \end{cases} \quad (2.35)$$

For weighted networks the notion of the degree k_i of a node i can be generalized to the node strength s_i , given by

$$s_i = \sum_{j \in \mathcal{V}} W_{ij}. \quad (2.36)$$

If $W_{ij} = A_{ij}$, the network is unweighted and it holds $s_i = k_i$. For a directed weighted network, the node properties analogous to the node in-degree and out-degree are the node input strength $s_i^{in} = \sum_{j \in \mathcal{V}} w_{ij}$ and output strength $s_i^{out} = \sum_{j \in \mathcal{V}} w_{ji}$.

2.2.2 Network structure models

In this section I will review some selected network models and their structural properties. For a wider and more general review and the comparison between network models and real networks see Refs. [2, 28, 42, 88].

Complete graph A complete graph is a network of N vertices with $K = N(N-1)/2$ edges. Every vertex is directly connected to every other vertex, so the average distance is minimal with $\langle d \rangle = 1$, and the clustering coefficient is maximal with $\langle C \rangle = 1$. The degree distribution is a delta function $p(k) = \delta[k - (N-1)]$.

Regular structures A very simple and regular network structure is a one-dimensional lattice of N vertices with periodic boundary conditions, that is a ring with next-neighbor coupling. For this network the adjacency looks as follows:

$$A = \begin{pmatrix} 0 & 1 & 0 & \cdots & 0 & 1 \\ 1 & 0 & 1 & 0 & \cdots & 0 \\ \cdots & \cdots & \cdots & \cdots & \cdots & \cdots \\ 1 & 0 & \cdots & 0 & 1 & 0 \end{pmatrix}. \quad (2.37)$$

For every vertex has the same degree $k_i = 2$, the degree distribution is given by a delta function $p(k) = \delta(k - 2)$. Due to the absence of any triangles in such a ring structure, the network shows vanishing clustering coefficient $\langle C \rangle = 0$, while the average distance $\langle d \rangle$ scales with the ring size N for large rings [88].

A generalization of this concept is the m -ring, that is a one-dimensional lattice with periodic boundary conditions, where every vertex is connected to its m neighbours on the left and on the right. The degree distribution is displayed by a delta function $P(k) = \delta(k - 2m)$, while the clustering coefficient can be calculated to be $\langle C \rangle = 3(m - 1)/2(2m - 1)$, and the average distance $\langle d \rangle \sim N/m$ for $1 \ll m \ll N$ [28].

Random graphs An undirected random graph in the sense of Erdős and Rényi (called a ER random graph or a Poisson graph) is constructed by connecting every possible pair out of a set of N vertices with probability p . On average such a ER random graph has $K = pN(N - 1)/2$ edges, and the average degree is $\langle k \rangle = p(N - 1)$. The degree distribution is a binomial distribution, which for large N and fixed $\langle k \rangle$ can be approximated by a Poisson distribution [42]:

$$p(k) = \exp[-\langle k \rangle] \frac{\langle k \rangle^k}{k!}. \quad (2.38)$$

Since the probability p of having an edge (j, k) is independent from the occurrence of edges (i, j) and (i, k) , the average clustering coefficient is given by $\langle C \rangle = p = \langle k \rangle / (N - 1)$, which converges to zero for large N and $\langle k \rangle \ll N$ (or $p \ll 1$). The average distance scales for large network sizes N as $\langle d \rangle \sim \ln[N] / \ln[\langle k \rangle]$ [28].

Small-world networks A complex network is said to have the small-world property if the average distance $\langle d \rangle$ depends at most logarithmically on the network size N [28]. This is the case for random graphs as defined in the last paragraph, whereas for m -rings the average distance grows lineary with N , so these regular networks do not have the small-world property. On the other hand m -rings show a highly clustered structure, in contrast to the the vanishing clustering coefficient of large random graphs [88].

The so-called small-world networks are constructed by methods similar to the seminal Watts and Strogatz model, proposed in Ref. [114]. These networks combine the

small-world property with a large clustering coefficient. The essential ingredient is the addition of short cuts to the regular network structures of m -rings by rewiring of edges or by the addition of randomly place new edges. On the one hand the connection of formerly unconnected neighbourhoods by these short cuts lowers the clustering coefficient $\langle C \rangle$, while on the other hand a decrease of the average distance $\langle d \rangle$ is induced. Since the decrease of the average distance happens faster than the decrease of the clustering coefficient, for a small, but non-zero short-cut density one obtains networks which show the small-world property but still have large clustering coefficients [28].

r -partite networks An r -partite network $(\mathcal{V}, \mathcal{E})$ of size N consists of r adjoint subsets of vertices $\mathcal{V}_1, \mathcal{V}_2, \dots, \mathcal{V}_r$ with $\bigcup_{i=1}^r \mathcal{V}_i = \mathcal{V}$, such that for every edge $(i, j) \in \mathcal{E}$ the vertices i and j lie in different sets $\mathcal{V}_{\alpha(i)}$ and $\mathcal{V}_{\alpha(j)}$. Here the discrete valued function $\alpha(i)$ allocates to every vertex i the corresponding label of the set with $v_i \in \mathcal{V}_{\alpha(i)}$. The number of vertices in every subset is denoted by $N_i = |\mathcal{V}_i|$.

By proper labeling of the vertices, the adjacency matrix A of such an r -partite network can be displayed in the following block form:

$$A = \begin{pmatrix} 0 & A_{(1,2)} & A_{(1,3)} & \cdots & A_{(1,r)} \\ A_{(2,1)} & 0 & A_{(2,3)} & \cdots & A_{(2,r)} \\ \vdots & & \ddots & & \vdots \\ A_{(r-1,1)} & \cdots & A_{(r-1,r-2)} & 0 & A_{(r-1,r)} \\ A_{(r,1)} & \cdots & A_{(r,r-2)} & A_{(r,r-1)} & 0 \end{pmatrix}, \quad (2.39)$$

with $A_{(i,j)}$ a $N_1 \times N_2$ matrix, and $A_{(i,j)} = A_{(j,i)}^T$ for undirected networks.

In later chapters I will devote some attention to undirected bipartite networks $(\mathcal{V}, \mathcal{E}) = (\mathcal{V}_1 \cup \mathcal{V}_2, \mathcal{E})$, that is r -partite networks with $r = 2$. With $A_{(1,2)} = B$, the corresponding adjacency matrix of such an undirected bipartite network is of the form

$$A = \begin{pmatrix} 0 & B \\ B^T & 0 \end{pmatrix}. \quad (2.40)$$

In a complete bipartite network, all $N_1 \cdot N_2$ edges between the two different subsets are present. The special case with $N_1 = (N - 1)$ and $N_2 = 1$ is called the star network. A bipartite m -ring is a one-dimensional lattice, where every vertex is connected to each m vertices on the left and on the right, under omittance of edges between vertices from the same subset. Analogously a bipartite random graph is constructed by connecting all pairs of nodes from the two subsets with probability p . It is easy to see that the average degree for such a random bipartite graph is given by $\langle k \rangle = 2pN_1N_2/N$, and the degree distribution is a superposition of two binomial distributions.

2.3 Coupled map networks

A coupled map network (CMN) is high-dimensional time-discrete dynamical system consisting of the following three ingredients:

- A weighted network $G^W = (\mathcal{V}, \mathcal{E}, \mathcal{W})$ which describes the network topology and the strength of the connections.
- Local variables $\mathbf{x}_i \in I$, lying in a local space $I \subset \mathbb{R}^m$ associated with every vertex $v_i \in \mathcal{V}$.
- Functions $\mathbf{f} : I \rightarrow I$ which act on the variables \mathbf{x}_i .

In the following a CMN will always be described by the update rules for the individual variables $\mathbf{x} \in I$. For a mathematically more rigorous definition of CMNs see Ref [71]. Unless otherwise stated, it is assumed that $I = [a, b]$ is an interval in \mathbb{R} and accordingly the x_i are one-dimensional variables. A wide class of coupled map networks is defined by

$$x_i(t+1) = (1 - s_i)f_i[x_i(t)] + \sum_{j=1}^N A_{ij}W_{ij}g_{ij}[x_j(t)]. \quad (2.41)$$

Here the $x_i(t)$ are time-dependent local variables and the A_{ij} are the entries of the adjacency matrix of a weighted network $G^W = (\mathcal{V}, \mathcal{E}, \mathcal{W})$. The functions $f_i : I \rightarrow I$ are called local functions, whereas the functions $g_{ij} : I \rightarrow I$ are denoted as coupling functions. The weight W_{ij} determines the strength of the link (i, j) from node j to node i . To assure that the orbits of the local variables stay in the interval I , the total input strength $s_i = \sum_j A_{ij}W_{ij}$ has to fulfill $0 \leq s_i \leq 1$.

Note that the CMN is in principle a high-dimensional map $\mathbf{F} : \tilde{I} \rightarrow \tilde{I}$, where \tilde{I} is the product space of the N local spaces. Consequently, the stability of periodic orbits, Lyapunov exponents, etc. can be calculated as described in the previous section. However, for large system sizes N this can be very complicated, and one treats CMNs rather as a complex system assembled from local maps than as one high-dimensional map.

The simplest realizations of CMNs belonging to this class are given by undirected networks with $A_{ij} = A_{ji}$ and the choice $W_{ij} = \epsilon/k_i$, where $\epsilon \in [0, 1]$ is denoted as the coupling strength. With the local functions $f_i(x) = f(x)$ being the same for all vertices i , and the coupling functions $g_{ij}(x) = g(x)$ also equal for all connected pairs of vertices, the evolution equation is written as

$$x_i(t+1) = (1 - \epsilon)f[x_i(t)] + \frac{\epsilon}{k_i} \sum_{j=1}^N A_{ij}g[x_j(t)]. \quad (2.42)$$

CMNs of this form will be denoted as standard coupled map networks.

2.3.1 Coupled map lattices

Coupled map lattices were introduced by Kaneko in the 80s as a simple model showing the essential features of spatiotemporal chaos [64]. In their simplest version they are defined as standard CMNs on a ring-network with $f(x) = g(x)$:

$$x_i(t+1) = (1 - \epsilon)f[x_i(t)] + \frac{\epsilon}{2} \left(f[x_{i-1}(t)] + f[x_{i+1}(t)] \right). \quad (2.43)$$

2 Chaotic map networks

The local function $f(x)$ is often given by the logistic map $f(x) = L(x) = ax(1 - x)$. Depending on the parameters a and ϵ , various patterns in these CMLs can be observed. For a respective phase diagram in the a - ϵ plane see Refs. [37, 66, 69, 70]. In the following I will qualitatively review different patterns, which are observed in this class of dynamical systems [69].

- A *frozen random pattern* is characterized by a sequence of regular and chaotic domains along the lattice, where the size and periodicity of the dynamics in this domains can greatly vary. These patterns are fixed in time and depend on the initial conditions.
- For increasing nonlinearity a , for a transient dynamics larger domains become unstable and split into smaller domains. The boundaries of the domains start to move, and domains of a few special sizes are selected. The spatial sequence of the domains after this selection process is then fixed in time. The dynamics in the domains is less chaotic, that is a motion with shorter temporal periods. This kind of dynamical behaviour is called *pattern selection*.
- For larger coupling parameter ϵ , the domain structures of the frozen random pattern or pattern selection can move in time, denoted as *travelling waves*.
- One special example of pattern selection is that of a zig-zag pattern. The dynamics in the zig-zag patterns varies with a spatial and temporal period 2. Regions of the zig-zag pattern with different phase are separated by a *defect*, which shows chaotic behaviour. The defect moves in space, which can be interpreted as a kind of *Brownian motion*. These moving defects pair-annihilate by collision. Depending on the nonlinearity parameter a , the number of defects thus decrease in time, or defects are recreated spontaneously (*defect turbulence*).
- In *spatiotemporal intermittency* (STI), ordered states with a spatially regular structure and periodic or weakly chaotic dynamics ('laminar regions') and spatially disorganized, temporally chaotic regions ('burst regions') coexist in space-time. One differentiates between two types of STI. For the first type (STI-I), a laminar lattice site remains laminar, as long as there are no bursts in its neighbourhood. This differs STI-I from the second type of spatiotemporal intermittency (STI-II), for which such spontaneous creation of bursts occur.
- For *fully developed spatiotemporal chaos* (FDSTC), the dynamics does not show an ordered spatial structure, but can rather be interpreted as a product state of local chaos with a rapid decay of spatial correlations.

In order to analyze quantitatively the coupled map lattice dynamics, several concepts from low-dimensional dynamical system theory have been extended to the spatio-temporal dynamics, for instance Lyapunov analysis, information flow or correlations [67, 69, 70]. Also different approaches towards a statistical mechanical theory of spatio-temporal chaos have been made, using a mapping to a statistical mechanics

of a higher-dimensional spin system, or the application of the Perron-Frobenius operator. For details see Refs. [31, 67, 69, 70].

Possible applications of coupled map lattice models include pattern formation, crystal growth and boiling, convection, spiral and traveling waves in excitable media, cloud dynamics or simple abstract models for ecological systems or evolution. For short reviews and references of the respective articles see Ref. [70]. Another application for coupled map lattices in quantum field theories and elementary particle physics was proposed in Ref.[17] and further developed in Refs. [18, 19, 20]. In these models certain classes of coupled map lattice called ‘chaotic strings’ are introduced as spatio-temporal chaotic models of vacuum fluctuations. Since this application is the main topic of this thesis, ‘chaotic strings’ are introduced separately in the next chapter.

In the physics community in the last decade the attention has shifted from studying regular CMLs to more general CMNs involving complex network topologies. However, there is still ongoing research in this field. As an example in Ref. [33] the behaviour of small truncated coupled map lattice with random inputs at the boundaries has been investigated. More recently, Ref. [95] considers desynchronized wave patterns in synchronized chaotic regions of CMLs, whereas in Ref. [109] the properties of Lyapunov vectors in CMLs are studied. The chaoticity of CMLs from the viewpoint of a thermodynamic formalism is accounted for by calculation of the statistics of Kolmogorov-Sinai entropy [22] and Lyapunov exponents in Ref. [104].

2.3.2 Globally coupled maps

Globally coupled maps (GCMs) are a mean-field version of the CML, given by

$$x_i(t+1) = (1 - \epsilon)f[x_i(t)] + \frac{\epsilon}{N} \sum_{j=1}^N f[x_j(t)]. \quad (2.44)$$

This corresponds to a standard CMN on a fully connected network structure. As the local dynamics usually the logistic map $L(x) = 1 - ax^2$ is chosen. By use of the transformation $y_i(t) = f[x_i(t)]$ Eq. (2.44) can be recast into

$$y_i(t+1) = f \left[(1 - \epsilon)y_i(t) + \frac{\epsilon}{N} \sum_{j=1}^N y_j(t) \right], \quad (2.45)$$

which is an equivalent model.

One observes the following dynamical attractors of the globally coupled map dynamics [70]:

- In a *coherent state with complete synchronization* all orbits $x_i(t)$ coincide, and the dynamics is governed by local logistic map $x(t+1) = f[x(t)]$.
- For a *completely desynchronized state* all network sites i have different values $x_i(t)$ at all times and oscillate without any synchronization.

2 Chaotic map networks

- *Cluster synchronization* denotes the state, where the set of vertices is partitioned into several clusters, whose vertices are mutually synchronized. One classifies the state of the GCMs by the size of the respective clusters N_k . The dynamics of r -cluster GCMs are governed by the equations

$$X_k(t+1) = (1 - \epsilon)f[X_k(t)] + \sum_{l=1}^r \epsilon_l f[X_l(t)], \quad (2.46)$$

where $X_k(t)$ denotes the value of $x(t)$ in the k -th cluster. The couplings ϵ_k are ‘effective couplings’, given by

$$\epsilon_k = \epsilon \frac{N_k}{N}. \quad (2.47)$$

The limits of cluster synchronization are the coherent state with $r = 1$ cluster, and the completely desynchronized state with $r = N$ different clusters.

As for the CML one can study the behaviour of the GCMs dependent on the nonlinearity a of the logistic map and the coupling parameter ϵ , and thus obtains a phase diagram in the a - ϵ plane [68]. In most cases one finds various states with different clusterings as attractors of the dynamics, whose selection depends on the initial condition. Dependent on the relative number of initial condition (basins of attraction) which lead to either coherent, few-cluster or many-cluster states, one differentiates four phases [70]:

- Coherent phase: Coherent states for (almost) all initial conditions
- Ordered phase: Few-cluster states for (almost) all initial conditions
- Partially ordered phase: Coexistence of few-cluster and many-cluster states, dependent on the initial conditions
- Desynchronized phase: Many-cluster states (with $k \approx N$) for (almost) all initial conditions

The respective phases and their bifurcations have been studied qualitatively as well as quantitatively in great detail (see Ref. [70] and references therein).

2.3.3 Coupled map networks with complex topology

These models provide a generalization from the lattice structure in CMLs and the fully connected network structure for GCMs to complex network topologies as introduced in Sec. 2.2.2. Up to now, the research in this field focuses on various synchronization phenomena. Respective models and results will be reviewed in Sec. 8.1 of this thesis.

2.3.4 Dynamical network structures

In the studies presented so far, the underlying network structure $(\mathcal{V}, \mathcal{E})$ and the weights \mathcal{W} were assumed to be static. Recently also CMNs on time-varying network structures have been studied, in some cases with an interplay between the dynamics on the network with the evolution of the network itself.

A very general and mathematically rigorous study on the synchronization of CMNs with time-varying couplings has been performed in [76]. In Ref. [99] the spatiotemporal dynamics of a standard CML with dynamical rewiring is studied. In this study at every time step a fraction p of randomly chosen nearest-neighbour edges are replaced by random edges. As a result the authors observe synchronized periodic orbits in an optimal window of p values. A generalization of this model is considered in Ref. [83], where different rewiring frequencies are taken into account. Keeping the rewiring probability p constant, two different types of dynamics are observed. For slow rewiring, the dynamics of the network is spatiotemporally chaotic, whereas for a high frequency of rewiring for a large range of coupling strengths the systems ends up in a spatiotemporal fixed point.

3 Chaotic strings

‘Chaotic strings’ are a class of coupled map lattices with second and third order Tchebycheff polynomials as the local dynamics [17]. These dynamical systems have been proposed by Beck as spatio-temporal models for rapidly fluctuating scalar fields associated with vacuum fluctuations [16, 17]. Apart from this application, these models are also very interesting from a dynamical point of view. Based on a simple time-discrete evolution equation with only a few parameters, the resulting dynamics show various spatio-temporal patterns, ranging from regular patterns to fully developed spatio-temporal chaos (for some impressions see Figs 3.1-3.12).

In the following chapter I will introduce the chaotic string dynamics and related observables, show some of the results connected with the coupling constants of the standard model of particle physics, and give a short review on a possible physical embedding. For more details see Refs. [16, 17, 18, 19, 20, 21].

3.1 Definition

Chaotic strings as defined in [17] are standard CMNs on a ring-network, with the evolution equation given by

$$x_i(t+1) = (1 - \epsilon)f[x_i(t)] + \frac{\epsilon}{2}\left(g[x_{i-1}(t)] + g[x_{i+1}(t)]\right), \quad (3.1)$$

where it is supposed that node i is connected to nodes $i+1$ and $i-1$. For $i=1$ and $i=N$ periodic boundary conditions are invoked (see the adjacency matrix displayed in Eq. (2.37)). The local space associated with every vertex is the interval $I = [-1, 1]$, and the functions $f(x)$ and $g(x)$ are given by positive and negative Tchebycheff polynomials $T_{\pm m}(x) = \pm T_m(x)$ up to order $m=3$ as defined in Sec. (2.1.2).

Various combinations of different Tchebycheff polynomials can be inserted into Eq. (3.1), but in Ref. [17] only the six combinations displayed in Tab. 3.1 are of interest. In the construction of the model presented in Ref. [17] it is assumed that at every time step two actions occur: The first part consists in an update of the variable $x_i(t) \rightarrow x_i(t')$ at every vertex i :

$$x_i(t) \rightarrow x_i(t') = T_{\pm m}[x_i(t)] = \pm T_m[x_i(t)]. \quad (3.2)$$

The second action $x_i(t') \rightarrow x_i(t+1)$ consists in the application of a diffusive coupling to the nearest neighbours:

$$x_i(t') \rightarrow x_i(t+1) = (1 - \epsilon)x_i(t') + \frac{\epsilon}{2}\left(x_{i-1}(t') + x_{i+1}(t')\right). \quad (3.3)$$

3 Chaotic strings

label	$[m, s, b]$	$f(x)$	$g(x)$
2A	$[2, +, 1]$	$T_2(x) = 2x^2 - 1$	$T_2(x) = 2x^2 - 1$
2B	$[2, +, 0]$	$T_2(x) = 2x^2 - 1$	$T_1(x) = x$
2A ⁻	$[2, -, 1]$	$T_2(x) = 2x^2 - 1$	$T_{-2}(x) = -(2x^2 - 1)$
2B ⁻	$[2, -, 0]$	$T_2(x) = 2x^2 - 1$	$T_{-1}(x) = -x$
3A	$[3, +, 1]$	$T_3(x) = 4x^3 - 3x$	$T_3(x) = 4x^3 - 3x$
3B	$[3, +, 0]$	$T_3(x) = 4x^3 - 3x$	$T_1(x) = x$

Table 3.1: The six dynamics considered in Ref. [17]. The label $[m, s, b]$ denotes the order of the Tchebycheff polynomial (m), and distinguishes between forward ($s = 1$) and backward coupling ($s = 0$), and diffusive (+) and anti-diffusive (-) coupling.

This kind of procedure is called diffusive forward coupling, and corresponds to the chaotic string dynamics labeled by 2A and 3A, depending on the order of the Tchebycheff polynomial which is applied in the first action of every time step [17]. In a variation of this procedure, in the second action the coupling occurs not to the already updated neighbouring variables $x_{i\pm 1}(t')$, but to the original variables $x_{i\pm 1}(t)$. This variation is denoted as backward coupling (in the literature also called linear coupling [37]), and is applied in the chaotic string dynamics labeled by 2B and 3B. Another variation is the application of a so-called anti-diffusive coupling, that is

$$x_i(t') \rightarrow x_i(t+1) = (1 - \epsilon)x_i(t') - \frac{\epsilon}{2}(x_{i-1}(t') + x_{i+1}(t')) \quad (3.4)$$

in the case of forward coupling (occurring for the 2A⁻ dynamics), or

$$x_i(t') \rightarrow x_i(t+1) = (1 - \epsilon)x_i(t') - \frac{\epsilon}{2}(x_{i-1}(t) + x_{i+1}(t)). \quad (3.5)$$

when backward coupling is applied (corresponding to the 2B⁻ dynamics).¹

The N one-dimensional local variables $x_i(t)$ of the chaotic string can be written as an N -dimensional vector $\mathbf{x}(t)$, with the evolution equation then defined as the application of an N -dimensional function $\mathbf{f}(\mathbf{x})$. To distinguish the different chaotic string dynamics, this function is given a label $[m, s, b]$, with $m \in \{\pm 2, \pm 3\}$, $s = \pm$, and $b \in \{0, 1\}$. The label m denotes the order of the (positive or negative) Tchebycheff polynomial which is applied, whereas the label s distinguishes between diffusive (+) or anti-diffusive (-) coupling. The label s accounts for either forward ($s = 1$) or backward ($s = 0$) coupling. With the definition $T_m^1(x) = T_m(x)$ and $T_m^0(x) := x$, the chaotic string dynamics can be written as

$$\mathbf{x}(t+1) = \mathbf{f}^{[m, s, b]}[\mathbf{x}(t); \epsilon], \quad (3.6)$$

¹ Note that this anti-diffusive coupling is only applicable if the local space is an interval of the form $I = [-a, a]$. For an asymmetric phase space $[-b, a]$ with $b \neq a$ the application of the evolution equation possibly yields a value outside the phase space.

with

$$f_i^{[m,s,b]}(\mathbf{x}; \epsilon) = (1 - \epsilon)T_m(x_i) + s\frac{\epsilon}{2}\left(T_m^b(x_{i-1}) + T_m^b(x_{i+1})\right). \quad (3.7)$$

For each choice of parameters $[m, s, b]$ the coupling ϵ is defined in the interval $[0, 1]$.

In principle the different combinations of positive/negative Tchebycheff polynomial, forward/backward coupling and diffusive/anti-diffusive coupling lead to eight different chaotic string dynamics for every order m of Tchebycheff polynomials. By symmetry arguments, the number of different chaotic strings can be reduced to the six dynamics displayed in Tab. 3.1 [17, 102]. These discrete symmetries of chaotic strings will be studied in detail in Chap. 4.

In order to get a first impression of how the dynamics looks like depending on the coupling parameter ϵ , in Figs. 3.1-3.6 for each of the six chaotic strings a snapshot of all $x_i(t)$ at some time t for $\epsilon \in [0, 1]$ is displayed. Figs. 3.8-3.12 show spatio-temporal pattern as well as overlaid return plots for some dynamics and coupling values (see Ref. [17] for similar and additional figures). One observes chaotic behaviour, with the x_i randomlike distributed in the interval $[-1, 1]$, but also synchronized states and various complicated patterns.

3 Chaotic strings

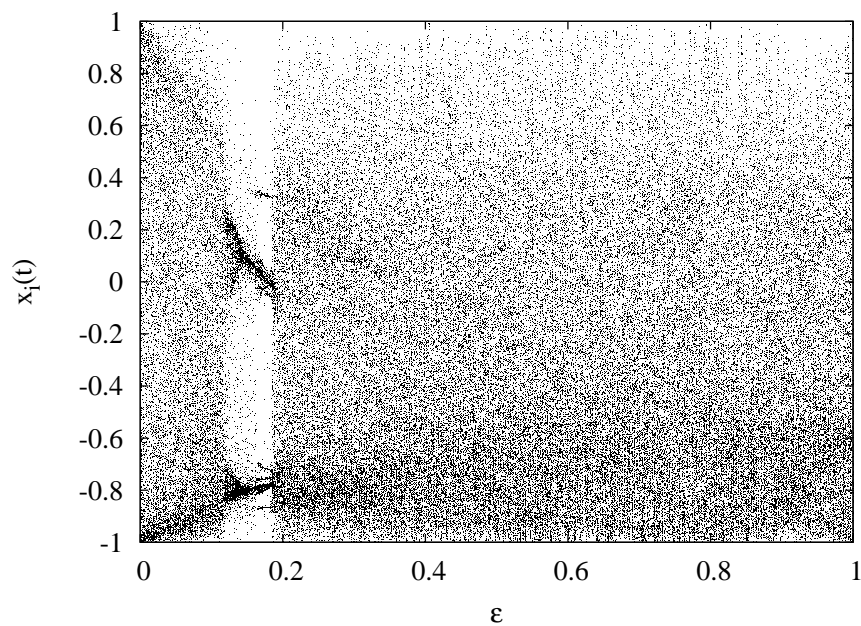


Figure 3.1: Snapshot of the $2A$ chaotic string dynamics. All $x_i(t)$ of the chaotic string dynamics of a lattice with size $N = 101$ are displayed at one time step t after $T = 10^3$ iterations.

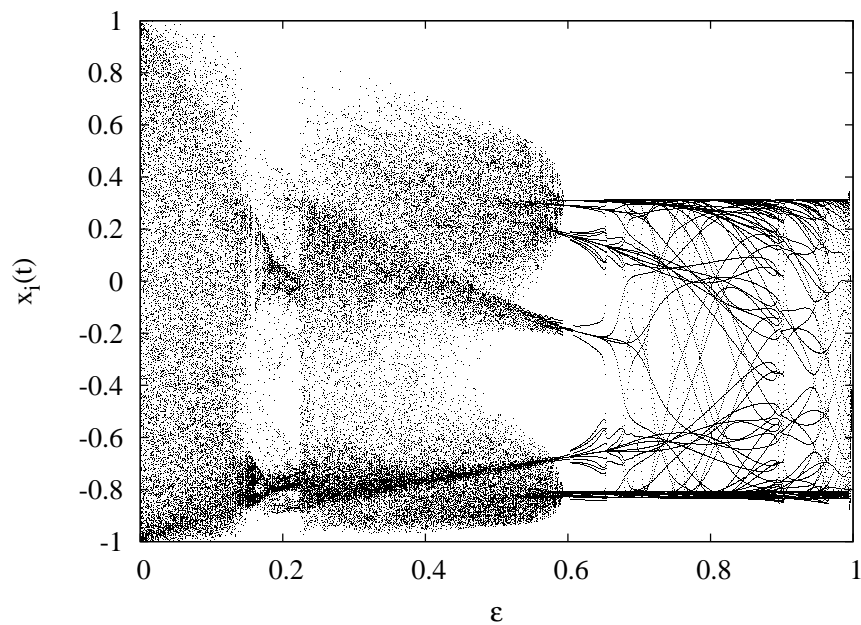


Figure 3.2: Same as Fig. 3.1, but for the $2B$ dynamics.

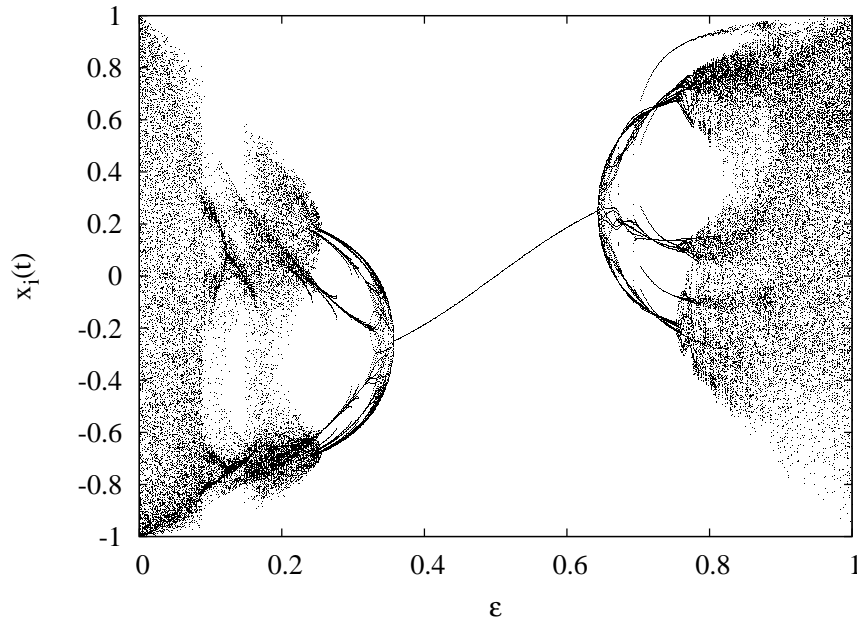


Figure 3.3: Same as Fig. 3.1, but for the $2A^-$ dynamics.

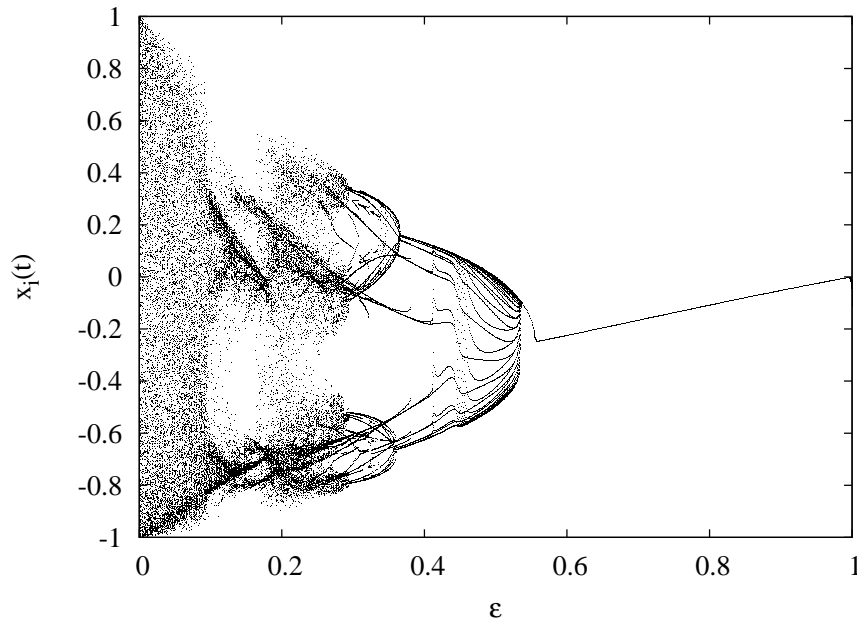


Figure 3.4: Same as Fig. 3.1, but for the $2B^-$ dynamics.

3 Chaotic strings

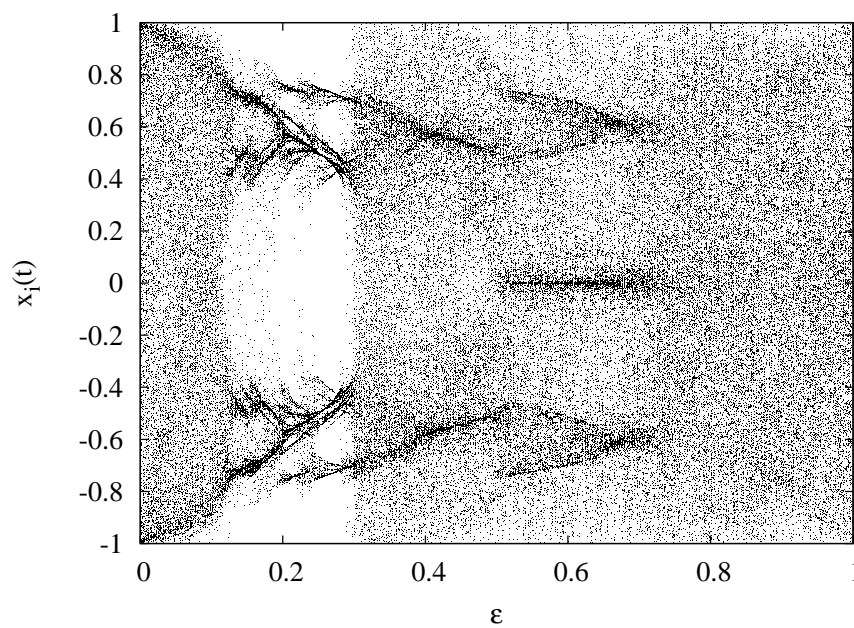


Figure 3.5: Same as Fig. 3.1, but for the $3A$ dynamics.

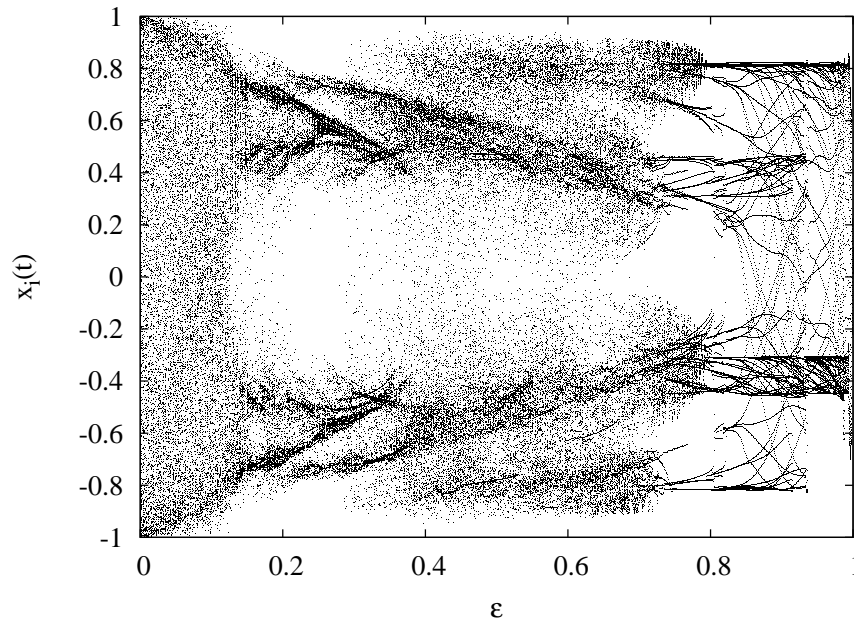


Figure 3.6: Same as Fig. 3.1, but for the $3B$ dynamics.

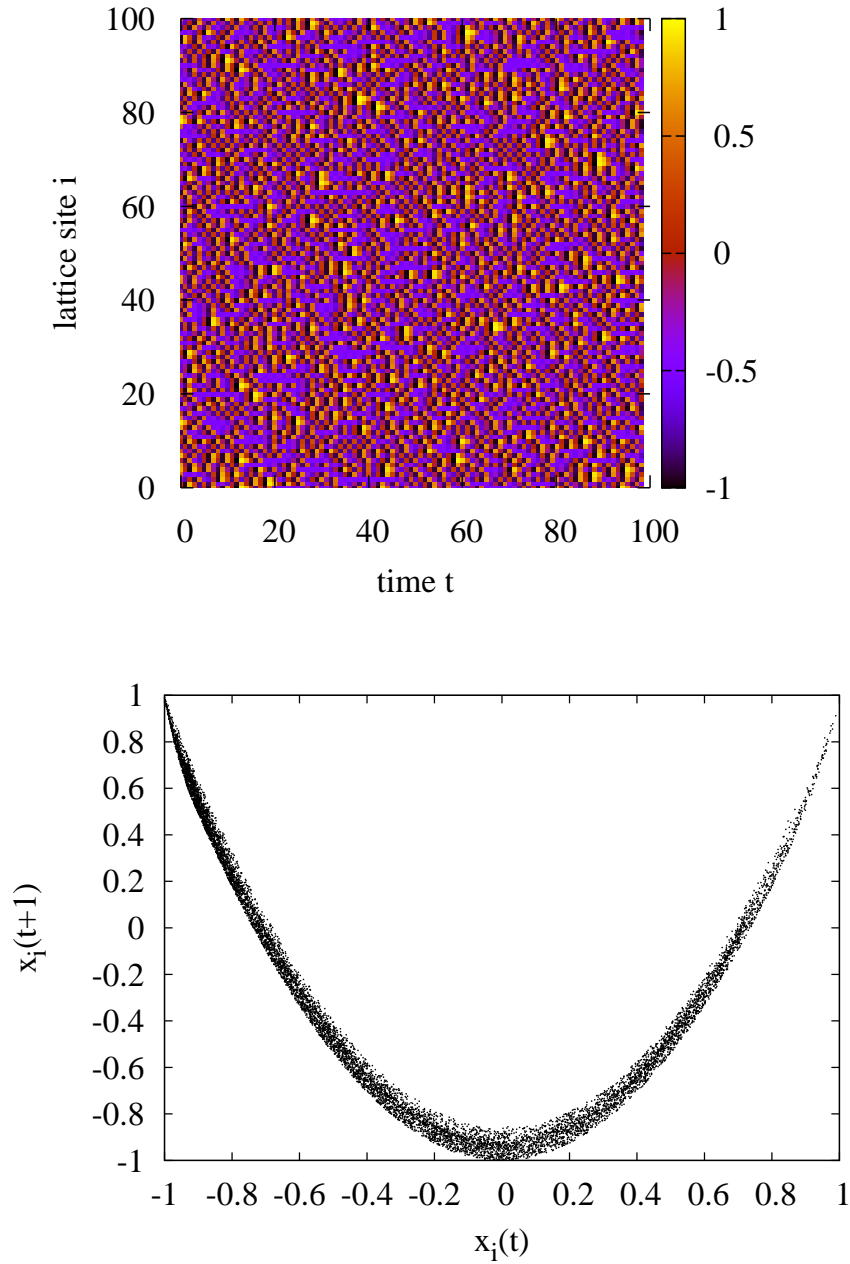


Figure 3.7: The 2A chaotic string dynamics for $\epsilon = 0.08$. Top: All $x_i(t)$ for 100 iterations after a transient $T_0 = 10^3$. Bottom: Scatterplot of all $x_i(t+1)$ vs. $x_i(t)$ for the iterations shown in the upper figure. Network size $N = 101$.

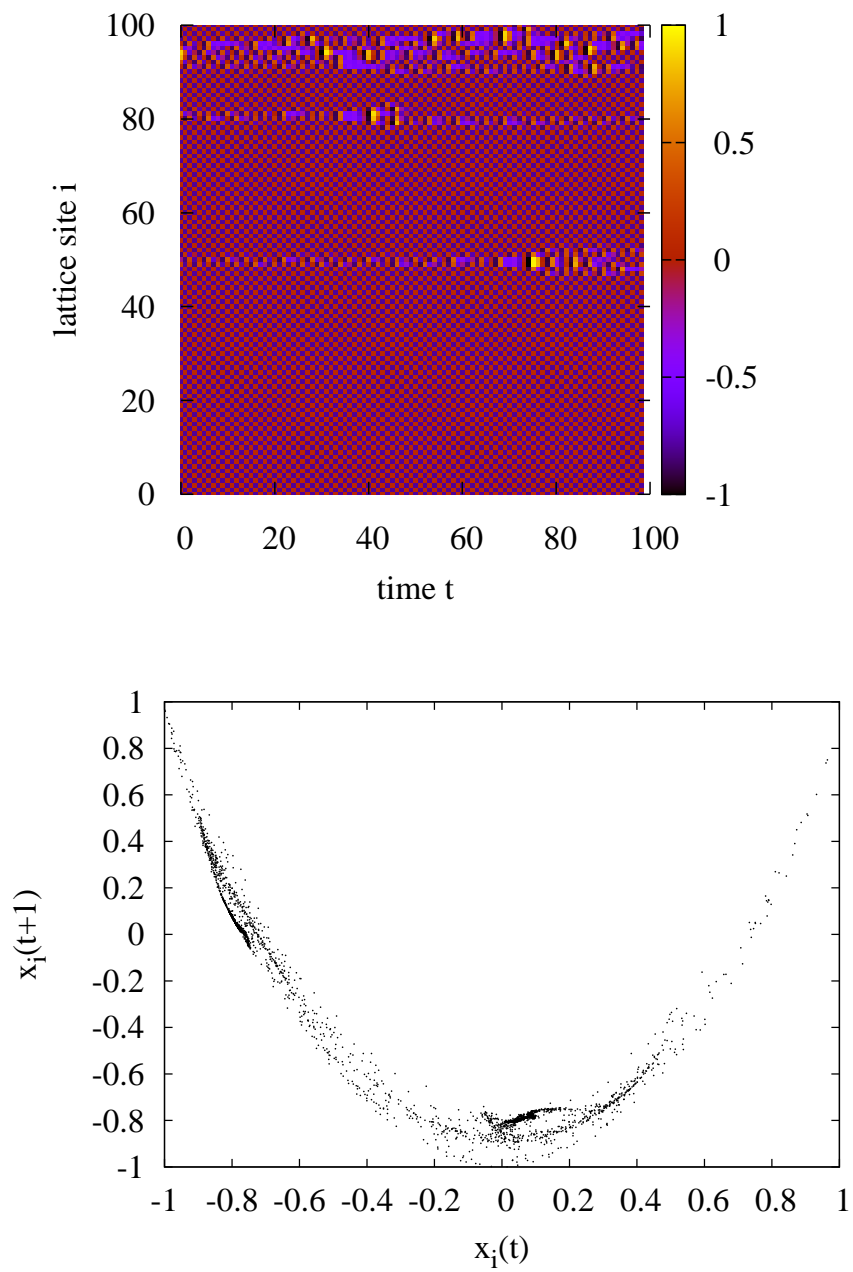


Figure 3.8: Same as Fig. 3.7, but for $\epsilon = 0.16$.

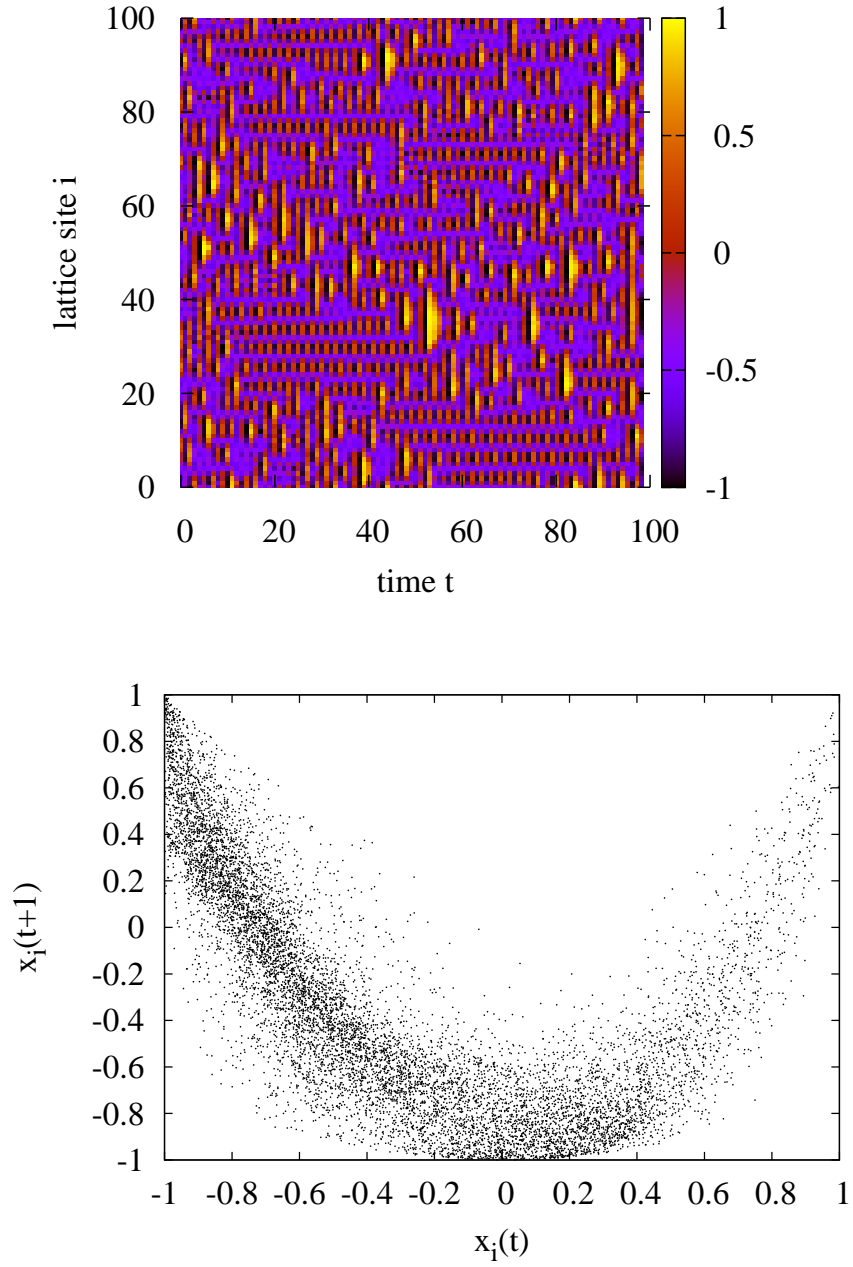


Figure 3.9: Same as Fig. 3.7, but for $\epsilon = 0.85$.

3 Chaotic strings

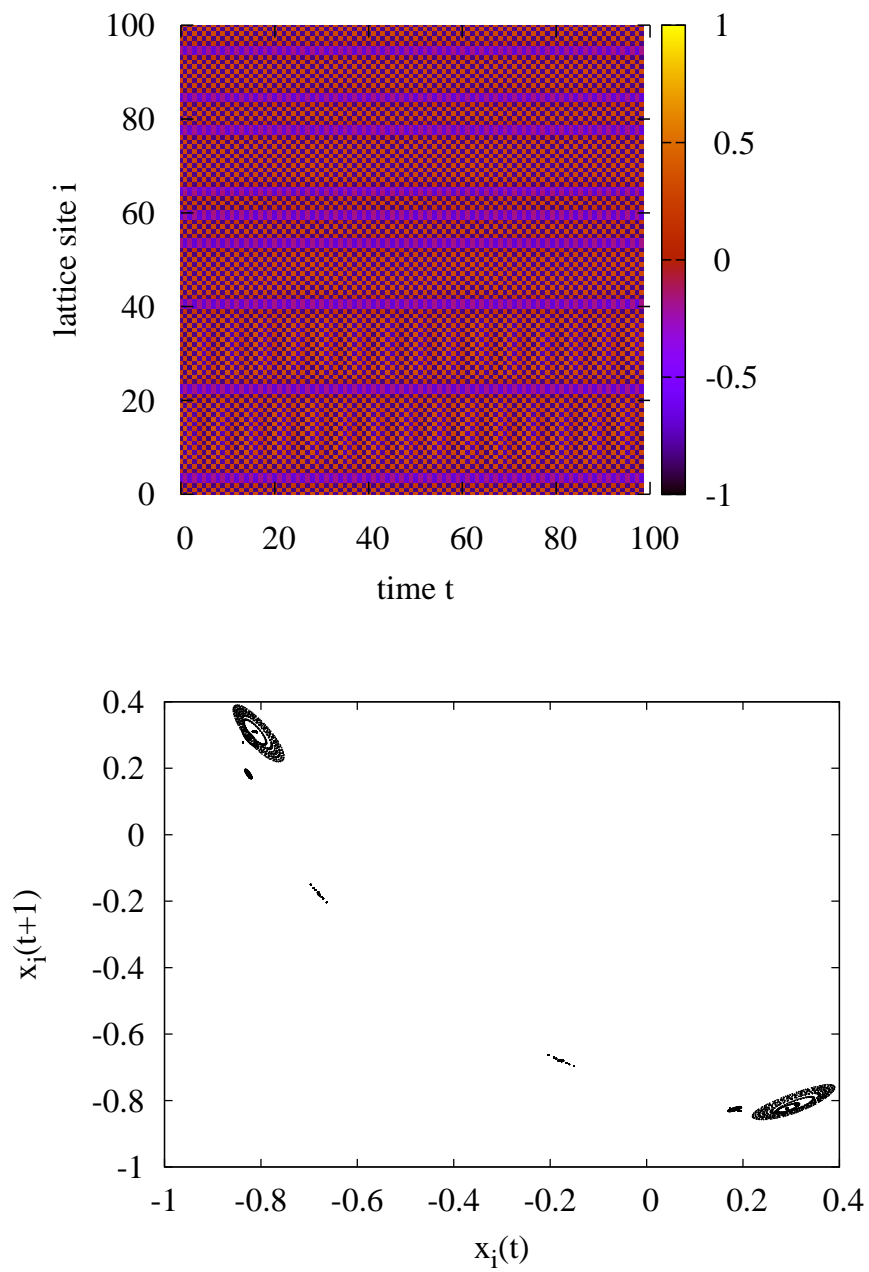


Figure 3.10: Same as Fig. 3.7, but for the $2B$ dynamics with $\epsilon = 0.59$.

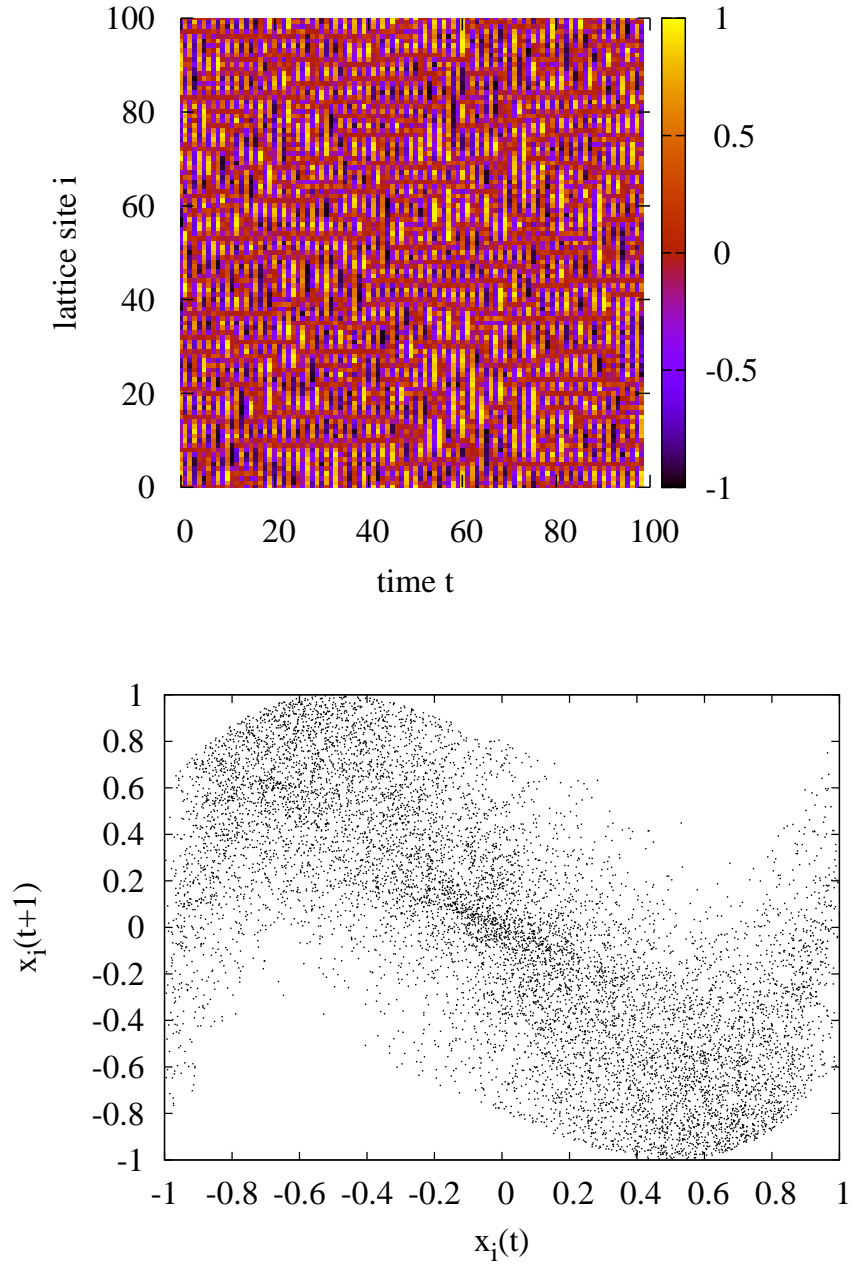


Figure 3.11: Same as Fig. 3.7, but for the 3A dynamics with $\epsilon = 0.8$.

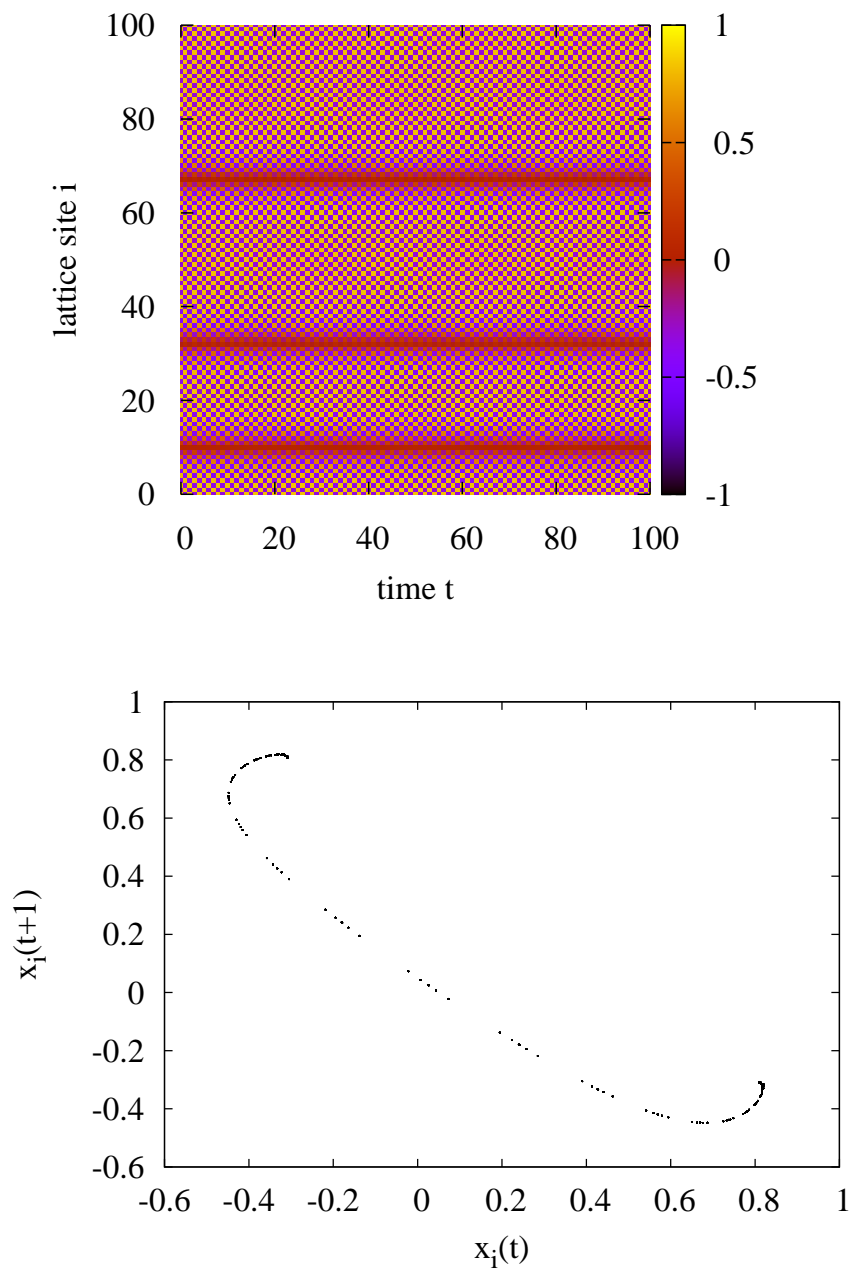


Figure 3.12: Same as fig. 3.7, but for the $3B$ dynamics with $\epsilon = 0.95$.

3.2 Interaction energy and self energy

In Ref. [17] two types of formal energies are introduced, which generate the chaotic string dynamics. Whereas the self energy is connected with the individual update, the interaction energy accounts for the diffusive or anti-diffusive coupling. Of main interest are time-averages of these observables, that is expectation values of the form

$$O^{[m,s,b]}(\epsilon) = \langle O(\mathbf{x}) \rangle = \lim_{T \rightarrow \infty} \frac{1}{T - T_0} \sum_{t=T_0+1}^T O[\mathbf{x}(t)], \quad (3.8)$$

with

$$\mathbf{x}(t) = (\mathbf{f}^{[m,s,b]})^t[\mathbf{x}(0); \epsilon] \quad (3.9)$$

The expectation depends on the underlying dynamics $[m, s, b]$, the coupling ϵ and the form of the observable O . It might also depend on the ring size N , but I assume that the network is large enough to neglect this dependence [33, 52]. The function O might explicitly depend on the whole set of local variables x_i (for instance as an average operator), or only on certain subsets or individual x_i . For numerical calculations one will choose a finite number of iterations T and a finite transient T_0 , resulting in some small statistical fluctuations. However, note that also for $T \rightarrow \infty$ for a given dynamics $\mathbf{f}^{[m,s,b]}(\mathbf{x}; \epsilon)$ the value $O^{[m,s,b]}(\epsilon)$ might depend on the initial value $\mathbf{x}(0)$. Unless otherwise stated I will assume that for the considered dynamics almost all initial values $\mathbf{x}(0)$ yield the same expectation value – if for some dynamics $\mathbf{f}^{[m,s,b]}(\mathbf{x}; \epsilon)$ the contrary is observed, the expectation is stated as not being well-defined. This topic will be of further interest in Sec. 5.1.

Self energy As stated before, the first action in the evolution equation of the chaotic string dynamics is an update of $x_i(t)$ at every node i by application of the m th order Tchebycheff polynomial. This can be written as

$$x_i(t') - x_i(t) = T_m[x_i(t)] - x_i(t) =: F[x_i(t)], \quad (3.10)$$

with $F(x)$ being a formal force causing the change of the variable $x_i(t)$. This force can be generated by a formal potential energy $V(x)$ via

$$F(x) = -\frac{\partial}{\partial x} V(x). \quad (3.11)$$

This energy $V(x)$, denoted as self-energy in Ref. [17], is then given by

$$V(x) = -\int_0^x [T_m(x') - x'] dx' + C, \quad (3.12)$$

where C is some constant. Since the self energy is not connected with the coupling term in the evolution equation, its definition does not depend on the choice of forward

3 Chaotic strings

or backward coupling (label b) and diffusive or anti-diffusive coupling (label s). For $m = \pm 2$ and $m = \pm 3$ one gets

$$\begin{aligned} V_{\pm}^{(2)}(x) &= \pm \left(-\frac{2}{3}x^3 + x \right) + \frac{1}{2}x^2 + C, \\ V_{\pm}^{(3)}(x) &= \pm \left(-x^4 + \frac{3}{2}x^2 \right) + \frac{1}{2}x^2 + C. \end{aligned} \quad (3.13)$$

The self energy of the chaotic string dynamics with the parameters $[m, s, b]$ at lattice site i is given by

$$\begin{aligned} V_i^{[\pm 2, s, b]}(\epsilon) &= \pm \left\langle -\frac{2}{3}(x_i)^3 + x_i \right\rangle + \left\langle \frac{1}{2}(x_i)^2 \right\rangle + C, \\ V_i^{[\pm 3, s, b]}(\epsilon) &= \pm \left\langle -(x_i)^4 + \frac{3}{2}(x_i)^2 \right\rangle + \left\langle \frac{1}{2}(x_i)^2 \right\rangle + C. \end{aligned} \quad (3.14)$$

The notation $\langle \cdot \rangle$ refers to the time-average as given in Eq. (3.8). In Ref. [17] the additive constant C is chosen as

$$C = -\frac{1}{2} \langle (x_i)^2 \rangle, \quad (3.15)$$

so only the first term on the left handed side of Eq. (3.14) remains. This choice of the additive constant is mainly motivated by aesthetical reasons – for instance it holds $V_{[+|m|, s, b]}(\epsilon) + V_{[-|m|, s, b]}(\epsilon) = 0$ (see Ref. [17] for details). However, this definition bears the problem that C is not a constant, but in fact a function of the coupling ϵ in the same way as the self energy itself. Therefore the theory put forward in Ref. [17] should provide further physical motivation for this specific choice.

Interaction energy Similar to the definition of the self energy, in Ref. [17] a formal interaction energy is defined. This interaction energy generates the second action applied in the evolution equation, that is the diffusive coupling (label $s = '+'$) as given in Eq. (3.3):

$$x_i(t+1) - x_i(t') = -\frac{\epsilon}{2} \left(x_i(t') - x_{i+1}(t') \right) - \frac{\epsilon}{2} \left(x_i(t') - x_{i-1}(t') \right). \quad (3.16)$$

For anti-diffusive coupling (label $s = '-'$) this reads

$$x_i(t+1) - x_i(t') = -\frac{\epsilon}{2} \left(x_i(t') + x_{i+1}(t') \right) - \frac{\epsilon}{2} \left(x_i(t') + x_{i-1}(t') \right). \quad (3.17)$$

The right-hand side can be interpreted as the sum over forces, each one given by the derivative of a formal interaction energy $W(x_i, x_j)$ times the coupling constant ϵ :

$$-\frac{\partial}{\partial x_j} W(x_i, x_j) = -\frac{1}{2} \left(x_i - s x_j \right), \quad (3.18)$$

where the label $s = \pm$ distinguishes forward from backward coupling. The interaction energy is then given by

$$\begin{aligned} W(x_i, x_j) &= \frac{1}{4}(x_i - sx_j)^2 + C \\ &= -\frac{s}{2}(x_i x_j) + \frac{1}{4}\left((x_i)^2 + (x_j)^2\right) + \hat{C}, \end{aligned} \quad (3.19)$$

where \hat{C} is again an additive constant.

By applying the time average one obtains the observable

$$W_{ij}^{[m,s,b]}(\epsilon) = \left\langle -\frac{s}{2}x_i x_j \right\rangle + \left\langle \frac{1}{4}\left((x_i)^2 + (x_j)^2\right) \right\rangle + \hat{C}, \quad (3.20)$$

which by the choice

$$\hat{C} = -\left\langle \frac{1}{4}\left((x_i)^2 + (x_j)^2\right) \right\rangle \quad (3.21)$$

simplifies to

$$W_{ij}^{[m,s,b]}(\epsilon) = -s \left\langle \frac{1}{2}x_i x_j \right\rangle \quad (3.22)$$

Note that for $\langle (x_i)^2 \rangle = \langle (x_j)^2 \rangle$, this constant \hat{C} has the same value as the constant C which occurs in the definition of the self energy. However, as already stated for the self energy, this \hat{C} is a function of ϵ , resulting in problems for the interpretation as an additive constant.

3.3 Chaotic strings and standard model couplings

Up to now the chaotic string dynamics has been defined as a special type of standard chaotic map networks, with the individual dynamics given by Tchebyscheff polynomials up to third order, and a one-dimensional lattice as the network topology. These kinds of systems are usually considered as prototypic models of complex spatio-temporal behaviour, with applications for pattern formation, flow systems or turbulence, to name just a few [29, 69, 70]. As a new application of coupled map lattices, Refs. [16, 17, 21] claim that the chaotic string model can be used as a model of vacuum fluctuations, which might fix the fundamental constants of the standard model of particle physics. The minimal standard model of particle physics depends on 19 free parameters [32, 49, 56, 110]:

- Three coupling constants g_S, g_W, g_1 for the gauge group $SU(3) \times SU(2) \times U(1)$,
- Yukawa coefficients determining the masses of the six quarks (u, d, c, s, t, b) and three lepton flavors (e, μ, τ),
- Higgs mass and vacuum expectation value,

3 Chaotic strings

zero	running SM coupling
$\epsilon_1^{(3A)} = 0.0008164$	$\alpha_{el}^d(3m_d) \approx 0.0008166$
$\epsilon_2^{(3A)} = 0.0073038$	$\alpha_{el}^e(3m_e) \approx 0.007303$
$\epsilon_1^{(3B)} = 0.0018012$	$\alpha_{weak}^{uR}(3m_u) + \alpha_{el}^d(3m_d) \approx 0.0018$
$\epsilon_2^{(3B)} = 0.017550$	$\alpha_{weak}^{\nu L}(3m_d) + \alpha_{el}^e(3m_e) \approx 0.01755$
$\epsilon_1^{(2A)} = 0.120093$	$\alpha_s(m_W + 2m_d) \approx 0.1208$
$\epsilon_1^{(2B)} = 0.3145$	$\alpha_s(m_{gg^{0++}} + 2m_u)$
$\epsilon_1^{(2A^-)} = 0.1758$	$\alpha_s(m_{gg^{2++}} + 2m_b)$
$\epsilon_1^{(2B^-)} = 0.095370$	$\alpha_s(m_H + 2m_t)$

Table 3.2: Zeros ϵ^* of the interaction energy $W(\epsilon)$ resulting from the coupled string dynamics, and the corresponding standard model (SM) couplings (taken from [17]).

- three angles and a phase of the Cabibbo-Kobayashi-Maskawa matrix,
- a phase for the QCD vacuum.

If one includes Einstein's classical theory of gravity, this amounts to at least 20 adjustable parameters of the standard model of particle physics.

In Sec. 3.2 two kinds of formal energies for the six chaotic string dynamics were introduced. The self and interaction energy are functions of the coupling parameter ϵ . The interesting finding is, that the energies show a distinguished behaviour (zeros with a negative slope for the interaction energy, minima for the self energy) for coupling values ϵ which coincide with running standard model or gravitational couplings $\alpha(E)$, the energy E given by the masses of the known quarks, leptons, and gauge bosons. By identifying $\epsilon = \alpha(E)$, thus one can obtain a large number of very precise predictions. In this thesis I will focus on the interaction energy. For results obtained by considering the self energy of chaotic strings, see Refs. [16, 17, 21, 80]. Table 3.3 displays distinguished zeros of the interaction energy $W(\epsilon)$ and associated running standard model couplings. One observes that the smallest zeros of the $3A$ and $3B$ dynamics numerically coincide with running electroweak couplings at the smallest fermionic mass scales, whereas the smallest zero of the $2A$ dynamics can be identified with the strong coupling at the W boson mass scale. The smallest zero of the $2B^-$ dynamics might allow a prediction of the Higgs mass. The smallest zeros of the $2B$ and $2B^-$ agree with strong couplings at energy scales given by certain glueball masses.

The numerical agreement between numerical values for the distinguished zeros and standard model couplings is impressive. In the next chapter possible physical embeddings for the chaotic string dynamics will be reviewed.

3.4 Physical embedding

In Refs. [16, 17] it was shown that the coupled map lattice dynamics can formally be derived from one-dimensional continuum field theories in the limit of infinite self-interaction strength. The key principles in this derivation are the use of the Parisi-Wu stochastic quantization approach and a transition to discrete space-time and discrete fictitious time, the latter being an additional dimension introduced in this quantization method [15, 82, 87]. A similar formal derivation was performed in Refs. [18, 19, 20, 21], where a stochastically quantized equation of motion of a homogeneous scalar field in Robertson-Walker metric was considered in discrete physical time and fictitious time. In this case one obtains, for a suitable choice of the parameters and the potential the coupled chaotic map lattice dynamics.

The chaotic string dynamics can be interpreted as a dynamics of vacuum fluctuations generating the noise of the Parisi-Wu approach of stochastic quantization [17]. A possible connection to the dark energy of the universe has been proposed in Refs. [20, 21]. The chaotic fields then generate effective potentials for moduli fields, which fix the parameters of the Standard Model. Further interpretations can be found in Ref. [17].

The observables of interest are the ‘self energy’ and the ‘interaction energy’ of the chaotic string, defined in Sec. 3.2. Whereas the self energy is only motivated by the formal derivation of the dynamical equations, the interaction energy can also be interpreted as a correlation measure of the dynamics.

Up to now there is no straightforward method to embed the chaotic strings in already existing physics, but rather different ways of interpreting different parts of the model. One aspect which occurs rather frequently is the notion of a ‘strongest possible chaotic behaviour’, which makes the dynamics suitable to model vacuum fluctuations. For the uncoupled Tchebyscheff maps this strongest possible chaotic behaviour is expressed by least higher-order correlations of the iterates of the map [14, 55]. In this sense these iterates can be called closest to Gaussian White Noise, but still being completely deterministic. For the coupled map lattice with non-vanishing coupling also spatial correlations between different lattice sites occur. Since the interaction energy is basically a correlation function for neighbouring lattices sites, a dynamical state with a vanishing interaction energy may be interpreted as a state of strongest random properties. From this point of view distinguished coupling values are those corresponding to dynamical states of strongest random properties.

4 Discrete symmetries of chaotic strings

In Sec. 3.1 the chaotic string dynamics has been defined. It has been shown that for every order m of the Tchebycheff polynomials invoked in the dynamics, there are eight different combinations of positive/negative polynomial, forward/backward and diffusive/anti-diffusive coupling. In Ref. [17] it has been stated that due to symmetry reasons some of these combinations lead to equivalent dynamics, but a detailed analysis of these symmetry relations has been missing up to now. In the following section I will study discrete symmetries of the chaotic string dynamics and show that several of the dynamics can be transformed into each other by simple discrete coordinate transformations. Also the symmetry properties of the interaction energy and the self energy are considered.

Although in Ref. [17] the dynamics is restricted to a ring network, the symmetry considerations presented here are valid for the more general class of bipartite networks as defined in Sec. 2.2.2, of which the ring network is only one specific example.¹

4.1 Symmetries for the coupled Tchebycheff map dynamics

Consider a standard coupled map network with the functions $f(x)$ and $g(x)$ given by the different combinations of Tchebycheff polynomials as defined in Sec. 3.1:

$$x_i(t+1) = (1 - \epsilon)T_m[x_i(t)] + s \frac{\epsilon}{k_i} \sum_{j=1}^N T_m^b[x_j(t)]. \quad (4.1)$$

For the definition of the labels $[m, s, b]$ see Tab. 3.1. As the underlying topology I consider bipartite networks $(\mathcal{V}, \mathcal{E})$ of size N , which consist of two subsets of vertices $\mathcal{V}_1, \mathcal{V}_2$. Recall that for a bipartite network $\mathcal{V} = \mathcal{V}_1 \cup \mathcal{V}_2$, $\mathcal{V}_1 \cap \mathcal{V}_2 = \emptyset$, and edges only exist between vertices from different sets. A ring is a special example of a bipartite network, reducing Eq. (4.1) to the chaotic string dynamics considered in Ref. [17].

Define the functions $\mathbf{P} : \tilde{I} \rightarrow \tilde{I}$, $\mathbf{P}^{(1)} : \tilde{I} \rightarrow \tilde{I}$ and $\mathbf{P}^{(2)} : \tilde{I} \rightarrow \tilde{I}$ by

$$P_i(\mathbf{x}) = -x_i, \quad (4.2)$$

¹Similar, but more complicated symmetries would hold for general r -partite networks.

$$P_i^{(1)}(\mathbf{x}) = \begin{cases} -x_i & : i \in \mathcal{V}_1 \\ x_i & : i \in \mathcal{V}_2 \end{cases}, \quad (4.3)$$

$$P_i^{(2)}(\mathbf{x}) = \begin{cases} x_i & : i \in \mathcal{V}_1 \\ -x_i & : i \in \mathcal{V}_2 \end{cases}. \quad (4.4)$$

Recall that here \tilde{I} denotes the combined product space of all local intervals $[-1, 1]$. Thus the function $\mathbf{P}^{(1)}$ ($\mathbf{P}^{(2)}$) just flips the sign of all x_i in the subset \mathcal{V}_1 (\mathcal{V}_2), whereas it leaves the x_i in the set \mathcal{V}_2 (\mathcal{V}_1) unaffected. On a ring this operation corresponds to a sign flip at every second ring site. The function \mathbf{P} without index flips the sign at all nodes x_i .

Obviously it holds

$$\mathbf{P} \circ \mathbf{P} = \mathbf{P}^{(1)} \circ \mathbf{P}^{(1)} = \mathbf{P}^{(2)} \circ \mathbf{P}^{(2)} = \mathbf{1}, \quad (4.5)$$

$$\mathbf{P}^{(1)} \circ \mathbf{P}^{(2)} = \mathbf{P}^{(2)} \circ \mathbf{P}^{(1)} = \mathbf{P}. \quad (4.6)$$

Of interest is the dynamical state $\mathbf{x}(t)$ of all variables at time t , which follows from the initial condition $\mathbf{x}(0)$ by applying t times the evolution equation:

$$\mathbf{x}(t) = \mathbf{f}^{[m,s,b]} \circ \left(\mathbf{f}^{[m,s,b]}[\mathbf{x}(t-2)] \right) = \dots = (\mathbf{f}^{[m,s,b]})^t[\mathbf{x}(0)]. \quad (4.7)$$

For convenience at this point I do not explicitly display the coupling ϵ in the function $\mathbf{f}^{[m,s,b]}(\mathbf{x}; \epsilon)$.

One can easily see that Tchebycheff maps of odd order $m_o = 1, 3, \dots$ are odd functions of x ,

$$T_{m_o}(-x) = -T_{m_o}, \quad (4.8)$$

whereas Tchebycheff maps of even order $m_e = 2, 4, \dots$ are even function of x ,

$$T_{m_e}(-x) = T_{m_e}(x). \quad (4.9)$$

Using the odd/even character of the Tchebyscheff polynomials and the transformations \mathbf{P} , $\mathbf{P}^{(1)}$ and $\mathbf{P}^{(2)}$, one can derive the following relations:

Coupled network dynamics based on odd- m Tchebyscheff polynomials ($m_o = 1, 3, \dots$):

$$(\mathbf{f}^{[-m_o,+,1]})^t = \begin{cases} (\mathbf{f}^{[m_o,+,1]})^t & : t \text{ even} \\ \mathbf{P} \circ (\mathbf{f}^{[m_o,+,1]})^t & : t \text{ odd,} \end{cases} \quad (4.10)$$

$$(\mathbf{f}^{[m_o,-,1]})^t = \mathbf{P}^{(1)} \circ (\mathbf{f}^{[m_o,+,1]})^t \circ \mathbf{P}^{(1)}, \quad (4.11)$$

$$(\mathbf{f}^{[-m_o,-,1]})^t = \begin{cases} \mathbf{P}^{(1)} \circ (\mathbf{f}^{[m_o,+,1]})^t \circ \mathbf{P}^{(1)} & : t \text{ even} \\ \mathbf{P}^{(2)} \circ (\mathbf{f}^{[m_o,+,1]})^t \circ \mathbf{P}^{(1)} & : t \text{ odd,} \end{cases} \quad (4.12)$$

$$(\mathbf{f}^{[m_o,-,0]})^t = \mathbf{P}^{(1)} \circ (\mathbf{f}^{[m_o,+,0]})^t \circ \mathbf{P}^{(1)}, \quad (4.13)$$

$$(\mathbf{f}^{[-m_o,+,0]})^t = \begin{cases} \mathbf{P}^{(1)} \circ (\mathbf{f}^{[m_o,+,0]})^t \circ \mathbf{P}^{(1)} & : t \text{ even} \\ \mathbf{P}^{(2)} \circ (\mathbf{f}^{[m_o,+,0]})^t \circ \mathbf{P}^{(1)} & : t \text{ odd,} \end{cases} \quad (4.14)$$

$$(\mathbf{f}^{[-m_o,-,0]})^t = \begin{cases} (\mathbf{f}^{[m_o,+,0]})^t & : t \text{ even} \\ \mathbf{P} \circ (\mathbf{f}^{[m_o,+,0]})^t & : t \text{ odd.} \end{cases} \quad (4.15)$$

Coupled network dynamics based on even- m Tchebyscheff polynomials ($m_e = 2, 4, \dots$):

$$(\mathbf{f}^{[-m_e,+,1]})^t = \mathbf{P} \circ (\mathbf{f}^{[m_e,+,1]})^t, \quad (4.16)$$

$$(\mathbf{f}^{[-m_e,-,1]})^t = \mathbf{P} \circ (\mathbf{f}^{[m_e,-,1]})^t, \quad (4.17)$$

$$(\mathbf{f}^{[-m_e,+,0]})^t = \mathbf{P} \circ (\mathbf{f}^{[m_e,+,0]})^t \circ \mathbf{P}, \quad (4.18)$$

$$(\mathbf{f}^{[-m_e,-,0]})^t = \mathbf{P} \circ (\mathbf{f}^{[m_e,-,0]})^{t-1} \circ \mathbf{f}^{[m_e,+,0]}. \quad (4.19)$$

These relations hold under the exchange $P^{(1)} \leftrightarrow P^{(2)}$, since the way of labeling the subsets \mathcal{V}_1 and \mathcal{V}_2 is arbitrary.

Eqs. (4.10)-(4.19) reveal that various apparently different dynamics yield trajectories which differ just by a sign of the $x_i(t)$ at either all nodes i , or at the nodes $i \in \mathcal{V}_1$, that is in one of the both sets of nodes contained in the bipartite network. By considering the right handed side of Eq. (4.10)-(4.19) one can deduce that for odd m there are only two essentially different dynamics ($[m_o, +, 1]$ and $[m_o, +, 0]$), while for even m , there remain four essentially different dynamics ($[m_e, +, 1], [m_e, +, 0], [m_e, -, 1], [m_e, -, 0]$). Accordingly, when considering $m = 2$ and $m = 3$, of interest are only the six chaotic string dynamics introduced in Sec. 3.1.

One should note, that some of these relations have to be taken with some care. Whereas the change $\mathbf{f}^{[-2,+,1]} \rightarrow \mathbf{f}^{[2,+,1]}$ results in a global sign flip of the trajectory for identical initial conditions (expressed by the application of the operator \mathbf{P} after t times iterating the function \mathbf{f}), for the change $\mathbf{f}^{[-2,+,0]} \rightarrow \mathbf{f}^{[2,+,0]}$ also a change of the initial conditions $\mathbf{x}(0) \rightarrow -\mathbf{x}(0)$ is required (the operator \mathbf{P} is applied before and after iterating the function \mathbf{f}). This leads to a different trajectory, but in general to the same dynamical behaviour, that is the trajectory ends up in the same attractor and expectations of observables coincide. Nevertheless, if the dynamics shows non-ergodic behaviour, this change of initial conditions might lead to the convergence to a different attractor and thus different expectations of observables. Consequently, the loss of ergodicity can lead to a breaking of the discrete symmetry due to the existence of multiple attractors. To provide for this finding, in Chap. 5 not only the behaviour of observables dependent on the coupling ϵ and the applied evolution equation function $\mathbf{f}^{[m,s,b]}$ is studied, but also indications about whether or not the dynamics shows ergodic behaviour.

Explicit calculations of Eqs. (4.10)-(4.19)

In the following I display the calculations which lead to the relations (4.10)-(4.19).

Coupled network dynamics based on odd- m Tchebyscheff polynomials ($m_o = 1, 3, \dots$): Recall that $T_{m_o}(-x) = -T_{m_o}$.

• **Eq (4.10):**

$$f_i^{[-m_o,+,1]}(\mathbf{x}) = (1 - \epsilon)(-T_{m_o}(x_i)) + \frac{\epsilon}{k_i} \sum_{j=1}^N (-T_{m_o}(x_j)). \quad (4.20)$$

With

$$\begin{aligned} P_i(\mathbf{f}^{[m_o,+,1]}(\mathbf{x})) &= -f_i^{[m_o,+,1]}(\mathbf{x}) \\ &= -\left\{ (1 - \epsilon)T_{m_o}(x_i) + \frac{\epsilon}{k_i} \sum_{j=1}^N T_{m_o}(x_j) \right\} \end{aligned}$$

and

$$\begin{aligned} f_i^{[m_o,+,1]}(\mathbf{P} \circ \mathbf{x}) &= f_i^{[m_o,+,1]}(-\mathbf{x}) \\ &= \left\{ (1 - \epsilon)T_{m_o}(-x_i) + \frac{\epsilon}{k_i} \sum_{j=1}^N T_{m_o}(-x_j) \right\}, \end{aligned} \quad (4.21)$$

one obtains

$$\mathbf{f}^{[-m_o,+,1]}(\mathbf{x}) = \mathbf{P} \circ \mathbf{f}^{[m_o,+,1]} = \mathbf{f}^{[m_o,+,1]}(\mathbf{P} \circ \mathbf{x}). \quad (4.22)$$

Accordingly, one can write

$$\begin{aligned} (\mathbf{f}^{[-m_o,+,1]})^t &= \begin{cases} (\mathbf{f}^{[m_o,+,1]} \circ \mathbf{P} \circ \mathbf{P} \circ \mathbf{f}^{[m_o,+,1]})^{t/2} & : t \text{ even} \\ \mathbf{P} \circ \mathbf{f}^{[m_o,+,1]} \circ (\mathbf{f}^{[m_o,+,1]} \circ \mathbf{P} \circ \mathbf{P} \circ \mathbf{f}^{[m_o,+,1]})^{(t-1)/2} & : t \text{ odd} \end{cases} \\ &= \begin{cases} (\mathbf{f}^{[m_o,+,1]})^t & : t \text{ even} \\ \mathbf{P} \circ (\mathbf{f}^{[m_o,+,1]})^t & : t \text{ odd.} \end{cases} \end{aligned} \quad (4.23)$$

• **Eq (4.11):**

$$f_i^{[m_o,-,1]}(\mathbf{x}) = (1 - \epsilon)T_{m_o}(x_i) - \frac{\epsilon}{k_i} \sum_{j=1}^N T_{m_o}(x_j). \quad (4.24)$$

4.1 Symmetries for the coupled Tchebycheff map dynamics

For $i \in \mathcal{V}_1$ one has

$$\begin{aligned}
f_i^{[m_o, -, 1]}(\mathbf{P}^{(1)} \circ \mathbf{x}) &= (1 - \epsilon)T_{m_o}(-x_i) - \frac{\epsilon}{k_i} \sum_{j=1}^N T_{m_o}(-x_j) \\
P_i^{(1)}(f_i^{[m_o, -, 1]}(\mathbf{P}^{(1)} \circ \mathbf{x})) &= - \left\{ (1 - \epsilon)T_{m_o}(-x_i) - \frac{\epsilon}{k_i} \sum_{j=1}^N T_{m_o}(-x_j) \right\} \\
&= (1 - \epsilon)T_{m_o}(x_i) + \frac{\epsilon}{k_i} \sum_{j=1}^N T_{m_o}(x_j). \tag{4.25}
\end{aligned}$$

For $i \in \mathcal{V}_2$ holds

$$\begin{aligned}
f_i^{[m_o, -, 1]}(\mathbf{P}^{(1)} \circ \mathbf{x}) &= (1 - \epsilon)T_{m_o}(x_i) - \frac{\epsilon}{k_i} \sum_{j=1}^N T_{m_o}(-x_j) \\
P_i^{(1)}(f_i^{[m_o, -, 1]}(\mathbf{P}^{(1)} \circ \mathbf{x})) &= (1 - \epsilon)T_{m_o}(x_i) - \frac{\epsilon}{k_i} \sum_{j=1}^N T_{m_o}(-x_j) \\
&= (1 - \epsilon)T_{m_o}(x_i) + \frac{\epsilon}{k_i} \sum_{j=1}^N T_{m_o}(x_j). \tag{4.26}
\end{aligned}$$

This leads to

$$\begin{aligned}
\mathbf{P}^{(1)} \circ \mathbf{f}^{[m_o, -, 1]} \circ \mathbf{P}^{(1)} &= \mathbf{f}^{[m_o, +, 1]} \\
\Rightarrow (\mathbf{f}^{[m_o, -, 1]})^t &= \mathbf{P}^{(1)} \circ (\mathbf{f}^{[m_o, +, 1]})^t \circ \mathbf{P}^{(1)} \tag{4.27}
\end{aligned}$$

• **Eq (4.12):**

$$\begin{aligned}
f_i^{[-m_o, -, 1]}(\mathbf{x}) &= (1 - \epsilon)(-T_{m_o}(x_i)) - \frac{\epsilon}{k_i} \sum_{j=1}^N (-T_{m_o}(x_j)) \\
&= - \left\{ (1 - \epsilon)T_{m_o}(x_i) - \frac{\epsilon}{k_i} \sum_{j=1}^N T_{m_o}(x_j) \right\} \\
&= (1 - \epsilon)T_{m_o}(-x_i) - \frac{\epsilon}{k_i} \sum_{j=1}^N T_{m_o}(-x_j) \\
\Rightarrow \mathbf{f}^{[-m_o, -, 1]} &= \mathbf{P} \circ \mathbf{f}^{[m_o, -, 1]} = \mathbf{f}^{[m_o, -, 1]} \circ \mathbf{P} \\
\Rightarrow (\mathbf{f}^{[-m_o, -, 1]})^t &= \begin{cases} \mathbf{P}^{(1)} \circ (\mathbf{f}^{[m_o, +, 1]})^t \circ \mathbf{P}^{(1)} & : t \text{ even} \\ \mathbf{P}^{(2)} \circ (\mathbf{f}^{[m_o, +, 1]})^t \circ \mathbf{P}^{(1)} & : t \text{ odd} \end{cases} . \tag{4.28}
\end{aligned}$$

In the last step $\mathbf{P} \circ \mathbf{P}^{(1)} = \mathbf{P}^{(2)}$ has been used.

• **Eq (4.13):**

$$f_i^{[m_o, -, 0]}(\mathbf{x}) = (1 - \epsilon)T_{m_o}(x_i) - \frac{\epsilon}{k_i} \sum_{j=1}^N x_j. \quad (4.29)$$

Performing similar steps as before this can be recast into

$$(\mathbf{f}^{[m_o, -, 0]})^t = \mathbf{P}^{(1)} \circ (\mathbf{f}^{[m_o, +, 0]})^t \circ \mathbf{P}^{(1)}. \quad (4.30)$$

• Eq (4.14):

$$\begin{aligned} f_i^{[-m_o, +, 0]}(\mathbf{x}) &= (1 - \epsilon)(-T_{m_o}(x_i)) + \frac{\epsilon}{k_i} \sum_{j=1}^N x_j \\ &= - \left\{ (1 - \epsilon)T_{m_o}(x_i) - \frac{\epsilon}{k_i} \sum_{j=1}^N x_j \right\} \\ &= (1 - \epsilon)T_{m_o}(-x_i) - \frac{\epsilon}{k_i} \sum_{j=1}^N (-x_j) \\ \Rightarrow \mathbf{f}^{[-m_o, +, 0]} &= \mathbf{P} \circ \mathbf{f}^{[m_o, -, 0]} = \mathbf{f}^{[m_o, -, 0]} \circ \mathbf{P} \\ \Rightarrow (\mathbf{f}^{[-m_o, +, 0]})^t &= \begin{cases} \mathbf{P}^{(1)} \circ (\mathbf{f}^{[m_o, +, 0]})^t \circ \mathbf{P}^{(1)} & : t \text{ even} \\ \mathbf{P}^{(2)} \circ (\mathbf{f}^{[m_o, +, 0]})^t \circ \mathbf{P}^{(1)} & : t \text{ odd} \end{cases}. \end{aligned} \quad (4.31)$$

• Eq (4.15):

$$\begin{aligned} f_i^{[-m_o, -, 0]}(\mathbf{x}) &= (1 - \epsilon)(-T_{m_o}(x_i)) - \frac{\epsilon}{k_i} \sum_{j=1}^N x_j \\ &= - \left\{ (1 - \epsilon)T_{m_o}(x_i) + \frac{\epsilon}{k_i} \sum_{j=1}^N x_j \right\} \\ &= (1 - \epsilon)T_{m_o}(-x_i) + \frac{\epsilon}{k_i} \sum_{j=1}^N (-x_j) \\ \Rightarrow \mathbf{f}^{[-m_o, -, 0]} &= \mathbf{P} \circ \mathbf{f}^{[m_o, +, 0]} = \mathbf{f}^{[m_o, +, 0]} \circ \mathbf{P} \\ \Rightarrow (\mathbf{f}^{[-m_o, -, 0]})^t &= \begin{cases} (\mathbf{f}^{[m_o, +, 0]})^t & : t \text{ even} \\ \mathbf{P} \circ (\mathbf{f}^{[m_o, +, 0]})^t & : t \text{ odd} \end{cases}. \end{aligned} \quad (4.32)$$

Coupled network dynamics based on even- m Tchebyscheff polynomials ($m_e = 2, 4, \dots$): Recall that $T_{m_e}(-x) = T_{m_o}$.

• Eq (4.16):

4.1 Symmetries for the coupled Tchebycheff map dynamics

$$\begin{aligned}
f_i^{[-m_e,+,1]}(\mathbf{x}) &= (1 - \epsilon) (-T_{m_e}(x_i)) + \frac{\epsilon}{k_i} \sum_{j=1}^N (-T_{m_o}(x_j)) \\
&= - \left\{ (1 - \epsilon) T_{m_e}(x_i) + \frac{\epsilon}{k_i} \sum_{j=1}^N T_{m_o}(x_j) \right\} \\
&= -f_i^{[m_e,+,1]}(\mathbf{x}) = -f_i^{[-m_e,+,1]}(-\mathbf{x}) \\
\Rightarrow (\mathbf{f}^{[-m_e,+,1]})^t &= (\mathbf{P} \circ \mathbf{f}^{[m_e,+,1]} \circ \mathbf{P})^{(t-1)} \circ \mathbf{P} \circ \mathbf{f}^{[m_e,+,1]} \\
&= \mathbf{P} \circ (\mathbf{f}^{[m_e,+,1]} \circ \mathbf{P} \circ \mathbf{P})^{(t-1)} \mathbf{f}^{[m_e,+,1]} \\
&= \mathbf{P} \circ (\mathbf{f}^{[m_e,+,1]})^t
\end{aligned} \tag{4.33}$$

• Eq (4.17):

$$\begin{aligned}
f_i^{[-m_e,-,1]}(\mathbf{x}) &= (1 - \epsilon) (-T_{m_e}(x_i)) - \frac{\epsilon}{k_i} \sum_{j=1}^N (-T_{m_o}(x_j)) \\
&= - \left\{ (1 - \epsilon) T_{m_e}(x_i) - \frac{\epsilon}{k_i} \sum_{j=1}^N T_{m_o}(x_j) \right\} \\
&= -f_i^{[m_e,-,1]}(\mathbf{x}) = f_i^{[m_e,-,1]}(-\mathbf{x}) \\
\Rightarrow (\mathbf{f}^{[-m_e,-,1]})^t &= \mathbf{P} \circ (\mathbf{f}^{[m_e,+,1]})^t
\end{aligned} \tag{4.34}$$

• Eq (4.18):

$$\begin{aligned}
f_i^{[-m_e,+,0]}(\mathbf{x}) &= (1 - \epsilon) (-T_{m_e}(x_i)) + \frac{\epsilon}{k_i} \sum_{j=1}^N x_j \\
&= - \left\{ (1 - \epsilon) T_{m_e}(-x_i) + \frac{\epsilon}{k_i} \sum_{j=1}^N (-x_j) \right\} \\
&= -f_i^{[m_e,+,0]}(-\mathbf{x}) \\
\Rightarrow (\mathbf{f}^{[-m_e,+,0]})^t &= (\mathbf{P} \circ \mathbf{f}^{[m_e,+,0]} \circ \mathbf{P})^t \\
&= \mathbf{P} \circ (\mathbf{f}^{[m_e,+,0]} \circ \mathbf{P} \circ \mathbf{P})^{(t-1)} \mathbf{f}^{[m_e,+,0]} \circ \mathbf{P} \\
&= \mathbf{P} \circ (\mathbf{f}^{[m_e,+,0]})^t \circ \mathbf{P}
\end{aligned} \tag{4.35}$$

• Eq (4.19):

$$\begin{aligned}
 f_i^{[-m_e, -, 0]}(\mathbf{x}) &= (1 - \epsilon)(-T_{m_e}(x_i)) - \frac{\epsilon}{k_i} \sum_{j=1}^N x_j \\
 &= - \left\{ (1 - \epsilon)T_{m_e}(x_i) + \frac{\epsilon}{k_i} \sum_{j=1}^N x_j \right\} \\
 &= -f_i^{[m_e, +, 0]}(\mathbf{x}) \\
 f_i^{[m_e, +, 0]}(-\mathbf{x}) &= (1 - \epsilon)T_{m_e}(-x_i) + \frac{\epsilon}{k_i} \sum_{j=1}^N (-x_j) \\
 &= (1 - \epsilon)T_{m_e}(x_i) - \frac{\epsilon}{k_i} \sum_{j=1}^N x_j \\
 &= f_i^{[m_e, -, 0]}(\mathbf{x}) \\
 \Rightarrow (\mathbf{f}^{[-m_e, -, 0]})^t &= (\mathbf{P} \circ \mathbf{f}^{[m_e, +, 0]})^t \\
 &= \mathbf{P} \circ (\mathbf{f}^{[m_e, +, 0]} \circ \mathbf{O})^{(t,1)} \circ \mathbf{f}^{[m_e, +, 0]} \\
 &= \mathbf{P} \circ (\mathbf{f}^{[m_e, -, 0]})^{(t-1)} \circ \mathbf{f}^{[m_e, +, 0]}
 \end{aligned} \tag{4.36}$$

4.2 Symmetries of the interaction energy and the self energy

In Sec. 3.2 the interaction energy $W_{ij}^{[m,s,b]}$ and self energy $V_i^{[m,s,b]}$ have formally been derived from the evolution equation of the chaotic string dynamics. The self energy is given by

$$\begin{aligned}
 V^{[\pm 2, s, b]} &= \pm \left\langle -\frac{2}{3}(x_i)^3 + x_i \right\rangle, \\
 V^{[\pm 3, s, b]} &= \pm \left\langle -(x_i)^4 + \frac{3}{2}(x_i)^2 \right\rangle
 \end{aligned} \tag{4.37}$$

for the chaotic string dynamics based on second and third order Tchebycheff polynomials, respectively. The interaction energy is defined as

$$W_{ij}^{[m,s,b]}(\epsilon) = -s \left\langle \frac{1}{2}x_i x_j \right\rangle, \tag{4.38}$$

The notion $\langle \cdot \rangle$ refers to a time average over long iteration times.

In Refs. [17] distinguished couplings ϵ are those which correspond to minima of the self energy $V(\epsilon)$, and to zeros of the interaction energy $W(\epsilon)$ displaying a negative slope $W'(\epsilon)$. For these notions the sign of $V(\epsilon)$ and $W(\epsilon)$ are of importance.

As derived in the last section, all 16 possible combinations $[\pm m, s, b]$ for $m = 2, 3$ basically lead to six different dynamics. I will now examine the effect of switching between positive and negative Tchebycheff polynomials ($m \rightarrow -m$) and between diffusive and anti-diffusive coupling ($s = 1$) \rightarrow ($s = -1$) for both types of energies.

4.2 Symmetries of the interaction energy and the self energy

Transformation $m \rightarrow -m$: For all chaotic string dynamics with $m = 2$ the energies transform as

$$V^{[+2,s,b]}(\epsilon) \rightarrow V^{[-2,s,b]}(\epsilon) = V^{[2,s,b]}(\epsilon), \quad (4.39)$$

$$W^{[+2,s,b]}(\epsilon) \rightarrow W^{[-2,s,b]}(\epsilon) = W^{[2,s,b]}(\epsilon). \quad (4.40)$$

In contrast, the $m = 3$ dynamics show a different behaviour:

$$V^{[+3,s,b]}(\epsilon) \rightarrow V^{[-3,s,b]}(\epsilon) = -V^{[3,s,b]}(\epsilon), \quad (4.41)$$

$$W^{[+3,s,1]}(\epsilon) \rightarrow W^{[-3,s,1]}(\epsilon) = W^{[3,s,1]}(\epsilon), \quad (4.42)$$

$$W^{[+3,s,0]}(\epsilon) \rightarrow W^{[-3,s,0]}(\epsilon) = -W^{[3,s,0]}(\epsilon). \quad (4.43)$$

Note that the above well-defined symmetry behaviour was only achieved due to the special choice of the additive constant C in Eq. (3.15) and Eq. (3.21). Other choices would not make the problem symmetric under the transformation $m \rightarrow (-m)$.

Transformation $(s = 1) \rightarrow (s = -1)$: Whereas for chaotic string dynamics with $m = 2$ this transformation yields a completely different behaviour, for $m = 3$ one obtains

$$V^{[\pm 3,+b]}(\epsilon) \rightarrow V^{[\pm 3,-b]}(\epsilon) = V^{[\pm 3,+b]}(\epsilon), \quad (4.44)$$

$$W^{[\pm 3,+b]}(\epsilon) \rightarrow W^{[\pm 3,-b]}(\epsilon) = W^{[\pm 3,+b]}(\epsilon). \quad (4.45)$$

These relations show that although several combinations of $[\pm m, s, b]$ yield equivalent dynamics, the respective interaction energy and self energy may differ by a sign. In Ref. [17] all results are obtained by considering Eqs. (4.37) and (4.37) for positive sign only. This is not consistent with the formal derivation of these observables, which lead to positive as well as negative leading sign, depending on the label $[\pm m, s, b]$, and thus needs clarification by the author of Ref. [17].

In the following chapters of this thesis I follow Ref. [17] and consider the interaction energy only with a positive leading sign, that is $W(\epsilon) = \langle x_i x_j \rangle$, where for simplicity the prefactor $1/2$ has been omitted.

5 Interaction energy of chaotic strings

In the following chapter I will take a closer look at the interaction energy of chaotic strings as defined in Sec. 3.2. The main purpose is to review and check the results given in Ref. [17]. In addition I will also investigate the aspect of spatial homogeneity of the interaction energy.

5.1 Dependence of the interaction energy on initial values and node

One of the main claims of the theory advocated in Ref. [17] is that there are particular coupling values of the chaotic string dynamics, which coincide with coupling constants of the standard model of particle physics. These couplings are distinguished as zeros ϵ^* with a negative slope of an observable called interaction energy $W(\epsilon)$ (see Sec. 3.2). In this section I will study the behaviour of $W(\epsilon)$ depending on the coupling ϵ for the six interesting chaotic string dynamics (see Sec. 3.1), thus reviewing some results from Ref. [17].

As an extension to the pure inspection of formerly known results I will also study whether or not the dynamics exhibits ergodic behaviour. For this purpose the notion of ergodicity is used in a mathematically rather sloppy sense, meaning that time-averages of observables do not depend on the initial value (up to a set of measure zero). Additionally it is demanded that expectations of observables defined at similar subsets of nodes, that is for structurally equivalent sets of nodes, yield the same result (see Sec. 2.2.1 for the definition of similar sets of nodes). For a more mathematical treatment of ergodicity in coupled map lattices see Refs. [30, 31].

In [17] the interaction energy has been calculated as an average

$$W(\epsilon) = \langle W_{ij} \rangle_{\text{ring}} = \langle \langle x_i(t)x_j(t) \rangle_{\text{time}} \rangle_{\text{ring}}, \quad (5.1)$$

that is an average not only over time but also over all coupled pairs of nodes, i.e. neighbouring ring sites. It is possible that for non-ergodic dynamics and thus spatially inhomogeneous values $W_{ij} \neq W_{i'j'}$ with $i \neq i', j \neq j'$, the interaction energy $W(\epsilon)$ in principle could vanish due to this spatial averaging procedure only, without vanishing locally for neighbouring nodes i and j . Recall that a main physical interpretation of

the chaotic string dynamics was the use as a noise field for stochastically quantized fields (see Sec. 3.4). According to this interpretation dynamical states of vanishing interaction energy could be associated with a strongest random or chaotic behaviour. In Chap. 6 I will evaluate this notion of a most random behaviour in more detail. But already at this point it is obvious, that a dynamical state where $W(\epsilon) = 0$ is only fulfilled due to the spatial average, but not because of $W_{ij} = 0$ for all connected pairs i, j , contradicts such an interpretation as being suitable as a spatiotemporal noise field.

Let us examine this notion of ergodic behaviour and spatial homogeneity with the help of natural invariant densities. Consider an ergodic dynamics where the invariant density can be obtained by iterating a single initial value and producing a histogram [22]. The notion of ergodicity at this points refers to the independence of the invariant density on the initial conditions. For a coupled map network with vanishing coupling $\epsilon = 0$ the invariant density $\rho(x_1, x_2, \dots, x_N)$ is given by

$$\rho(x_1, x_2, \dots, x_N) = \prod_{i=1}^N \rho(x_i), \quad (5.2)$$

that is the product of the densities at the respective nodes. These local densities $\rho(x_i)$ are identical, as long as the local maps coincide. Thus although the dynamical state $x_i(t), i = 1, \dots, N$ in general will show a behaviour with $x_i(t) \neq x_j(t)$ for $i \neq j$, time averages $\langle F[x_i(t)] \rangle_{\text{time}}$ will yield the same value for all nodes i .¹

If the coupling is switched on, necessarily spatial correlations occur and the factorization of the density does not hold anymore. However, one might consider locally restricted densities $\tilde{\rho}(x_i)$, given by

$$\tilde{\rho}(x_i) = \prod_{j \neq i} \int dx_j \rho(x_1, x_2, \dots, x_N). \quad (5.3)$$

Numerically these locally restricted densities are obtained by histograms evaluated only at the respective node i , ignoring the dynamics at the other nodes $j \neq i$. This concept can easily be extended to subsets of nodes larger than one, for instance $\tilde{\rho}(x_i, x_j)$, where node i and j are neighbours in the network.

In Sec. 2.2.1 the notion of similar nodes in a network has been introduced, for which the network structure looks identical. For a spatially ergodic dynamics it is expected that the dynamics at similar nodes show analogous behaviour. A counterexample is the occurrence of spatial patterns (for instance a frozen random pattern [69]) in a coupled map lattice, where attractors can have strong spatial dependence despite of the spatial symmetry of the underlying dynamical model. In terms of densities this implies that for similar nodes i and j one expect that the locally restricted densities are identical, that is $\tilde{\rho}(x_i) = \tilde{\rho}(x_j)$. The same should hold for similar subsets of nodes. For the special case of a ring structure and edges $(i, j), (i', j')$ it is hence demanded that

$$\tilde{\rho}(x_i, x_j) = \tilde{\rho}(x_{i'}, x_{j'}), \quad (5.4)$$

¹Dynamical states with $x_i(t) = x_j(t)$ are called synchronized and will be of interest in Chap. 8 of this thesis.

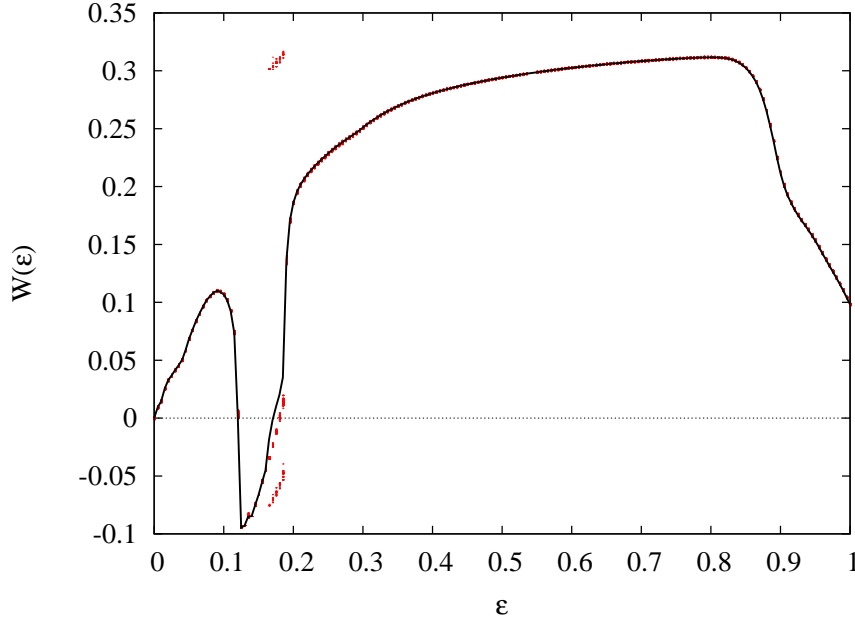


Figure 5.1: Interaction energy for the 2A dynamics. The thick line shows the spatial average $W(\epsilon)$, whereas the red dots show all the respective $W_{ij}(\epsilon)$. Ring size $N = 500$, $T = 10^6$ iterations, transient $T_0 = 5 \cdot 10^4$, one realization.

since all directly coupled pairs of nodes in a ring structure are similar. Consequently for a homogeneous dynamics all time averages over functions $F(x_i, x_j)$ should yield the same result for every coupled pair of nodes.

Obviously from $W_{ij}(\epsilon) = W_{i',j'}(\epsilon)$ does not follow that $\tilde{\rho}(x_i, x_j) = \tilde{\rho}(x_{i'}, x_{j'})$, since the interaction energy is only one specific test function. However, in order to avoid numerically expensive calculations, at this point I restrict the studies to this specific function, which is of relevance for the theory put forward in [17].

Figures 5.1-5.6 show the interaction energy for the six interesting chaotic string dynamics for the whole coupling range $\epsilon \in [0, 1]$. Apart from displaying the spatial average $W(\epsilon)$ as it is done in Ref. [17], the figures also visualize $W_{ij}(\epsilon)$ for all edges (i, j) in the ring. These figures reveal that depending on the dynamics, for large intervals in the coupling range the interaction energy is not spatially homogeneous.

It is of interest to study this dependence of W_{ij} on the respective edge (i, j) more quantitatively. For this purpose I define the following inhomogeneity measures:

$$\begin{aligned} \sigma_{\text{init}}(W; \epsilon) &= \left\langle \sqrt{\langle (W_{ij}(\epsilon))^2 \rangle_{\text{init}} - \langle W_{ij}(\epsilon) \rangle_{\text{init}}^2} \right\rangle_{\text{edges}}, \\ \sigma_{\text{edges}}(W; \epsilon) &= \left\langle \sqrt{\langle (W_{ij}(\epsilon))^2 \rangle_{\text{edges}} - \langle W_{ij}(\epsilon) \rangle_{\text{edges}}^2} \right\rangle_{\text{init}} \end{aligned} \quad (5.5)$$

where $\langle \cdot \rangle_{\text{edges}}$ refers to an average taken over all edges in the ring-network, and $\langle \cdot \rangle_{\text{init}}$ to an average taken over an ensemble of initial values $x_i(0)$. I will explain these definitions: To calculate σ_{init} , I choose some dynamics, for instance the 2A chaotic

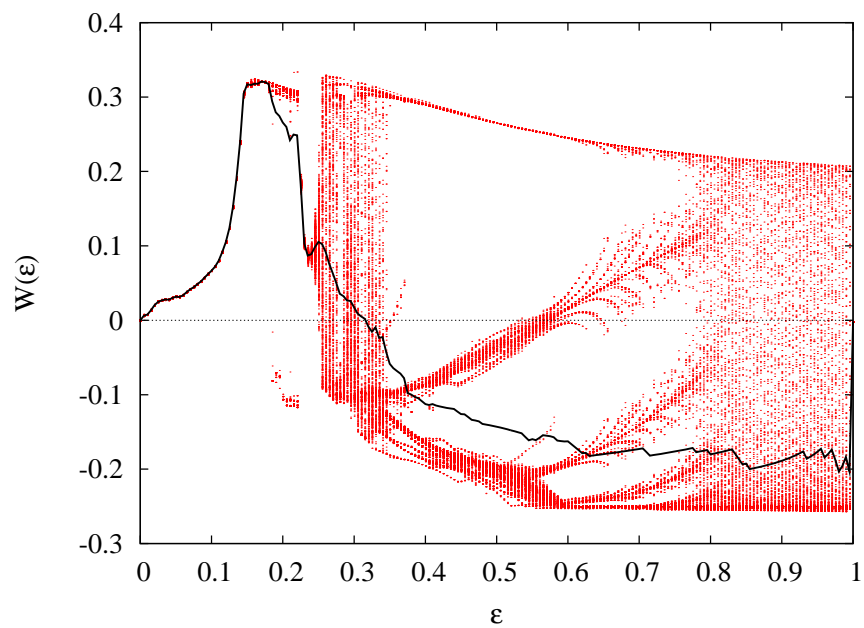


Figure 5.2: Same as Figure 5.1, but for the $2B$ dynamics.

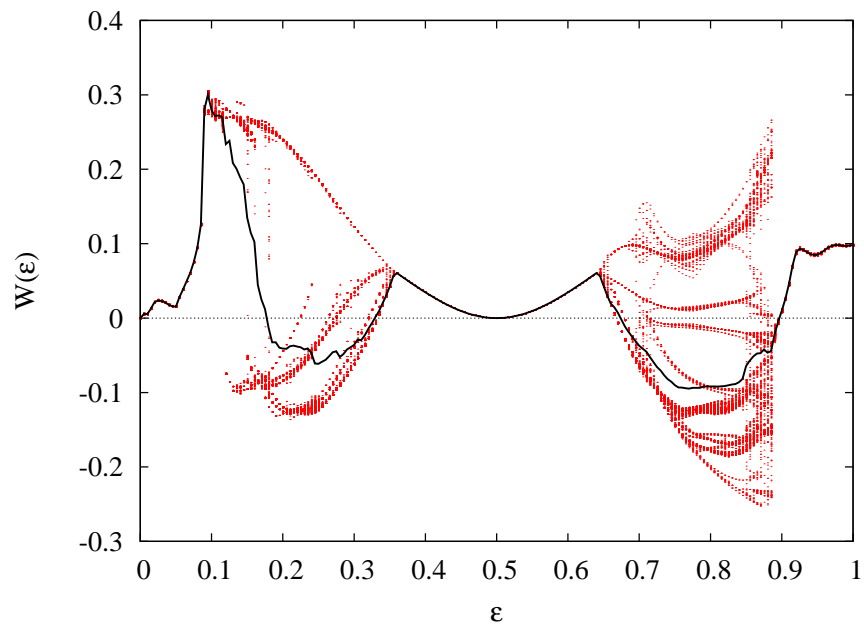


Figure 5.3: Same as Figure 5.1, but for the $2A^-$ dynamics.

5.1 Dependence of the interaction energy on initial values and node

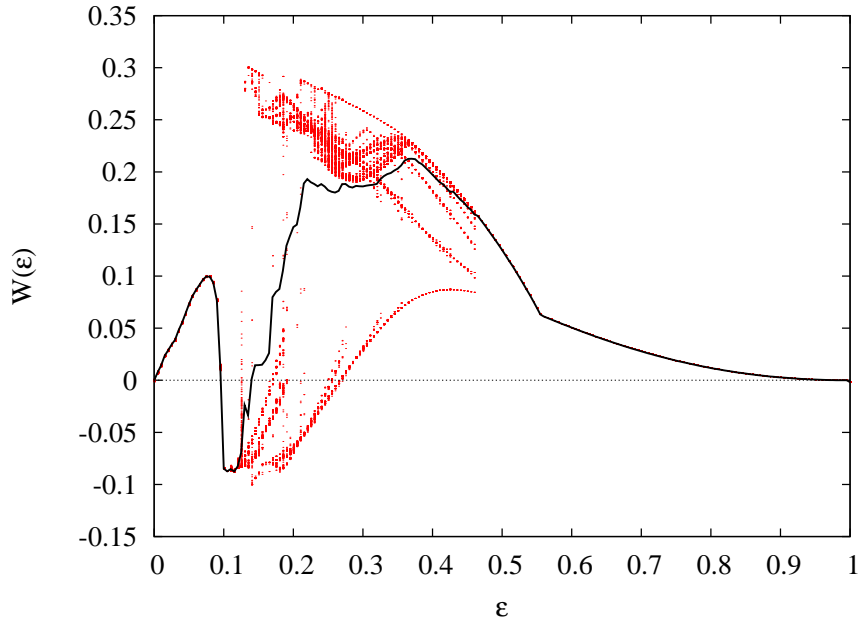


Figure 5.4: Same as Figure 5.1, but for the $2B^-$ dynamics.

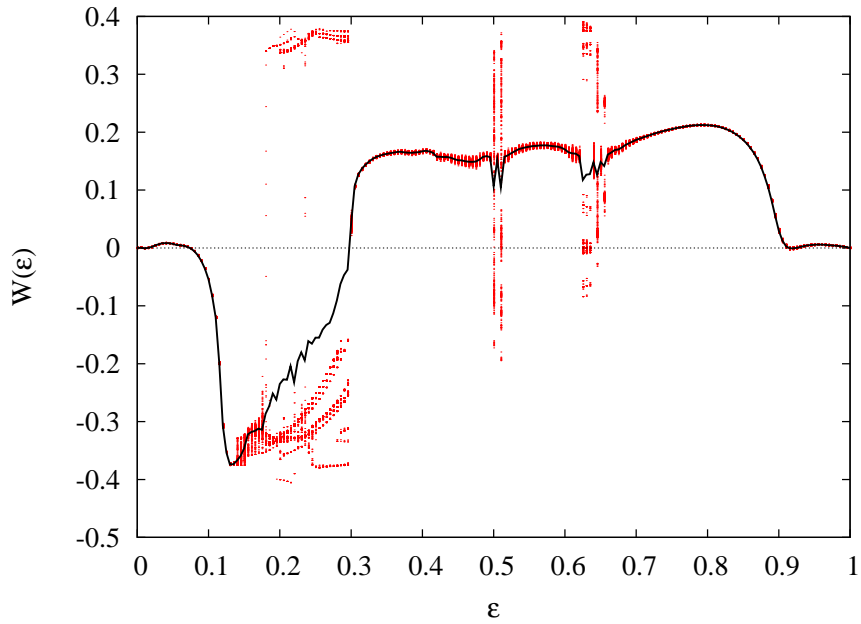
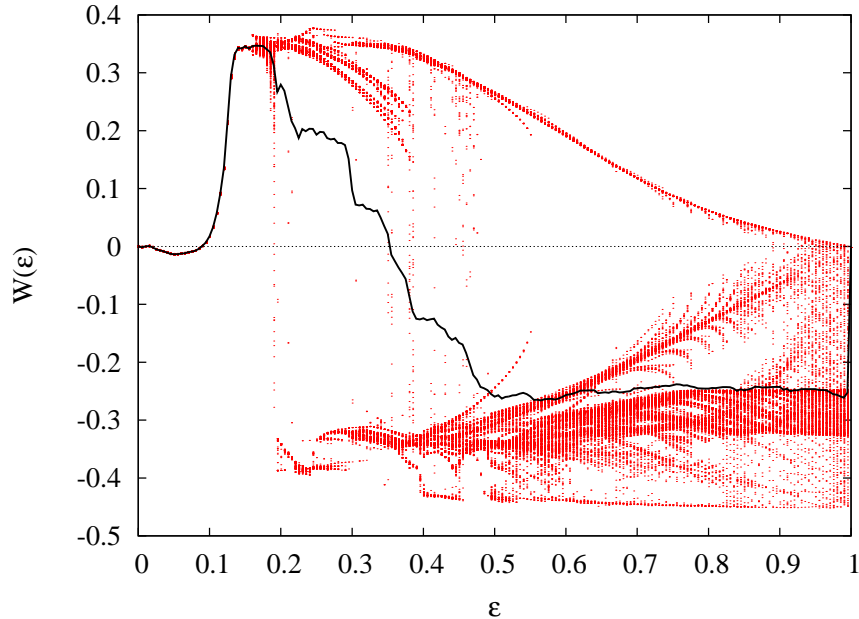


Figure 5.5: Same as Figure 5.1, but for the $3A$ dynamics.

Figure 5.6: Same as Figure 5.1, but for the $3B$ dynamics.

string, and some coupling value ϵ and calculate for an ensemble of initial values the local observable, in this case the interaction energy $W_{ij}(\epsilon)$ for all neighbouring edges. Then I determine the standard deviation of this quantity with respect to the ensemble of initial values. Finally, I take the average over all edges, thus getting a measure of the inhomogeneity of the interaction energy at a specific pair of nodes with respect to different initial values. To calculate the quantity σ_{edges} I perform the above averaging procedure in reverse order.

Figures 5.7-5.12 show the results of the numerical calculations for the six interesting chaotic string dynamics as a function of the coupling ϵ . Apparently both σ_{init} and $\sigma_{\text{edges}}(W; \epsilon)$ show nearly identical behaviour and are non-vanishing for large ranges of the coupling parameter ϵ , thus indicating non-ergodic behaviour in the sense of expectation values which depend on the node at the network and the initial value chosen. In the regions where $\sigma_{\text{init}}(W; \epsilon)$ and σ_{edges} is significantly different from zero, one has to be very careful when numerically calculating expectations of observables since the result may strongly depend on the initial values. Typical phenomena that occur in these regions are multiple attractors and frozen random patterns with very large relaxation times.

Since σ_{init} and σ_{edges} show very similar behaviour, I consider now the combined homogeneity measure $\sigma(W; \epsilon)$ given by

$$\sigma(W; \epsilon) = \sqrt{\langle (W_{ij}(\epsilon))^2 \rangle_{\text{edges,init}} - \langle W_{ij}(\epsilon) \rangle_{\text{edges,init}}^2}, \quad (5.6)$$

where the standard deviation is now simultaneously determined from an average over all initial values and all coupled pairs of nodes.

5.1 Dependence of the interaction energy on initial values and node

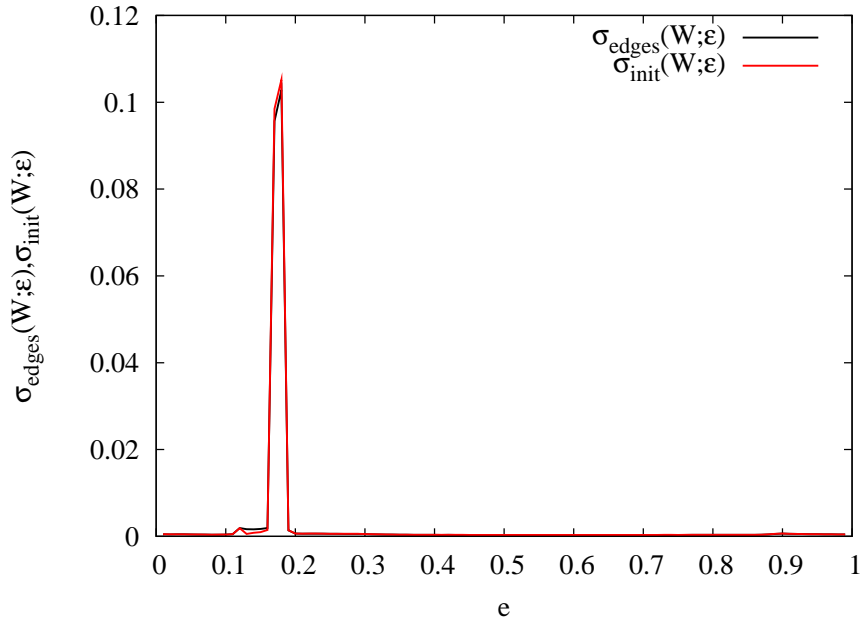


Figure 5.7: Inhomogeneity measures $\sigma_{\text{init}}(W; \epsilon)$ and $\sigma_{\text{edges}}(W; \epsilon)$ for the 2A dynamics. For the numerical calculations I used 50 different initial conditions, a ring with $N = 500$ nodes, $T = 10^7$ iterations and a transient of $T_0 = 5 \times 10^4$.

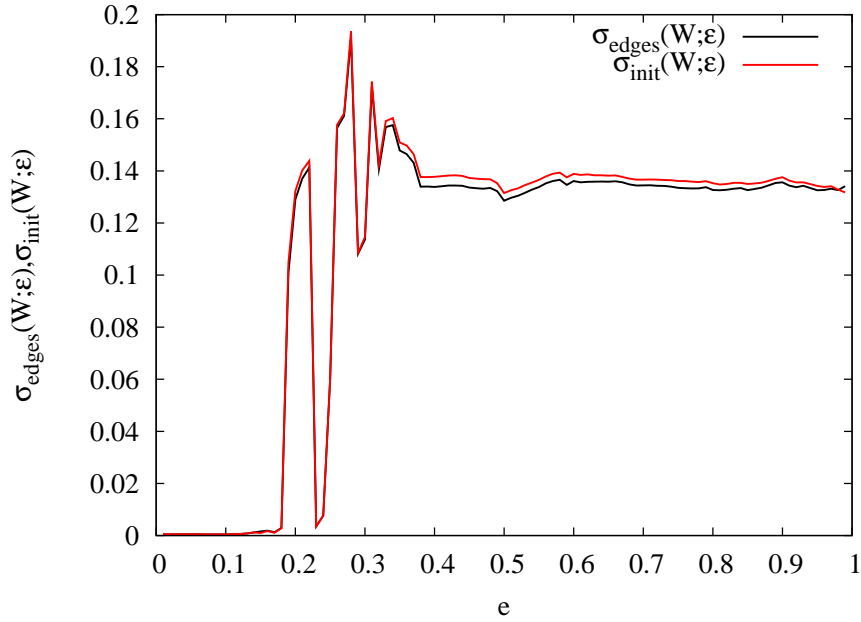


Figure 5.8: Same as Fig. 5.7, but for the 2B dynamics.

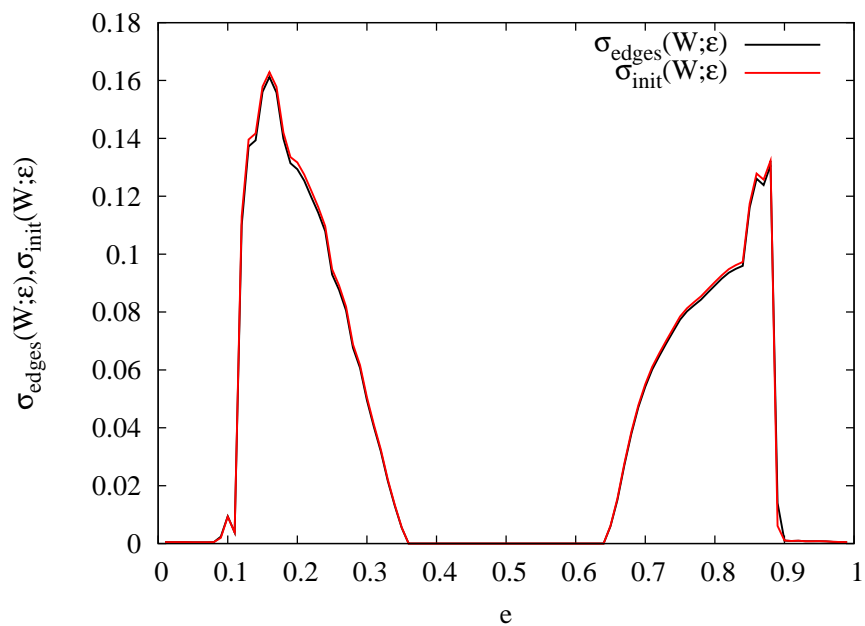


Figure 5.9: Same as Fig. 5.7, but for the $2A^-$ dynamics.

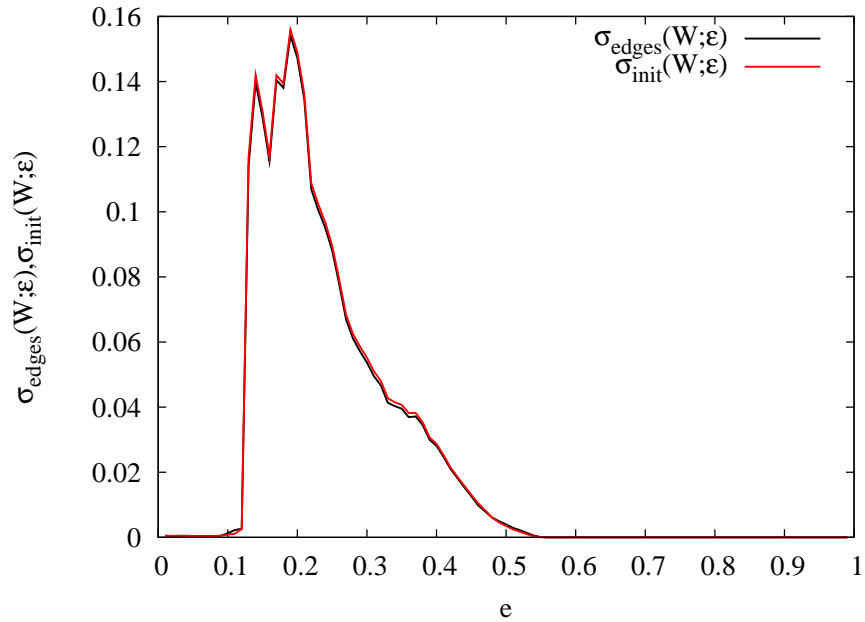


Figure 5.10: Same as Fig. 5.7, but for the $2B^-$ dynamics.

5.1 Dependence of the interaction energy on initial values and node

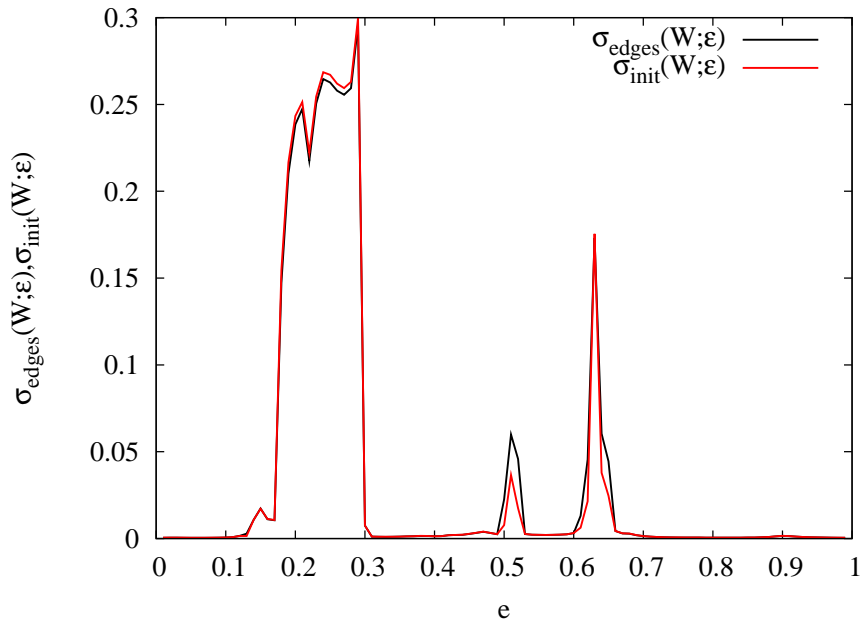


Figure 5.11: Same as Fig. 5.7, but for the 3A dynamics.

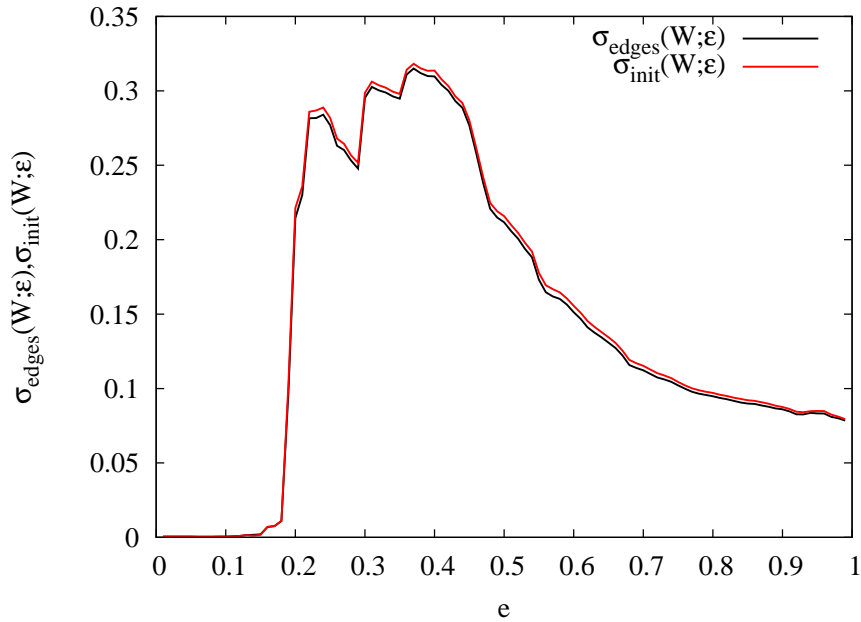


Figure 5.12: Same as Fig. 5.7, but for the 3B dynamics.

5 Interaction energy of chaotic strings

In the theory of chaotic strings the zeros of the interaction energy $W(\epsilon)$ are of main interest. I now study the behaviour of $\sigma(W; \epsilon)$ for the zeros ϵ^* associated with standard model coupling in Ref. [17], checking for non-ergodic behaviour. Unfortunately for a finite number of iterations T and for finite network size N , statistical disorder will prevent a completely vanishing inhomogeneity measure $\sigma(W; \epsilon)$. To discriminate between an inhomogeneous non-ergodic dynamics and a homogeneous ergodic dynamics with a nonzero $\sigma(W; \epsilon)$ due to finite-iteration time/size statistical fluctuations, I determine $\sigma(W; \epsilon)$ as a function of the number of iterations (recall that $W_{ij}(\epsilon)$ is a time average $\langle x_i(t)x_j(t) \rangle_T$). For statistical fluctuations it is expected that

$$\sigma(W; \epsilon|T) \propto T^{-1/2}, \quad (5.7)$$

due to the Central Limit Theorem, whereas for an inhomogeneous (non-ergodic) dynamics it should hold

$$\sigma(W; \epsilon|T) \approx \text{constant} \quad (5.8)$$

due to very slow decay of correlations and different attractors in the system.

Fig. 5.13 shows $\sigma(W; \epsilon|T)$ for the eight interesting zeros which were associated with standard model couplings in Ref. [17]. Whereas one observes for six of these zeros the decay $\sigma(W; \epsilon|T) \propto T^{-1/2}$, two of them correspond to dynamical states which show $\sigma(W; \epsilon) \approx \text{constant}$. These two zeros correspond to non-ergodic behaviour and the interaction energy $W(\epsilon)$ only vanishes due to an average over all edges in the ring, or over various initial conditions. As a consequence these zeros should be discarded from being possibly associated with standard model couplings, since an interpretation of the dynamical states as noise fields for chaotic quantization is not applicable. Interestingly, the interpretation of these zeros in Ref. [17] as corresponding to strong coupling constants between glueballs was rather speculative and far-fetched, so their exclusion due to this dynamical reasoning is actually advantageous for the theory of chaotic strings.

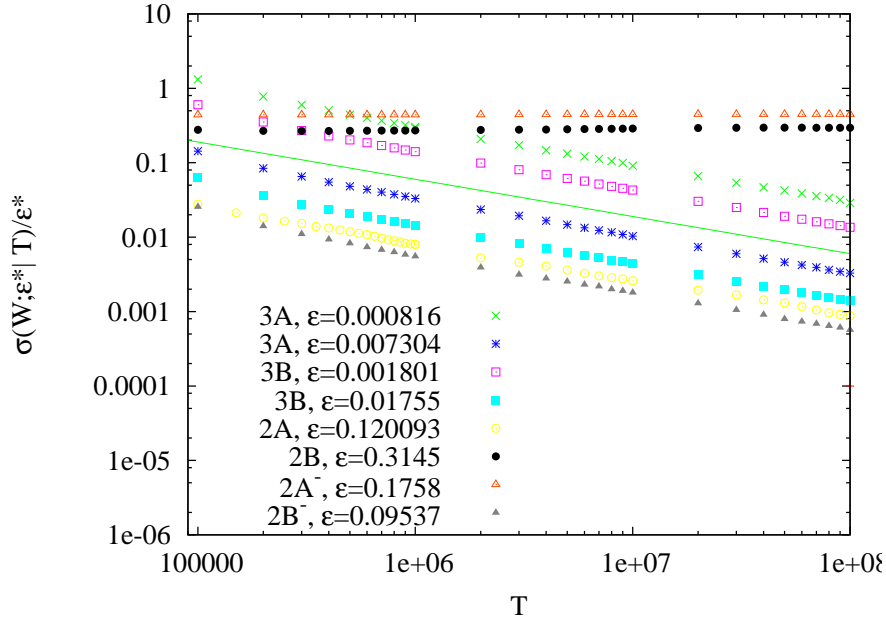


Figure 5.13: The relative time-dependent inhomogeneity measure $\sigma(W; \epsilon | T) / \epsilon$ for eight distinguished values ϵ^* with $W(\epsilon^*) = 0$. The numerical values of these zeros have been taken from Ref. [17]. The relative value σ / ϵ rather than the absolute value σ has been plotted to facilitate the distinction between the different curves and to give an idea about the numerical accuracy of the calculations. As a visual guide also $\sigma(W; \epsilon | T) \propto T^{-1/2}$ is displayed. Parameters are ring size $N = 500$, ten different initial conditions, transient $T = 5 \times 10^4$.

5.2 Precise numerical determination of the zeros

In this section I review and check some of the results given in Ref. [17] concerning the zeros of the interaction energy of the chaotic string dynamics. In Ref. [17] the interesting zeros of the interaction energy have been numerically calculated with high precision (up to seven digits). Since the respective calculations have not been repeated by any other sources, these results need to be checked. For this purpose I determine six of the eight interesting zeros reported in Ref. [17], excluding the zeros which correspond to non-ergodic dynamical states as shown in the last section.

The determination of the zeros is realized by means of the following procedure. I choose a ring of size $N = 10^4$, as it has been done in Ref. [17]. Then I calculate the interaction energy $W(\epsilon)$ for ten different initial conditions, which are randomly drawn from a distribution that is given by the natural density of the uncoupled Tchebycheff maps. The calculation incorporates the average over T iterations and over all edges. The latter average can be performed, since it has been checked in the last section that the interaction energy does not depend on the considered coupled pair of nodes for the dynamics at these zeros. I start with some interval in the coupling range around the zero and some moderate number of iterations, that is $T = 10^5$. For all ϵ in the coupling range $W(\epsilon)$ is calculated, that is the average over ten different initial conditions, and the standard deviation of this average. I then fit a continuous line through the data points obtained from the average $W(\epsilon)$, and also through the values which are given by the average plus/minus the standard deviation. This yields the zero ϵ^* with $W(\epsilon^*) = 0$ and an estimation of the error. In the next step this procedure is repeated for the coupling range given by the error around the zero, and higher precision up to $T = 10^7$. See Fig. 5.14.

In Tab. 5.1 the respective numerical results are compared to the values given in Ref. [17]. It is observed that although the same network size and number of iterations was used for calculation, the obtained results are in parts less precise than the numerical values given in Ref. [17]. I expect this slight discrepancy to have its origin in the way how the error was obtained. Since in Ref. [17] the calculation of the error has not been described in detail, it is not possible to compare the procedures, but the present method rather overestimates the uncertainty in the numerical value of the zeros. However, the important result is that all zeros obtained in Ref. [17] are situated in the range of the errorbars of our calculations, which are of the order of 10^{-6} .

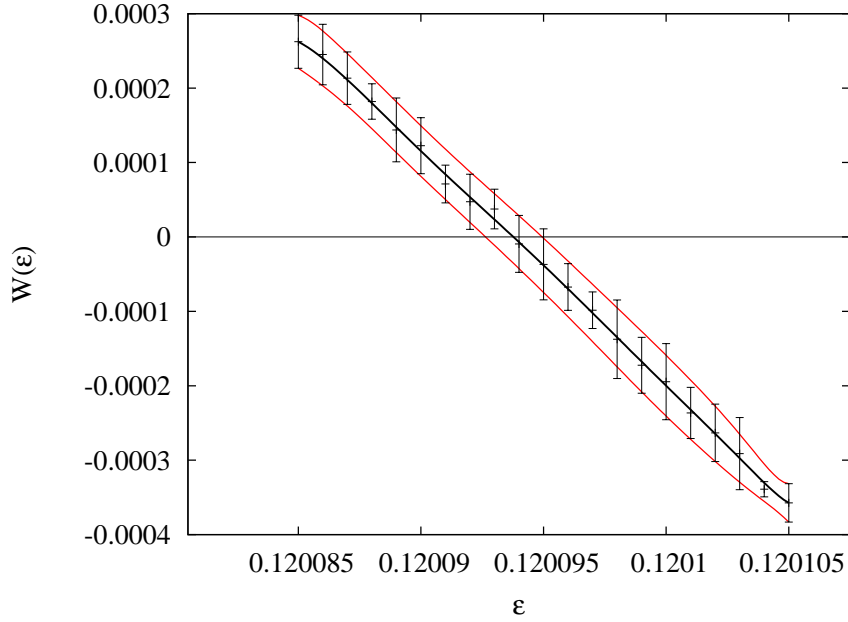


Figure 5.14: Numerical determination of the zeros ϵ^* with $W(\epsilon^*) = 0$, here for the $2A$ dynamics. I obtain $W(\epsilon)$ by taking the average over ten different initial conditions, and estimate the zero by fitting a continuous line through the respective data points. The error is estimated by doing the same for the average plus/minus the standard deviation with respect to the average over the different realizations. For this figure network size $N = 10^4$, $T = 10^7$ iterations, transient $T_0 = 10^4$.

zero	Ref. [17]	our result
$\epsilon_1^{(3A)}$	0.0008164(8)	0.000813(8)
$\epsilon_2^{(3A)}$	0.0073038(1)	0.007308(9)
$\epsilon_1^{(3B)}$	0.0018012(4)	0.001804(6)
$\epsilon_2^{(3B)}$	0.017550(1)	0.017550(3)
$\epsilon_1^{(2A)}$	0.120093(3)	0.120094(1)
$\epsilon_1^{(2B^-)}$	0.095370(1)	0.095370(1)

Table 5.1: Zeros of the interaction energy: Comparison between the obtained numerical results and the values given in Ref. [17]. For details about the numerical methods see the text.

6 Correlations and most-random behaviour in coupled Tchebycheff map networks

6.1 Interaction energy and most-random behaviour

In Ref. [21] an interpretation of the chaotic string dynamics as vacuum fluctuations has been proposed. A key notion of this concept is the most random or most chaotic behaviour. It can be shown that deterministic maps with strongest chaotic properties are those conjugated to a Bernoulli shift [22]. Amongst this class of maps, Tchebyscheff polynomials are distinguished by having least higher-order correlations and thus can be interpreted as being most chaotic [17]. If one considers a chaotic string dynamics with vanishing coupling $\epsilon = 0$, one obtains a population of uncoupled chaotic maps with strongest chaotic behaviour and without any spatial correlations in the system. But what is the most random/chaotic behaviour for coupling $\epsilon > 0$? In Ref. [21] it has been proposed that such a most random behaviour is distinguished by a vanishing correlation function

$$\langle x_i(t)x_j(t) \rangle_{\text{time}}, \quad (6.1)$$

where i and j are neighbouring lattice sites and the average is taken over long iteration times. One recognizes this measure as being the interaction energy $W(\epsilon)$. It has been tempting to evoke the most random principle to the chaotic string dynamics in order to justify the found zeros of the interaction energy.

In this chapter I will take a closer look at this so-called most random behaviour. The interaction energy is only one spatial correlation function, which does not take into account the temporal evolution of the dynamics. To overcome this, different Lyapunov measures are calculated. Subsequently, other spatial correlation measures like higher-order cumulants and mutual information are considered. The question is: are dynamical states distinguished by a vanishing interaction energy also ‘special’ with respect to other correlation measures, or does one have to rely on this specific measure in order to get the results advocated in Refs. [17, 21]?

6.2 Lyapunov exponents of chaotic strings

The aim of the following section is to evaluate the chaoticity of the chaotic string dynamics by means of Lyapunov measures [11, 43, 65, 111]. As pointed out in Sec. 2.3, the dynamics of a coupled map lattice of size N corresponds to the iteration of an N -dimensional map. Accordingly the Lyapunov spectrum is formed by N exponents $\mu_{max} = \mu_1 \geq \dots \geq \mu_N$, one for each independent eigendirection (see Sec. 2.1.3 or Ref. [94]). Note that this Lyapunov spectrum describes the spatiotemporal evolution of the system, whereas the interaction energy defined in Sec. 3.2 only measures spatial, but not temporal correlations.

The multiplicative ergodic theorem by Oseledec guarantees the existence of well-defined Lyapunov exponents under rather general conditions [94]. With respect to the natural measure on an attractor one obtains Lyapunov exponents independent from the initial conditions (as long they are in the basin of attraction), except for a set of Lebesgue measure zero. So by numerically iterating a random initial condition, one obtains the right Lyapunov exponent of the dynamical system. For coupled map lattices there might be different attractors with possibly different Lyapunov spectra. Therefore the measures based on the Lyapunov spectrum defined in the following will be averaged over several different realizations in order to evaluate the chaoticity under general conditions. Any possible dependence on initial conditions will not be considered.

The maximum Lyapunov exponent of the dynamics μ_{max} describes the rate of amplification of an arbitrary small displacement [94] and can be used as a first measure of the chaoticity of the dynamics. Recall that already one positive Lyapunov exponent renders the dynamics chaotic, since small displacements grow exponentially in time. Depending on the coupling and the individual dynamics, many Lyapunov exponents might be positive, so another quantity of interest is the net-average of positive Lyapunov exponents:

$$h = \langle \mu_i \rangle_{i, \mu_i > 0} = \frac{1}{N} \sum_{i=1}^N \mu_i \Theta(\mu_i). \quad (6.2)$$

Here $\Theta(\mu)$ is the Heaviside function

$$\Theta(\mu) = \begin{cases} 0 & : \mu < 0 \\ 1 & : \mu \geq 0. \end{cases} \quad (6.3)$$

Note that the sum in Eq. (6.2) is divided by the system size N , not by the number of positive Lyapunov exponents. In the following, h will be denoted as the average positive Lyapunov exponent of the system. In the literature, this quantity is often set equal with the Kolmogorov-Sinai entropy (KS entropy), although in general it is only an upper bound for this measure [22].

Another possible measure of the chaoticity of the dynamics is based on the geometrical structure of the attractor. Divide the N -dimensional phase space into a grid of N -dimensional cubes with side-length δ and consider the relative number of iterations, in which typical orbits pass the respective cubes. To be precise, for a certain

choice of cubes labeled with i and cube side-length δ , define for coupled map lattices the weight

$$\omega_i = \lim_{T \rightarrow \infty} \frac{n_i(T)}{T}, \quad (6.4)$$

with T the number of iterations and $n_i(T)$ the number of times the orbit $x_1(t), \dots, x_N(t)$ passes the cube labeled by i . For cube side-length δ , let $\tilde{n}(\delta)$ denote the total number of cubes i with $\omega_i \geq 0$, that is the number of cubes necessary to cover the attractor set. The box-counting dimension [94] of the attractor set is defined as

$$D_0 = \lim_{\delta \rightarrow 0} \frac{\ln[\tilde{n}(\delta)]}{\ln[1/\delta]}. \quad (6.5)$$

In order to measure the chaoticity of the dynamics, apart from being numerically expensive to calculate, this box-counting dimension has one major drawback. Although it estimates the fraction of the phase space which is covered by the attractor, it does not incorporate the magnitude of the respective weights ω_j . A measure which overcomes this problem is the information dimension D_I , defined by [44]

$$D_I = \lim_{\delta \rightarrow 0} \frac{\sum_{j=1}^{\tilde{n}(\delta)} \omega_j \ln[\omega_j]}{\ln[\delta]}, \quad (6.6)$$

where the summation takes place over all cubes j with non-zero weights ω_j . For the determination of this quantity, cubes i with a larger weight ω_i have a greater influence than cubes which are only rarely passed by the trajectory of the dynamical system. For higher-dimensional systems it is numerically difficult to obtain the information dimension by straightforward calculations, but it can be estimated by the Lyapunov dimension (also called Kaplan-Yorke dimension), which is based on the Lyapunov spectrum [44]. Let K be the largest integer such that

$$\sum_{i=1}^K \mu_i \geq 0. \quad (6.7)$$

Recall that the Lyapunov exponents μ_i can be positive as well as negative, and are arranged in decreasing order $\mu_1 \geq \dots \geq \mu_N$. The Lyapunov dimension D_L is defined as

$$D_L = \begin{cases} 0 & \text{if all } \mu_i < 0, \\ K + \frac{1}{|\mu_{K+1}|} \sum_{i=1}^K \mu_i & \text{if } K < N, \\ N & \text{if } K = N. \end{cases} \quad (6.8)$$

In order to get a better understanding of these three measures, consider the 2A dynamics. For vanishing coupling $\epsilon = 0$, one obtains N independent chaotic map dynamics, each with Lyapunov exponent $\mu_i = \ln 2$. Consequently, it holds $\mu_{max} = h = \ln 2$, and $D_I = N$. If the dynamics is completely synchronized, that is $s(t) = x_1(t) = \dots = x_N(t)$, then according to Chap. 8.3 this synchronized trajectory is given by the individual second-order Tchebycheff dynamics with Lyapunov exponent $\ln 2$.

In order to have stable synchronization, all the remaining Lyapunov exponents have to be negative. This results in $\mu_{max} = \ln 2$, $h = \ln 2/N$ and D_L given by Eq. (6.8) with $D_L \geq 1$. As a further example consider a hypothetical stable fixed point of a coupled map lattice dynamics. For the fixed point to be stable, all Lyapunov exponents have to be negative. Consequently, in this case $\mu_{max} < 0$, $h = D_L = 0$.

These estimations show that the different measures have a maximum for the uncoupled case, which corresponds to the trivial most chaotic or most random dynamics, since there are no spatial correlations and the dynamics at every node is given by the respective chaotic map. On the other hand, the respective minima are given for a synchronized fixed point, which is the most regular structure possible in a higher-dimensional system. Consequently, these are suitable measures to evaluate the chaoticity or randomness of the spatio-temporal dynamics.

Figures 6.1-6.12 display the Lyapunov spectrum, the maximum and the average positive Lyapunov exponent, and the Lyapunov dimension for the six chaotic string dynamics for the coupling range $\epsilon \in [0, 1]$. One observes that for small couplings up to around $\epsilon \approx 0.1$, all Lyapunov exponents are non-negative, corresponding to a Lyapunov dimension $D_L = N$. For larger couplings, a part or even all of the Lyapunov exponents become negative, and one obtains smaller values for μ_{max} , h , D_L . These dynamical states correspond to spatio-temporal patterns different from the fully developed spatio-temporal chaos obtained for the small-coupling region [66]. Note that there is some concurrence between the behaviour of D_L and h on the one hand and the inhomogeneity measure considered in Sec. 5.1. This concurrence does not always hold, since the respective quantities estimate different, not always equivalent facets of the dynamics. For instance a fully synchronized fixed point does not show any spatial inhomogeneity, whereas its Lyapunov dimension is zero. On the other hand, if the dynamics is spatially inhomogeneous in the sense defined in Sec. 5.1, this corresponds to patterns different from fully developed spatio-temporal chaos and accordingly $D_L < N$.

Figure 6.13 displays the average positive Lyapunov exponent h and the maximum Lyapunov exponent μ_{max} for the small coupling regions of all six dynamics. For the coupling values ϵ in these ranges, the dynamics only has positive Lyapunov exponents and thus Lyapunov dimension $D_L = N$. If one tries to observe a most random behaviour of the dynamics for non-zero coupling, it should be for a coupling in this region. However, as Fig. 6.13 reveals, both Lyapunov measures μ_{max} and h monotonically decrease for increasing coupling ϵ . Thus with respect to these measures, the dynamical states characterized by the zeros of the interaction energy do not show a most chaotic/most random behaviour.

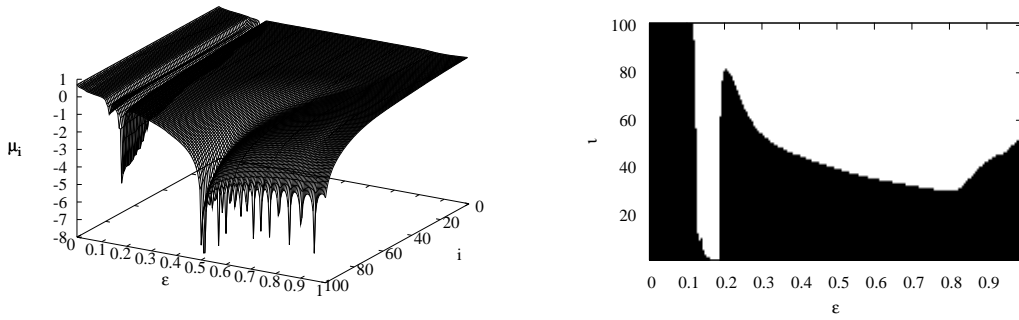


Figure 6.1: Left: Lyapunov spectrum for the 2A dynamics, depending on the coupling ϵ . Right: Lyapunov exponents larger zero (black) and smaller or equal to zero (white). Calculations were performed for lattice size $N = 101$, $T = 10^4$ iterations, a transient $T_0 = 10^3$ and one realization. It has been checked that other initial conditions yield similar results.

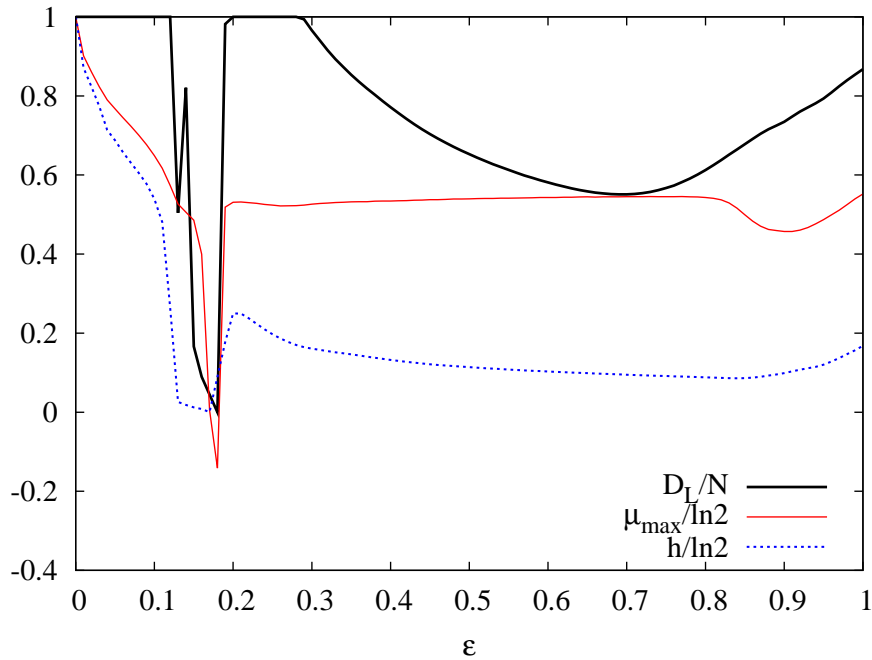


Figure 6.2: 2A dynamics. Maximum Lyapunov exponent μ_{\max} , average positive Lyapunov exponent h , and Lyapunov dimension D_L depending on the coupling ϵ . All measures have been normalized by the value for the uncoupled dynamics, that is $\ln 2$ for μ_{\max} and h , and lattice size N for D_L . Parameters are the lattice size $N = 101$, number of iterations $T = 10^4$ and transient $T_0 = 10^3$. All quantities have been averaged over 10 realizations.

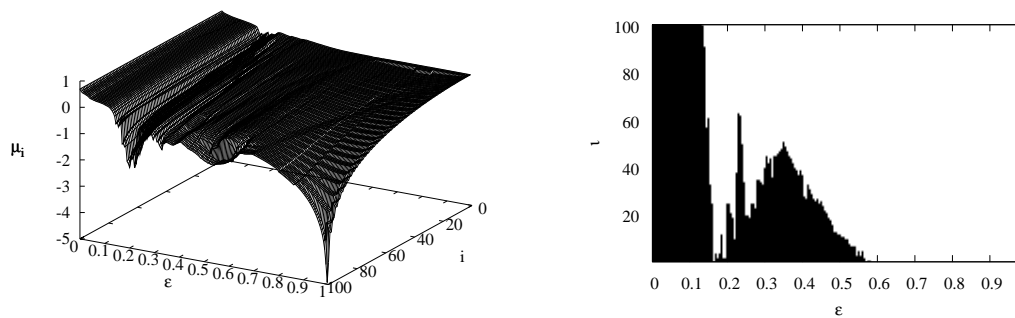


Figure 6.3: Same as Fig. 6.1, but for the $2B$ dynamics.

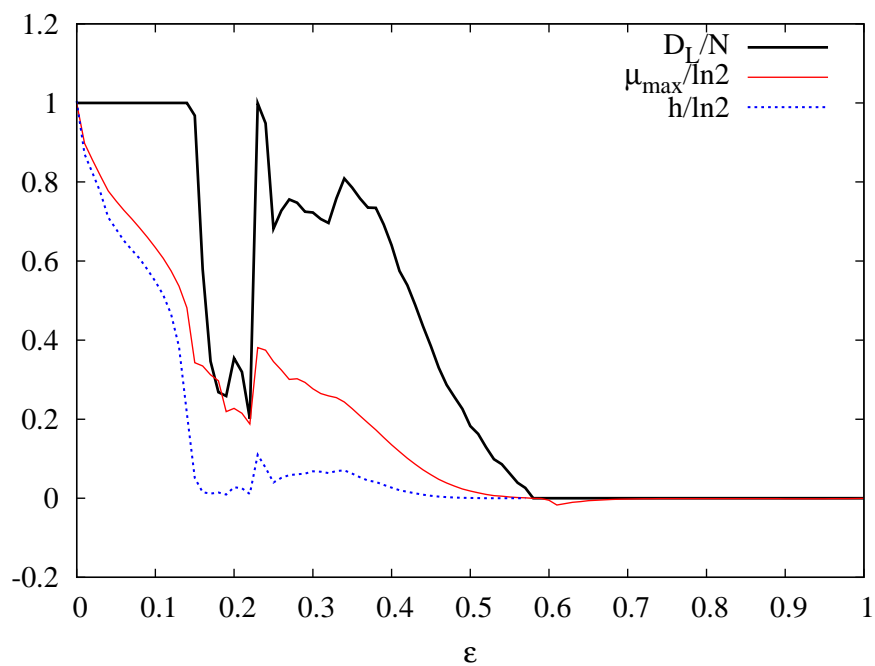


Figure 6.4: Same as Fig. 6.2, but for the $2B$ dynamics.

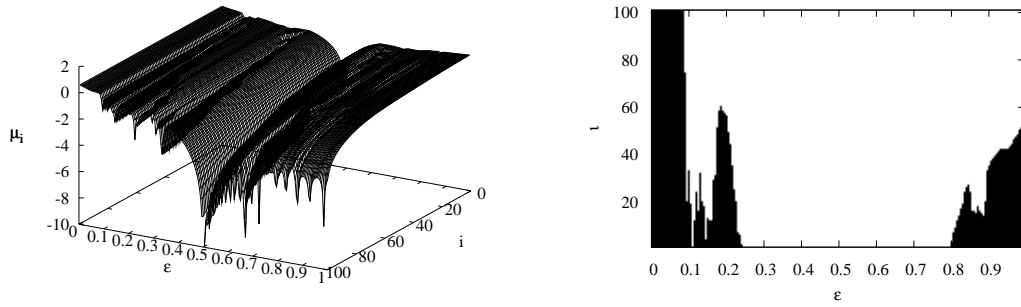


Figure 6.5: Same as Fig. 6.1, but for the $2A^-$ dynamics.

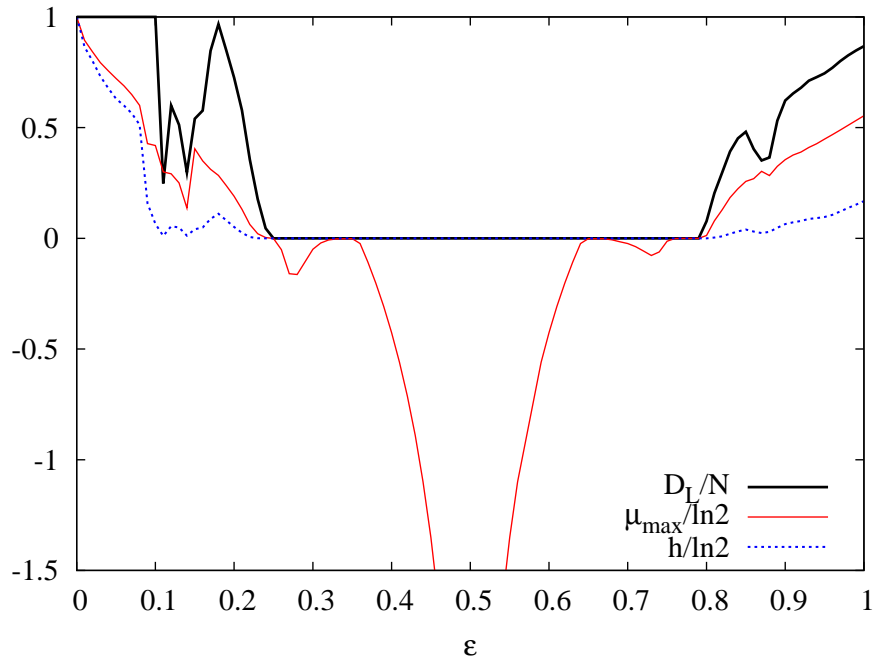


Figure 6.6: Same as Fig. 6.2, but for the $2A^-$ dynamics. The plot has been truncated at $\mu_{max}/\ln 2 = -1.5$.

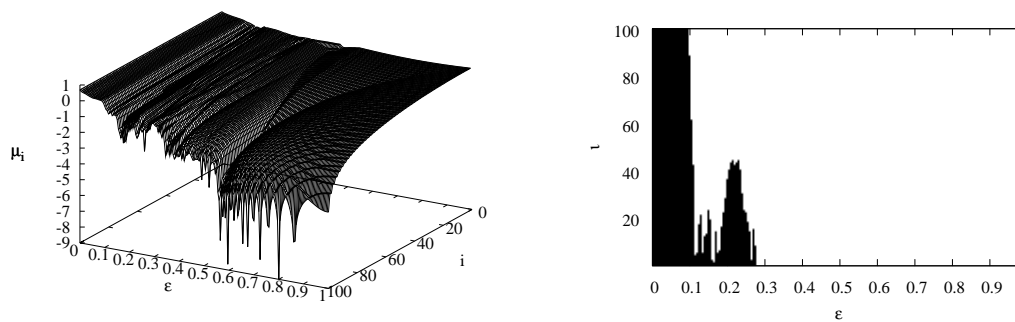


Figure 6.7: Same as Fig. 6.1, but for the $2B^-$ dynamics.

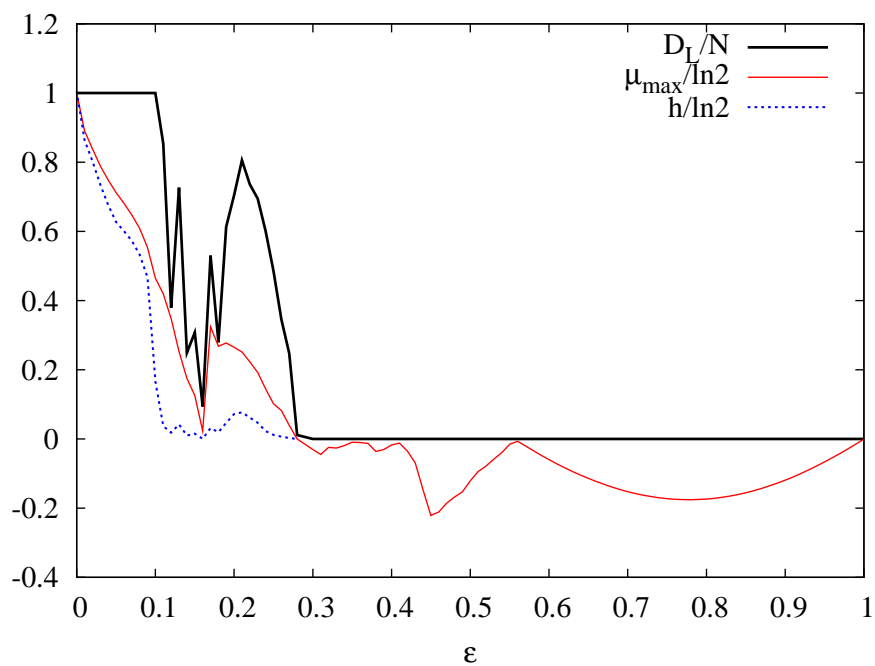


Figure 6.8: Same as Fig. 6.2, but for the $2B^-$ dynamics.

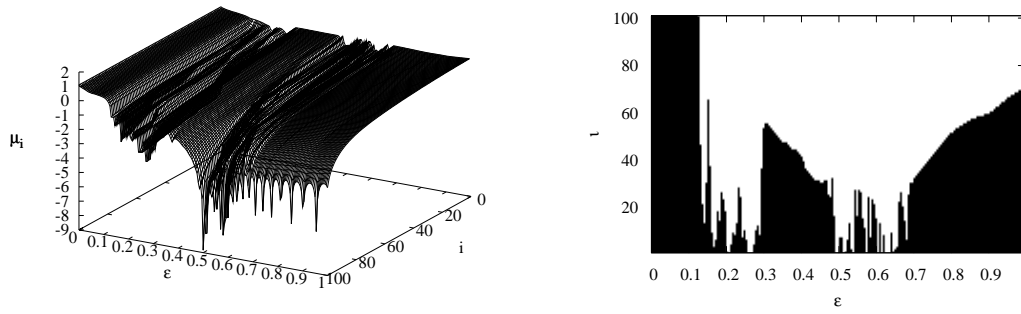


Figure 6.9: Same as Fig. 6.1, but for the 3A dynamics.

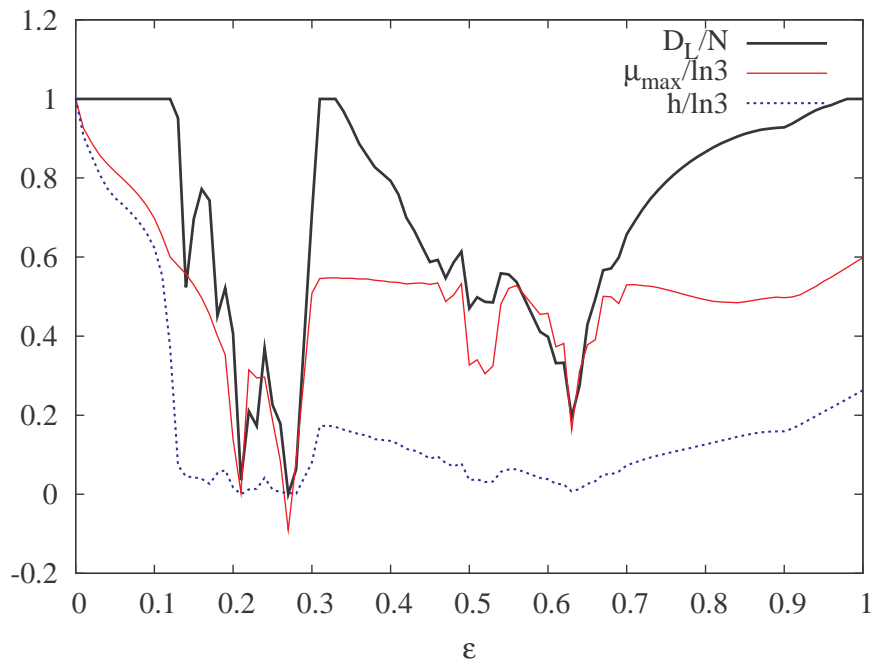


Figure 6.10: Same as Fig. 6.2, but for the 3A dynamics, with normalization $\ln 3$.

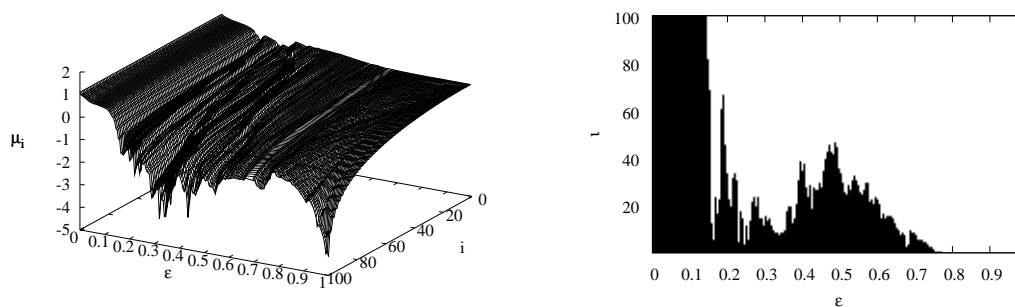


Figure 6.11: Same as Fig. 6.1, but for the $3B$ dynamics.

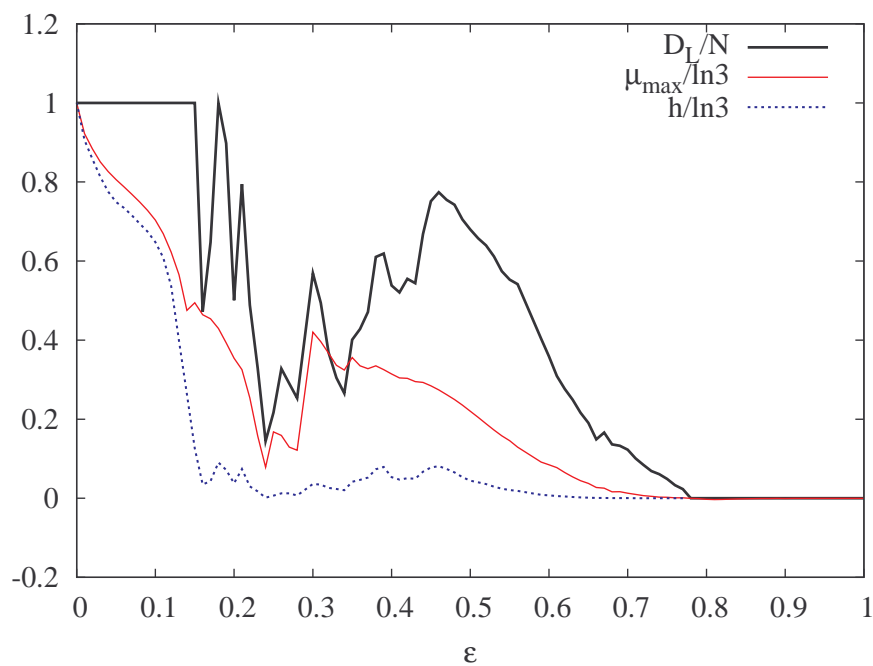


Figure 6.12: Same as Fig. 6.2, but for the $3B$ dynamics, with normalization $\ln 3$.

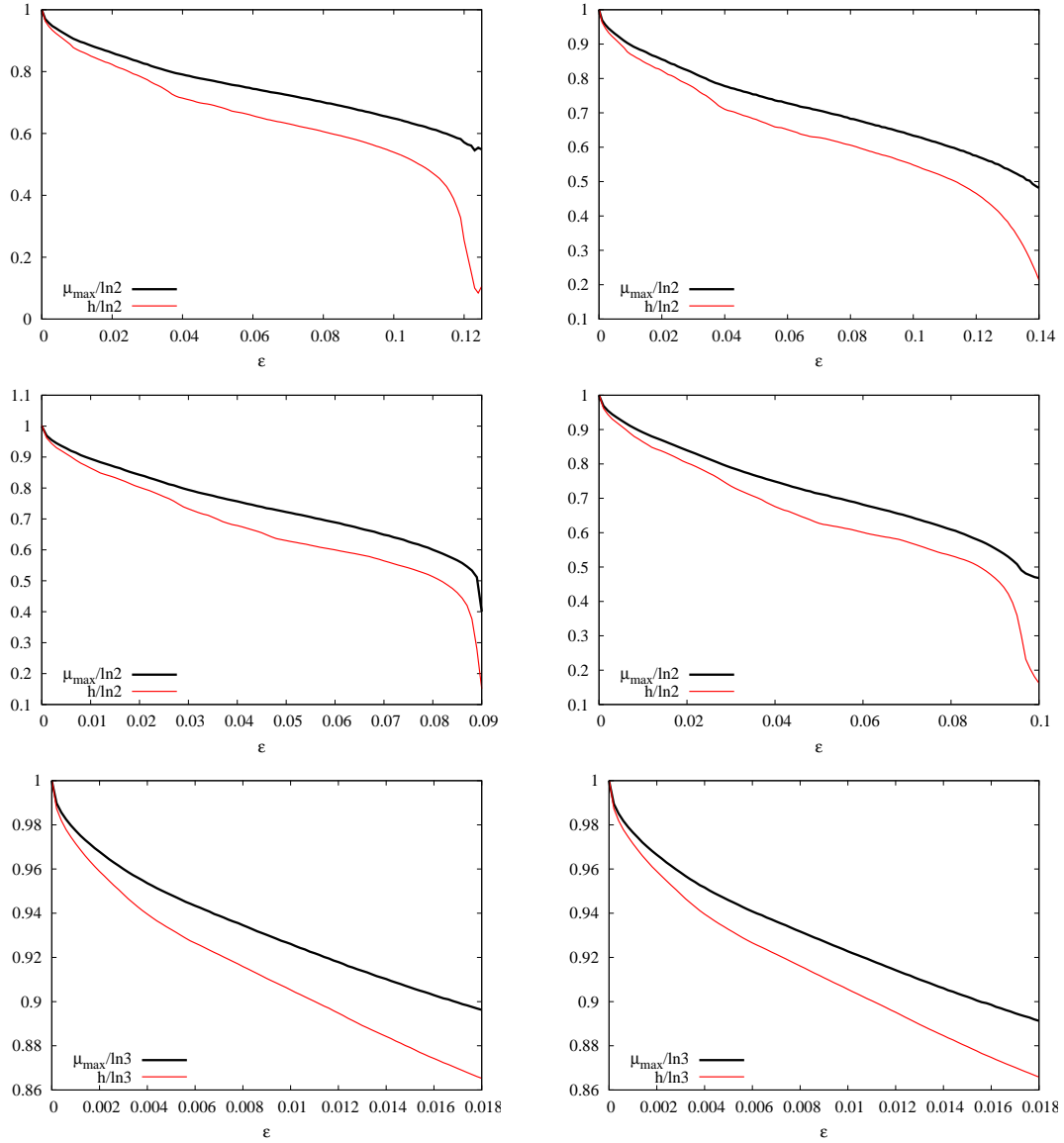


Figure 6.13: Rescaled maximum Lyapunov exponent $\mu_{\max}/\ln m$ and average positive Lyapunov exponent $h/\ln m$ for all six dynamics in the small coupling range, where all Lyapunov exponents are positive and thus $D_L = N$. Parameter $m = 2$ for 2A (top left), 2B (top right), 2A⁻ (middle left), 2B⁻ (middle right), $m = 3$ for 3A (bottom left), 3B (bottom right). Calculations were done for $N = 101$, $T = 10^4$ (2A, 2B, 2A⁻, 2B⁻) or $T = 10^5$ (3A, 3B), $T_0 = 10^3$. An average over 10 different initial conditions has been taken.

6.3 Spatial correlation measures

In the last section it has been shown that for the small coupling region all Lyapunov exponents of the chaotic string dynamics are positive. The maximum Lyapunov exponent μ_{max} as well as the average positive Lyapunov exponent h show a monotonically decreasing behaviour for increasing coupling strength. There is no distinguished behaviour for the zeros of the interaction energy $W(\epsilon)$, which contradicts an interpretation of the dynamics as being most random for these specific coupling values. The interaction energy only quantifies spatial correlations, whereas the Lyapunov measures introduced in the last section depend on the spatio-temporal dynamics as a whole. Accordingly, a possibility to keep the interpretation of a most random behaviour would be a reference to spatial correlations only. In order to follow this argument, in this section spatial correlation measures like higher order cumulants and mutual information are studied. For the sake of simplicity, only next neighbour-correlations will be considered.

6.3.1 Higher order cumulants

In Sec. 5.1 the density $\tilde{\rho}(x_i, x_j)$ has been introduced, where nodes i and j are neighbours in the ring-network. This quantity defines the probability density for observing simultaneously the value x_i at a node i and the value x_j at a neighbouring node j during the iteration of the dynamics, independently from the dynamical state of the remaining nodes. In the following only spatially homogeneous chaotic string dynamics will be considered, so this density is the same for all pairs of coupled nodes. Set the two-dimensional vectors $\tilde{\mathbf{x}} = (x_1, x_2)^T$ and $\mathbf{a} = (a_1, a_2)^T$. Suppose that the density $\tilde{\rho}(x_1, x_2) = \tilde{\rho}(\tilde{\mathbf{x}})$ is given, then the characteristic function [50] is defined by

$$\phi(\mathbf{a}) = \int d\tilde{\mathbf{x}} \exp[i\mathbf{a} \cdot \tilde{\mathbf{x}}] \tilde{\rho}(\tilde{\mathbf{x}}), \quad (6.9)$$

which characterizes the density $\tilde{\rho}$ by means of the Fourier inversion formula

$$\tilde{\rho}(\tilde{\mathbf{x}}) = \frac{1}{(2\pi)^2} \int d\mathbf{a} \exp[-i\tilde{\mathbf{x}} \cdot \mathbf{a}] \phi(\mathbf{a}). \quad (6.10)$$

If the moments $\langle x_1^{m_1} x_2^{m_2} \rangle$ exist, then

$$\langle x_1^{m_1} x_2^{m_2} \rangle = \left[\left(-i \frac{\partial}{\partial a_1}\right)^{m_1} \left(-i \frac{\partial}{\partial a_2}\right)^{m_2} \phi(\mathbf{a}) \right]_{\mathbf{a}=0}. \quad (6.11)$$

The logarithm of the characteristic function

$$\Phi(\mathbf{a}) = \log [\phi(\mathbf{a})] \quad (6.12)$$

is called the cumulant generating function [50]. If all moments exist, then $\phi(\mathbf{a})$ and accordingly $\Phi(\mathbf{a})$ can be expanded in a power series. Whereas the coefficients in the

Taylor expansion of the characteristic functions are the moments of the density $\tilde{\rho}$, the corresponding coefficients in the expansion of the cumulant generating functions are called cumulants:

$$\langle\langle x_1^{m_1} x_2^{m_2} \rangle\rangle. \quad (6.13)$$

In the case of vanishing coupling, the density $\tilde{\rho}(x_1, x_2)$ factorizes, and for the cumulant generating function holds

$$\Phi(\mathbf{a}) = \log [\phi(a_1)] + \log [\phi(a_2)]. \quad (6.14)$$

All mixed terms $\langle\langle x_1^{m_1} x_2^{m_2} \rangle\rangle$ must then be zero. The cumulants are a measure of the degree of correlation of the density $\tilde{\rho}$ [50].

By comparing the Taylor expansion of the characteristic function and the cumulant generating function, one can express the different cumulants by means of the moments. For the general formula to calculate the cumulants, see Ref. [50]. In the following, all cumulants up to fourth order, that is $\langle\langle x_1^{m_1} x_2^{m_2} \rangle\rangle$ with $m_1 + m_2 \leq 4$ will be displayed. As an abbreviation the notation

$$C(m_1, m_2) = \langle\langle x_1^{m_1} x_2^{m_2} \rangle\rangle \quad (6.15)$$

is used. Note that due to the spatial homogeneity of the dynamics, $C(m_1, m_2) = C(m_2, m_1)$, so only terms with $m_1 \geq m_2$ will be considered.

Cumulants of order 1:

$$C(1, 0) = \langle x_1 \rangle. \quad (6.16)$$

Cumulants of order 2:

$$C(1, 1) = \langle x_1 x_2 \rangle - \langle x_1 \rangle \langle x_2 \rangle, \quad (6.17)$$

$$C(2, 0) = \langle x_1^2 \rangle - \langle x_1 \rangle^2. \quad (6.18)$$

Cumulants of order 3:

$$\begin{aligned} C(2, 1) &= \langle x_1^2 x_2 \rangle - \langle x_1^2 \rangle \langle x_2 \rangle \\ &\quad - 2 \langle x_1 x_2 \rangle \langle x_1 \rangle + 2 \langle x_1 \rangle^2 \langle x_2 \rangle, \end{aligned} \quad (6.19)$$

$$C(3, 0) = \langle x_1^3 \rangle - 3 \langle x_1^2 \rangle \langle x_1 \rangle + 2 \langle x_1 \rangle^3. \quad (6.20)$$

Cumulants of order 4:

$$\begin{aligned}
C(2,2) &= \langle x_1^2 x_2^2 \rangle - 2 \langle x_1^2 x_2 \rangle \langle x_2 \rangle - 2 \langle x_2^2 x_1 \rangle \langle x_1 \rangle \\
&\quad - \langle x_1^2 \rangle \langle x_2^2 \rangle - 2 \langle x_1 x_2 \rangle^2 + 2 \langle x_1^2 \rangle \langle x_2 \rangle^2 \\
&\quad + 2 \langle x_2^2 \rangle \langle x_1 \rangle^2 + 8 \langle x_1 x_2 \rangle \langle x_1 \rangle \langle x_2 \rangle - 6 \langle x_1 \rangle^2 \langle x_2 \rangle^2, \tag{6.21}
\end{aligned}$$

$$\begin{aligned}
C(3,1) &= \langle x_1^3 x_2 \rangle - 3 \langle x_1 \rangle \langle x_1^2 x_2 \rangle - \langle x_2 \rangle \langle x_1^3 \rangle \\
&\quad - 3 \langle x_1^2 \rangle \langle x_1 x_2 \rangle + 6 \langle x_1^2 \rangle \langle x_1 \rangle \langle x_2 \rangle \\
&\quad + 6 \langle x_1 x_2 \rangle \langle x_1 \rangle^2 - 6 \langle x_1 \rangle^3 \langle x_2 \rangle, \tag{6.22}
\end{aligned}$$

$$\begin{aligned}
C(4,0) &= \langle x_1^4 \rangle - 4 \langle x_1 \rangle \langle x_1^3 \rangle - 3 \langle x_1^2 \rangle^2 \\
&\quad + 12 \langle x_1^2 \rangle \langle x_1 \rangle^2 - 6 \langle x_1 \rangle^4. \tag{6.23}
\end{aligned}$$

Figures 6.14-6.16 show higher order cumulants for the small coupling region for all six chaotic string dynamics. It seems that the $2A$ and $2B^-$ dynamics share a similar behaviour, as well as the $2B$ and $2A^-$ dynamics. The reason for this coincidence is not clear and should be the aim of future studies.

As a comparison to the different cumulants the interaction energy $W(\epsilon)$ is displayed. For all dynamics based on second order Tchebyscheff polynomials, the interaction energy differs from the first order cumulant $C(1,1)$. This is due to non-vanishing moments $\langle x_i \rangle$ at the respective nodes for these dynamics. Accordingly, when considering the first order cumulant as the lowest-order spatial correlation function, zeros are shifted to different, smaller coupling values for the $2A$ and $2B^-$ dynamics. For the $2B$ and $2A^-$ dynamics, there are no zeros in the small coupling region.

For the $3A$ and $3B$ dynamics the situation is slightly different. Due to the symmetry $T_3(-x) = -T_3(x)$ for the third order Tchebyscheff polynomial, the moments $\langle x_i \rangle$ vanish and the interaction energy is equal to the first order cumulant $C(1,1)$. However, higher-order cumulants do not vanish for the zeros of the interaction energy. So these distinguished couplings are only ‘special’ with respect to these first order correlations, but not with respect to higher order correlation measures.

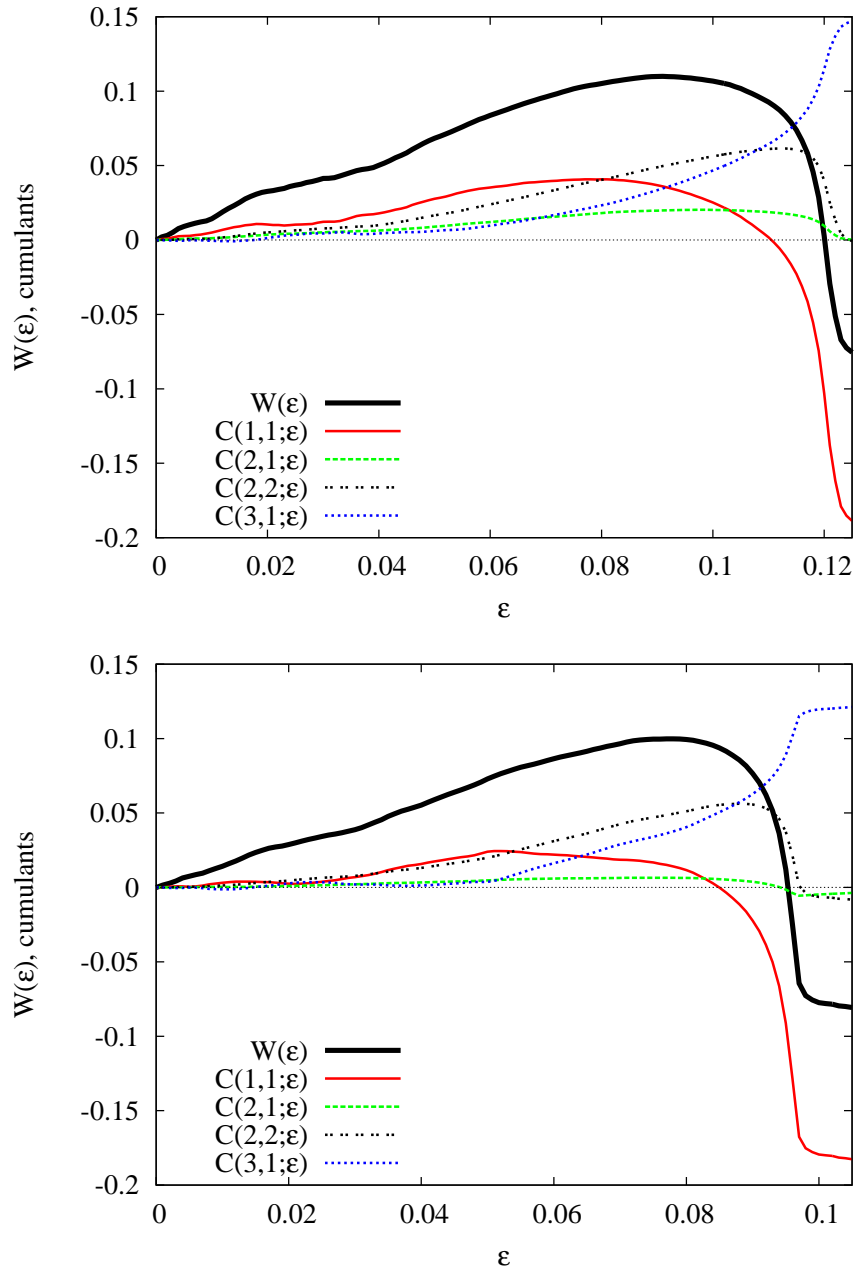


Figure 6.14: Higher order cumulants for the small coupling region of the $2A$ (top) and $2B^-$ (bottom) dynamics. For this coupling region all Lyapunov exponents are positive and accordingly $D_L = N$. Parameters are the network size $N = 101$, $T = 10^4$ iterations, transient $T_0 = 10^3$. The cumulants have been averaged over all coupled pairs in the ring-network.

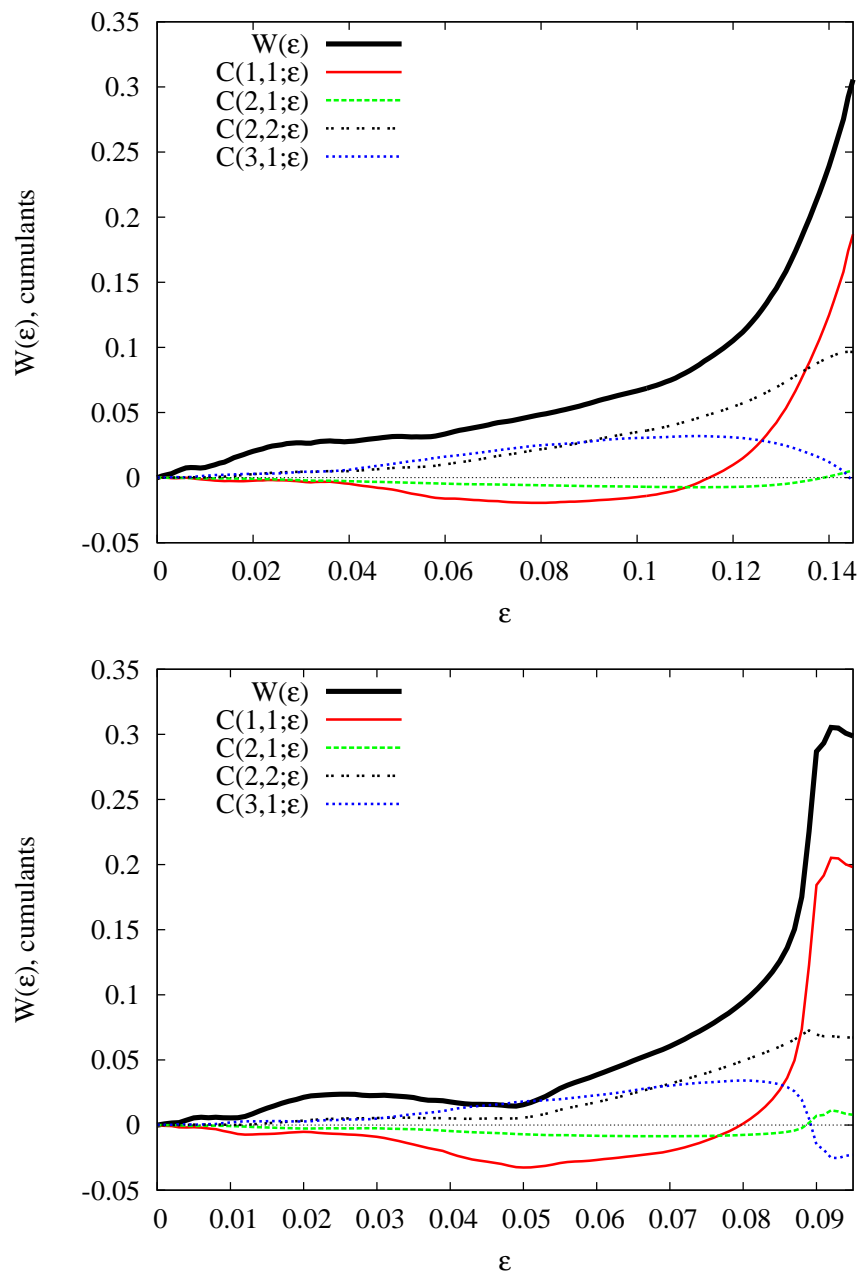


Figure 6.15: Same as Fig. 6.14, but for the $2B$ (top) and the $2A^-$ (bottom) dynamics.

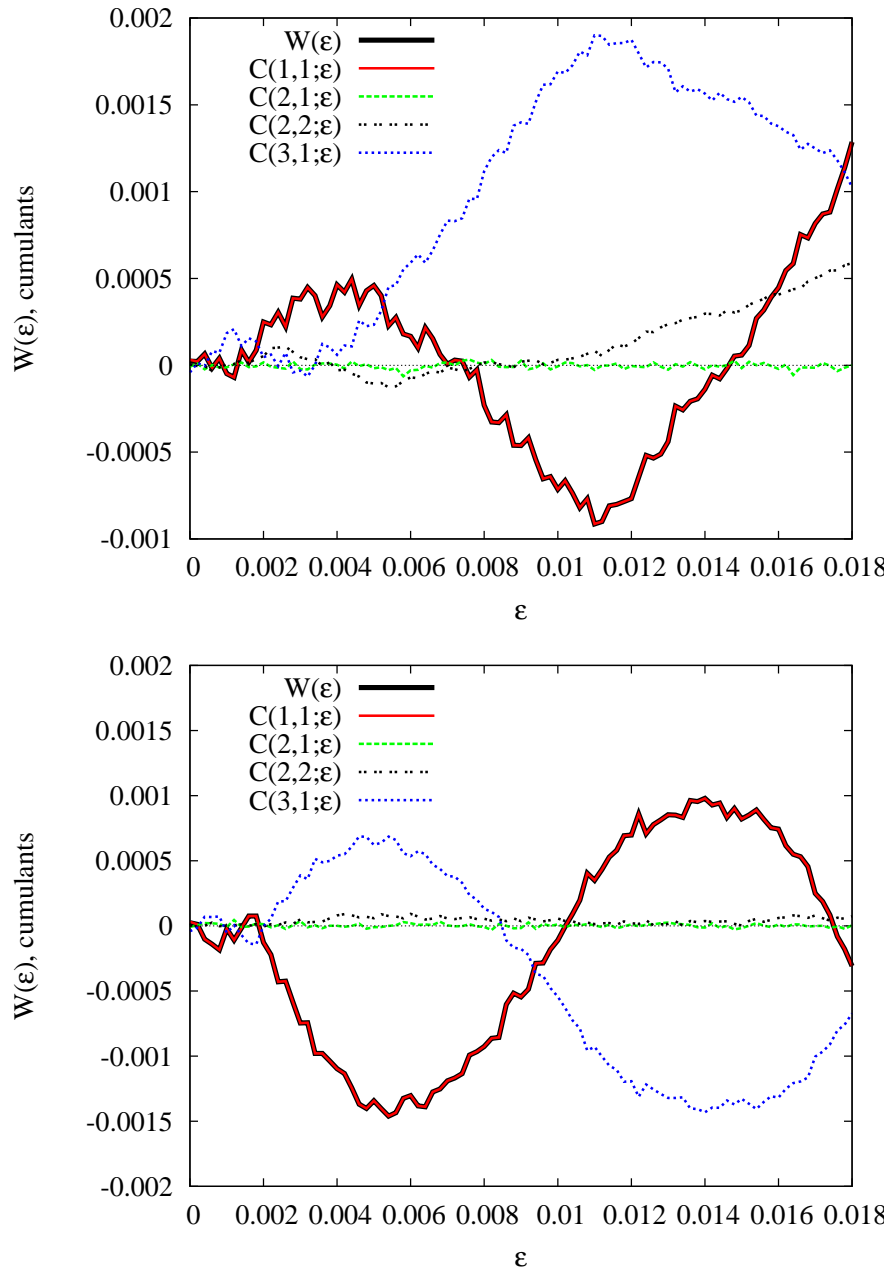


Figure 6.16: Same as Fig. 6.14, but for the 3A (top) and the 3B (bottom) dynamics. Since the moment $\langle x_i \rangle$ vanishes for these dynamics in the small coupling region, the interaction energy and the first-order coincide, and the respective curves lie on top of each other in these figures.

6.3.2 Mutual information

The mutual information I evaluates the difference between the density $\tilde{\rho}(x_1, x_2)$ and the product of the individual densities $\tilde{\rho}_1(x_1)\tilde{\rho}_2(x_2)$ [103].

For the calculation of I consider two neighbouring nodes i and j . Divide the phase space $[-1, 1]$ of the individual map into L cells of equal size $2/L$, labeled with integers $1, \dots, L$. For a large number of iterations T of the dynamics, let $n_i(\alpha)$ ($n_j(\beta)$) count the number of times $x_i(t)$ ($x_j(t)$) lies in the cell α (β). Let $n_{ij}(\alpha, \beta)$ count the number of times where $x_1(t)$ lies in cell α and simultaneously $x_j(t)$ lies in cell β . After a sufficient long iteration time T define

$$\begin{aligned} w_i(\alpha) &= \frac{n_i(\alpha)}{T}, \\ w_j(\beta) &= \frac{n_j(\beta)}{T}, \\ w_{ij}(\alpha, \beta) &= \frac{n_{ij}(\alpha, \beta)}{T}. \end{aligned} \quad (6.24)$$

In the limit $L \rightarrow \infty$ the quantity $w_i(\alpha)$ corresponds to the density $\tilde{\rho}(x_i)$ (the same holds for w_j and w_{ij}). The mutual information is defined as

$$I = \sum_{\alpha, \beta} w_{ij}(\alpha, \beta) \log \left[\frac{w_{ij}(\alpha, \beta)}{w_i(\alpha)w_j(\beta)} \right]. \quad (6.25)$$

Since this quantity depends on the number of cells L , all numerical calculations will be performed for increasing L in order to assure the convergence of the mutual information.

For vanishing coupling it holds

$$w_{ij}(\alpha, \beta) = w_i(\alpha)w_j(\beta) \quad (6.26)$$

and consequently $I = 0$.

Figures. 6.17-6.20 display the mutual information for the coupling regions where the interesting zeros of the interaction energy are observed. For the $2A$ and $2B$ as well as the $3A$ and $3B$ dynamics basically a monotonically increasing behaviour of $I(\epsilon)$ for increasing coupling ϵ is observed. For the $2A^-$ and the $2B^-$ dynamics local minima at $\epsilon \approx 0.7$ are observed, but these minima do not correspond to zeros of the interaction energy. Thus the mutual information confirms the findings of the previous sections: The dynamical states corresponding to a vanishing interaction energy $W(\epsilon) = 0$ are distinguished by $W(\epsilon)$ only, but not by other correlation measures. This contradicts an interpretation of these states in terms of a most random behaviour.

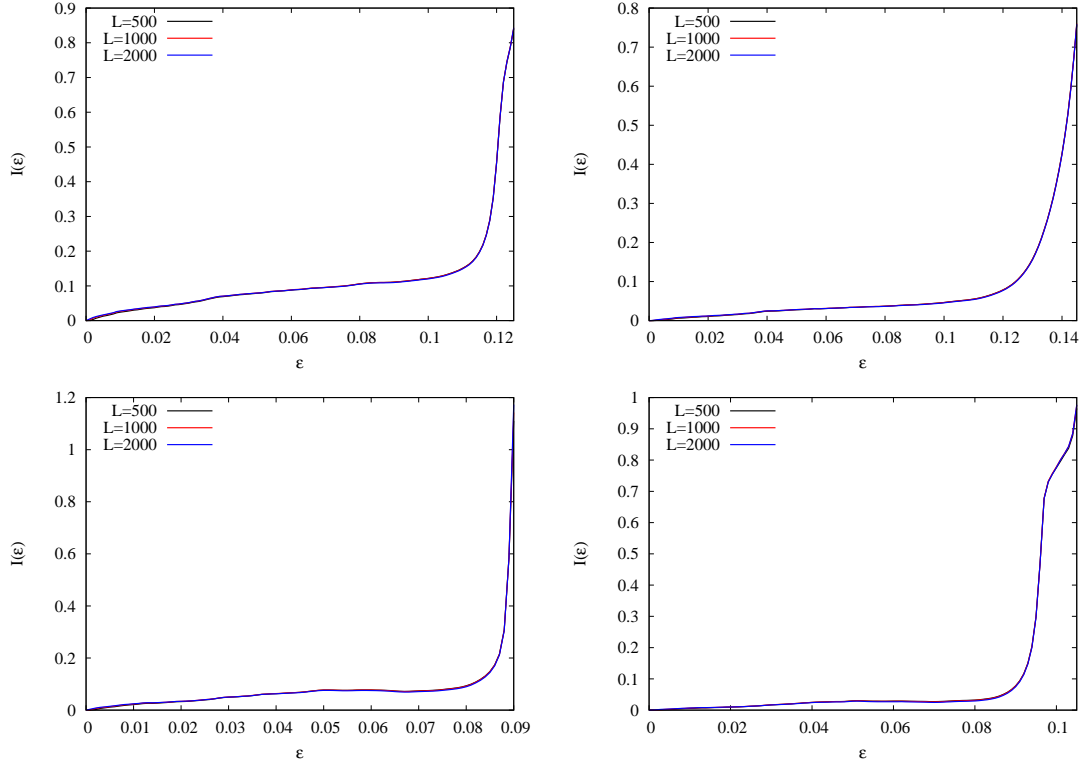


Figure 6.17: Mutual information I for the coupling region with Lyapunov dimension $D_L = N$ of the chaotic string dynamics based on second order Tchebycheff polynomials. Top left: $2A$. Top right: $2B$. Bottom left: $2A^-$. Bottom right: $2B^-$. Calculations were done for ring size $N = 101$, and an average over all coupled pair of nodes and 10 different initial conditions has been performed. The ratio between the number of iterations T and the number of boxes L has been fixed to $T/L = 5 \cdot 10^3$, so the statistics for the different choices of L is approximately the same. In the figures, the curves for the three different values of L coincide and thus lie on top of each other.

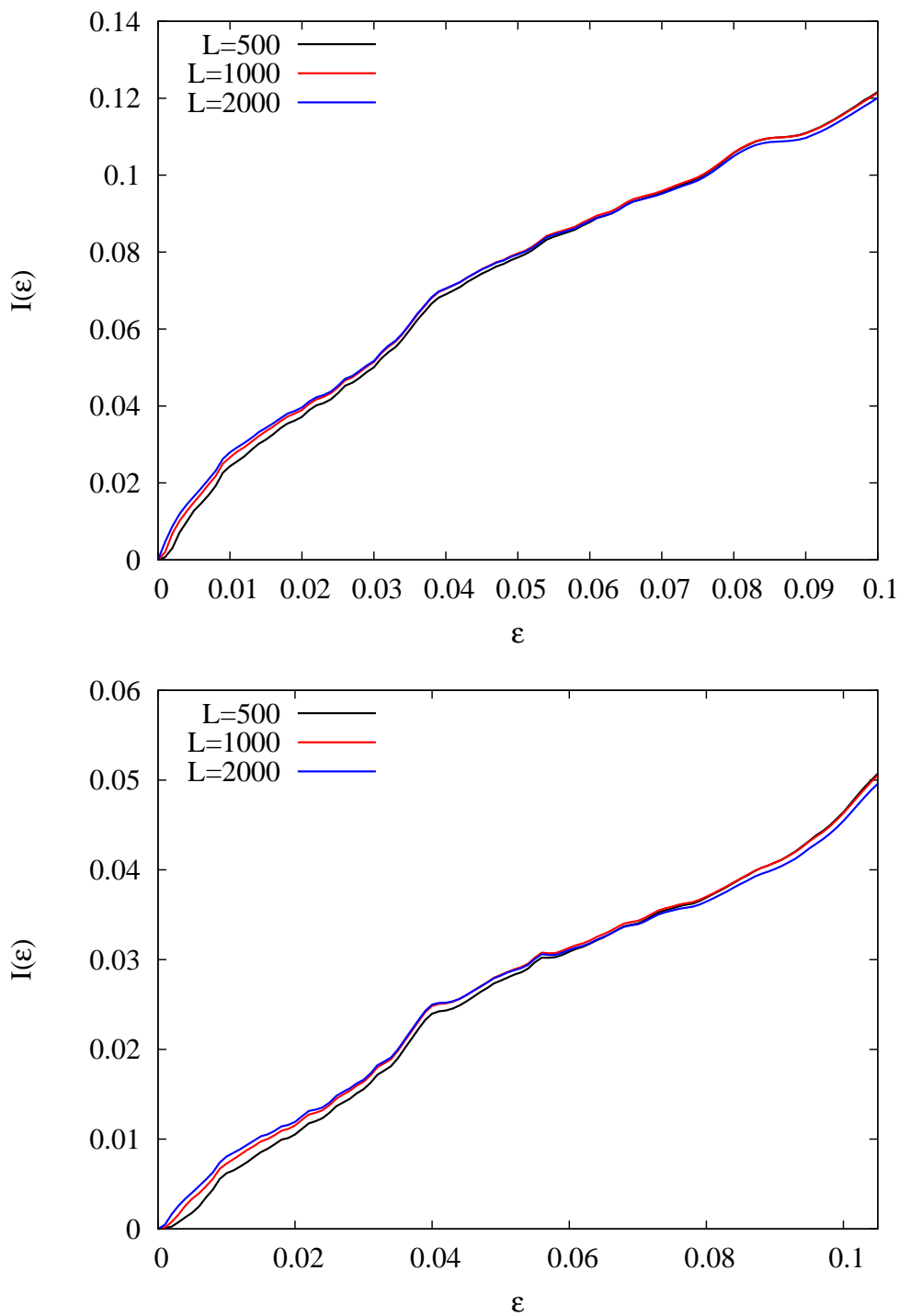


Figure 6.18: Same as Fig. 6.17 for the small coupling region. Top: $2A$ dynamics. Bottom: $2B$ dynamics.

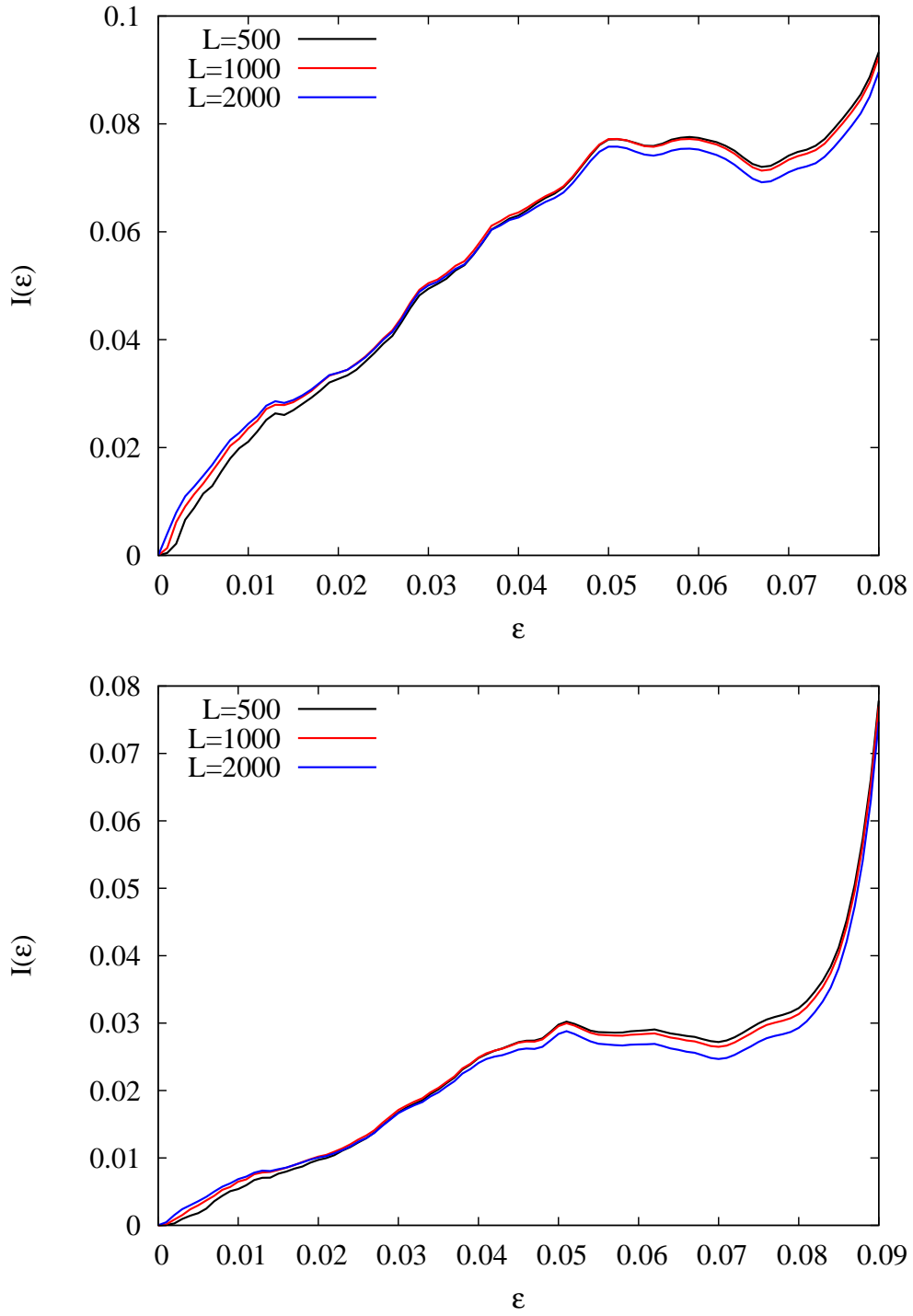


Figure 6.19: Same as Fig. 6.19, but for the $2A^-$ (top) and the $2B^-$ (bottom) dynamics.

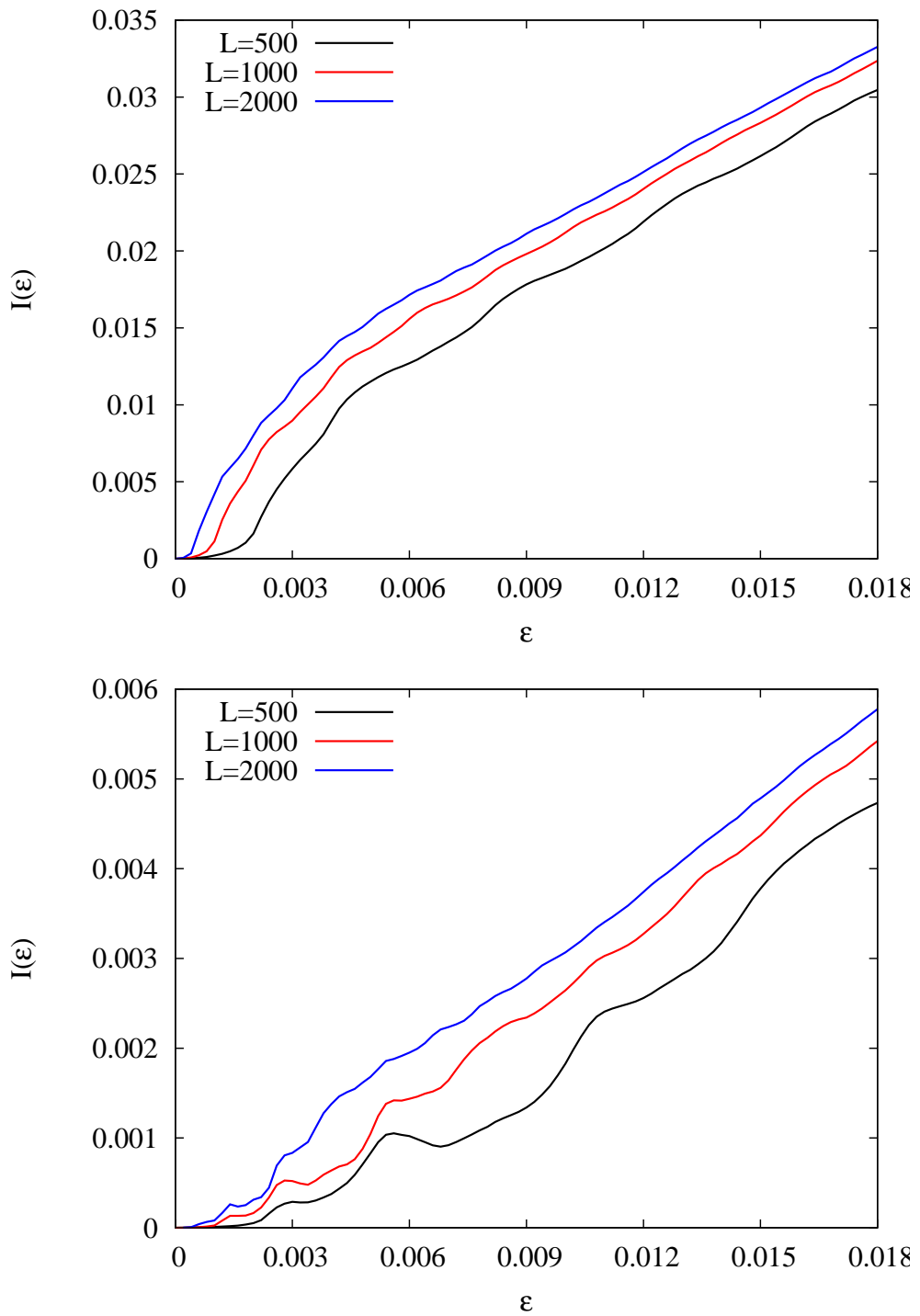


Figure 6.20: Same as Fig. 6.18, but for the small coupling region of the 3A (top) and 3B (bottom) dynamics. For the respective calculations the ratio between the number of iterations T and the number of boxes L has been fixed to $T/L = 5 \cdot 10^4$.

7 Disordered chaotic strings

In the last chapter I have shown that the interpretation of dynamical states with a vanishing interaction energy in terms of a most random behaviour cannot be applied. The dynamics for couplings ϵ^* with $W(\epsilon^*) = 0$ thus is ‘special’ with respect to $W(\epsilon)$ only. Although the physical embedding of the interaction energy needs more clarification, it seems to be the relevant observable for the theory proposed by Beck [17].

Instead of studying alternative measures as done in the last chapter, in the following chapter I will keep the interaction energy as the relevant observable, but alter the chaotic string model itself by the introduction of disorder phenomena. The first extension is coupling disorder and addresses the local randomization of the coupling weights of the Tchebyscheff maps. The second extension is network disorder and addresses the random small-world deformation of the ring topology.

7.1 Coupling disorder

The network generalization of the chaotic string dynamics as defined in Sec. 3.1 is given by

$$x_i(t+1) = (1 - \epsilon_i)f[x_i(t)] + \sum_{j=1}^N \frac{A_{ij}\epsilon_{ij}}{k_i}g[x_j(t)]. \quad (7.1)$$

Here A_{ij} is the adjacency matrix representing the network structure, k_i is the degree of node i , and ϵ_{ij} denotes the coupling weight of the link from node j to node i . The quantity

$$\epsilon_i = \frac{1}{k_i} \sum_{j=1}^N A_{ij}\epsilon_{ij} \quad (7.2)$$

measures the average weight of links connected to node i . The functions $f(x)$ and $g(x)$ are given in Tab. 3.1.

A straightforward way to introduce perturbations to a uniform coupling is random disorder. It allows different coupling weights ϵ_{ij} between different neighbouring vertices. In order to assure that $x_i(t)$ is bound to $[-1, 1]$, some care has to be taken. For every edge a random disorder number ξ_{ij} is drawn from the uniform distribution defined on $[1 - \Delta, 1 + \Delta]$ with $\Delta \in [0, 1]$. The disordered coupling weight ϵ_{ij} is then defined as

$$\epsilon_{ij} = \frac{k_i \xi_{ij}}{\sum_{j=1}^N A_{ij} \xi_{ij}} \epsilon. \quad (7.3)$$

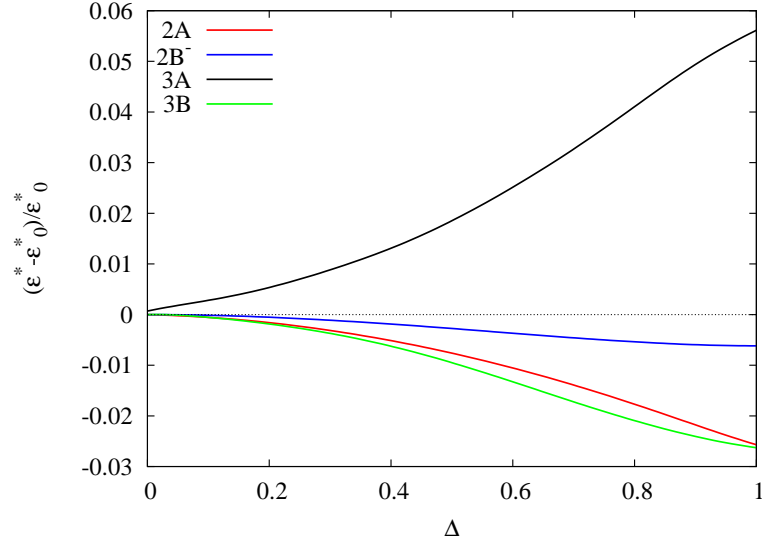


Figure 7.1: Relative shift $(\epsilon^*(\Delta) - \epsilon_0^*)/\epsilon_0^*$ of the zeros $\epsilon_1^{(2A)}$ (red), $\epsilon_1^{(2B^-)}$ (blue), $\epsilon_2^{(3A)}$ (black), $\epsilon_2^{(3B)}$ (green) as a function of the coupling disorder Δ . ϵ_0^* denotes the respective zero for zero disorder $\Delta = 0$. The interaction energy has been calculated with a ring size $N = 1001$, $T = 10^6$ (2A and 2B⁻ dynamics) and $T = 10^7$ (3A and 3B dynamics) iterations, and an average over 10 disorder realizations, respectively.

The coupling weights ϵ_{ij} obtained by this procedure are symmetrically distributed around the average value ϵ , and it holds $\epsilon_i = \epsilon$ for all i .

The interaction energy $W(\epsilon, \Delta)$ has now also become a function of the coupling disorder Δ . The zeros of the interaction energy, given in Tab. 3.3 will shift as a function of Δ . This is illustrated in Fig. 7.1. The numerical calculations reveal that the zeros $\epsilon_2^{(3B)}$, $\epsilon_1^{(2A)}$ and $\epsilon_1^{(2B^-)}$ are shifted to smaller coupling values for increasing disorder parameter Δ , whereas the zero $\epsilon_2^{(3A)}$ is shifted to larger coupling values. The zeros $\epsilon_1^{(3A)}$ and $\epsilon_1^{(3B)}$ have not been considered. Due to their smallness the numerical calculations are too expensive to reach acceptable convergence.

7.2 Network disorder

Network disorder is different to coupling disorder. The ring-network structure is perturbed and the coupling is kept homogeneous. A straightforward way to introduce perturbations to the ring-structure is to add random short-cuts, thus obtaining a small world network [89, 114]. I start with the original one-dimensional lattice, where every vertex i is only coupled to its respective neighbours on each side, and thus has degree $k_i = 2$, leading to an average degree $\langle k \rangle = 2$ of the network. In order to obtain a small world network, additional edges \mathcal{E}_{add} are randomly placed between previously uncoupled vertices. Since every new edge increases the degree of both adjacent vertices, the average degree of the resulting small world network is given by

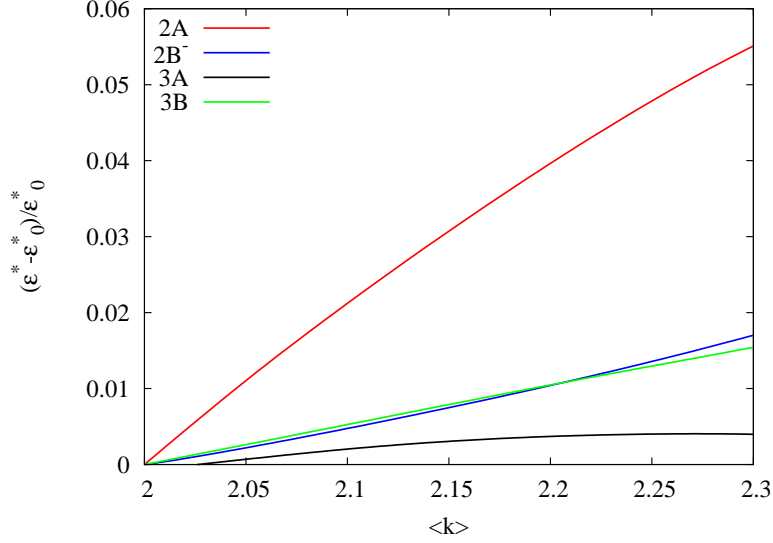


Figure 7.2: Relative shift $(\epsilon^*(\langle k \rangle) - \epsilon_0^*)/\epsilon_0^*$ of the zeros $\epsilon_1^{(2A)}$ (red), $\epsilon_1^{(2B^-)}$ (blue), $\epsilon_2^{(3A)}$ (black), $\epsilon_2^{(3B)}$ (green) as a function of the network disorder $\langle k \rangle$. ϵ_0^* denotes the respective zero for zero disorder, that is a ring structure with $\langle k \rangle = 2$. The interaction energy has been calculated with a ring size $N = 1001$, $T = 10^6$ iterations ($2A$ and $2B^-$ dynamics), $T = 10^7$ iterations ($3A$ and $3B$ dynamics) and 10 network realizations.

$\langle k \rangle = 2 + (2|\mathcal{E}_{add}|/N)$, which in the following is used as the disorder parameter.

The interaction energy $W(\epsilon, \langle k \rangle)$ is now also a function of the network disorder parameter. Its zeros will shift as a function of $\langle k \rangle$. This is illustrated in Fig. 7.2. The numerical calculations reveal that for increasing network disorder all zeros are shifted to larger coupling values.

7.3 Discussion

In Ref. [17] the $2A$ and $2B^-$ couplings are associated with running strong coupling constants $\alpha_s(E)$ at certain energy scales. A shift of the zeros $\epsilon^* = \alpha_s(E)$ thus can be related to a shift of the associated energy scale E . Figure 7.3 shows this energy shift for the $2B^-$ dynamics. According to Ref. [17], the zero $\epsilon_1^{(2B^-)}$ is associated with the strong coupling constant at an energy scale given by $E = 2m_t + E'$, with m_t the mass of the top quark and E' proposed to be the Higgs mass m_H . For zero coupling disorder and a ring-network one obtains $m_H \approx 160$ GeV.¹ This value is just above the currently estimated energy range $115 - 150$ GeV of the Higgs mass [84]. In case of an experimental detection of the Higgs boson, the introduction of network disorder could then allow to shift the energy scale E' to the observed value, and thus to keep the interpretation $E' = m_H$.

¹Numerical differences to the result given in Ref. [17] arise from the way how the quark masses and thresholds are handled in the calculation of the running strong coupling constant.

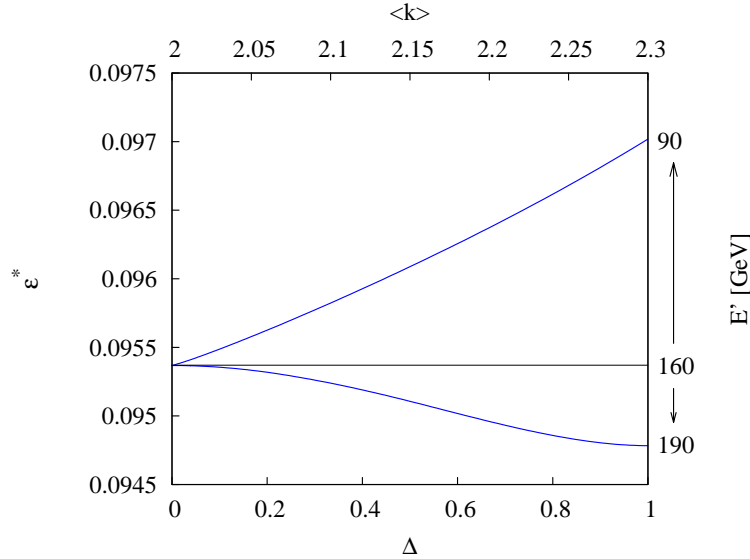


Figure 7.3: Energy shift in the interpretation of the zero $\epsilon_1^{(2B^-)}$ as a running strong coupling constant $\alpha_s(E)$. According to Ref. [17] the energy is given by $E = E' + 2m_t$, where m_t is the top quark mass (literature value $m_t = 170.9$ GeV [5]), and E' is supposed to be the Higgs mass m_H . The lower part shows the shift due to coupling disorder, whereas the upper part shows the shift due to network disorder. The running strong coupling $\alpha_s(E)$ has been calculated as in Ref. [25].

The $3B$ zero is supposed to be related to a combination of two electroweak couplings. Hence a shift can be associated to a different combination or a change in the energy scale. Note however, that the energy-dependence of the electroweak coupling is much smaller than for the strong coupling.

As one can see in Figs. 7.1, 7.2, for three out of the four considered zeros the coupling and network disorder shift the zero ϵ^* in different directions. For these zeros I find a curve $\langle k \rangle (\Delta)$ with $W(\epsilon^*)=0$, where ϵ^* is fixed to the respective value obtained for a homogeneous coupling and an unperturbed ring-network structure as in Ref. [17] (see Fig. 7.4). This finding implies that for these zeros the specific combination of coupling and network disorder reproduces the zero ϵ^* as given in Ref. [17] for the ring with homogeneous couplings. In contrast to the zeros of the $2A$, $2B^-$ and $3B$ dynamics, the zero $\epsilon_2^{(3A)}$ of the $3A$ dynamics is shifted to larger values for coupling as well as network disorder. Thus it is not possible to combine the two forms of disorder in order to maintain the value as given in Ref. [17]. In Ref. [17] the zero $\epsilon_2^{(3A)}$ is related to the running electromagnetic coupling $\alpha_{el}(E)$ at three times the electron mass scale $E = 3m_e$. This is a rather small energy. In fact, the fine structure constant $\alpha_{el}(0)$ at zero energy is a lower bound for a running electromagnetic coupling. It is an interesting observation that the zero of the $3A$ dynamics is only shifted to larger values, but not to smaller values. These would not allow for an interpretation in terms of smaller energies due to the lower bound. The larger values are associated to larger energy scales, which are of the order 10 MeV for network disorder and of the

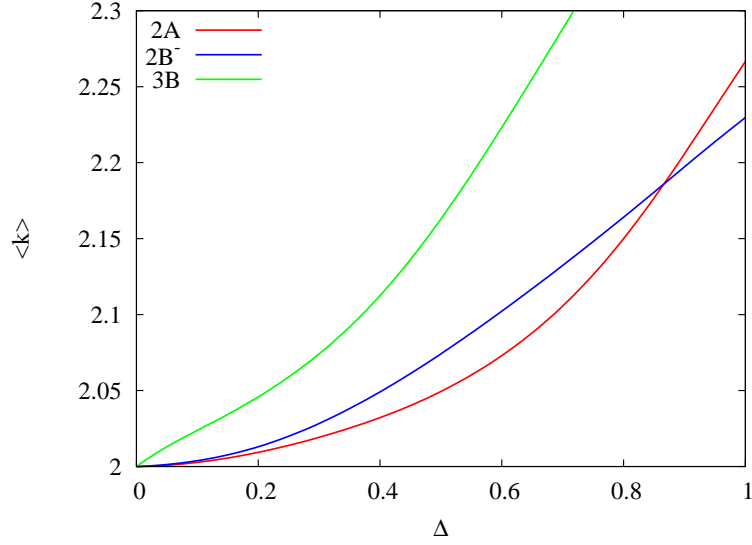


Figure 7.4: Specific combinations of coupling and network disorder, which leave the zero ϵ^* of the interaction energy independent of Δ and $\langle k \rangle$, and keep it equal to its non-perturbed value. The interaction energy has been calculated with $N = 1001$ and $T = 10^6$, 10 coupling/network disorder realizations for the 2A (red) and 2B⁻ (blue) dynamics, and 100 coupling/network disorder realizations for the 3B (green) dynamics.

order 10 GeV for coupling disorder (see Fig. 7.5).

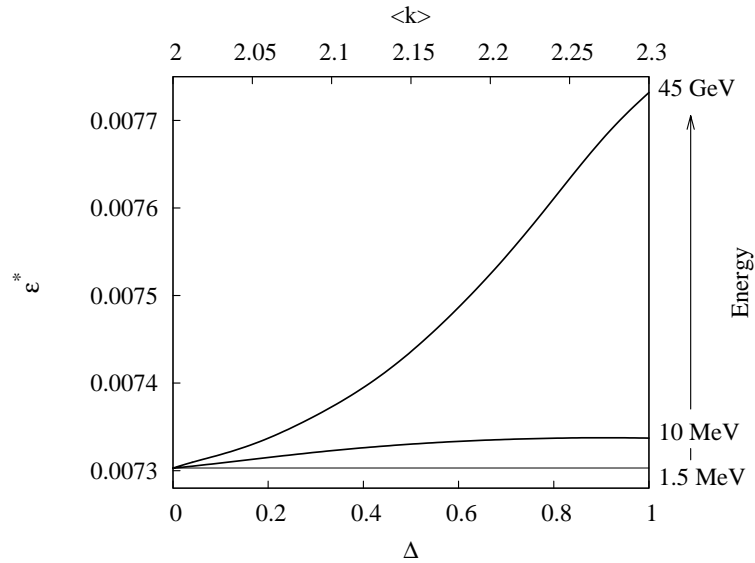


Figure 7.5: Energy shift in the interpretation of the zero $\epsilon_2^{(3A)}$ as a running electromagnetic coupling constant $\alpha_{el}(E)$. According to Ref. [16] the energy is $E \approx 1.5 \text{ MeV} \approx 3m_e$ for zero coupling and network disorder. The lower curve shows the energy shift for increasing network disorder, whereas the upper curve shows the shift due to increasing coupling disorder. The running electromagnetic coupling $\alpha_{el}(E)$ has been calculated as given in Ref. [17], with particle masses and the fine structure constant $\alpha_{el}(0)$ taken from Ref. [5].

8 Complete synchronization of networks

In the previous chapters various properties of coupled chaotic Tchebycheff map networks were studied. For such systems, due to the complicated spatio-temporal dynamics in general only a numerical treatment is possible. One of the few properties which allows an investigation via analytical measures is the synchronized behaviour of the dynamics. Here complete synchronization denotes the dynamical state in which every node follows the same trajectory.

The following studies on complete synchronization of coupled Tchebycheff map networks, that is chaotic strings and their network generalizations, are motivated by two arguments. On the one hand the analytical results allow to obtain a deeper understanding of the dynamics, beyond the insights offered by the various numerical results. On the other hand, synchronization is a topic of general interest in the research field of complex networks, to which much attention has been devoted in the last years (see Ref. [7] for a recent review). Although several results on the complete synchronization of coupled map networks have been obtained (see Sec. 8.1), a detailed and extensive study of different concrete systems is still missing in the literature. Accordingly, the application of the master stability formalism to the six coupled Tchebycheff dynamics is not only of interest in connection with the theory by Beck, but also for the research of synchronization phenomena on complex networks in general.

After giving a short review over the research field of coupled map network synchronization, in the following chapter I will display various results concerning the stability of complete synchronization on coupled Tchebycheff networks. These results are obtained by means of the master stability formalism as introduced by Pecora and Carrol [96].

8.1 Synchronization in coupled map networks

Synchronization denotes a coherent dynamical behaviour of two or more units, where this coherence might be expressed by the coincidence of trajectories, frequencies or phases, or by another kind of mutual relation [98]. The simplest case is that of complete or identical synchronization, where every unit shows exactly the same behaviour and all respective trajectories coincide [7, 98]. A more general concept is

that of nearly-synchronous states or ‘fuzzy’ synchronization, where the behaviour of the system is slightly detuned from identical synchronization [98]. These types of synchronization are mostly studied by coupled map models or models involving diffusively-coupled oscillators. In another approach, systems of phase oscillators are used to study the interlocking of oscillation frequencies, with the most prominent model for this kind of synchronization proposed by Kuramoto [1]. Mainly of importance for the field of neuroscience are pulse-coupled models, which aim to reproduce the dynamics of neurons [7].

Whereas in this field initially mostly systems of only a few dynamical units were studied, nowadays the focus has shifted to the synchronization of large populations, which are coupled in a way that can be described in the language of complex networks [2, 28, 88]. These models allow to study the connection between local dynamics, structure of the network, and the emergent global behaviour of the system. Applications include genetic networks, circadian rhythms, neuronal networks, wireless communication networks or power grids [7].

In the following section a brief overview about results on the synchronization of coupled map networks is given. For further information on synchronization in general, and the synchronization of complex networks, the reader is referred to Refs. [1, 7, 8, 26, 27, 28, 93, 98, 106, 107] and references therein.

Coupled map lattices with a distance-dependent coupling are considered in Refs. [6, 47, 112]. For these systems the evolution equation is given by

$$x_i(t+1) = (1 - \epsilon)f[x_i(t)] + \frac{\epsilon}{\sum_{j=1}^N B(d_{ij})} \sum_{j=1}^N B(d_{ij})f[x_j(t)], \quad (8.1)$$

where the function $B(d)$ depends on the distance d_{ij} between nodes i and j in the network. This corresponds to a global coupling, with coupling weights determined by the distances on the network. Although these kind of models in principal could include all kind of network models, in the literature only one- or two-dimensional lattices are considered. A common choice for the distance-dependent function is $B(d) = 1/d^\alpha$ with $\alpha \geq 0$, or $B(d)$ constant for distances smaller or equal to some cutoff parameter d_{cut} and zero otherwise. The common standard coupled map lattice is then obtained for $B(d)$ constant and cut-off parameter $d_{cut} = 1$, and the global coupling for $B(d) = 1$ and no cut-off.

In Ref. [81] the mutual synchronization and clustering in randomly coupled logistic map networks is studied. The evolution equation for this model is given by

$$x_i(t+1) = (1 - \tilde{\epsilon}_i) f[x_i(t)] + \frac{\tilde{\epsilon}_i}{k_i} \sum_{j=1}^N A_{ij} f[x_j(t)], \quad (8.2)$$

where the matrix A_{ij} is a symmetric random matrix with entries either zero or one, such that for the average degree holds $0.5 < \langle k \rangle / (N - 1) \leq 1$. The coupling $\tilde{\epsilon}_i$

depends on the degree of the respective node:

$$\tilde{\epsilon}_i = \epsilon \frac{k_i}{\langle k \rangle}. \quad (8.3)$$

Here $\epsilon \in [0, 1]$ is an overall coupling strength. The authors numerically study different measures of synchronization dependent on the average connectivity $\langle k \rangle / (N - 1)$ and the coupling ϵ , observing not complete synchronization, but fuzzy synchronization of the whole network or of dynamical clusters, which vary in time.

Reference [62] presents conditions for the stability of the complete synchronized state for coupled map networks by use of linear stability analysis, dependent on the spectral properties of the network structure. The authors also obtain some sufficient conditions for synchronization using global stability analysis. Apart from these analytical results, numerical results for synchronization on various network structures are given.

The authors of Ref. [74] consider coupled maps on scale-free networks, where the dynamics is given by

$$x_i(t + 1) = (1 - \epsilon)f[x_i(t)] + \frac{\epsilon}{\sum_{j=1}^N A_{ij}k_j^\alpha} \sum_{j=1}^N A_{ij}k_j^\alpha f[x_j(t)]. \quad (8.4)$$

The parameter α controls the coupling strength from node j to node i , depending on the degree k_j . For larger α the coupling from nodes with higher degree is strengthened, whereas for $\alpha < 0$ the opposite effect is obtained. The authors numerically study the synchronization for different random and deterministic scale-free networks and the role of the most connected nodes in the collective dynamics.

The synchronization between two coupled map networks is analytically and numerically studied in Ref. [72]. This kind of synchronization between separate networks is called ‘outer’ synchronization, compared to the ‘inner’ synchronization of just one network. The authors show results for the synchronization between networks with identical as well as different connection topologies.

In Refs. [12, 13] the authors study complete synchronization for coupled map networks, including directed networks with positive and negative weights and general pairwise coupling functions. This generalization allows non-diffusive coupling schemes, for which the authors observe synchronous behaviour which differs from the behaviour of the respective single units in isolation.

Phase synchronization and cluster formation in coupled maps on different networks is studied in Refs. [4, 60, 61]. The authors consider standard coupled map networks of the form

$$x_i(t + 1) = (1 - \epsilon)f[x_i(t)] + \frac{\epsilon}{k_i} \sum_{j=1}^N A_{ij}g[x_j(t)], \quad (8.5)$$

with $f(x)$ being the logistic map and $g(x) = f(x)$ or $g(x) = x$. Phase synchronization between two nodes is defined as the number of times the respective variables show simultaneously a local minimum. To be precise, let n_i and n_j denote the number

of times the variables $x_i(t)$ and $x_j(t)$ have a local minimum in the time interval T , respectively. The number of times these local minima coincide is denoted by n_{ij} . The phase distance between the nodes i and j is defined as

$$d_{ij} = \frac{n_i + n_j - 2n_{ij}}{n_i + n_j}, \quad (8.6)$$

which is zero if all local minima match with each other, and $d_{ij} = 1$ if none of the minima occur simultaneously. A cluster of nodes is defined as being phase synchronized, if $d_{ij} = 0$ for all pairs of nodes in the cluster. In Ref. [60] two mechanisms of cluster formation are described. Synchronized clusters, where network connections occur mostly between nodes of the same cluster, is denoted as self-organized phase synchronization. If the network connections are dominantly present between different phase synchronized clusters, the mechanism is called driven phase synchronization. In Ref. [61] various numerical studies on cluster (phase) synchronization on various network topologies are presented. The authors consider scale-free networks, coupled map lattices, small-world networks, a Caley tree, higher dimensional lattices and random networks. As an extension to the model described by Eq. (8.6), also a small parameter mismatch for the individual maps, and the circle map as the individual dynamics of the system is discussed. The stability analysis of synchronized chaotic and periodic states in globally coupled networks and complete bipartite networks is presented in Ref. [4], where the results are compared to the numerical results displayed in Refs. [60, 61].

Complete synchronization of coupled logistic maps on small-world networks is studied in Ref. [48]. The authors derive the connection between the linear stability of the synchronized state and the spectral properties of the network. By numerical determination of the respective eigenvalue spectrum it is shown that synchronization is always possible in the thermodynamical limit of infinite network size.

8.2 Master stability functions for complete synchronization on complex networks

The articles reviewed in the last section mostly treat different synchronization phenomena in specific systems. The method of master stability functions [96] differs from these approaches by relating the stability of the synchronized state of a networked system to the spectral properties of a general, not explicitly defined underlying network topology.

In the literature usually the case of coupled time-continuous systems is treated (oscillators). For these systems it is common to consider a diffusive coupling, so for a synchronized state the dynamics is given by the local function at the respective nodes. Since the phase space is usually unbounded, one does not have to take care of a renormalization as it is done for coupled map networks, where the dynamics always is bounded to a product space of intervals. Due to this renormalization, the

evolution equations for coupled map networks are initially not formulated by means of a diffusive coupling, and the synchronized dynamics in general differs from the local function.

Nevertheless, in order to connect to the literature, in the following I will review the derivation of the formalism for this case, and later formulate the master stability formalism for coupled map networks.

Consider a weighted network $G = (\mathcal{V}, \mathcal{E}, \mathcal{W})$ with N nodes, where at every node i an M -dimensional variable \mathbf{x}_i is defined. Note that this differs from the notation for CMNs which I have used up to now, where at every node a one-dimensional variable was defined.

Without coupling the dynamics at every node is given by the same equation

$$\frac{\partial \mathbf{x}}{\partial t} = \mathbf{F}(\mathbf{x}), \quad \mathbf{x} \in \mathbb{R}^m. \quad (8.7)$$

One assumes a diffusive-type coupling, where node i receives input from node j via the coupling function $\mathbf{G} : \mathbb{R}^M \rightarrow \mathbb{R}^M$:

$$\frac{\partial \mathbf{x}_i}{\partial t} = \mathbf{F}(\mathbf{x}_i) + \epsilon \sum_{j=1}^N A_{ij} W_{ij} \{ \mathbf{G}(\mathbf{x}_j) - \mathbf{G}(\mathbf{x}_i) \}. \quad (8.8)$$

Here W_{ij} is the weight of the connection from node j to node i , and ϵ is an overall coupling strength. Although in principle one could insert the overall coupling strength into the weight matrix by replacing $W \rightarrow \epsilon W$, it is often convenient to keep it separately. In most cases the weight matrix is set to $W_{ij} = 1$ for all entries, or used as a renormalization of the input strength via $W_{ij} = 1/k_i$ for every node, but more general assignments are possible. The adjacency matrix A_{ij} has only entries 0 and 1, but does not have to be symmetric, that is, directed networks are not excluded.

From the diffusive-type coupling used in Eq. (8.8) and the use of identical functions $\mathbf{F}(\mathbf{x})$ and $\mathbf{G}(\mathbf{x})$ for every node i , it follows that the synchronization manifold is an invariant manifold of the dynamics. This means that solutions $\mathbf{x}_1 = \mathbf{x}_2 = \dots = \mathbf{x}_N$ remain synchronized under the time evolution, since for these solutions for every node the dynamics of Eq. (8.8) reduces to Eq. (8.7).

It is convenient to rewrite Eq. (8.8) by use of the generalized Laplacian

$$L_{ij} = \begin{cases} \sum_{j=1}^N A_{ij} W_{ij} & : j = i \\ -A_{ij} W_{ij} & : j \neq i, \end{cases} \quad (8.9)$$

obtaining

$$\frac{\partial \mathbf{x}_i}{\partial t} = \mathbf{F}(\mathbf{x}_i) - \epsilon \sum_{j=1}^N L_{ij} \mathbf{G}(\mathbf{x}_j). \quad (8.10)$$

Consider the time evolution of small perturbations from a synchronized solution $\mathbf{s}(t)$, denoted by $\xi_i(t) = \mathbf{x}_i(t) - \mathbf{s}(t)$ for all nodes i :

$$\frac{\partial \xi_i}{\partial t} = D\mathbf{F}(\mathbf{s})\xi_i - \epsilon \sum_{j=1}^N L_{ij} D\mathbf{G}(\mathbf{s})\xi_j \quad (8.11)$$

with $D\mathbf{F}(\mathbf{s})$ and $D\mathbf{G}(\mathbf{s})$ the Jacobians of the respective functions evaluated at the synchronized solution $\mathbf{s}(t)$. Unite all perturbations into an $M \times N$ matrix ξ , where the entry ξ_{ij} denotes the i th component of the perturbation of node j . For clarity, I display Eq. (8.11) explicitly for these components:

$$\frac{\partial \xi_{ij}}{\partial t} = \sum_{k=1}^M \left(\frac{\partial F_i}{\partial x_k} \Big|_{\mathbf{s}(t)} \right) \xi_{kj} - \epsilon \sum_{l=1}^N \sum_{k=1}^M L_{jl} \left(\frac{\partial G_i}{\partial x_k} \Big|_{\mathbf{s}(t)} \right) \xi_{kl}. \quad (8.12)$$

This is a variational equation in matrix form:

$$\frac{\partial \xi}{\partial t} = D\mathbf{F}(\mathbf{s})\xi - \epsilon D\mathbf{G}(\mathbf{s})\xi L^T, \quad (8.13)$$

where L^T is the transpose of L . In the original approach in Ref. [96] the matrix L was supposed to be diagonalizable, but this has been generalized in Ref. [90] to be applicable to non-diagonalizable matrices by use of the Jordan canonical transformation of L .

For any $N \times N$ matrix L there exists an invertible matrix S , which transforms L into Jordan canonical form as

$$S^{-1}LS = J = \begin{pmatrix} 0 & & & \\ & B_1 & & \\ & & \ddots & \\ & & & B_r \end{pmatrix}, \quad (8.14)$$

where the B_i 's are Jordan blocks of the form

$$B_i = \begin{pmatrix} \lambda & & & \\ 1 & \lambda & & \\ & \ddots & \ddots & \\ & & 1 & \lambda \end{pmatrix} \quad (8.15)$$

and λ are the eigenvalues of L , which may be complex. Since $\sum_{j=1}^N L_{ij} = 0$, there is always one eigenvector $\lambda_1 = 0$, corresponding to the eigenvector $(1, 1, \dots, 1)^T$, which has already been included into the matrix in (8.14). Due to the Gerschgorin Circle Theorem [57] all eigenvalues have nonnegative real components, and accordingly can be sorted by the magnitude of their real parts in ascending order $\lambda_1 = 0, \lambda_2, \dots, \lambda_N$ with $\Re(\lambda_2) \geq \dots \geq \Re(\lambda_N)$.

By applying $L = SJS^{-1}$ to Eq. (8.13) one obtains

$$\begin{aligned} \frac{\partial \xi}{\partial t} &= D\mathbf{F}(\mathbf{s})\xi - \epsilon D\mathbf{G}(\mathbf{s})\xi(SJS^{-1})^T \\ &= D\mathbf{F}(\mathbf{s})\xi - \epsilon D\mathbf{G}(\mathbf{s})\xi(S^{-1})^T J^T S^T. \end{aligned} \quad (8.16)$$

Multiplication with $(S^T)^{-1} = (S^{-1})^T$ from the right and the change of variables $\eta = \xi(S^{-1})^T$ leads to the variational equation

$$\frac{\partial \eta}{\partial t} = D\mathbf{F}(\mathbf{s})\eta - \epsilon D\mathbf{G}(\mathbf{s})\eta J^T. \quad (8.17)$$

Whereas the column vector i of the original matrix ξ stands for the perturbation associated with the respective node i , the columns of the new matrix η are associated with linear combinations of different column vectors of ξ , thus corresponding to perturbation modes of the entire network. Consequently, if all entries of the matrix η converge to zero, complete synchronization is linearly stable and viceversa. A special role plays the mode η_1 associated with the eigenvalue $\lambda_1 = 0$. As one can see by the form of the eigenvector $(1, 1, \dots, 1)^T$, this perturbation always lies in the direction of the synchronization manifold and hence does not explicitly influence the stability of the synchronized state.

If L is diagonalizable, for the i th column of η , Eq. (8.17) reads

$$\frac{\partial}{\partial t} \eta_i = [D\mathbf{F}(\mathbf{s}) - \epsilon \lambda_i D\mathbf{G}(\mathbf{s})] \eta_i, \quad (8.18)$$

with λ_i the i th eigenvalue of L . Thus the equations for the different columns η_i decouple and are all of the following form:

$$\frac{\partial}{\partial t} \mathbf{z} = [D\mathbf{F}(\mathbf{s}) - \gamma D\mathbf{G}(\mathbf{s})] \mathbf{z}. \quad (8.19)$$

The (in general complex) parameter γ stands for $\epsilon \lambda_i$, if the i th column of η is considered. In this case \mathbf{z} stands for η_i .

Eq. (8.19) is called a master stability equation. Of interest is the linear stability of the solution $\mathbf{z} = 0$ dependent on the parameter γ . This stability is usually accounted for by the largest Lyapunov exponent $\Lambda_{1c}(\gamma)$ for the solution $\mathbf{z} = 0$, which is called the master stability function of the system. Here the index ‘1c’ distinguishes the one-cluster synchronization (all nodes are identically synchronized) from the two-cluster synchronization studied in the next chapter. The important point is that the network structure only enters via the Laplacian eigenvalue λ . Thus for determining the linear stability of the synchronized state of the network one performs the following two steps:

- Calculate the master stability function $\Lambda_{1c}(\gamma)$ in the whole complex plane, that is the Lyapunov exponent of Eq. (8.19) for the solution $\mathbf{z} = 0$, and determine the regions where $\Lambda_{1c}(\gamma)$ is negative.
- Determine the Laplacian eigenvalues of the weighted network. The synchronized state is stable if all eigenvalues times the coupling strength ϵ are situated in regions with $\Lambda_{1c}(\gamma) < 0$.

The first step considers the dynamical component, that is the individual function $\mathbf{F}(\mathbf{x})$, the coupling function $\mathbf{G}(\mathbf{x})$ and the synchronized solution $\mathbf{s}(t)$. The network structure is incorporated in the second step via the Laplacian eigenvalues. By means of this separation it is possible to study on the one hand the structure of the master stability equation of different dynamical systems without considering explicit network structures (first step), or on the other hand the synchronizability of networks for general classes of dynamical systems (second step).

If one considers networks with a real Laplacian eigenvalue spectrum, the master stability function $\Lambda_{1c}(\gamma)$ only has to be evaluated for real parameter γ . One observes that for most systems either one of two cases occur [7]: In the first case there is an interval $[\gamma_{min}, \gamma_{max}]$, for which $\Lambda_{1c}(\gamma) < 0$ (bounded master stability function), for the other case (unbounded master stability function) it holds $\Lambda_{1c}(\gamma) < 0$ for $\gamma > \gamma_{min}$.

Recall that for a networked system the parameter in the master stability function $\gamma = \epsilon\lambda_i$ stands for the overall coupling strength times the respective Laplacian eigenvalues of the network. Hence for unbounded master stability functions it is in principle always possible to achieve stable synchronization by applying a sufficient large coupling strength, in order to have $\epsilon\lambda_2 > \gamma_{min}$. Accordingly for unbounded master stability a large smallest non-zero eigenvalue λ_2 points to good synchronizability of the network.

More interesting is the case of bounded master stability functions, where for stable synchronization it has to hold that $\epsilon\lambda_2 > \gamma_{min}$ and simultaneously $\epsilon\lambda_N < \gamma_{max}$, where according to the conventional ordering λ_2 is the smallest non-zero eigenvalue, and λ_N is the largest eigenvalue. That is, for a given dynamical system with $\gamma_{min}, \gamma_{max}$ and a explicit network structure with Laplacian eigenvalues λ_2, λ_N , the coupling range for which synchronization is stable is given by $[\epsilon_{min}, \epsilon_{max}]$, with $\epsilon_{min} = \gamma_{min}/\lambda_2$ and $\epsilon_{max} = \gamma_{max}/\lambda_N$. Consequently, synchronization is only possible if $\lambda_N/\lambda_2 < \gamma_{max}/\gamma_{min}$. This ratio between the largest and smallest non-zero eigenvalue

$$\frac{\lambda_N}{\lambda_2} := R \quad (8.20)$$

is an objective measure of the synchronizability of the network, with the optimal value $R = 1$. The key advantage of the master stability formalism is that R can be studied for various networks without considering an explicit dynamical systems. In recent years there has been a great number of studies following this approach in order to connect the synchronizability R of networks to structural properties like average distance, degree distribution or clustering [59, 86, 92, 115], find and design networks with optimal synchronization properties [41, 58, 90, 91] or study specific network topologies like small-world networks [10] or network motifs [75]. For a recent review see Ref. [7].

If the generalized Laplacian has complex eigenvalues, it is more difficult to obtain general predictions about the synchronizability of networks, since in this case the specific form of the area of negative master stability function in the complex plane might be important [7, 45].

In Ref. [90] it has been shown that this formalism also holds if the generalized Laplacian is not diagonalizable. In this case the perturbation modes η_i do not decouple in the respective Jordan blocks of Eq. (8.15). However, it can be shown that also for non-diagonalizable networks the master stability function assures the linear stability of the synchronized solution (see Ref. [90] for details). Compared to the case of networks with a diagonalizable Laplacian, in the case of nondiagonalizability, the transient to synchronization might be longer.

The master stability formalism as presented here is only applicable to complete (identical) synchronization of networks of identical units, where all individual trajectories exactly coincide. An application of this concept to fuzzy synchronization, where the dynamics is slightly detuned from identical synchronization was recently proposed in Ref. [108]. This approach allows to study systems with non-identical units, which is an important step to a more general use of master stability functions.

Master stability functions for standard coupled map networks

In order to connect to the literature in the field, up to now I have reviewed the master stability formalism for networked systems, where the local dynamics is given by a higher-dimensional continuous-time system. In the following I formulate this technique for standard coupled map networks, where locally without coupling the dynamics is given by an one-dimensional map.

A standard coupled map network is defined by the evolution equation (see Sec. 2.3)

$$x_i(t+1) = (1 - \epsilon)f[x_i(t)] + \frac{\epsilon}{k_i} \sum_{j=1}^N A_{ij}g[x_j(t)], \quad (8.21)$$

where A_{ij} is the symmetric adjacency matrix of an undirected network. In contrast to systems of coupled oscillators, these evolution equations are not of a diffusively coupled type, and thus the synchronized dynamics does not have to be given by the individual dynamics $f(x)$. In order to get an equation which is of the same form as Eq. (8.10), this has to be recast into

$$x_i(t+1) = (1 - \epsilon)f[x_i(t)] + \epsilon g[x_i(t)] - \epsilon \sum_{j=1}^N L_{ij}g[x_j(t)] \quad (8.22)$$

with

$$L_{ij} = \delta_{ij} - \frac{A_{ij}}{k_i}, \quad (8.23)$$

that is Eq. (8.9) with $W_{ij} = 1/k_i$. The important difference between Eq. (8.10) and Eq. (8.22) is that the synchronized dynamics with $s(t) = x_1(t) = \dots = x_N(t)$ is governed by the function

$$h_\epsilon(x) := (1 - \epsilon)f(x) + \epsilon g(x), \quad (8.24)$$

which depends on the coupling ϵ . In the following the function $h_\epsilon(x)$ will be denoted as the synchronized dynamics. Up to now this concept of a coupling-dependent synchronized solution has not been stated explicitly in the literature. Note that for the case $g(x) = f(x)$ it holds $h_\epsilon(x) = f(x)$.

Perturbations $\xi_i(t)$ from the synchronized solution are united into a row vector ξ , for which the evolution equation analogous to Eq. (8.13) reads

$$\xi(t+1) = h'_\epsilon(s)\xi - \epsilon g'(s)\xi L^T. \quad (8.25)$$

Instead of Jacobian matrices, in this equation occur one-dimensional derivatives:

$$h'_\epsilon(s) = \left. \frac{\partial h_\epsilon}{\partial x} \right|_{x=s(t)}, \quad g'(s) = \left. \frac{\partial g'}{\partial x} \right|_{x=s(t)}. \quad (8.26)$$

The generalized Laplacian L with $L_{ij} = \delta_{ij} - A_{ij}/k_i$ for a symmetric adjacency matrix A_{ij} is similar to a symmetric matrix Q and thus diagonalizable with real eigenvalues:

$$Q = D^{-1}LD \text{ with } D_{ij} = \frac{\delta_{ij}}{\sqrt{k_i}}, D_{ij}^{-1} = \delta_{ij}\sqrt{k_i}. \quad (8.27)$$

By diagonalization of Eq. (8.25) one obtains the following master stability equation, which is the analogon of Eq. (8.19):

$$z(t+1) = [h'_\epsilon(s) - \epsilon\lambda g'(s)]z(t), \quad (8.28)$$

where λ are the different Laplacian eigenvalues $\lambda_2, \dots, \lambda_N$ (recall that the eigenvalue $\lambda_1 = 0$ does not affect the stability of the synchronized solution).

The largest Lyapunov exponent of the solution $z = 0$ of Eq. (8.28) is the master stability function for the system. It has to be evaluated for real parameters $\gamma = \epsilon\lambda$, with $\epsilon \in [0, 1]$ and $\lambda \in [0, 2]$ [35]. Note that the coupling ϵ does not only enter explicitly as a multiplicative factor in Eq. (8.28), but also implicitly by determining the dynamics of the synchronized solution

$$s(t+1) = h_\epsilon[s(t)]. \quad (8.29)$$

An exception to this ϵ -dependence is the case of $f(x) = g(x)$, for which $h_\epsilon(x) = f(x)$, and thus the master stability function only depends on the product $\epsilon\lambda$, that is $\Lambda_{1c}(\epsilon, \lambda) = \Lambda_{1c}(\epsilon\lambda)$.

Numerically $\Lambda_{1c}(\epsilon, \lambda)$ is calculated by means of

$$\Lambda_{1c}(\epsilon, \lambda) = \lim_{T \rightarrow \infty} \frac{1}{T} \sum_{t=T_0+1}^{T_0+T} \ln [|h'_\epsilon[s(t)] - \epsilon\lambda g'[s(t)]|], \quad (8.30)$$

where $s(t)$ is obtained by iteration of Eq. (8.29) for a random initial condition, T_0 is some transient and T is the number of iterations used for the determination. The master stability function $\Lambda_{1c}(\epsilon, \lambda = 0)$ yields the Lyapunov exponent of the synchronized solution itself.

8.3 Complete synchronization of coupled Tchebycheff map networks

In the last section the technique of master stability functions has been introduced. By means of this technique one can consider the synchronizability of networks without referring to a specific dynamical system, or one can study the synchronization

properties of specific systems for general network topologies. In the following I will use this formalism in the latter sense to study the stability of synchronized solutions of coupled Tchebycheff map networks. Of interest are the six dynamics which have been introduced in Chap. 3. The results show which kind of synchronized dynamics can occur, and gives the conditions for having stable synchronized states on arbitrary networks. In order to explicitly study the synchronization of these dynamics on a specific network, one has just to put in the eigenvalues of the generalized Laplacian of the respective network.

The determination of synchronization properties for each dynamics is performed in different steps. Table (8.1) shows the synchronized solution $h_\epsilon(x)$ for all six dynamics. Whereas $h_\epsilon(x)$ for the 2A and 3A dynamics is given by the respective Tchebycheff polynomials, for the four other dynamics new functions, depending on ϵ , are obtained. These functions are studied numerically by means of the calculation of the respective bifurcation diagrams and Lyapunov exponents. In the next step the master stability functions for these dynamics are numerically obtained. Finally, for some dynamics explicit solutions of $h_\epsilon(x)$ and the respective stability regions are analytically determined. These are the chaotic solutions of the 2A and 3A dynamics, and synchronized fixed points and period-2 orbits for the remaining four dynamics. The latter case has been solved in Ref. [38] for a ring network by standard techniques. However, the approach with master stability functions allows to address the stability of synchronization for general synchronized orbits and arbitrary network structures. Accordingly, the results of Ref. [38] are only one special case for the application of the master stability function and will be used to check the calculations.

The analytical results for the fixed points and period-2 orbits have been obtained by use of a symbolic manipulation package. After the determination of the respective orbits, the Lyapunov exponent $\mu(\epsilon)$ of the synchronized solution $h_\epsilon(x)$ and the associated range of stability is calculated. The results allow to check the numerical results obtained in the respective bifurcation diagrams. Subsequently, the master stability function $\Lambda_{1c}(\epsilon, \lambda)$ for the respective orbit and the region of stable synchronization in the ϵ - λ plane is determined, which has to be compared to the numerical result. Note that the Lyapunov exponent of the synchronized solution $\mu(\epsilon)$ is identical to the master stability function $\Lambda_{1c}(\epsilon, \lambda = 0)$. As an application the range of stability for a ring network, that is a chaotic string, is calculated and compared to the results given in Ref. [38].

label	$f(x)$	$g(x)$	$h_\epsilon(x)$
2A	$2x^2 - 1$	$2x^2 - 1$	$2x^2 - 1$
2B	$2x^2 - 1$	x	$(1 - \epsilon)(2x^2 - 1) + \epsilon x$
2A ⁻	$2x^2 - 1$	$-(2x^2 - 1)$	$(1 - 2\epsilon)(2x^2 - 1)$
2B ⁻	$2x^2 - 1$	$-x$	$(1 - \epsilon)(2x^2 - 1) - \epsilon x$
3A	$4x^3 - 3x$	$4x^3 - 3x$	$4x^3 - 3x$
3B	$4x^3 - 3x$	x	$(1 - \epsilon)(4x^3 - 3x) + \epsilon x$

Table 8.1: Coupled Tchebycheff map network dynamics

8.3.1 2A dynamics

For the 2A dynamics it holds $h_\epsilon(x) = T_2(x)$, hence the synchronized solution $s(t)$ is given by the dynamics of the second order Tchebycheff polynomial, $s(t+1) = T_2[s(t)]$. The master stability equation reads

$$z(t+1) = [(1 - \lambda\epsilon)T_2'[s(t)]] z(t), \quad (8.31)$$

with $T_2(x) = (2x^2 - 1)$, and $T_2'[s(t)]$ the derivative of the polynomial evaluated along the synchronized solution $s(t)$. The Lyapunov exponent of the solution $z = 0$ of this equation and thus the master stability function is obtained via

$$\begin{aligned} \Lambda_{1c}(\epsilon, \lambda) &= \lim_{T \rightarrow \infty} \frac{1}{T} \left(\sum_{t=T_0+1}^{T_0+T} \ln [|(1 - \lambda\epsilon)T_2'[s(t)]|] \right) \\ &= \ln[|1 - \epsilon\lambda|] + \ln 2, \end{aligned} \quad (8.32)$$

where the Lyapunov exponent $\ln 2$ of $T_2(x)$ has been used (see Sec. 2.1.2). As a consequence, the master stability function $\Lambda_{1c}(\epsilon, \lambda)$ is negative and synchronization is stable in the region of the ϵ - λ plane determined by

$$1/2 < \epsilon\lambda < 3/2. \quad (8.33)$$

This result can be interpreted in different ways. On the one hand it is possible to consider a fixed coupling ϵ and different network structures. Synchronization is stable for networks which have Laplacian eigenvalues $\lambda_2, \dots, \lambda_N$ in the range $(1/2\epsilon, 3/2\epsilon)$. Since the eigenvalues are restricted to the range $\lambda \in [0, 2]$, one immediately learns that for $\epsilon \leq 1/4$ synchronization is never stable. On the other hand one might be interested in a network with smallest non-zero Laplacian eigenvalue λ_2 and largest eigenvalue λ_N and different couplings. In this case, synchronization is stable for couplings $\epsilon \in (1/2\lambda_2, 3/2\lambda_N)$. Due to the restriction $\epsilon \in [0, 1]$, for networks with $\lambda_2 \leq 1/2$, synchronization is never stable. An important example for this case is a ring network with nearest neighbour coupling, that is the chaotic string dynamics considered in Chap. 3. For a ring network $\lambda_2 \approx 0$, and consequently for the 2A chaotic string dynamics complete synchronization is not stable for any $\epsilon \in [0, 1]$.

Another simple example is a network consisting of only two connected nodes. The respective Laplacian has eigenvalues $\lambda_1 = 0$ and $\lambda_2 = 2$ [35], so synchronization is stable for $\epsilon \in (1/4, 3/4)$. This latter case will be of interest in the next chapter, where two-cluster synchronization of bipartite networks is studied.

8.3.2 3A dynamics

Analogously to the 2A dynamics considered in the last section, it holds $h_\epsilon(x) = T_3(x)$, resulting in the master stability equation

$$z(t+1) = [(1 - \lambda\epsilon)T_3'(s(t))] z(t). \quad (8.34)$$

By means of the Lyapunov exponent $\ln 3$ of $T_3(x)$ and the same arguments as in the last section, one can show that the region of stability is given by

$$\frac{2}{3} < \epsilon\lambda < \frac{4}{3}. \quad (8.35)$$

Consequently, for the 3A chaotic string dynamics (that is a large ring network) complete synchronization is never stable in the coupling range $\epsilon \in [0, 1]$. If only two connected nodes are considered, synchronization is stable for $\epsilon \in (1/3, 2/3)$.

8.3.3 2B dynamics

For the 2B dynamics, the synchronized solution $h_\epsilon(x)$ depends on the coupling (see Tab. 8.1). Figure 8.1 shows the phase diagram of $h_\epsilon(x)$ for different couplings ϵ , and the Lyapunov exponent $\mu(\epsilon)$ for random initial conditions. Apart from regions with chaotic behaviour, the synchronized solution for the 2B dynamics is periodic for a large coupling range. The synchronized dynamics

$$h_\epsilon(x) = (1 - \epsilon)(2x^2 - 1) + \epsilon x \quad (8.36)$$

has two fixed points $x_{(f,1)} = -1/2$ and $x_{(f,2)} = 1$. At first the stability for these fixed points is checked by considering the Lyapunov exponent of the synchronized solution $\mu(\epsilon) = \ln[|h_\epsilon(x_f)|]$. One obtains that $x_{(f,2)}$ is never stable in the range $\epsilon \in [0, 1]$, whereas $x_{(f,1)}$ is stable for $\epsilon \in (1/3, 1]$ (see Fig. 8.1). The master stability equation with $x_{(f,1)} = -1/2$ inserted reads

$$z(t+1) = [4x_{(f,1)}(1 - \epsilon) + \epsilon(1 - \lambda)]z(t), \quad (8.37)$$

leading to the master stability function

$$\Lambda_{1c}(\epsilon, \lambda) = \ln[|4x_{f,1}(1 - \epsilon) + \epsilon(1 - \lambda)|]. \quad (8.38)$$

Recall that $\mu(\epsilon) = \Lambda_{1c}(\epsilon, \lambda = 0)$. The master stability function is shown in Fig. 8.2.

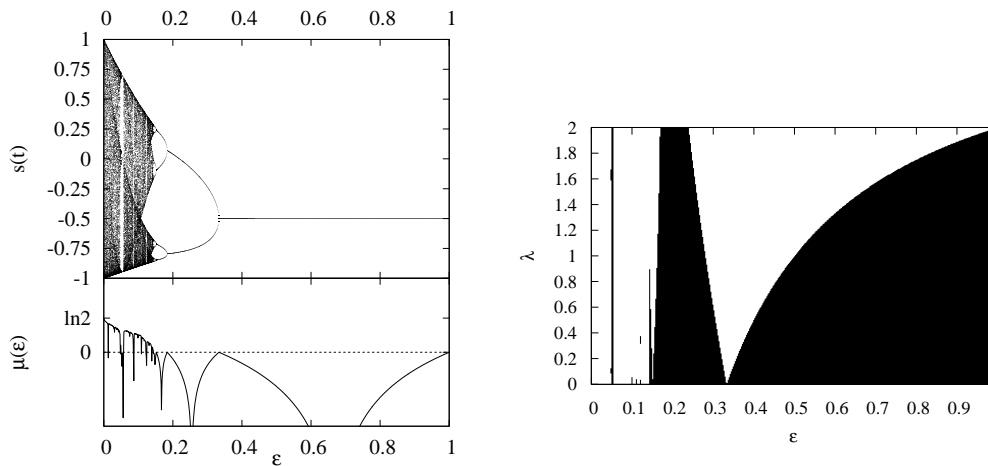


Figure 8.1: Left: Bifurcation diagram and Lyapunov exponent $\mu(\epsilon)$ of $h_\epsilon(x)$ for the $2B$ dynamics. The fixed point is stable in the range $(1/3, 1]$, the period-2 orbit is stable for $\epsilon \in (0.183\dots, 1/3)$, consistently with the analytical results. The bifurcation diagram has been obtained by displaying 200 iterates after a transient of 10^5 steps. Right: Area of stability (black) in the λ - ϵ plane for complete synchronization determined by a negative master stability function for the $2B$ dynamics. The Lyapunov exponent of the synchronized solution and the master stability function have been numerically determined over 10^6 iterates, after a transient of 10^4 iterates. Both have been checked for various initial conditions.

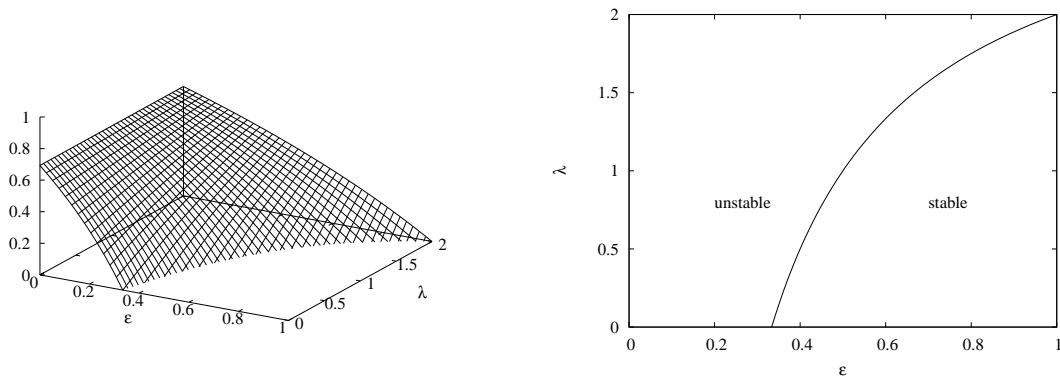


Figure 8.2: Left: Analytical obtained master stability function $\Lambda_{1c}(\epsilon, \lambda)$ for the fixed point of the completely synchronized $2B$ dynamics. The plot has been truncated at $\Lambda_{1c}(\epsilon, \lambda) = 0$ in order to identify the boundaries between the regions with positive and negative values. Right: Region of stable synchronized fixed point for the $2B$ dynamics, consistent with the numerically obtained result in Fig. 8.1

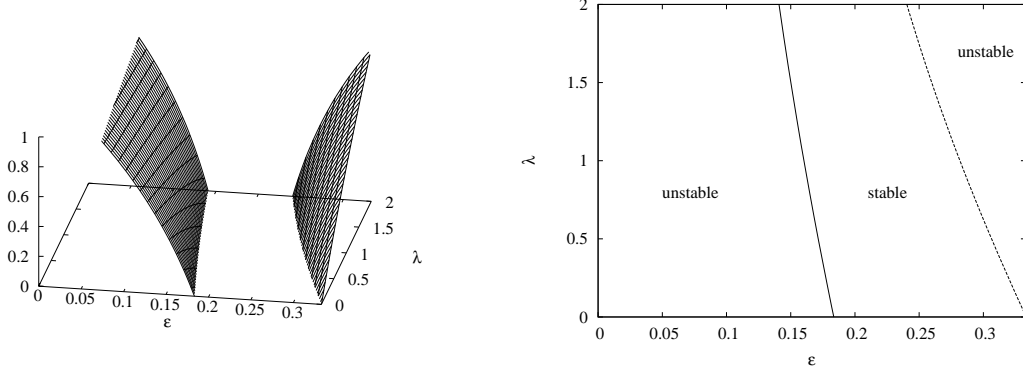


Figure 8.3: Left: Analytical obtained master stability function $\Lambda_{1c}(\epsilon, \lambda)$ for the period-2 orbit of the completely synchronized $2B$ dynamics. Right: Regions of stable synchronized period-2 orbit for the $2B$ dynamics, consistent with the numerically obtained result in Fig. 8.1.

The curve in the ϵ - λ plane separating the regions of stable/unstable synchronization is given by

$$\lambda = \frac{3\epsilon - 1}{\epsilon}. \quad (8.39)$$

Note that the coupling range of stable synchronization is determined by the largest Laplace eigenvalue λ_N . For a large ring network it holds $\lambda_N \approx 2$ and accordingly the synchronized fixed point is not stable for any $\epsilon \in [0, 1]$. The same holds for a network consisting of two connected nodes.

The period-2 orbit of the synchronized solution $h_\epsilon(x)$ is given by

$$x_{(p,\pm)} = \frac{1 - \epsilon \pm \sqrt{5 - 18\epsilon + 9\epsilon^2}}{4(1 - \epsilon)}, \quad (8.40)$$

which are real numbers for $\epsilon \in [0, 1/3]$ (denoted as the range of validity). Straight-forward calculations show that this orbit is stable for $h_\epsilon(x)$ for

$$\epsilon \in \left(\frac{1}{3}(3 - \sqrt{6}), \frac{1}{3} \right) = (0.183\dots, 0.333\dots). \quad (8.41)$$

The master stability function for the range of validity is shown in Fig. 8.3. Stability is stable in the region between the curves in the ϵ - λ plane given by

$$\begin{aligned} \lambda &= \frac{-1 + \sqrt{4 - 18\epsilon + 9\epsilon^2}}{\epsilon}, \\ \lambda &= \frac{-1 + \sqrt{3}\sqrt{2 - 6\epsilon + 3\epsilon^2}}{\epsilon}. \end{aligned} \quad (8.42)$$

In order to obtain the coupling range of stability for the ring structure, these relations have to be solved for $\lambda = 0$, and $\lambda = 2$, respectively. One obtains a stable

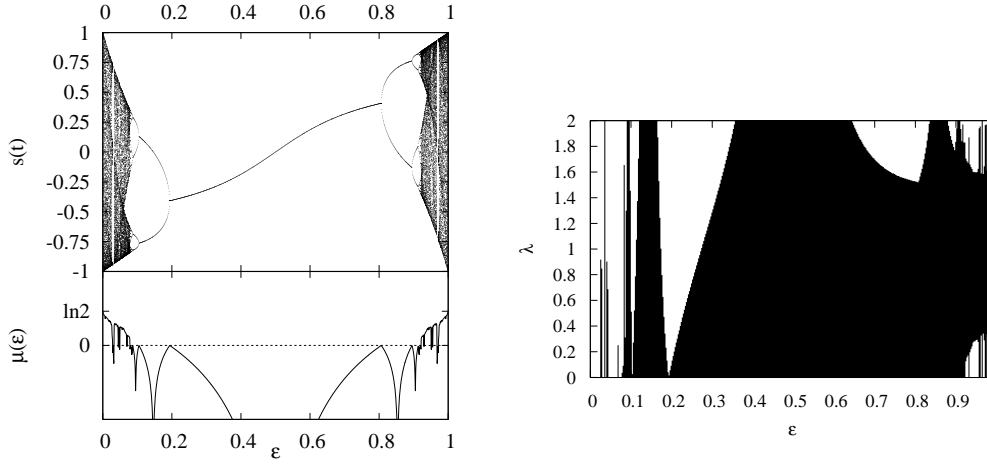


Figure 8.4: Same as Fig. 8.1, but for the $2A^-$ dynamics. Note the symmetry $h_\epsilon(x) = -h_{(1-\epsilon)}(x)$ in the bifurcation diagram of the synchronized dynamics (left figure).

synchronized period-2 orbit for

$$\epsilon \in \left(\frac{1}{3}(3 - \sqrt{6}), \frac{1}{5}(11 - \sqrt{96}) \right). \quad (8.43)$$

8.3.4 $2A^-$ dynamics

Figure 8.4 shows the bifurcation diagram of $h_\epsilon(x)$ for different couplings ϵ , and the Lyapunov exponent $\mu(\epsilon)$ for random initial conditions. One immediately observes some symmetry in the figure. The synchronized solution is given by

$$h_\epsilon(x) = (1 - 2\epsilon)(2x^2 - 1), \quad (8.44)$$

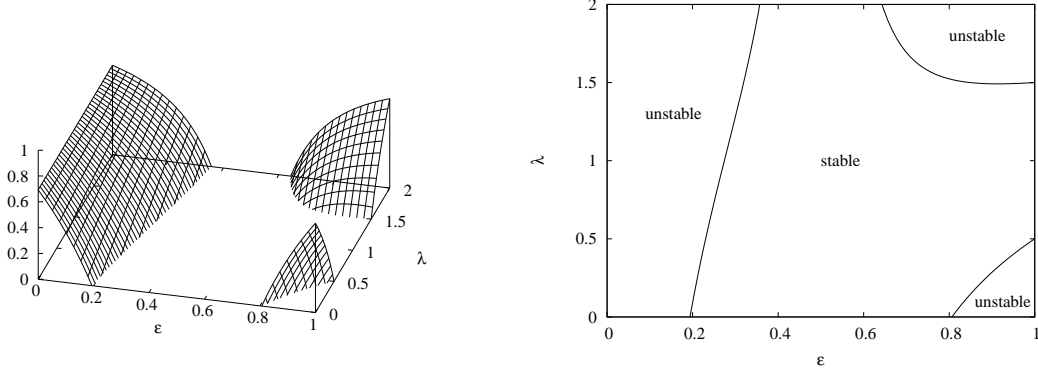
so it holds $h_\epsilon(x) = -h_{(1-\epsilon)}(x)$, as can be seen in the bifurcation diagram in Fig. 8.4. Since the Lyapunov exponent depends on the absolute value of the function it follows $\mu(\epsilon) = \mu(1-\epsilon)$. Due to the parameter λ , this symmetry is lost for the master stability function $\Lambda_{1c}(\epsilon, \lambda)$, which is displayed in Fig. 8.4. The fixed points of the synchronized solution are given by

$$x_{(f,\pm)} = \frac{1 \pm \sqrt{9 - 32\epsilon + 32\epsilon^2}}{4(2\epsilon - 1)}. \quad (8.45)$$

For $\epsilon \in [0, 1]$ the fixed point $x_{(f,+)}$ is complex, whereas $x_{(f,-)}$ is real. The range of stability for $x_{(f,-)}$ for the synchronized solution is given by

$$\epsilon \in \left(\frac{1}{8}(4 - \sqrt{6}), \frac{1}{8}(4 + \sqrt{6}) \right) = (0.193\dots, 0.806\dots). \quad (8.46)$$

Note the symmetry $\epsilon \leftrightarrow (1-\epsilon)$. Figure 8.5 shows the master stability function and the


 Figure 8.5: Same as Fig. 8.2, but for the fixed point of the $2A^-$ dynamics.

region of stability for this fixed point. The boundaries between the stable/unstable region are given by

$$\lambda = \frac{(1 - 2\epsilon)\sqrt{9 - 32\epsilon + 32\epsilon^2}}{\epsilon(1 - \sqrt{9 - 32\epsilon + 32\epsilon^2})} \quad (8.47)$$

for larger ϵ and λ , and

$$\lambda = \frac{(1 - 2\epsilon)(2 - \sqrt{9 - 32\epsilon + 32\epsilon^2})}{\epsilon(-1 + \sqrt{9 - 32\epsilon + 32\epsilon^2})} \quad (8.48)$$

for smaller ϵ , and for larger ϵ and smaller λ . For a ring network it follows that the fixed point is stable for $\epsilon \in (5/14, 9/14) = (0.357\dots, 0.642\dots)$. The period-2 orbit of the synchronized $2A^-$ dynamics is given by

$$x_{(p,\pm)} = \frac{-1 \pm \sqrt{5 - 32\epsilon + 32\epsilon^2}}{4(1 - 2\epsilon)}, \quad (8.49)$$

which in the coupling range $[0, 1]$ are real numbers for the two intervals

$$\epsilon \in \left[0, \frac{1}{8}(4 - \sqrt{6})\right] \text{ and } \epsilon \in \left[\frac{1}{8}(4 + \sqrt{6}), 1\right]. \quad (8.50)$$

This period-2 orbit is stable for the synchronized dynamics in the regions

$$\epsilon \in \left(\frac{1}{8}(4 - \sqrt{10}), \frac{1}{8}(4 - \sqrt{6})\right) \text{ and } \epsilon \in \left(\frac{1}{8}(4 + \sqrt{6}), \frac{1}{8}(4 + \sqrt{10})\right). \quad (8.51)$$

Again, there is a symmetry $\epsilon \leftrightarrow (1 - \epsilon)$. This symmetry is lost for the master stability function $\Lambda_{1c}(\epsilon, \lambda)$ due to the introduction of the parameter λ . Figure 8.6 shows $\Lambda_{1c}(\epsilon, \lambda)$ and the region of stability for the period-2 orbit in the lower coupling interval of validity. The boundaries between the stable/unstable region are given by

$$\lambda = \frac{1 - 2\epsilon}{\epsilon} \left(-1 + \frac{1}{2\sqrt{\pm(1 - 8\epsilon + 8\epsilon^2)}} \right). \quad (8.52)$$

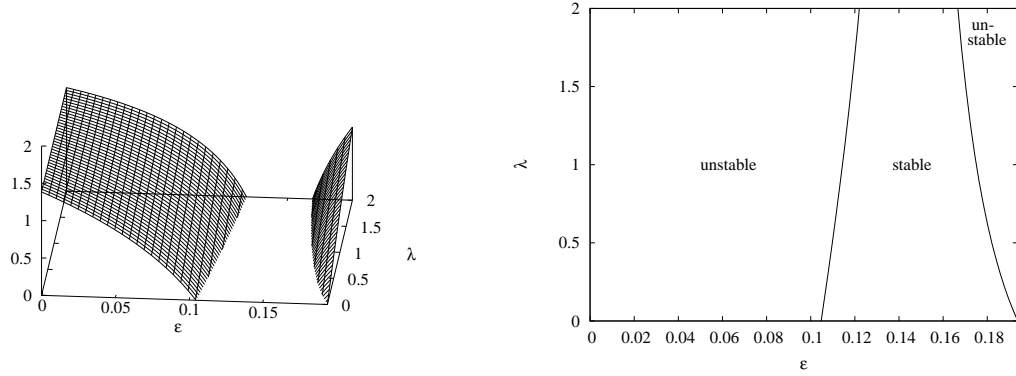


Figure 8.6: Left: Analytical obtained master stability function $\Lambda_{1c}(\epsilon, \lambda)$ for the period-2 orbit of the completely synchronized $2A^-$ dynamics in the low-coupling region of validity. Right: Regions of stable synchronized period-2 orbit for the $2A^-$ dynamics, consistent with the numerically obtained result in Fig. 8.4

For the ring-network this has to be solved for $\lambda = 2$, which leads to a stable synchronized period-2 orbit in the coupling range

$$\epsilon \in \left(\frac{1}{2} - \frac{1}{\sqrt{7}}, \frac{1}{6} \right) = (0.122\dots, 0.166\dots). \quad (8.53)$$

For the higher coupling interval of validity, the corresponding master stability function and region of stability is shown in Fig. 8.7. The curves which separate regions of stable/unstable synchronization read

$$\lambda = \frac{1 - 2\epsilon}{\epsilon} \left(-1 \pm \frac{2}{2\sqrt{1 - 8\epsilon + 8\epsilon^2}} \right) \quad (8.54)$$

and

$$\lambda = \frac{1 - 2\epsilon}{\epsilon} \left(-1 - \frac{2}{2\sqrt{-1 + 8\epsilon - 8\epsilon^2}} \right). \quad (8.55)$$

For the ring network, with $\lambda = 2$ the completely synchronized period-2 orbit is stable for

$$\epsilon \in \left(\frac{5}{6}, \frac{1}{14}(7 + 2\sqrt{7}) \right). \quad (8.56)$$

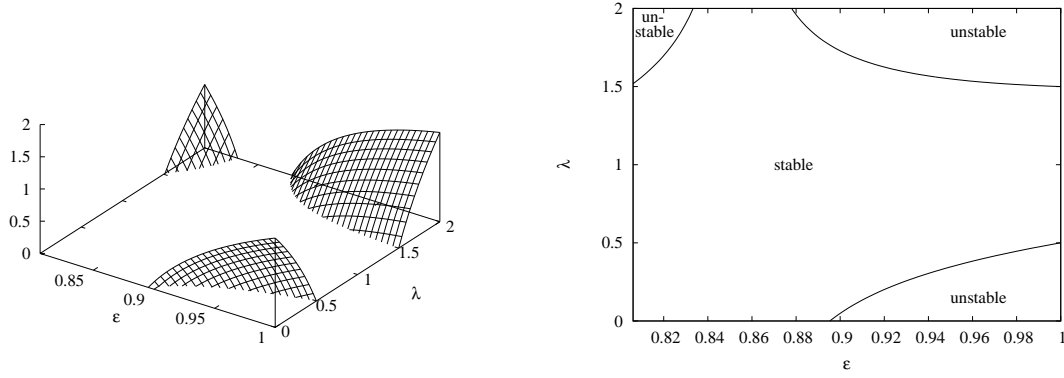


Figure 8.7: Left: Analytical obtained master stability function $\Lambda_{1c}(\epsilon, \lambda)$ for the period-2 orbit of the completely synchronized $2A^-$ dynamics in the low-coupling region of validity. Right: Regions of stable synchronized period-2 orbit for the $2A^-$ dynamics, consistent with the numerically obtained result in Fig. 8.4

8.3.5 $2B^-$ dynamics

The bifurcation diagram and the Lyapunov exponent for general initial conditions of the synchronized $2B^-$ dynamics is shown in Fig. 8.8. One observes periodic solutions for a wide interval of the coupling range.

The fixed points are given by

$$x_{(f,\pm)} = \frac{1 + \epsilon \pm \sqrt{9 - 14\epsilon + 9\epsilon^2}}{4(1 - \epsilon)}, \quad (8.57)$$

where $x_{(f,+)}$ is complex, and $x_{(f,-)}$ is real in the coupling range $\epsilon \in [0, 1]$. The fixed point $x_{(f,-)}$ is stable for the synchronized solution in the interval $\epsilon \in (5/9, 1)$. Fig. 8.9 shows the master stability function and the range of stability for the synchronized fixed point of the $2B^-$ dynamics. The boundary between the region of stable/unstable synchronization is given by

$$\lambda = \frac{-1 + \sqrt{9 - 14\epsilon + 9\epsilon^2}}{\epsilon}. \quad (8.58)$$

As it is visible in the second part of Fig. 8.9, the stability of the fixed point on a network is determined by the eigenvalue $\lambda = 0$, that is, by the Lyapunov exponent $\mu(\epsilon)$ expressing the stability of the fixed point for the synchronized solution itself. Accordingly, the stability of the completely synchronized fixed point of the $2B^-$ dynamics does not depend on the network structure.

The period-2 orbit of $h_\epsilon(x)$ is

$$x_{(p,\pm)} = \frac{-1 + \epsilon \pm \sqrt{5 - 14\epsilon + 9\epsilon^2}}{4(1 - \epsilon)}, \quad (8.59)$$

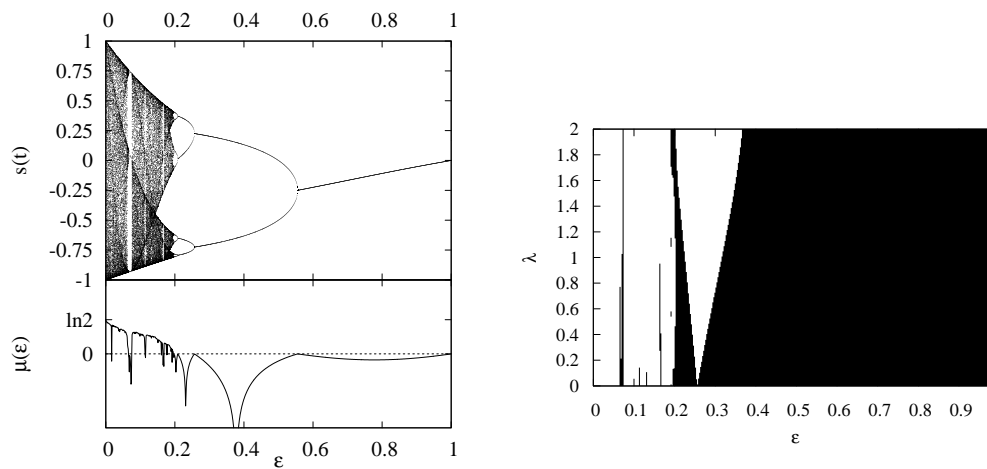


Figure 8.8: Same as Fig. 8.1, but for the $2B^-$ dynamics.

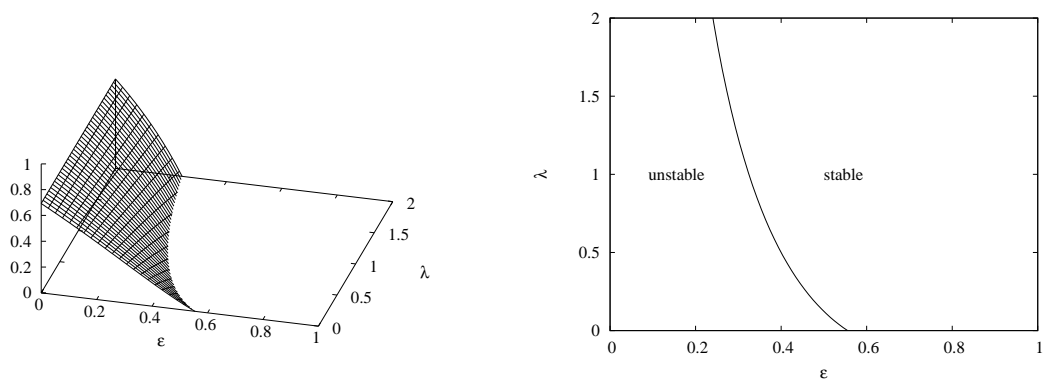


Figure 8.9: Same as Fig. 8.2, but for the fixed point of the $2B^-$ dynamics.

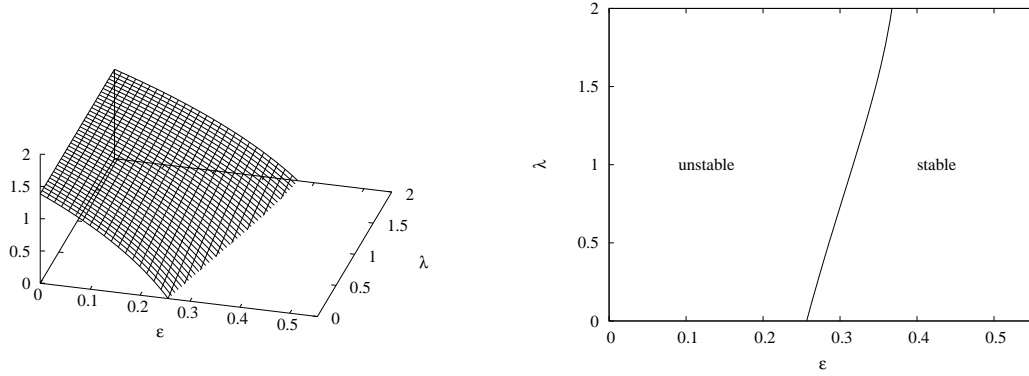


Figure 8.10: Left: Analytical obtained master stability function $\Lambda_{1c}(\epsilon, \lambda)$ for the period-2 orbit of the completely synchronized $2B^-$ dynamics. Right: Regions of stable synchronized period-2 orbit, consistent with the numerically obtained result in Fig. 8.8

which are real numbers for $\epsilon \in [0, 5/9]$ and are stable for the synchronized solution for

$$\epsilon \in \left(\frac{1}{9}(7 - \sqrt{22}), \frac{1}{6} \right) = (0.256\dots, 0.555\dots). \quad (8.60)$$

The boundary between stable/unstable period-2 orbit synchronization

$$\lambda = \frac{1 - \sqrt{4 - 14\epsilon + 9\epsilon^2}}{\epsilon} \quad (8.61)$$

is displayed in the second part of Fig. 8.10. The coupling range of stable synchronization for a ring network is determined by the boundary for $\lambda = 2$:

$$\epsilon \in \left(\frac{1}{5}(5 - \sqrt{10}), \frac{1}{6} \right) = (0.367\dots, 0.555\dots). \quad (8.62)$$

8.3.6 $3B$ dynamics

The synchronized solution of the $3B$ dynamics is given by

$$h_\epsilon(x) = (1 - \epsilon)(4x^3 - 3x) + \epsilon x. \quad (8.63)$$

This function differs from the other dynamics by being a polynomial of third order and showing the symmetry $h_\epsilon(x) = -h_\epsilon(-x)$. According to this symmetry, for every orbit $x(0), x(1), \dots$, there is an orbit $-x(0), -x(1), \dots$, leading to a symmetric bifurcation diagram. The first part of Fig. 8.11 shows this bifurcation diagram. Different to the other cases, for this function for a certain parameter range ϵ the bifurcation diagram depends on the initial condition. In this case one observe two attractors, with the orbits and basin of attraction of the first attractor given by the negative values of the orbits and and basin of attraction of the second attractor (see the third part of

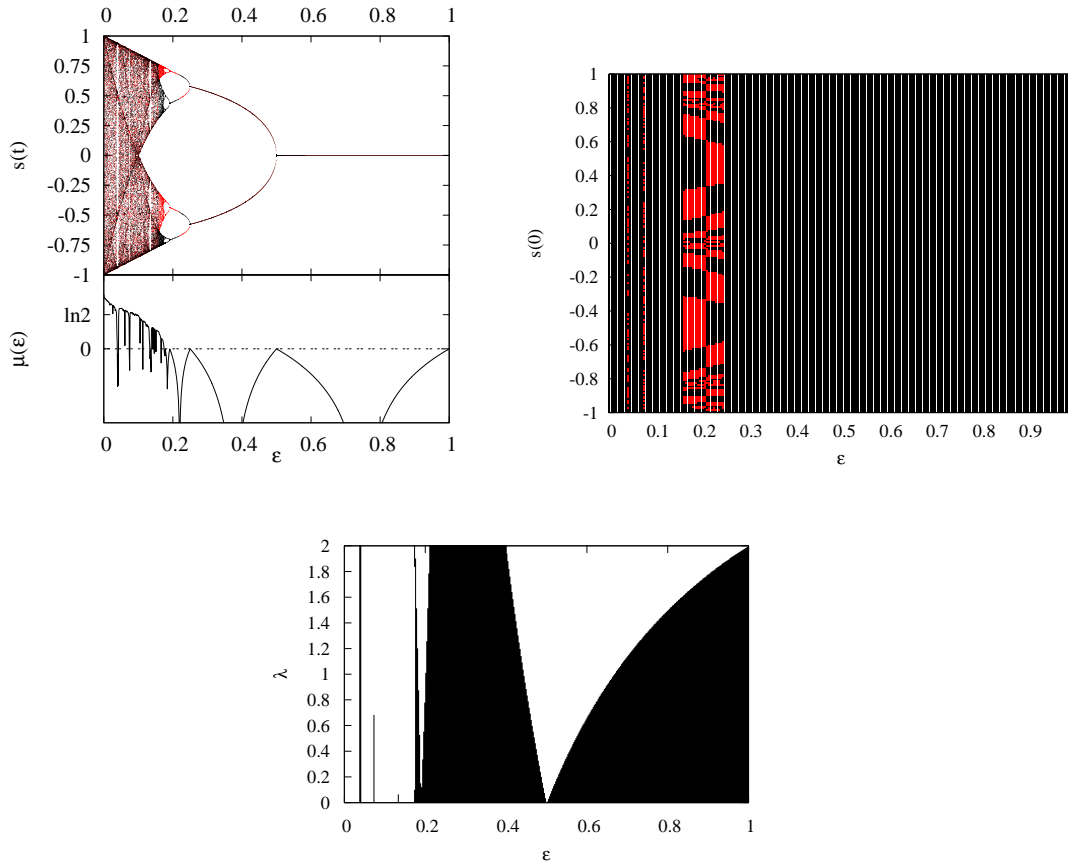


Figure 8.11: Top left: Bifurcation diagram of the synchronized solution $h_\epsilon(x)$ of the $3B$ dynamics. For a certain range of the coupling parameter ϵ one observes two attractors, displayed by black and red dots in the figure. The orbits in the respective attractors only differ by a sign, hence the Lyapunov exponents $\mu(\epsilon)$ are identical. Top right: Basin of attraction for the respective attractors, determined by 200 different initial conditions. Bottom: Region of stability in the ϵ - λ plane (black), associated with a negative master stability function $\Lambda_{1c}(\epsilon, \lambda)$ of the dynamics. Parameters as in Fig. 8.1.

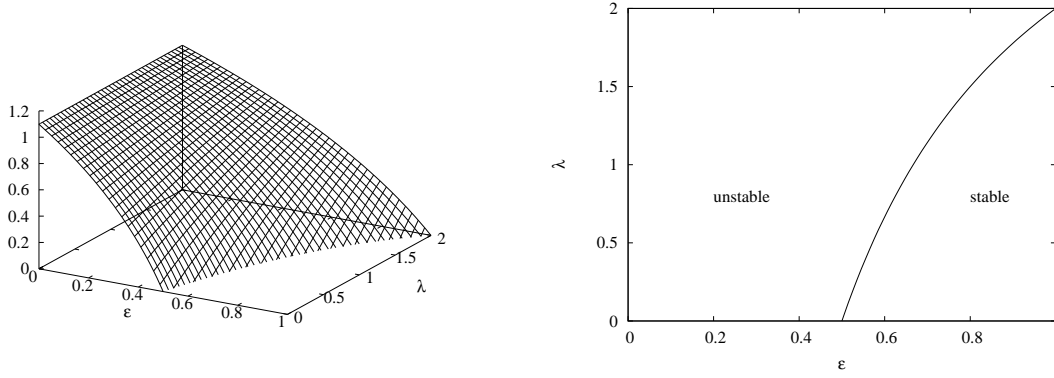


Figure 8.12: Same as Fig. 8.2, but for the fixed point of the $3B$ dynamics.

Fig. 8.11). Since the stability of periodic orbits of the synchronized solution, and the master stability function only depend on even functions of x , the respective stability does not depend on the initial condition.

The synchronized solution has the fixed points $x_{(f_1, \pm)} = \pm 1$ and $x_{(f_2)} = 0$. Whereas the first ones are not stable in the range $\epsilon \in [0, 1]$, the fixed point $x_{(f_2)}$ is stable in the range $(1/2, 1)$. The respective master stability function and the range of stability is displayed in Fig. 8.12. The region of stable synchronized fixed point is separated from the region of instability by the curve

$$\lambda = \frac{2(2\epsilon - 1)}{\epsilon}. \quad (8.64)$$

Accordingly, this fixed point is not stable for the ring network.

There are three different period-2 orbits. The first one

$$x_{(p_1, \pm)} = \pm \left(\frac{\sqrt{1 - 2\epsilon}}{\sqrt{2(1 - \epsilon)}} \right) \quad (8.65)$$

contains real numbers for $\epsilon \in [0, 1/2]$. This orbit is stable for $\epsilon \in (1/4, 1/2)$. The respective master stability function and region of stability is displayed in Fig. 8.13. The curves separating regions of stable/unstable synchronization for this orbit are given by

$$\lambda = \frac{4(1 - 2\epsilon)}{\epsilon} \text{ and } \lambda = \frac{2(1 - 4\epsilon)}{\epsilon}. \quad (8.66)$$

Thus one obtains stability for a ring network for $\epsilon \in (1/4, 2/5)$.

The synchronized dynamics has two more period-2 orbits, which only differ by a sign:

$$\begin{aligned} x_{(p_2, \pm)} &= \pm \sqrt{\frac{3 - 4\epsilon \mp \sqrt{5 - 24\epsilon + 16\epsilon^2}}{8(1 - \epsilon)}}, \\ x_{(p_3, \pm)} &= \mp \sqrt{\frac{3 - 4\epsilon \mp \sqrt{5 - 24\epsilon + 16\epsilon^2}}{8(1 - \epsilon)}}. \end{aligned} \quad (8.67)$$

8 Complete synchronization of networks

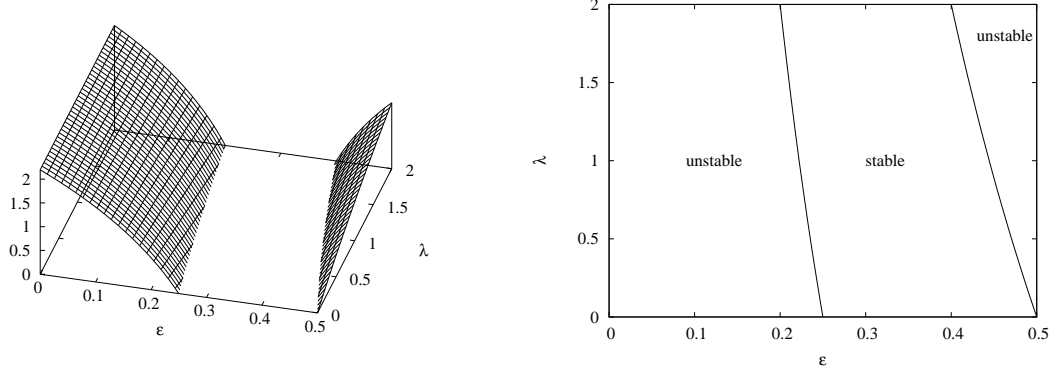


Figure 8.13: Same as Fig. 8.2, but for the first period-2 orbit of the $3B$ dynamics.

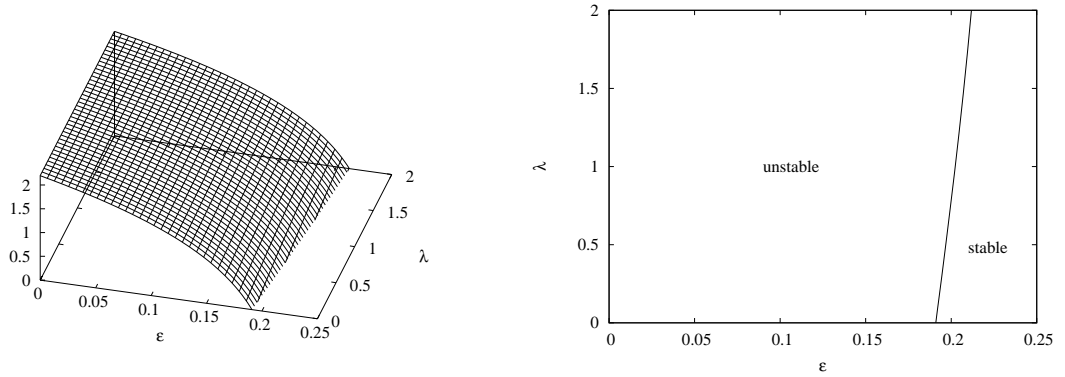


Figure 8.14: Same as Fig. 8.2, but for the second and third period-2 orbit of the $3B$ dynamics.

These orbits are real numbers for $\epsilon \in [0, 1/4]$ and stable for the synchronized dynamics h_ϵ for

$$\epsilon \in \left(\frac{1}{4}(3 - \sqrt{5}), \frac{1}{4} \right). \quad (8.68)$$

In Fig. 8.14 the master stability function and the region of stability is displayed. The upper bound is given by the range of validity $\epsilon < 1/4$, whereas the lower bound of stability is determined by the curve

$$\lambda = \frac{-3 + 4\epsilon + \sqrt{41 - 216\epsilon + 144\epsilon^2}}{2\epsilon}, \quad (8.69)$$

which leads to the range of stability

$$\epsilon \in \left(\frac{1}{20}(21 - \sqrt{281}), \frac{1}{4} \right) \quad (8.70)$$

for a ring-network.

9 Cluster synchronization

In the literature mostly complete synchronization as presented in the last chapter is studied. Another type of coherent behaviour is cluster synchronization, where subgroups of the population of dynamical units mutually synchronize, but the various groups or clusters show different behaviour.

For diffusively coupled systems of identical units, complete synchronization is always possible. This is due to the fact that the coupling only incorporates terms depending on the difference in the state of the respective system, which vanish for identical states. For cluster synchronization in general this is not the case. Accordingly many works focus on the conditions of having cluster synchronization as well as on the stability of these specific states [23, 24, 77, 79]. Also adaptive approaches [78], generation of clusters by pinning [73] or cluster synchronization of systems with non-identical nodes [113] is studied.

In the following chapter I will take a different approach. One can easily see, that for standard coupled map networks with a bipartite topology, that is two groups of nodes only with intergroup links, two-cluster synchronization is always possible. Of interest is the type and the stability of the synchronized dynamics for arbitrary bipartite networks. The class of bipartite networks not only covers all tree-like networks, but also all networks containing loops with an even number of nodes. The stability is studied by master stability functions for two-cluster synchronization similar to the formalism put forward in Ref. [105], which is a generalization of the method introduced in Ref. [96].

9.1 Master stability functions for two-cluster synchronization on bipartite networks

In this section the application of the master stability formalism to the case of two-cluster synchronization on bipartite networks is generalized. Bipartite networks consist of two adjoint sets of nodes \mathcal{V}_1 and \mathcal{V}_2 , with links only between nodes from different sets (see Sec. 2.2). This class of networks not only covers all tree-like networks, but also all networks containing loops with an even number of nodes [40]. One example of a bipartite network is a ring-structure with an even number of nodes, another one the star-network with a central node, which is connected to all other nodes of the network.

Label the nodes of the bipartite network in such a way that nodes $1, 2, \dots, N_1$ belong to the first set \mathcal{V}_1 , and nodes $N_1 + 1, \dots, N$ belong to the second set \mathcal{V}_2 . The size of the respective sets is $|\mathcal{V}_1| = N_1$, $|\mathcal{V}_2| = N_2$, with $N_1 + N_2 = N$ the size of the whole network. The adjacency matrix A is then of the form

$$A = \begin{pmatrix} 0 & B \\ B^T & 0 \end{pmatrix}, \quad (9.1)$$

where B is an $N_1 \times N_2$ matrix. As a generalization of the class of dynamical systems considered in the last chapter, different functions $f(x)$ and $g(x)$ are allowed for the corresponding evolution of first- or second-set nodes, respectively. With the notation

$$\alpha(i) = \begin{cases} 1 & : \quad i = 1, \dots, N_1 \quad (i \in \mathcal{V}_1) \\ 2 & : \quad i = N_1 + 1, \dots, N \quad (i \in \mathcal{V}_2), \end{cases} \quad (9.2)$$

the more general evolution equation reads

$$x_i(t+1) = (1 - \epsilon)f_{\alpha(i)}[x_i(t)] + \frac{\epsilon}{k_i} \sum_{j=1}^N A_{ij}g_{\alpha(i)}[x_j(t)]. \quad (9.3)$$

A two-cluster synchronized solution is $x_i(t) = s_{\alpha(i)}(t)$ for all nodes i . Inserting this into Eq. (9.3) leads to the evolution equation for $s_1(t)$ and $s_2(t)$:

$$\begin{aligned} s_1(t+1) &= (1 - \epsilon)f_1[s_1(t)] + \epsilon g_1[s_2(t)], \\ s_2(t+1) &= (1 - \epsilon)f_2[s_2(t)] + \epsilon g_2[s_1(t)]. \end{aligned} \quad (9.4)$$

This solution corresponds to the occurrence of synchronized clusters due to intercluster couplings (see Sec.8.1). There are two synchronized clusters, the respective sets \mathcal{V}_1 and \mathcal{V}_2 , with no links within the respective clusters, but only between nodes from different clusters.

In the following, master stability functions for two-cluster synchronization for arbitrary functions $f_{\alpha(i)}(x)$, $g_{\alpha(i)}(x)$ and arbitrary bipartite network configurations of the type displayed in Eq. (9.1) are derived. By application of these functions one does not have to linearize every specific bipartite network dynamics for itself, but is able to assess the stability properties of different networks by means of their spectral characteristics, analogous to the formalism presented in the last chapter for complete synchronization.

The dynamics of small perturbations $\xi_i(t) = x_i(t) - s_{\alpha(i)}(t)$ from the two-cluster synchronized state is given by

$$\xi_i(t+1) = (1 - \epsilon)f'_{\alpha(i)}[s_{\alpha(i)}(t)]\xi_i(t) + \frac{\epsilon}{k_i} \sum_{j=1}^N A_{ij}g'_{\alpha(i)}[s_{\alpha(j)}(t)]\xi_j(t). \quad (9.5)$$

Due to the restriction to bipartite network configurations with couplings only among nodes from different sets this can be recast into

$$\xi_i(t+1) = (1 - \epsilon)f'_{\alpha(i)}[s_{\alpha(i)}(t)]\xi_i(t) + \frac{\epsilon}{k_i}g'_{\alpha(i)}[s_{\bar{\alpha}(i)}(t)] \left(\sum_{j=1}^N A_{ij}\xi_j(t) \right), \quad (9.6)$$

where the label

$$\bar{\alpha}(i) = \begin{cases} 2 & : \quad i = 1, \dots, N_1 \quad (i \in \mathcal{V}_1), \\ 1 & : \quad i = N_1 + 1, \dots, N \quad (i \in \mathcal{V}_2) \end{cases} \quad (9.7)$$

has been used. By use of the normalized Laplacian $L = \delta_{ij} - A_{ij}/k_i$, this can be rewritten as

$$\xi_i(t+1) = \left\{ (1-\epsilon)f'_{\alpha(i)}[s_{\alpha(i)}(t)] + \epsilon g'_{\alpha(i)}[s_{\bar{\alpha}(i)}(t)] \right\} \xi_i(t) - \epsilon g'_{\alpha(i)}[s_{\bar{\alpha}(i)}(t)] \sum_{j=1}^N L_{ij} \xi_j(t), \quad (9.8)$$

This is an equation similar to Eq. (8.9) in the last chapter. The introduction of the generalized Laplacian L allows to derive a master stability function for two-cluster synchronization, which is very similar to the one derived in the last chapter for complete synchronization.

In the following all perturbations ξ_i are united into one vector ξ of dimension N . Define the time-dependent diagonal $N \times N$ matrices

$$\begin{aligned} \hat{f}' &= \begin{pmatrix} f'_1(s_1)\mathbf{1}_{N_1} & 0 \\ 0 & f'_2(s_2)\mathbf{1}_{N_2} \end{pmatrix}, \\ \hat{g}' &= \begin{pmatrix} g'_1(s_2)\mathbf{1}_{N_1} & 0 \\ 0 & g'_2(s_1)\mathbf{1}_{N_2} \end{pmatrix}, \end{aligned} \quad (9.9)$$

where $\mathbf{1}_M$ denotes the unity matrix of dimension M . The matrix equation (9.8) then reads

$$\xi(t+1) = \left[(1-\epsilon)\hat{f}' + \epsilon\hat{g}' - \epsilon\hat{g}' \cdot L \right] \xi(t). \quad (9.10)$$

For the derivation of the master stability function for complete synchronization one would now diagonalize L in Eq. (9.10), obtaining a decoupling of different perturbation modes. Due to the appearance of the matrices \hat{f}' and \hat{g}' the situation for two-cluster synchronization is more complicated. In this case one needs to incorporate specific properties of the eigenvectors and eigenvalues of the normalized Laplacian L for bipartite networks, which are derived in the following paragraphs.

Properties of the normalized Laplacian for bipartite networks

Define the matrix Q as

$$Q_{ij} = \delta_{ij} - \frac{A_{ij}}{\sqrt{k_i k_j}}, \quad (9.11)$$

which is similar to L by means of the transformation $L = K^{-1/2} Q K^{1/2}$, with $K_{ij} = \delta_{ij} k_i$. Since Q is a real symmetric matrix, it can be diagonalized and has a basis of orthonormal real eigenvectors $\{\mathbf{v}_i\}_{i=1}^N$ [85]. Write all eigenvectors in the form $\mathbf{v} = (\mathbf{y}^T, \mathbf{z}^T)^T$ with $\mathbf{y} \in \mathbb{R}^{N_1}$, $\mathbf{z} \in \mathbb{R}^{N_2}$.

Let \mathbf{v} be such an eigenvector of Q corresponding to the eigenvalue λ . Then $\mathbf{u} = (-\mathbf{y}^T, \mathbf{z}^T)^T$ is also an eigenvector of Q , associated with the eigenvalue $(2-\lambda)$ [9, 35]. Without loss of generality it is assumed in the following that $N_1 \geq N_2$. If one chooses

$\mathbf{v} = (\mathbf{y}^T, 0)$ and evaluates the eigenvalue equation $Q\mathbf{v} = \lambda\mathbf{v}$ for $\lambda = 1$, due to the block structure of the adjacency matrix A in Eq. (9.1) it follows

$$\sum_{j=1}^{N_1} \frac{A_{ij}}{\sqrt{k_i k_j}} y_j = 0, \quad i = N_1 + 1, \dots, N. \quad (9.12)$$

This set of equations has at least $(N_1 - N_2)$ non-zero solutions [57]. So there exist at least $(N_1 - N_2)$ eigenvectors $\mathbf{v} = (\mathbf{y}^T, 0)^T$ with $\mathbf{y} \in \mathbb{R}^{N_1}$, associated with the eigenvalue $\lambda = 1$. Depending on the rank of A there might be additional $\lambda = 1$ solutions of the eigenvalue equation $Q\mathbf{v} = \lambda\mathbf{v}$, which then come in pairs as for the eigenvalues $\lambda \neq 1$ [57].

The matrix Q can be diagonalized by the transformation $J = S^{-1}QS$, where J is a diagonal matrix with the eigenvalues λ_i of Q on the diagonal. The columns of S are just the eigenvectors \mathbf{v} of Q . In the following these columns are ordered in such a way that S has the form

$$S = \begin{pmatrix} C & -C & E \\ D & D & 0 \end{pmatrix}, \quad S^{-1} = S^T = \begin{pmatrix} C^T & D^T \\ -C^T & D^T \\ E^T & 0 \end{pmatrix}, \quad (9.13)$$

where for $i = 1, \dots, N_2$ the i th column of S is the eigenvector corresponding to the eigenvalue λ_i , and the respective $(i + N_2)$ th column is the eigenvector for $\lambda_{i+N_2} = (2 - \lambda_i)$. The remaining columns are the eigenvectors $\mathbf{v} = (\mathbf{y}^T, 0)^T$ associated with the eigenvalue $\lambda = 1$. Thus for $N_1 \geq N_2$ it holds $C \in \mathbb{R}^{N_1 \times N_2}$, $D \in \mathbb{R}^{N_2 \times N_2}$ and $E \in \mathbb{R}^{N_1 \times (N_1 - N_2)}$. From the condition $S^{-1}S = \mathbb{1}_N$ one obtains $2C^T C = 2D^T D = \mathbb{1}_{N_2}$, $E^T E = \mathbb{1}_{(N_1 - N_2)}$ and $E^T C = 0$, $C^T E = 0$.

The relations derived in the last three paragraphs are now applied to Eq. (9.10). Using the transformations $Q = SJS^{-1}$, $L = K^{-1/2}QK^{1/2}$ and the fact that K, \hat{f}', \hat{h}', J are all diagonal matrices, one obtains from Eq. (9.10)

$$S^{-1}K^{1/2}\xi(t+1) = [(1 - \epsilon)S^{-1}\hat{f}'S + \epsilon S^{-1}\hat{g}'S - \epsilon(S^{-1}\hat{g}'S)J]S^{-1}K^{1/2}\xi(t), \quad (9.14)$$

which is an evolution equation for the new perturbation variable $\eta = S^{-1}K^{1/2}\xi$. The matrices $S^{-1}\hat{f}'S$ and $S^{-1}\hat{g}'S$ with S and S^{-1} as given in Eq. (9.13) become

$$S^{-1}\hat{f}'S = \frac{1}{2} \begin{pmatrix} f'_{(+)}\mathbb{1}_{N_2} & f'_{(-)}\mathbb{1}_{N_2} & 0 \\ f'_{(-)}\mathbb{1}_{N_2} & f'_{(+)}\mathbb{1}_{N_2} & 0 \\ 0 & 0 & 2f'_1(s_1)\mathbb{1}_{(N_1 - N_2)} \end{pmatrix}, \quad (9.15)$$

$$S^{-1}\hat{g}'S = \frac{1}{2} \begin{pmatrix} g'_{(+)}\mathbb{1}_{N_2} & g'_{(-)}\mathbb{1}_{N_2} & 0 \\ g'_{(-)}\mathbb{1}_{N_2} & g'_{(+)}\mathbb{1}_{N_2} & 0 \\ 0 & 0 & 2g'_1(s_1)\mathbb{1}_{(N_1 - N_2)} \end{pmatrix}, \quad (9.16)$$

where the abbreviations

$$\begin{aligned} f'_{(\pm)} &= f'_2(s_2) \pm f'_1(s_1), \\ g'_{(\pm)} &= g'_2(s_1) \pm g'_1(s_2) \end{aligned} \quad (9.17)$$

have been introduced.

For the last $(N_1 - N_2)$ components of η , the matrix equation (9.14) is already diagonal:

$$\eta_i(t+1) = [(1-\epsilon)f'_1[s_1(t)] + \epsilon g'_1[s_2(t)] - \lambda_i \epsilon g'_1[s_2(t)]] \eta_i(t). \quad (9.18)$$

Since the eigenvalues and corresponding columns in S were ordered in such a way that $\lambda_i = 1$ for $i = 2N_2 + 1, \dots, N$, this simplifies to

$$\eta_i(t+1) = (1-\epsilon)f'_1[s_1(t)]\eta_i(t). \quad (9.19)$$

It remains the calculation for the remaining first $2N_2$ components of η . For $i = 1, \dots, N_2$ one obtains by use of Eq. (9.15) and $\lambda_{i+N_2} = (2 - \lambda_i)$ the set of equations

$$\begin{aligned} 2\eta_i(t+1) &= [(1-\epsilon)f'_{(+)} + \epsilon(1-\lambda_i)g'_{(+)}] \eta_i(t) \\ &\quad + [(1-\epsilon)f'_{(-)} - \epsilon(1-\lambda_i)g'_{(-)}] \eta_{i+N_2}(t), \\ 2\eta_{i+N_2}(t+1) &= [(1-\epsilon)f'_{(-)} + \epsilon(1-\lambda_i)g'_{(-)}] \eta_i(t) \\ &\quad + [(1-\epsilon)f'_{(+)} - \epsilon(1-\lambda_i)g'_{(+)}] \eta_{i+N_2}(t). \end{aligned} \quad (9.20)$$

For $i = 1, \dots, N_2$ define new variables

$$\begin{aligned} \chi_i(t) &= \eta_i(t) - \eta_{i+N_2}(t), \\ \nu_i(t) &= \eta_i(t) + \eta_{i+N_2}(t) \end{aligned} \quad (9.21)$$

and obtain the evolution equations

$$\begin{aligned} \chi_i(t+1) &= (1-\epsilon)f'_1[s_1(t)]\chi_i(t) + \epsilon(1-\lambda_i)g'_1[s_2(t)]\nu_i(t), \\ \nu_i(t+1) &= (1-\epsilon)f'_2[s_2(t)]\nu_i(t) + \epsilon(1-\lambda_i)g'_2[s_1(t)]\chi_i(t). \end{aligned} \quad (9.22)$$

For every $i = 1, \dots, N_2$ this is a two-dimensional stability equation of the form

$$\begin{pmatrix} \chi_i(t+1) \\ \nu_i(t+1) \end{pmatrix} = \left[\begin{pmatrix} (1-\epsilon)f'_1[s_1(t)] & \epsilon g'_1[s_2(t)] \\ \epsilon g'_2[s_1(t)] & (1-\epsilon)f'_2[s_2(t)] \end{pmatrix} - \epsilon \lambda_i \begin{pmatrix} 0 & g'_1[s_2(t)] \\ g'_2[s_1(t)] & 0 \end{pmatrix} \right] \cdot \begin{pmatrix} \chi_i(t) \\ \nu_i(t) \end{pmatrix}. \quad (9.23)$$

This equation is the analogue of Eq. (8.28), with the first matrix inside the square brackets being the Jacobian of the synchronized dynamics as given in Eq. (9.4), and the second term being the Jacobian of the coupling function times the eigenvalue λ of the normalized Laplacian L .

In the following I will denote the synchronized dynamics as defined in Eq. (9.4) by the two-dimensional function $\mathbf{h}_\epsilon(\mathbf{s})$, analogous to the case of complete synchronization presented in the last chapter:

$$\mathbf{h}_\epsilon(\mathbf{s}) = \begin{pmatrix} (1-\epsilon)f_1(s_1) + \epsilon g_1(s_2) \\ (1-\epsilon)f_2(s_2) + \epsilon g_2(s_1) \end{pmatrix}. \quad (9.24)$$

The largest Lyapunov exponent $\Lambda_{2c}(\epsilon, \lambda)$ of Eq. (9.23) depending on the coupling ϵ and the eigenvalue parameter λ of the generalized Laplacian is the master stability function for two-cluster synchronization on bipartite networks. For numerical methods to calculate the Lyapunov exponent for higher-dimensional systems see Refs. [3, 94].

One has to give special attention to the eigenvalue $\lambda = 1$. For $N_1 \neq N_2$ at least $(N_1 - N_2)$ of the eigenvalues of L are equal to 1 and the Lyapunov exponent of Eq. (9.19) has to be considered, where $\lambda = 1$ was already inserted. If there are more than $(N_1 - N_2)$ eigenvalues $\lambda = 1$ of L , these additional eigenvalues come in pairs, as for $\lambda \neq 1$, and Eq. (9.23) – that is $\Lambda_{2c}(\epsilon, \lambda = 1)$ – has to be evaluated.

Recall that the eigenvalues λ of the generalized Laplacian L are bound to the interval $[0, 2]$, and for bipartite networks always occur in pairs $\lambda, (2 - \lambda)$. According to the calculations in the last paragraphs, in Eq. (9.23) the parameter λ stands for such pairs $\lambda, (2 - \lambda)$. Accordingly $\Lambda_{2c}(\epsilon, \lambda)$ only has to be evaluated in the range $\lambda \in [0, 1]$. Analogously to the case of complete synchronization the largest Lyapunov exponent $\Lambda_{2c}(\epsilon, \lambda = 0)$ – where again $\lambda = 0$ stands for the pair $\lambda = 0, \lambda = 2$ – does not affect the stability of the synchronized state, since the associated perturbations lie in the direction of the synchronization manifold.

For the special case $f_1(x) = f_2(x) = f(x)$ and $g_1(x) = g_2(x) = g(x)$ the synchronized dynamics $\mathbf{h}_\epsilon(\mathbf{s})$ is equivalent to a coupled map network consisting of only two nodes. Accordingly the stability condition for complete synchronization $s_1 = s_2$ of these two coupled maps can be studied by means of the master stability function $\Lambda_{1c}(\epsilon, \lambda)$. The Laplacian L of a network of two coupled nodes has eigenvalues $\lambda = 0$ and $\lambda = 2$, so the two nodes synchronize to a common trajectory if $\Lambda_{1c}(\epsilon, \lambda = 2) < 0$. Consequently complete synchronization on a bipartite network is stable if two-cluster synchronization is stable – determined by $\Lambda_{2c}(\epsilon, \lambda)$ – and additionally complete synchronization for two coupled maps is stable – determined by $\Lambda_{1c}(\epsilon, \lambda = 2)$.

9.2 Two-cluster synchronization on bipartite Tchebycheff networks

In the following section the master stability formalism for two-cluster synchronization will be applied to the six chaotic string dynamics presented in Chap. 3. The original model proposed by Beck in Ref. [17] is defined on a ring-network, that is a one-dimensional lattice. Such a network is a bipartite network¹. Accordingly, two cluster synchronization is possible, with $s_1(t)$ and $s_2(t)$ alternating on the lattice. However, the chaotic string model can be generalized to all kind of networks as a special realization of standard coupled map networks, see Chap. 7. The master stability formalism for two-cluster synchronization can then be applied to all network realizations, which show a bipartite structure.

The respective synchronized dynamics for each of the six chaotic string dynamics

¹For simplicity, an even network size is assumed.

label	$f(x)$	$g(x)$
2A	$T_2(x) = 2x^2 - 1$	$T_2(x) = 2x^2 - 1$
2B	$T_2(x) = 2x^2 - 1$	$T_1(x) = x$
2A ⁻	$T_2(x) = 2x^2 - 1$	$T_{-2}(x) = -(2x^2 - 1)$
2B ⁻	$T_2(x) = 2x^2 - 1$	$T_{-1}(x) = -x$
3A	$T_3(x) = 4x^3 - 3x$	$T_3(x) = 4x^3 - 3x$
3B	$T_3(x) = 4x^3 - 3x$	$T_1(x) = x$

Table 9.1: The six chaotic string dynamics considered in Ref. [17].

is given by

$$\mathbf{h}_\epsilon(\mathbf{s}) = \begin{pmatrix} (1 - \epsilon)f(s_1) + \epsilon g(s_2) \\ (1 - \epsilon)f(s_2) + \epsilon g(s_1) \end{pmatrix}, \quad (9.25)$$

with $f(x)$ and $g(x)$ as displayed in Tab. 9.1 (see also Chap. 3).

For each of the six dynamics, Eq. (9.25) yields a different two-dimensional dynamics, depending on the coupling ϵ . These types of two coupled map systems often show rather complicated behaviour, including multistability and period-doubling or Naimark-Sacker bifurcations [34, 100, 101]. A detailed analytical treatment for each of the possible synchronized two coupled map dynamics and its network stability properties for the whole coupling range $\epsilon \in [0, 1]$ is far beyond the scope of this thesis. As a first approach in this direction, in the following apart from numerical studies exact analytical results on the stability of selected two-cluster synchronized fixed points and period-2 orbits of bipartite Tchebyscheff networks will be given.

9.2.1 Two-cluster synchronized fixed points and period-2 orbits

A fixed point is determined by the equation $\mathbf{h}_\epsilon(\mathbf{s}) = \mathbf{s}$, that is

$$\begin{aligned} s_1 &= (1 - \epsilon)f(s_1) + \epsilon g(s_2), \\ s_2 &= (1 - \epsilon)f(s_2) + \epsilon g(s_1). \end{aligned} \quad (9.26)$$

Here only the fixed points with $s_1 \neq s_2$ are considered, for fixed points with $s_1 = s_2$ (complete synchronization) see Chap. 8. Obviously the equation is symmetric under $s_1 \leftrightarrow s_2$.

Denote the fixed point by $\mathbf{s}^* = (s_1^*, s_2^*)$. Its stability as a synchronized two-cluster state on a network is determined by the master stability function $\Lambda_{2c}(\epsilon, \lambda)$. Consider the matrix occurring in the stability equation (9.23) for the fixed point \mathbf{s}^* :

$$\begin{pmatrix} (1 - \epsilon)f'(s_1^*) & (1 - \lambda)\epsilon g'(s_2^*) \\ (1 - \lambda)\epsilon g'(s_1^*) & (1 - \epsilon)f'(s_2^*) \end{pmatrix}. \quad (9.27)$$

The eigenvalues are the solutions $\kappa_1(\epsilon, \lambda)$, $\kappa_2(\epsilon, \lambda)$ of the characteristic polynomial

$$[(1 - \epsilon)f'(s_1^*) - \kappa] \cdot [(1 - \epsilon)f'(s_2^*) - \kappa] - \epsilon^2(1 - \lambda)^2 g'(s_1^*)g'(s_2^*) = 0, \quad (9.28)$$

9 Cluster synchronization

and the master stability function is then given by

$$\Lambda_{2c}(\epsilon, \lambda) = \max_{i=1,2} \ln[|\kappa_i(\epsilon, \lambda)|]. \quad (9.29)$$

For $\lambda = 0$, the master stability function expresses the stability of the fixed point for the two-dimensional synchronized dynamics itself. In case $\Lambda_{2c}(\epsilon, \lambda = 0) < 0$, the fixed point is stable for \mathbf{h}_ϵ . The stability of the synchronized fixed point in the network is then determined by $\Lambda_{2c}(\epsilon, \lambda)$ for $\lambda \in (0, 1]$, where λ stands for the eigenvalues of the generalized Laplacian.

In principle the stability of two-cluster synchronized states with higher periodicity can be studied in the same way as for the fixed point. In the following I will treat one special kind of period-2 dynamics, given by

$$\begin{aligned} s_1(t+2) &= s_2(t+1) = s_1(t), \\ s_2(t+2) &= s_1(t+1) = s_2(t). \end{aligned} \quad (9.30)$$

This is a zig-zag pattern [37], with $s_1(t)$ and $s_2(t)$ alternating in time and space. The pattern is defined by the following set of equations:

$$\begin{aligned} s_1 &= (1 - \epsilon)f(s_2) + \epsilon g(s_1), \\ s_2 &= (1 - \epsilon)f(s_1) + \epsilon g(s_2). \end{aligned} \quad (9.31)$$

There is a symmetry for the case when $g(x) = f(x)$. By replacing $\epsilon \rightarrow \epsilon' = (1 - \epsilon)$ one obtains

$$\begin{aligned} s_1 &= (1 - \epsilon')f(s_1) + \epsilon'f(s_2), \\ s_2 &= (1 - \epsilon')f(s_2) + \epsilon'f(s_1), \end{aligned} \quad (9.32)$$

which defines a fixed point. Accordingly, for $f(x) = g(x)$ a fixed point \mathbf{s} of \mathbf{h}_ϵ corresponds to a zig-zag pattern for $\mathbf{h}_{(1-\epsilon)}$. This symmetry will be generalized to general periodic orbits in Sec. 9.2.2.

Denote the two points of the zig-zag patterns by s_1^*, s_2^* . In order to obtain the master stability function, one has to consider the eigenvalues κ_1, κ_2 of the product matrix

$$\begin{pmatrix} (1 - \epsilon)f'(s_2^*) & (1 - \lambda)\epsilon g'(s_1^*) \\ (1 - \lambda)\epsilon g'(s_2^*) & (1 - \epsilon)f'(s_1^*) \end{pmatrix} \cdot \begin{pmatrix} (1 - \epsilon)f'(s_1^*) & (1 - \lambda)\epsilon g'(s_2^*) \\ (1 - \lambda)\epsilon g'(s_1^*) & (1 - \epsilon)f'(s_2^*) \end{pmatrix}. \quad (9.33)$$

The characteristic polynomial is given by

$$\begin{aligned} 0 &= [(1 - \epsilon)^2 f'(s_1^*) f'(s_2^*) + \epsilon^2 (1 - \lambda)^2 g'(s_1^*)^2 - \kappa] \cdot \\ &\quad [(1 - \epsilon)^2 f'(s_1^*) f'(s_2^*) + \epsilon^2 (1 - \lambda)^2 g'(s_2^*)^2 - \kappa] \\ &\quad - \epsilon^2 (1 - \epsilon)^2 (1 - \lambda)^2 (f'(s_1^*) \cdot f'(s_2^*)) \cdot (g'(s_1^*) + g'(s_2^*))^2, \end{aligned} \quad (9.34)$$

which is solved by

$$\begin{aligned} \kappa_{\pm} = & (1 - \epsilon)^2 f'(s_1^*) f'(s_2^*) + \frac{\epsilon^2 (1 - \lambda)^2}{2} \left[g'(s_1^*)^2 + g'(s_2^*)^2 \right. \\ & \left. \pm (g'(s_1^*) + g'(s_2^*)) \sqrt{(g'(s_1^*) - g'(s_2^*))^2 + 4 \frac{(1 - \epsilon)^2}{\epsilon^2 (1 - \lambda)^2} f'(s_1^*) f'(s_2^*)} \right]. \end{aligned} \quad (9.35)$$

Accordingly, the master stability function for synchronized zig-zag patterns on bipartite networks reads

$$\Lambda_{2c}(\epsilon, \lambda) = \max_{\pm} \ln[|\kappa_{\pm}(\epsilon, \lambda)|]. \quad (9.36)$$

9.2.2 Symmetries of two coupled maps

For the 2A and the 3A dynamics the synchronized two-cluster dynamics \mathbf{h}_{ϵ} has the following form:

$$\begin{aligned} s_1(t+1) &= (1 - \epsilon) f[s_1(t)] + \epsilon f[s_2(t)], \\ s_2(t+1) &= (1 - \epsilon) f[s_2(t)] + \epsilon f[s_1(t)], \end{aligned} \quad (9.37)$$

with $f(x)$ the respective Tchebycheff polynomial. One obtains the trajectory $\mathbf{s}(t) = (s_1(t), s_2(t))$ by iterating this equation for some initial value $\mathbf{s}(0)$. Consider $\mathbf{h}_{(1-\epsilon)}$, which is given by

$$\begin{aligned} s_1(t+1) &= \epsilon f[s_1(t)] + (1 - \epsilon) f[s_2(t)], \\ s_2(t+1) &= \epsilon f[s_2(t)] + (1 - \epsilon) f[s_1(t)]. \end{aligned} \quad (9.38)$$

By comparing Eq. (9.37) and Eq. (9.38) one observes that the application of $\mathbf{h}_{(1-\epsilon)}$ corresponds to the application of \mathbf{h}_{ϵ} before or after s_1 and s_2 have been interchanged. With the function $\mathcal{X} : \mathbb{R}^2 \rightarrow \mathbb{R}^2$ defined by

$$\mathcal{X}\left(\begin{pmatrix} s_1 \\ s_2 \end{pmatrix}\right) = \begin{pmatrix} s_2 \\ s_1 \end{pmatrix} \quad (9.39)$$

this can be formulated as

$$\mathbf{h}_{(1-\epsilon)} = \mathbf{h}_{\epsilon} \circ \mathcal{X} = \mathcal{X} \circ \mathbf{h}_{\epsilon}. \quad (9.40)$$

Compare an orbit $\mathbf{s}(t)$ obtained by iterating the function \mathbf{h}_{ϵ} , and the orbit $\tilde{\mathbf{s}}(t)$ generated by $\mathbf{h}_{(1-\epsilon)}$. Assume that $\mathbf{s}(0) = \tilde{\mathbf{s}}(0)$. With Eq. (9.40) and $\mathcal{X} \circ \mathcal{X} = \mathbb{1}$ one obtains

$$\begin{aligned} \tilde{\mathbf{s}}(t) &= (\mathbf{h}_{(1-\epsilon)})^t [\tilde{\mathbf{s}}(0)] \\ &= (\mathbf{h}_{(1-\epsilon)})^t [\mathbf{s}(0)] \\ &= \begin{cases} \mathcal{X} \circ (\mathbf{h}_{\epsilon})^t [\mathbf{s}(0)] & : t \text{ odd,} \\ (\mathbf{h}_{\epsilon})^t [\mathbf{s}(0)] & : t \text{ even,} \end{cases} \\ &= \begin{cases} \mathcal{X} \circ \mathbf{s}(t) & : t \text{ odd,} \\ \mathbf{s}(t) & : t \text{ even.} \end{cases} \end{aligned} \quad (9.41)$$

This shows that the orbits of \mathbf{h}_ϵ and $\mathbf{h}_{(1-\epsilon)}$ for identical initial conditions coincide up to a swap of s_1 and s_2 . As a consequence, all periodic points of \mathbf{h}_ϵ with even period are also periodic points of $\mathbf{h}_{(1-\epsilon)}$. Periodic points with an odd period of \mathbf{h}_ϵ are also periodic points of $\mathbf{h}_{(1-\epsilon)}$, but with double the period in order to cancel the operator \mathcal{X} . Consequently, a fixed point of \mathbf{h}_ϵ is transformed into a zig-zag pattern with period 2 for $\mathbf{h}_{(1-\epsilon)}$, which has been shown as a special case of this symmetry in the last section.

In order to evaluate the linear stability of the periodic orbits, one has to consider the Jacobian

$$\mathbf{Dh}_\epsilon^t[\mathbf{s}(0)] = \prod_{\tau=0}^{t-1} \mathbf{Dh}_\epsilon[\mathbf{s}(\tau)], \quad (9.42)$$

where the chain rule has been used (see Sec. 2.1.3). The respective Jacobians are given by

$$\mathbf{Dh}_\epsilon(\mathbf{s}) = \begin{pmatrix} (1-\epsilon)f'(s_1) & \epsilon f'(s_2) \\ \epsilon f'(s_1) & (1-\epsilon)f'(s_2) \end{pmatrix}. \quad (9.43)$$

One can easily show that

$$\begin{aligned} \mathbf{Dh}_{(1-\epsilon)}(\mathbf{s}) &= \begin{pmatrix} 0 & 1 \\ 1 & 0 \end{pmatrix} \bullet \mathbf{Dh}_\epsilon(\mathbf{s}), \\ \mathbf{Dh}_{(1-\epsilon)}(\mathcal{X} \circ \mathbf{s}) &= \mathbf{Dh}_\epsilon(\mathbf{s}) \bullet \begin{pmatrix} 0 & 1 \\ 1 & 0 \end{pmatrix}. \end{aligned} \quad (9.44)$$

With $\tilde{\mathbf{s}}(t)$ as given in Eq. 9.41 this leads to

$$\prod_{\tau=0}^{t-1} \mathbf{Dh}_{(1-\epsilon)}[\tilde{\mathbf{s}}(\tau)] = \prod_{\tau=0}^{t-1} \mathbf{Dh}_\epsilon[\mathbf{s}(\tau)] \quad (9.45)$$

for even t and

$$\prod_{\tau=0}^{2t-1} \mathbf{Dh}_{(1-\epsilon)}[\tilde{\mathbf{s}}(\tau)] = \prod_{\tau=0}^{2t-1} \mathbf{Dh}_\epsilon[\mathbf{s}(\tau)] \quad (9.46)$$

for odd t . Since the stability of the respective periodic orbits depends on these products, one obtains equal ranges of stability for parameter ϵ and $(1-\epsilon)$.

Example: Two-cluster synchronized fixed point and zig-zag pattern of the 2A dynamics For the 2A dynamics, $f(x) = g(x)$ is given by the second-order Tchebyscheff polynomial. In Ref. [46] the stability of a fixed point with spatial period two for a coupled logistic map lattice was calculated. Since the second-order Tchebycheff polynomial is conjugated to the logistic map, the results obtained in Ref. [46] can be used to check the following calculation of a two-cluster synchronized fixed point of the 2A dynamics.

Equation (9.26) for this dynamics is solved by

$$s_{\pm} = \frac{1 \pm \sqrt{9 - 36\epsilon + 32\epsilon^2}}{4(1 - 2\epsilon)}. \quad (9.47)$$

This fixed point is a real value for two different coupling ranges:

$$\epsilon \in \left[0, \frac{3}{8}\right], \quad \epsilon \in \left[\frac{3}{4}, 1\right]. \quad (9.48)$$

The left part of Fig. 9.1 displays s_+ and s_- depending on the coupling value ϵ . One can easily show that for the lower coupling $\epsilon \in (0, 3/8]$ the value s_+ lies outside the phase space $[-1, 1]$. For $\epsilon = 0$ it holds $s_+ = 1$, but for vanishing coupling the $2A$ dynamics reduces to uncoupled Tchebyscheff maps, so this point can be excluded from consideration. Consequently one has to consider only the coupling range $[3/4, 1]$. With $f(x) = g(x) = T_2(x) = 2x^2 - 1$ the characteristic polynomial (9.28) reads

$$0 = [4(1 - \epsilon)s_+ - \kappa] \cdot [4(1 - \epsilon)s_- - \kappa] - 16\epsilon^2(1 - \lambda)^2 s_+ s_-. \quad (9.49)$$

In order to compare with the results from Ref. [46], consider explicitly the solutions for $\lambda = 0$:

$$\kappa_{\pm}(\epsilon, \lambda = 0) = -\frac{1 - \epsilon \pm \sqrt{9 - 54\epsilon + 105\epsilon^2 - 64\epsilon^3}}{2\epsilon - 1}. \quad (9.50)$$

The solutions κ_{\pm} are real for

$$\epsilon \leq \left[\frac{35}{62} + \frac{1}{192} \left(22329 - 10368\sqrt{2} \right)^{1/3} + \frac{1}{64} \left(827 + 384\sqrt{2} \right)^{1/3} \right] \approx 0.8231. \quad (9.51)$$

When solving $\ln[|\kappa_{\pm}(\epsilon, \lambda = 0)|] = 0$, one observes that the lower bound for stability is determined by the relation $\kappa_- = (-1)$, which is given by

$$\epsilon = \frac{1}{8} \left(4 + \sqrt{6} \right) \approx 0.806186. \quad (9.52)$$

The upper limit is determined by the absolute value of the complex solutions $|\kappa_+| = |\kappa_-| = 1$. This fixes the upper limit of the coupling range of having a stable fixed point for \mathbf{h}_{ϵ} as

$$\epsilon = \frac{1}{32} \left(19 + \sqrt{73} \right) \approx 0.86075. \quad (9.53)$$

These results coincide with the findings in Ref. [46]. The solutions of Eq. (9.49) with $\lambda \neq 0$ are given by

$$\begin{aligned} \kappa_{\pm}(\epsilon, \lambda) &= \frac{1 - \epsilon}{1 - 2\epsilon} \\ &\pm \frac{\sqrt{9 - 54\epsilon + 32\epsilon^4(2 - \lambda)\lambda - \epsilon^3(64 + 72\lambda - 36\lambda^2) + \epsilon^2(105 + 16\lambda - 8\lambda^2)}}{1 - 2\epsilon}. \end{aligned} \quad (9.54)$$

The curve in the ϵ - λ plane separating real from complex values of $\kappa(\epsilon, \lambda)$ is given by

$$\lambda(\epsilon) = 1 - \frac{(1 - \epsilon)\sqrt{18 - 153\epsilon + 460\epsilon^2 - 576\epsilon^3 + 256\epsilon^4}}{2\epsilon(2 - 9\epsilon + 8\epsilon^2)}. \quad (9.55)$$

9 Cluster synchronization

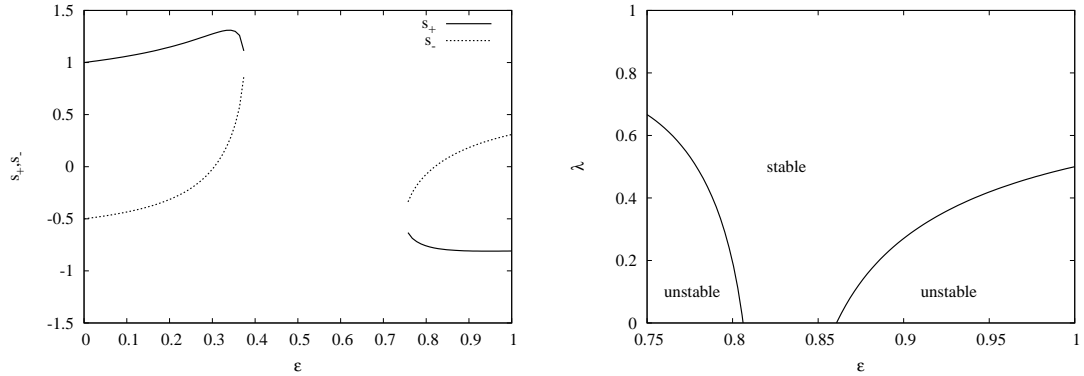


Figure 9.1: Left: The fixed point (s_+, s_-) of the synchronized dynamics \mathbf{h}_ϵ for the $2A$ dynamics. Right: Region of stability for the fixed point in the ϵ - λ plane for $\epsilon \in [3/4, 1]$, determined by a negative master stability function $\Lambda_{2c}(\epsilon, \lambda)$ for this fixed point.

Analogous to the case for $\lambda = 0$, one obtains the boundary curves for stable synchronization in the ϵ - λ plane by setting $\kappa_- = (-1)$, which yields

$$\lambda(\epsilon) = 1 + \frac{\sqrt{10 - 129\epsilon + 626\epsilon^2 - 1472\epsilon^3 + 1796\epsilon^4 - 1088\epsilon^5 + 256\epsilon^6}}{2\epsilon(2 - 9\epsilon + 8\epsilon^2)}, \quad (9.56)$$

and $|\kappa_+| = |\kappa_-| = 1$, leading to

$$\lambda(\epsilon) = 1 - \frac{\sqrt{18 - 193\epsilon + 808\epsilon^2 - 1692\epsilon^3 + 1892\epsilon^4 - 1088\epsilon^5 + 256\epsilon^6}}{2\epsilon(2 - 9\epsilon + 8\epsilon^2)}. \quad (9.57)$$

The right part of Fig. 9.1 shows the region of negative master stability function $\Lambda_{2c}(\epsilon, \lambda)$ in the ϵ - λ plane. The range of stability for $\lambda = 0$ is smaller than for all $\lambda > 0$, so for this fixed point the stability is determined by the behaviour of \mathbf{h}_ϵ itself, independently from the bipartite network structure. One obtains the values for the upper and lower limit by solving Eq. (9.56) and (9.57) for $\lambda = 0$. The range of stability is $[(4 + \sqrt{6})/8, (19 + \sqrt{73})/32]$, which corresponds to the numerical values $[0.806\dots, 0.860\dots]$. For this interval, the synchronization of the two-clustered fixed point is stable for arbitrary bipartite networks. Due to the symmetry of the dynamics one can immediately deduce a period-2 orbit of the dynamics. By the substitution $\epsilon \rightarrow (1 - \epsilon)$ in Eq. 9.47, one obtains the zig-zag pattern

$$s_\pm = \frac{1 \pm \sqrt{5 - 28\epsilon + 32\epsilon^2}}{4(2\epsilon - 1)}. \quad (9.58)$$

These are real values in the phase space $[-1, 1]$ for $\epsilon \in [0, 1/4]$. The range of stability for the synchronized dynamics is obtained by replacing ϵ by $(1 - \epsilon)$ in Eqs. (9.52) and (9.53). However, for determining the stability of this two-cluster synchronized state on bipartite networks, in general one cannot use the result for the fixed point,

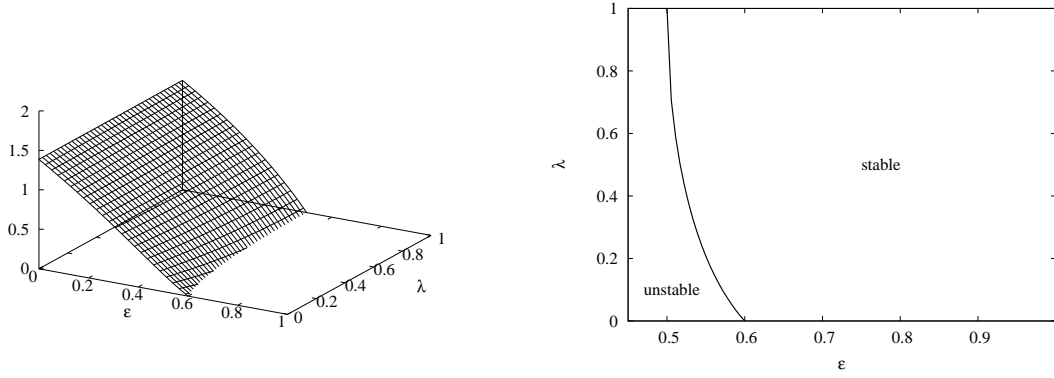


Figure 9.2: Left: Master stability function $\Lambda_{2c}(\epsilon, \lambda)$ for the zig-zag pattern of the $2B$ dynamics. Right: Regions with positive and negative master stability function in the ϵ - λ plane.

since the introduction of the network parameter λ in the respective master stability function breaks the symmetry of the problem. Instead one would have to consider Eq. (9.35).

Example: Two-cluster synchronized zigzag pattern of the $2B$ dynamics For the $2B$ dynamics with $f(x) = T_2(x) = 2x^2 - 1$ and $g(x) = x$, Eq. (9.31) is solved by

$$s_{\pm} = -\frac{1}{4}(1 \pm \sqrt{5}). \quad (9.59)$$

Inserting this in Eq. (9.35) yields

$$\kappa_{\pm}(\epsilon, \lambda) = -4 + 8\epsilon + \epsilon^2(-3 - 2\lambda + \lambda^2) \pm 4i(1 - \epsilon)\epsilon(\lambda - 1). \quad (9.60)$$

By setting

$$\Lambda_{2c}(\epsilon, \lambda) = \ln[|\kappa_{\pm}(\epsilon, \lambda)|] = 0, \quad (9.61)$$

one obtains the curve separating the regions of positive and negative master stability function in the ϵ - λ plane:

$$\lambda = 1 - \frac{\sqrt{-3 + 8\epsilon - 4\epsilon^2}}{\epsilon}. \quad (9.62)$$

The master stability function $\Lambda_{2c}(\epsilon, \lambda)$ and the curve given by Eq. (9.62) is displayed in Fig. 9.2. The region of stability has its narrowest range for $\lambda = 0$. This corresponds to the condition for stability of the zig-zag pattern for the synchronized solution \mathbf{h}_{ϵ} itself. By solving Eq. (9.62) for $\lambda = 0$, one obtains the range as $(3/5, 1)$. In this interval, the two-cluster synchronized zig-zag pattern is stable for arbitrary bipartite networks.

9.2.3 Numerical results

The iteration of Eq. (9.24) for the synchronized dynamics \mathbf{h}_ϵ , and the calculation of the respective master stability function $\Lambda_{2c}(\epsilon, \lambda)$ by determination of the Lyapunov exponents of Eq. (9.23) can be numerically performed by standard methods. Unfortunately, dynamical systems of two coupled maps might show multistability, that means coexistent stable attractor. Accordingly the trajectory and hence the stability of two-cluster synchronization might depend on the initial conditions. A numerically complete treatment of this problem would include the determination of possibly different attractors, and the application of the master stability formalism separately to each attractor dynamics. Although this would be an interesting problem, at this point I will limit the calculations to the general behaviour of the dynamics, without considering multiple attractors and dependence on initial conditions.

For each of the six chaotic string dynamics, in the following I will display three different figures. For a randomly picked initial condition, a phase portrait of the synchronized dynamics \mathbf{h}_ϵ depending on ϵ is given. Due to the limitation on one initial condition, this phase portrait picks for every coupling value ϵ only one attractor. Nevertheless this kind of figure gives a first impression about the different kinds of behaviour of \mathbf{h}_ϵ depending on ϵ .

To get a further understanding of the dynamics, also the average difference

$$\Delta(\epsilon) = \sqrt{\langle (s_1 - s_2)^2 \rangle} \quad (9.63)$$

is displayed, where the average is performed over all iterations minus some transient. This measure shows whether or not the synchronized two-cluster dynamics is fully synchronized.

A second figure shows the Lyapunov exponents of the synchronized dynamics. Again, although I will restrict the calculations to one initial condition and thus capture only one specific attractor for each coupling ϵ , the calculation shows whether or not the synchronized dynamics is chaotic or periodic.

Finally, for each of the six dynamics the region of stability in the ϵ - λ plane is displayed. The respective figures are obtained by numerically calculating the respective master stability functions $\Lambda_{2c}(\epsilon, \lambda)$ for the whole range of $\epsilon \in [0, 1]$ and $\lambda \in [0, 1]$ and checking whether or not the master stability functions adopts a positive or negative value. These calculations are done for various realizations, so it is differentiated whether $\Lambda_{2c}(\epsilon, \lambda) < 0$ for all or only some of the initial conditions.

Figures 9.3-9.8 display these plots for all six chaotic string dynamics. For the synchronized dynamics \mathbf{h}_ϵ the phase plots reveal period-doubling bifurcations as well as Sacker-Naimark bifurcations. The respective master stability functions $\Lambda_{2c}(\epsilon, \lambda)$ show that two-cluster synchronization is stable for a wide range of coupling values, depending on the respective dynamics.

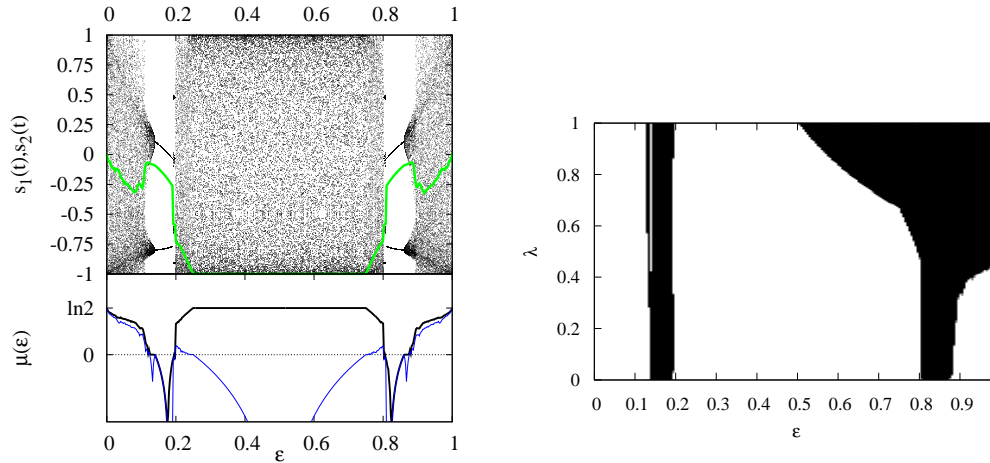


Figure 9.3: Left top: Phase portrait of the synchronized solution in two-cluster synchronization for the $2A$ dynamics. The green line shows the synchronization difference Δ . Left bottom: Larger (black) and smaller (blue) Lyapunov exponent of \mathbf{h}_ϵ . Right: Regions of negative $\Lambda_{2c}(\epsilon, \lambda)$ (black) in the ϵ - λ plane. Points where depending on the initial conditions one numerically obtains negative as well as positive master stability functions are colored grey. Parameters are 100 different realizations for the right figure, one realization for the left figures, $T = 10^4$, $T_0 = 10^3$.

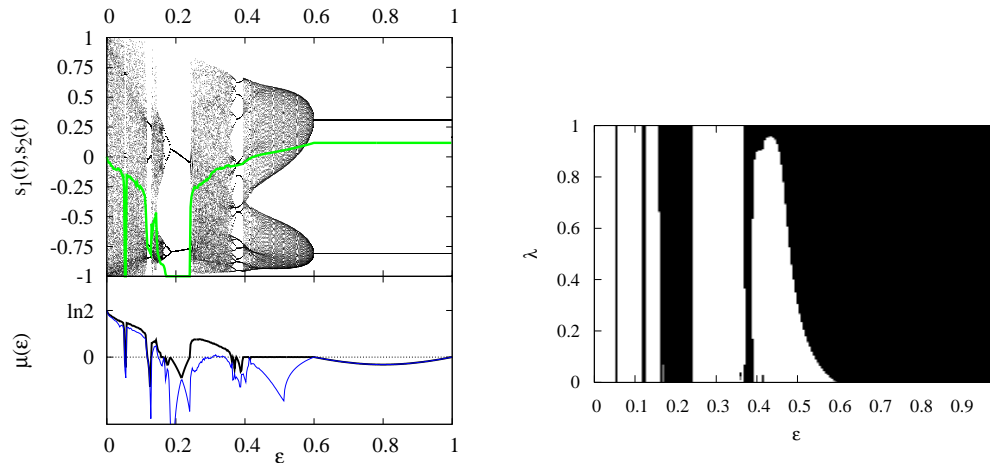


Figure 9.4: Same as Fig. 9.3, but for the $2B$ dynamics.

9 Cluster synchronization

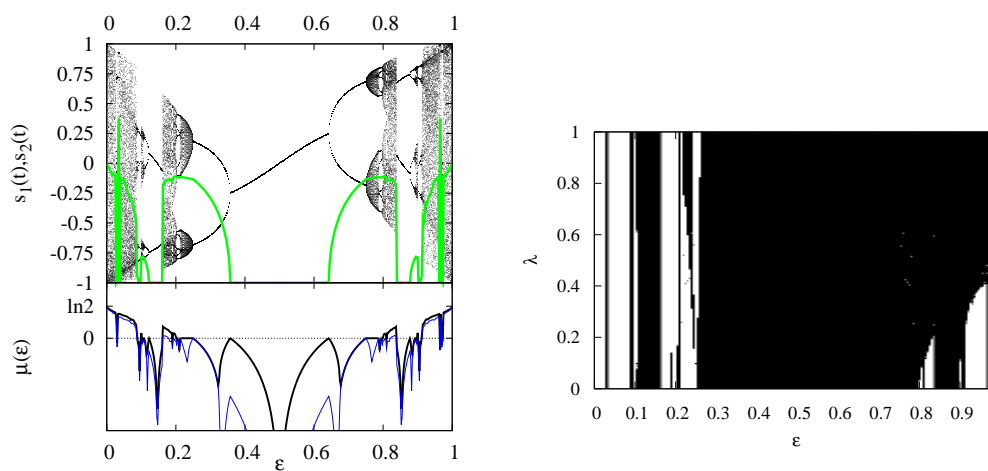


Figure 9.5: Same as Fig. 9.3, but for the $2A^-$ dynamics.

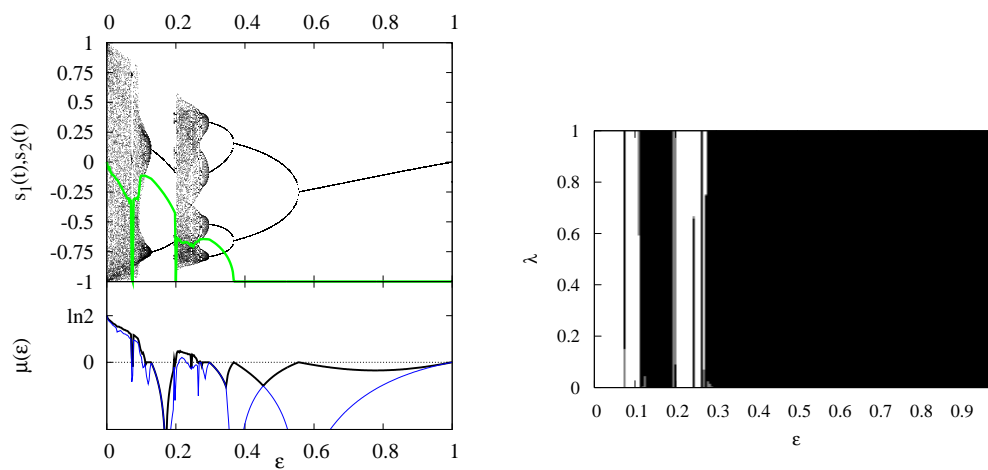


Figure 9.6: Same as Fig. 9.3, but for the $2B^-$ dynamics.

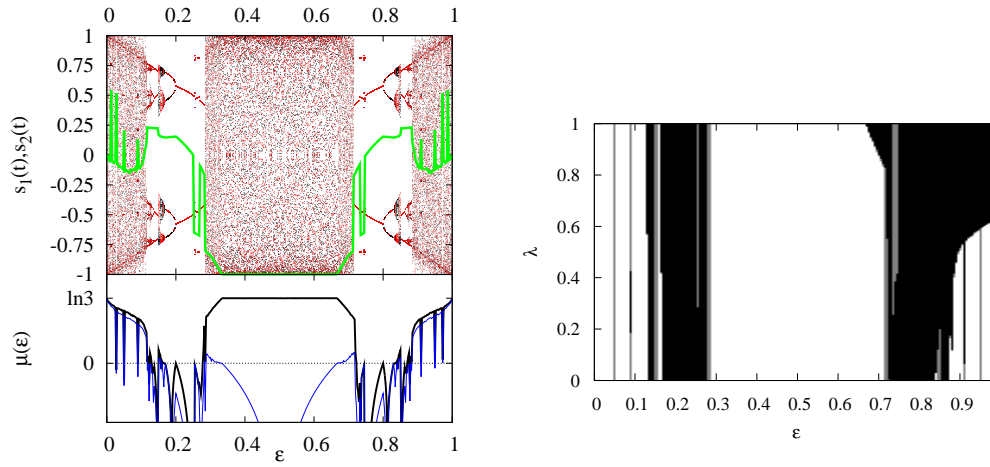


Figure 9.7: Similar as Fig. 9.3, but for the 3A dynamics. Since the synchronized solution \mathbf{h}_ϵ shows a symmetry for $\mathbf{s} \rightarrow (-\mathbf{s})$, the phase portrait is shown for two trajectories which differ by the sign.

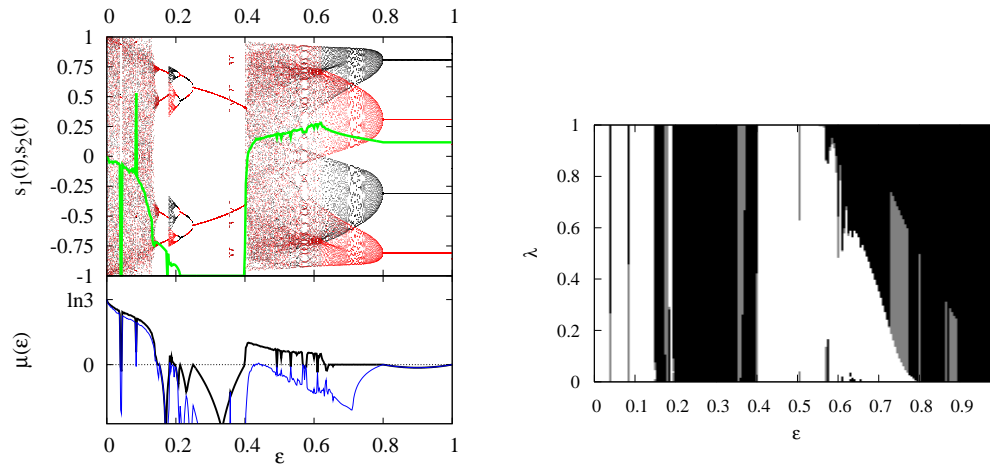


Figure 9.8: Same as Fig. 9.7, but for the 3B dynamics.

10 Conclusion

The main topic of this thesis is the investigation of dynamical properties of coupled Tchebycheff map networks. At every node of the network the dynamics is given by the iteration of a Tchebycheff map, which shows strongest possible chaotic behaviour [17]. By applying a coupling between the various individual dynamics along the links of the network, a rich structure of complex dynamical patterns emerges. Accordingly, coupled chaotic map networks provide prototypical models for studying the interplay between local dynamics, network structure, and the emergent global dynamics. Apart from being of major interest in the theory of dynamical systems and the science of complex networks, there are also various applications for these systems, including models for turbulence, pattern formation or synchronization [69, 70]. An exciting application of coupled Tchebycheff map lattices in quantum field theory has been proposed in Ref. [17] by Beck. In the so-called chaotic string model, the coupled map lattice dynamics generates the noise needed for the Parisi-Wu approach of stochastic quantization. The remarkable observation is that the respective dynamics seems to reproduce distinguished numerical values of coupling constants that coincide with those observed in the standard model of particle physics [16, 17]. Although the physical embedding proposed by Beck in Refs. [16, 17, 20, 21] does not provide a complete theory relating particle physics to coupled map lattices, due to its numerical results the chaotic string model deserves further attention.

The results of this thesis give insights into the chaotic string model and its network generalization from a dynamical point of view. This leads to a deeper understanding of the dynamics, which is essential for a critical discussion of possible physical embeddings. Apart from this specific application to particle physics, the investigated concepts like synchronization or a most random behaviour of the dynamics are of general interest for dynamical system theory and the science of complex networks.

Discrete symmetries of coupled Tchebycheff map networks are discussed in Chap. 4. The construction of the chaotic string model in Ref. [17] leads to a total number of 16 different dynamics based on first and second order Tchebycheff polynomials. By symmetry arguments, in Ref. [17] this number was reduced to six dynamics. The results of Chap. 4 confirm this finding by giving a detailed analysis of discrete symmetry transformations. These transformations are formulated in a general way in order to be also applicable to similar dynamics on bipartite network structures. The class of bipartite networks consists of structures, which are build up by two set of nodes with links only between nodes from different sets, respectively. It is straightforward to expand this notion to dynamics on r -partite networks, which then

will show more complicated transformational symmetries. It would be interesting to study these generalized symmetries and the impact of a potential symmetry breaking on the dynamics.

An observable of main interest in the chaotic string model is the interaction energy. In Ref. [17] it is observed that certain chaotic string couplings, corresponding to a vanishing interaction energy, coincide with coupling constants of the standard model of elementary particle physics. Since the interaction energy is basically a spatial correlation measure, an interpretation of the respective dynamical states in terms of a most random behaviour is tempting. Such an interpretation would provide a dynamical principle to distinguish certain dynamics in a more general way. A presumed most random behaviour as the guiding principle is particularly attractive in connection with a possible physical embedding of the dynamics as generating the noise of the Parisi-Wu approach to stochastic quantization (see Ref. [17, 21] for details). The interaction energy is only one specific spatial correlation measure and thus gives limited information about the dynamics. In order to distinguish certain states as ‘most random’, or evoke another dynamical principle, a deeper understanding beyond this measure is essential.

A first approach is taken in Chap. 5. Although the interaction energy is defined locally for all pairs of coupled nodes in the ring-network, in order to provide better statistics, in Ref. [17] the spatial average of this measure over all nodes is performed. The results presented in Sec. 5.1 show that this procedure in general yields misleading results. For a wide range of coupling values, the dynamics show non-ergodic behaviour, and observables depend on the node in the network and the initial conditions. In particular, two zeros of the interaction energy stated in Ref. [17] turn out to be the result of this spatial average instead of a vanishing interaction energy for every coupled pair of nodes. Accordingly, these zeros should be omitted from consideration as being connected to standard model couplings. Since the physical interpretation of the corresponding coupling values has been far less obvious than for the remaining zeros, this exclusion is actually in favor for the chaotic string model. For the remaining six interesting zeros, an ergodic behaviour with locally vanishing interaction energy is observed, so the respective results of Ref. [17] remain valid from a dynamical system point of view. In Sec. 5.2 these six zeros of the interaction energy are computed numerically with high precision, and the respective results of Ref. [17] are confirmed.

Chapter 6 assesses the notion of a most random behaviour of the dynamics by considering various observables beyond the interaction energy of Ref. [17]. In Sec. 6.2 the chaoticity of the dynamics is estimated by three measures based on the Lyapunov spectrum of the system, which characterizes the separation of infinitesimally close orbits. These are the maximum Lyapunov exponent, the net-average of positive Lyapunov exponents, and the Lyapunov dimension. All measures show a maximum for uncoupled chaotic dynamics and a minimum for a stable fixed point, and thus are suitable for estimating the chaoticity of the dynamics. For larger couplings a large part or even all of the Lyapunov exponents are non-positive, which means that there are numerous directions in the phase space in which the dynamics is non-chaotic. For small couplings it is found that all Lyapunov exponents are positive, thus indicating

strong chaotic behaviour. The zeros of the interaction energy connected to standard model couplings (those which have not been excluded from consideration due to non-ergodic behaviour) are situated in this low coupling region. However, the respective couplings are not distinguished by the Lyapunov measures, which monotonically decrease with increasing coupling. Consequently, with respect to Lyapunov measures there is no indication of a most random or most chaotic behaviour of the dynamics for these couplings.

Whereas the Lyapunov spectrum characterizes the spatio-temporal behaviour of the dynamics, the interaction energy is a purely spatial correlation measure, which does not account for temporal correlations. Accordingly, a possibility to keep the dynamical principle of a most-random behaviour would be to refer to spatial correlations only. The results of Sec. 6.3 contradict this interpretation. Other spatial correlation measures like higher order cumulants and the mutual information do not distinguish the coupling values corresponding to a vanishing interaction energy. For the dynamics based on second order Tchebycheff polynomials, the first order cumulant vanishes for other couplings values than the interaction energy, so the respective zeros are shifted and an interpretation as standard model couplings is not possible. The zeros of the first order cumulant and the interaction energy coincide for the dynamics based on third order Tchebycheff polynomials. However, higher order cumulants do not vanish for these couplings. Also the mutual information does not show a distinguished behaviour for the zeros of the interaction energy.

The results of Chap. 6 contradict an interpretation of the dynamics in terms of a most random behaviour. The respective states corresponding to a vanishing interaction energy are distinguished by this specific measure only, but not by a more general dynamical principle. As a consequence, the model proposed by Beck in Ref. [17] should provide strong physical motivation for this observable, and cannot rely on an interpretation in terms of a most random dynamics.

The chaotic string model is defined on a one-dimensional lattice (ring-network) as the underlying network topology. Chapter 7 studies a modification of the model based on the introduction of tunable disorder. The effects of inhomogeneous coupling weights as well as small-world perturbations of the ring-network structure on the interaction energy are discussed. It is observed that certain combinations of coupling and network disorder preserve the empirical relationship between the chaotic string couplings and the running coupling constants of the standard model of elementary particle physics. For the zero of the interaction energy associated with the electromagnetic coupling it has been found that already a small disorder pushes the associated energy scale of the running coupling constant far away from the result without disorder.

Synchronization properties of the chaotic string model and its network generalization are studied in Chaps. 8 and 9. The analysis is based on the master stability formalism, which relates the stability of the synchronized state to the spectral properties of the network [96]. Chapter 8 considers complete synchronization, where the dynamics at all nodes of the network coincide. Two-cluster synchronization on bipartite networks is studied in Chap. 9. For both types of synchronization it is shown that

depending on the type of coupling the synchronized dynamics can display chaotic as well as periodic or quasi-periodic behaviour. The semi-analytical calculations reveal that the respective synchronized states are often stable for a wide range of coupling values even for the ring-network, although the respective basins of attraction may inhabit only a small fraction of the phase space. To provide analytical results in closed form, for complete synchronization the stability of all fixed points and period-2 orbits of all chaotic string networks are determined analytically. The master stability formalism allows to treat the ring-network of the chaotic string model as a special case, but the results are valid for coupled Tchebycheff maps on arbitrary networks. For two-cluster synchronization on bipartite networks, selected fixed points and period-2 orbits are analyzed.

The results of Chaps. 8 and 9 provide insights into the chaotic string dynamics beyond the numerical results obtained in earlier works. These findings are not only relevant for this application of coupled map networks, but for network synchronization in general.

There are several interesting topics which can be addressed using methods and concepts from this work. In Chap. 6, the various Lyapunov measures and higher order cumulants were calculated for the chaotic string model. It would be interesting to perform similar studies on general network topologies, and thus investigate the connection between network structure and chaoticity of the dynamics. Another interesting topic would be the application of the methods used in Chap. 8 and 9 to the disordered ring-like networks of Chap. 7. This would provide insights into the question, whether the synchronizability of networks is reduced or enhanced by disorder. A similar problem could be addressed by methods based on the formalism presented in Chap. 9. Up to now, the analysis is applied to two-cluster synchronization on bipartite networks. But what happens, if the bipartite structure is perturbed by additional links? Does the two-cluster synchronization survive as a ‘fuzzy’ synchronized state, or do new patterns emerge? It would also be interesting to realize the perturbations of the network topology in a way that create distinguished patterns (called ‘motifs’) in the network, and investigate the effects which these local structural patterns leave on the global dynamics. Other possible future topics include the introduction of coupling delays and non-identical local dynamics.

With respect to the chaotic string model as proposed by Beck in Ref. [17], the present work provides various results from a dynamical system point of view. The findings on symmetries, ergodicity, chaoticity, effect of disorder and synchronization properties have to be considered for any physical embedding and interpretation of the model.

A Publications

Parts of the Chaps. 4 and 5 have been published as a peer reviewed article [102]. An article based on Chap. 7 has been accepted for publication.

During the preparation of this thesis, the author contributed to Ref. [54]. For completeness, this publication is also included facsimile here.

Robustness of networks against fluctuation-induced cascading failures

Dominik Heide,^{1,*} Mirko Schäfer,^{1,†} and Martin Greiner^{2,‡}

¹Frankfurt Institute for Advanced Studies and Frankfurt International Graduate School for Science, Johann Wolfgang Goethe Universität, Ruth-Moufang-Straße 1, D-60438 Frankfurt am Main, Germany

²Corporate Technology, Information & Communications, Siemens AG, D-81730 München, Germany

(Received 9 November 2007; published 8 May 2008)

Fluctuating fluxes on a complex network lead to load fluctuations at the vertices, which may cause them to become overloaded and to induce a cascading failure. A characterization of the one-point load fluctuations is presented, revealing their dependence on the nature of the flux fluctuations and on the underlying network structure. Based on these findings, an alternate robustness layout of the network is proposed. Taking load correlations between the vertices into account, an analytical prediction of the probability for the network to remain fully efficient is confirmed by simulations. Compared to previously proposed mean-flux layouts, the alternate layout comes with significantly less investment costs in the high-confidence limit.

DOI: 10.1103/PhysRevE.77.056103

PACS number(s): 89.75.Hc, 02.50.Fz, 89.75.Da

I. INTRODUCTION

Much of the infrastructure of modern societies is organized in complex networks. A failure may lead to dramatic consequences. It is important to understand the properties and vulnerabilities of these networks. Error and attack tolerance against random and intentional removal of vertices and links has already been widely studied [1–8]. Also dynamical failures have been discussed [9–15], where a component failure and a subsequent network-wide redistribution of loads might trigger further cascading failures.

A simple network model to describe a cascading failure has been put forward by [9]. Every vertex i of the network $G=(\mathcal{V},\mathcal{E})$, described by the sets of vertices \mathcal{V} and edges \mathcal{E} , sends a unit flux $s_{if}=1$ to every other vertex $f\neq i$ along the shortest-hop paths $[i\rightarrow f]$. This results in an accumulated vertex load

$$L_v = \frac{1}{N(N-1)} \sum_{i,f\in\mathcal{V}} r_{sp}([i\rightarrow f];v) s_{if}. \quad (1)$$

The value of the path function $r_{sp}([i\rightarrow f];v)$ is either 1 or 0, depending on whether the vertex v is part of the shortest-hop path from vertex i to f or not [16]. Based on the load (1), the capacities

$$C_v(\alpha) = (1 + \alpha)\langle L_v \rangle \quad (2)$$

are assigned to the vertices. If for some reason one or more vertices fail, a network-wide redistribution of the loads (1) occurs due to a modification of the shortest paths. The new load L_v of vertex v may become larger than its capacity C_v and subsequent failures can occur. This sequence of events is referred to as a cascading failure. In order to reduce or ideally prevent the occurrence of such cascading failures, other capacity layouts have been proposed [15,17] besides (2). So far, all of these approaches have one thing in common. They

assume the flux matrix s_{if} to be uniform and constant. There are many interesting examples where this is not the case. In communication and transportation networks s_{if} is known as the traffic matrix which is subject to temporal fluctuations. Electricity networks with a large share of renewable power generation come with strongly fluctuating source fluxes. More fluctuations in electricity networks are introduced by power exchange markets.

There is a strong need to study the impact of fluctuating fluxes on the robustness of networks. Vertices may fail either directly due to an accumulation of extreme flux fluctuations or due to a subsequent overload cascade. Immediate questions that arise are: How does an efficient capacity layout look, which is able to cope with the fluctuating fluxes? Given various classes of fluctuating fluxes, how do they determine the resulting fluctuations in the accumulated vertex loads? Are there correlations between the accumulated loads of different vertices and how do they look? In the following we will give answers to these important questions.

II. LOAD FLUCTUATIONS RESULTING FROM FLUX FLUCTUATIONS

Flux fluctuations are introduced into the modeling (1) by varying the strengths s_{if} according to some distribution. For demonstration, we pick a lognormal distribution with mean $\langle s \rangle = 1$. The fluctuation strength is defined as its standard deviation $\sigma = \sqrt{\langle (s-1)^2 \rangle}$. We distinguish two fluctuation scenarios. The first is denoted as pathlike, where all s_{if} are drawn independently from each other. For the second, which we denote as sourcelike, all $s_{if}=s_i$ belonging to the same source vertex i are given the same value sampled from the lognormal distribution.

In order to develop a new capacity layout beyond the mean-flux case (2), a good understanding is needed on how the flux fluctuations determine the load distributions across the network. We begin by looking at the one-point distribution $p_v(L_v)$. Expression (1) can be read as a weighted sum of independently and identically distributed random fluxes s_{if} . In the case of lognormal fluxes with small fluctuation strengths $\sigma \lesssim 1$, this sum can be approximated again by a

*dheide@fias.uni-frankfurt.de

†schaef@fias.uni-frankfurt.de

‡martin.greiner@siemens.com

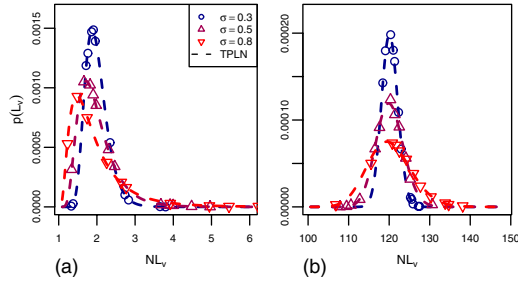


FIG. 1. (Color online) Simulated load distributions $p(L_v)$ due to sourcelike flux fluctuations for three fluctuation strengths. Two vertices with minimum (a) and maximum (b) load are depicted. One typical realization of a random scale-free network, for which the number of vertices, scale-free exponent, and minimum degree have been set to $N=1000$, $\gamma=2.5$ and $k_{\min}=2$, has been used with 10^4 fluctuation realizations. The dashed curves correspond to the three-parameter lognormal distribution (TPLN, 3) with predicted parameters (4) and (5).

lognormal distribution [18]. To allow for some more flexibility we choose a three-parameter generalization of the lognormal distribution

$$p_v(L_v) = \frac{1}{\sqrt{2\pi}\eta(L_v - \kappa_v)} \exp\left[-\frac{(\ln[L_v - \kappa_v] - \mu_v)^2}{2\eta_v^2}\right] \quad (3)$$

for the description of the load distribution. To fit the load distribution at vertex v , the three parameters μ_v, η_v, κ_v are calculated from the first three cumulants of Eq. (3) which have to be equal to the first three cumulants of the load (1). These are for pathlike fluxes

$$\langle L_v^n \rangle_c = \langle s^n \rangle_c \sum_{i \neq j=1}^N \left(\frac{r_{sp}([i \rightarrow j]; v)}{N(N-1)} \right)^n, \quad (4)$$

and for sourcelike fluxes

$$\langle L_v^n \rangle_c = \langle s^n \rangle_c \sum_{i=1}^N \left(\sum_{f=1(f \neq i)}^N \frac{r_{sp}([i \rightarrow f]; v)}{N(N-1)} \right)^n. \quad (5)$$

Figure 1 compares the predicted three-parameter lognormal distribution (3)–(5) with simulated one-point load distributions, which have been sampled from a large number of independent flux fluctuation realizations on a typical random scale-free network. For pathlike (not shown) as well as sourcelike flux fluctuations and for all vertices ranging from minimum to maximum average load, the analytical distributions fit the numerical data very well. Note that the one-point load distribution (3) needs not to be mixed up with the distribution $p(\langle L_v \rangle)$ of average loads across all vertices of the network. For the latter we reproduce the result $p(\langle L \rangle) \sim \langle L \rangle^{-\delta}$ with $\delta \approx 2.2$, which has been shown [19] to be universal for all scale-free networks with exponent $2 < \gamma \leq 3$.

The $n=2$ cumulants of Eqs. (4) and (5) are depicted in Fig. 2 as a function of the averaged vertex loads. For pathlike flux fluctuation (inset in Fig. 2) a scaling relation of the type $\sqrt{\langle L_v^2 \rangle_c} \sim \langle L_v \rangle^\beta$ is found with exponent $\beta=0.5$. This disper-

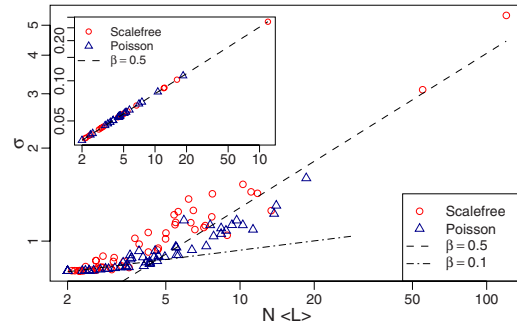


FIG. 2. (Color online) The moment $\sigma(L_v) = \sqrt{\langle L_v^2 \rangle_c}$ of Eqs. (4) and (5) as a function of the average vertex load $\langle L_v \rangle$ for one realization of pathlike (inset) and sourcelike fluctuations on random scale-free (circles) and Poisson (triangles) networks. Parameters are $N=1000$, $\gamma=2.5$, $k_{\min}=2$ for the scale-free networks, and $N=1000$, $\langle k \rangle=5$ for the Poisson networks. Fifty out of 10^3 vertices are shown. The dashed and dashed-dotted straight lines represent the scaling exponents $\beta=0.5$ and 0.1 .

sion relation has already been observed in [20] and related to internal collective dynamics on the network. However, it has not been clear whether the found value of the scaling exponent is universal or not. For sourcelike flux fluctuations no good overall scaling is observed. This is due to the fact that only the load distribution for high average loads are Gaussian shaped, whereas load distributions of vertices with small loads have a long tail that increases the variance; consult again Fig. 1. The asymptotic high or low load regimes are in accordance with $\beta=0.5$ and 0.1 , respectively, indicating that the scaling exponent $\beta \approx 0.5$ is not universal.

III. EFFICIENT CAPACITY LAYOUT

The good agreement of the predicted three-parameter lognormal distributions with the vertex loads allows for a direct construction of a new capacity layout, which is robust against the flux fluctuations up to some confidence level. For a single vertex the quantile

$$q = \int_0^{C_v} p_v(L_v) dL_v = F_v(C_v) \quad (6)$$

describes the confidence level that its load L_v remains smaller than its capacity C_v . Since $1-q$ describes the probability that the vertex will fail due to direct overloading, a confidence level very close to one is desirable. A typical value in engineering is $q=0.9999$. By presetting the confidence level to such a targeted value, the capacity $C_v(q) = F_v^{-1}(q)$ needed at the vertex is obtained from the inverse of the cumulative distribution function F_v . Since $p_v(L_v)$ is three-parameter lognormal, F_v can be expressed in terms of the inverse of the cumulative distribution function Φ of a centered normal distribution with unit variance. This leads to the capacity assignment

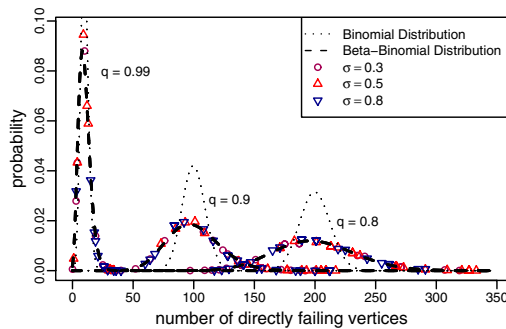


FIG. 3. (Color online) Probability distributions for the number of directly failing vertices due to sourcelike flux fluctuations in a scale-free network. Network parameters are as in the previous figures. 10^4 flux realizations have been used for various fluctuation strengths. The distributions only depend on the quantile (6): $q = 0.8$ (right), 0.9 (center), and 0.99 (left). The dotted and dashed curves correspond to binomial and beta-binomial distributions with the same mean $(1-q)N$. The correlation parameter ρ of the beta-binomial distribution has been calculated with Eqs. (9) and (10).

$$C_v(q) = e^{\eta_v \Phi^{-1}(q) + \mu_v} + \kappa_v. \quad (7)$$

In principle, different q values could be assigned to different vertices, but for simplicity we chose the same q for all vertices.

By this construction, the distribution of the number of directly failing vertices M due to the fluctuating fluxes will have a mean of $\langle M \rangle = (1-q)N$. As can be seen in Fig. 3 the actual number may deviate much from this mean. Note that the shown distributions only depend on the quantile q and not on the strength of the flux fluctuations. The distributions would be binomial if the direct failure of a vertex were independent of the other vertices, however, this is not the case. The probabilities of directly failing vertices are correlated since all vertices on a shortest path receive the same flux strength from the transmitting vertex.

A good approximation to the observed distributions is provided by the beta-binomial distribution

$$p(M; a, b) = \binom{N}{M} \frac{B(M+a, N-M+b)}{B(a, b)}, \quad (8)$$

where $B(\cdot, \cdot)$ is the beta function. It is known to describe correlated Bernoulli random variables [21]. The two parameters a and b can be rewritten as the mean $\langle M \rangle / N = (1-q) = \frac{a}{a+b}$ and the correlation measure $\rho = \frac{1}{a+b+1}$. From best fits of Eq. (8) to the distributions of Fig. 3 we find the empirical relation

$$\rho = \omega_N (1-q)^\xi, \quad (9)$$

(see Fig. 4). Within acceptable precision the exponent ξ turns out to be independent of the network size. For ω_N the N dependence

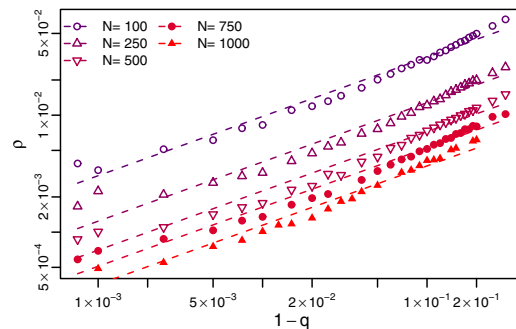


FIG. 4. (Color online) Relation between the parameters ρ and $(1-q)$ of the beta-binomial distributions (8), which have been directly fitted to the sampled distributions of Fig. 3.

$$\omega_N = \omega N^{-\nu} \quad (10)$$

is found. The following table lists the fitted parameter values for pathlike and sourcelike flux fluctuations on scale-free ($\gamma=2.5$, $k_{\min}=2$) as well as Poisson networks ($\langle k \rangle=5$).

Path	ω	ξ	ν	Source	ω	ξ	ν
Poisson	1.50	0.53	0.80	Poisson	5.40	0.70	0.80
Scale-free	1.47	0.41	0.80	Scale-free	3.34	0.51	0.80

The good description by the beta-binomial distribution (8) allows one to make an analytical prediction of the probability that with the capacity layout (7) no vertex of the network will fail due to flux fluctuations. This probability $p(M=0; 1-q, \rho)$ with ρ from Eqs. (9) and (10) is equal to the probability that the network efficiency [6]

$$E = \frac{1}{N(N-1)} \sum_{i \neq f \in V} \frac{1}{d_{if}} \quad (11)$$

remains equal to its initial value E_0 of the intact network, thus $p(\frac{E}{E_0}=1) = p(M=0; 1-q, \rho)$. The network efficiency represents a measure to evaluate the quality of a capacity layout. It includes direct as well as cascading failure of vertices. d_{if} is the shortest-hop distance between vertices i and f . Figure 5 compares the predicted $p(M=0; 1-q, \rho)$ with numerical data.

Since the correlation ρ of the beta-binomial distribution goes to zero as q goes to one, the probability $p(\frac{E}{E_0}=1)$ can also be approximated using the binomial distribution $p_{bin}(M=0; 1-q)$; see again Fig. 5. This gives a parameter-free approximation to the probability that no vertex fails. The same relation also holds for pathlike flux fluctuations.

Finally, we compare the investment costs $I = \sum_{v \in V} C_v = I(\alpha) = I(q)$ relative to $I_0 = \sum_{v \in V} \langle L_v \rangle$ of the two capacity layouts (2) and (7). These are functions of the tolerance parameter α and the quantile q , respectively. Figure 6 shows the efficiency (11) of a scale-free network as a function of I . For sourcelike flux fluctuations the efficiency of Eq. (7) remains close to zero up to a critical investment cost, only then to jump up and to overtake the efficiency of Eq. (2). In the limit

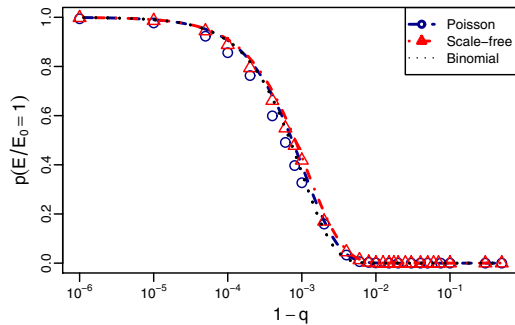


FIG. 5. (Color online) Probability for the relative efficiency to remain $\frac{E}{E_0}=1$ given the capacity layout (7) against sourcelike flux fluctuations. The symbols have been determined from a simulation of 10^3 fluctuation realizations with strength $\sigma=0.5$ on a representative random scale-free (triangles) and Poisson (circles) network of size $N=1000$ (other parameters as stated before). The dashed and dotted curves represent the analytical prediction based on the beta-binomial distribution (8) and the binomial simplification, respectively.

$E/E_0 \rightarrow 1$ the investment costs into the newly proposed capacity layout (7) are significantly smaller than for the standard layout (2). For pathlike flux fluctuations both capacity layouts reveal an abrupt transition from low to high efficiency at very low investment costs.

IV. CONCLUSION

A robust capacity layout has been developed. It is able to cope with the load fluctuations induced by flux fluctuations transported on the network. Within a given confidence level it supports the network to operate at full efficiency and guar-

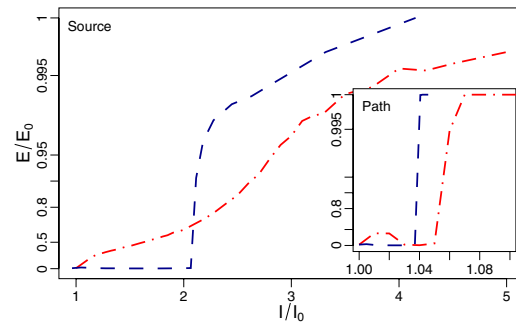


FIG. 6. (Color online) Relative efficiency of a typical $N=1000$ scale-free network as a function of investment costs against direct vertex failures as well as subsequent cascading failures induced by pathlike (inset) and sourcelike fluctuations of strength $\sigma=0.8$. Dashed-dotted and dashed curves represent the capacity layouts (2) and (7), respectively. All curves come with a confidence level of 0.99, meaning that 10 out of the simulated 10^3 fluctuation realizations result in relative efficiencies below the curve.

antees robustness against a cascading failure. Since these findings have been based on a simple network model [9], it will make sense to discuss various model extensions, such as those proposed in Refs. [22–24], which distinguish between internal and external fluctuation dynamics. The ultimate challenge will be to carry over these ideas to real-life infrastructure networks such as, for example, electricity networks facing a growing fraction of fluctuating renewable energy sources.

ACKNOWLEDGMENTS

We gratefully acknowledge support by the Frankfurt Center for Scientific Computing and thank Jan Scholz and Clemens Hoffmann for valuable comments.

- [1] R. Albert, H. Jeong, and A.-L. Barabási, *Nature (London)* **406**, 378 (2000).
- [2] R. Cohen, K. Erez, D. ben-Avraham, and S. Havlin, *Phys. Rev. Lett.* **85**, 4626 (2000).
- [3] D. S. Callaway, M. E. J. Newman, S. H. Strogatz, and D. J. Watts, *Phys. Rev. Lett.* **85**, 5468 (2000).
- [4] R. Cohen, K. Erez, D. ben-Avraham, and S. Havlin, *Phys. Rev. Lett.* **86**, 3682 (2001).
- [5] A. E. Motter, T. Nishikawa, and Y. C. Lai, *Phys. Rev. E* **66**, 065103(R) (2002).
- [6] P. Crucitti, V. Latora, M. Marchiori, and A. Rapisarda, *Physica A* **320**, 622 (2003).
- [7] R. Albert, I. Albert, and G. L. Nakarado, *Phys. Rev. E* **69**, 025103(R) (2004).
- [8] L. K. Gallos, R. Cohen, P. Argyrakis, A. Bunde, and S. Havlin, *Phys. Rev. Lett.* **94**, 188701 (2005).
- [9] A. E. Motter, and Y. C. Lai, *Phys. Rev. E* **66**, 065102(R) (2002).
- [10] A. E. Motter, *Phys. Rev. Lett.* **93**, 098701 (2004).
- [11] P. Crucitti, V. Latora, and M. Marchiori, *Phys. Rev. E* **69**, 045104(R) (2004).
- [12] P. Crucitti, V. Latora, and M. Marchiori, *Physica A* **338**, 92 (2004).
- [13] R. Kinney, P. Crucitti, R. Albert, and V. Latora, *Eur. Phys. J. B* **46**, 101 (2005).
- [14] E. J. Lee, K. I. Goh, B. Kahng, and D. Kim, *Phys. Rev. E* **71**, 056108 (2005).
- [15] M. Schäfer, J. Scholz, and M. Greiner, *Phys. Rev. Lett.* **96**, 108701 (2006).
- [16] In the case of shortest-path degeneracy, the value of the path function is reduced by a factor depending on the degrees and depths of the respective branching points.
- [17] P. Li, B. H. Wang, H. Sun, P. Gao, and T. Zhou, *Eur. Phys. J. B* **62**, 101 (2008).
- [18] M. Romeo, V. Da Costa, and F. Bardou, *Eur. Phys. J. B* **32**, 513 (2003).
- [19] K.-I. Goh, B. Kahng, and D. Kim, *Phys. Rev. Lett.* **87**, 278701 (2001).

- [20] M. A. de Menezes and A.-L. Barabási, Phys. Rev. Lett. **92**, 028701 (2004).
- [21] M. Hisakado and S. Kitsukawa, J. Phys. A **39**, 15365 (2006).
- [22] A.-L. Barabási, M. A. de Menezes, S. Balensiefer, and J. Brockman, Eur. Phys. J. B **38**, 169 (2004).
- [23] Z. Eisler, J. Kertész, S.-H. Yook, and A.-L. Barabási, Europhys. Lett. **69**, 664 (2005).
- [24] S.-H. Yook and M. A. de Menezes, Europhys. Lett. **72**, 541 (2005).

Bibliography

- [1] J.A. Acebrón, L.L. Bonilla, C.J. Pérez Vicente, F. Ritort, and R. Spigler. The kuramoto model: A simple paradigm for synchronization phenomena. *Reviews of Modern Physics*, 77(1):137–185, 2005.
- [2] R. Albert and A.-L. Barabási. Statistical mechanics of complex networks. *Reviews of Modern Physics*, 74(1):47–97, 2002.
- [3] K.T. Alligood, T.D. Sauer, and J.A. Yorke. *Chaos – An Introduction to Dynamical Systems*. Springer, 1996.
- [4] R.E. Amritkar, S. Jalan, and C.-K. Hu. Synchronized clusters in coupled map networks. II. stability analysis. *Physical Review E*, 72:016212, 2005.
- [5] C. Amsler and others (Particle Data Group). Review of particle physics. *Physics Letters*, 667(1), 2008.
- [6] C. Anteneodo, A.M. Batista, and R.L. Viana. Synchronization threshold in coupled logistic map lattices. *Physica D*, 223:270–275, 2006.
- [7] A. Arenas, A. Diaz-Guilera, J. Kurths, Y. Moreno, and C. Zhou. Synchronization in complex networks. *Physics Reports*, 469:93–153, 2008.
- [8] A. Balanov, N. Janson, D. Postnov, and O. Sosnovtseva. *Synchronization: From Simple to Complex*. Springer Series in Synergetics. Springer, 2009.
- [9] A. Banerjee and J. Jost. On the spectrum of the normalized graph laplacian. *Linear Algebra and its Applications*, 428:3015, 2008.
- [10] M. Barahona and L.M. Pecora. Synchronization in small-world systems. *Physical Review Letters*, 89(5):054101, 2002.
- [11] A.M. Batista and R.L. Viana. Lyapunov exponents of a lattice of chaotic maps with a power-law coupling. *Physics Letters A*, 286:134–140, 2001.
- [12] F. Bauer, F.M. Atay, and J. Jost. Synchronization in discrete-time networks with general pairwise coupling. *Nonlinearity*, 22:2333–2351, 2009.
- [13] F. Bauer, F.M. Atay, and J. Jost. Synchronized chaos in networks of simple units. *Europhysics Letters*, 89:20002, 2010.

Bibliography

- [14] C. Beck. Higher order correlation functions of chaotic maps: A graph theoretical approach. *Nonlinearity*, 4:1131, 1991.
- [15] C. Beck. Chaotic quantization of field theories. *Nonlinearity*, 8:423–441, 1995.
- [16] C. Beck. Chaotic strings and standard model parameters. *Physica D*, 171:72, 2002.
- [17] C. Beck. *Spatio-Temporal Chaos and Vacuum Fluctuations of Quantized Fields*, volume 21 of *Advanced Series in Nonlinear Dynamics*. World Scientific, 2002.
- [18] C. Beck. Chaotic scalar fields as models for dark energy. *Physical Review D*, 69:123515, 2004.
- [19] C. Beck. Nonextensive scalar field theories and dark energy models. *Physica A*, 340:459–466, 2004.
- [20] C. Beck. Dark energy, chaotic fields, and fundamental constants. In B.G. Sidharth, F. Honsell, and A. de Angelis, editors, *Frontiers of Fundamental Physics*, 2006.
- [21] C. Beck. Complexity of chaotic fields and standard model parameters. In *The Logic of Nature, Complexity and New Physics: From Quark-Gluon Plasma to Superstrings, Quantum Gravity and Beyond*, volume 44 of *The Subnuclear Series*. World Scientific, 2007.
- [22] C. Beck and F. Schlögl. *Thermodynamics of Chaotic Systems*, volume 4 of *Cambridge Nonlinear Science Series*. Cambridge University Press, 1993.
- [23] I. Belykh, V. Belykh, K. Nevidin, and M Hasler. Persistent clusters in lattices of coupled nonidentical chaotic systems. *Chaos*, 13:165–178, 2003.
- [24] V.N. Belykh, G.V. Osipov, V.S. Petrov, and J.A.K. Suykens. Cluster synchronization modes in an ensemble of coupled chaotic oscillators. *Chaos*, 18:037106, 2008.
- [25] S. Bethke. The 2009 world average of α_s . *European Physical Journal C*, 64:689, 2009.
- [26] S. Boccaletti. *The Synchronized Dynamics of Complex Systems*, volume 6 of *Monograph Series on Nonlinear Science and Complexity*. Elsevier, 2008.
- [27] S. Boccaletti, J. Kurths, G. Osipov, D.L. Valladares, and C.S. Zhou. The synchronization of chaotic systems. *Physic Reports*, 366:1–101, 2002.
- [28] S. Boccaletti, V. Latora, Y. Moreno, and M. Chavez and. D.-U. Hwang. Complex networks: Structure and dynamics. *Physic Reports*, 424:175–308, 2006.

- [29] T. Bohr and M.H. Jensen. *Dynamical Systems Approach to Turbulence*. Cambridge University Press, 1998.
- [30] L.A. Bunimovich. Coupled map lattices: Some topological and ergodic properties. *Physica D*, 103:1–17, 1997.
- [31] L.A. Bunimovich and Y.G. Sinai. Spacetime chaos in coupled map lattices. *Nonlinearity*, 1:491–516, 1988.
- [32] R.N. Cahn. The eighteen arbitrary parameters of the standard model in your everyday life. *Reviews of Modern Physics*, 68(3):951–959, 1996.
- [33] R. Carretero-Gonzalez, S.Orstavik, J. Huke and. D.S. Broomhead, and J. Stark. Thermodynamic limit from small lattices of coupled maps. *Physical Review Letters*, 83(18):3633, 1999.
- [34] R. Carvalho, B. Fernandez, and R. Vilela Mendes. From synchronization to multistability in two coupled quadratic maps. *Physics Letters A*, 285:327–338, 2001.
- [35] F. R. K. Chung. *Spectral Graph Theory*. American Mathematical Society, 1997.
- [36] P. Collet and J.-P. Eckmann. *Iterated Maps of the Interval as Dynamical Systems*. Birkhäuser, 1980.
- [37] J.P. Crutchfield and K. Kaneko. Phenomenology of spatio-temporal chaos. In J. Bai-lin, editor, *Directions in Chaos*. World Scientific Publishing Co., 1987.
- [38] C.P. Dettmann. Stable synchronised states of coupled tchebyscheff maps. *Physica D*, 172:88–102, 2002.
- [39] R.L. Devaney. *An Introduction to Chaotic Dynamical Systems*. Addison-Wesley, second edition, 1989.
- [40] R. Diestel. *Graph Theory*. Springer, third edition, 2005.
- [41] L. Donetti, P.I. Hurtado, and M. A. Munoz. Entangled networks, synchronization and optimal network topology. *Physical Review Letters*, 95:188701, 2005.
- [42] S.N. Dorogovtsev and J.F.F. Mendes. *Evolution of Networks*. Oxford University Press, 2003.
- [43] A.M. dos Santos, C.F. Woellner, S.R. Lopes, A.M. Batista, and R.L. Viana. Lyapunov spectrum of a lattice of chaotic systems with local and non-local couplings. *Chaos, Solitons & Fractals*, 32:702–710, 2007.
- [44] J.D. Farmer, E. Ott, and J.A. Yorke. The dimension of chaotic attractors. *Physica D*, 7:153–180, 1983.

Bibliography

- [45] K.S. Fink, G. Johnson, T. Carroll, D. Mar, and L. Pecora. Three coupled-oscillators as a universal probe of synchronization stability in coupled oscillator arrays. *Physical Review E*, 61(5):5080, 2000.
- [46] P.M. Gade and R.E. Amritkar. Spatially periodic orbits in coupled-map lattices. *Physical Review E*, 47(1):143, 1993.
- [47] P.M. Gade and C.-K. Hu. Synchronization and coherence in thermodynamic coupled map lattices with intermediate-range coupling. *Physical Review E*, 60(4):4966, 1999.
- [48] P.M. Gade and C.-K. Hu. Synchronous chaos in coupled map lattices with small-world interactions. *Physical Review E*, 62(5):6409, 2000.
- [49] M.K. Gaillard, P.D. Grannis, and F.J. Sciulli. The standard model of particle physics. *Reviews of Modern Physics*, 71(2):96, 1999.
- [50] C.W. Gardiner. *Handbook of Stochastic Methods*. Springer, 1997.
- [51] W. Greiner and B. Müller. *Gauge Theory of Weak Interactions*. Springer, 2010.
- [52] S. Groote and H. Veermäe. Short chaotic strings and their behaviour in the scaling region. *Chaos, Solitons & Fractals*, 41:2354–2359, 2009.
- [53] F. Halzen and A.D. Martin. *Quarks and Leptons: An Introductory Course in Modern Particle Physics*. John Wiley & Sons, 1984.
- [54] D. Heide, M. Schäfer, and M. Greiner. Robustness of networks against fluctuation-induced cascading failures. *Physical Review E*, 77:056103, 2008.
- [55] A. Hilgers and C. Beck. Higher-order correlations of tchebyscheff maps. *Physica D*, 156:1, 2001.
- [56] C.J. Hogan. Why the universe is just so. *Reviews of Modern Physics*, 72(4):1149–1161, 2000.
- [57] R. Horn and C.R. Johnson. *Matrix analysis*. Cambridge University Press, 1990.
- [58] L. Huang, Y.-C. Lai, and R.A. Gatenby. Optimization of synchronization in complex clustered networks. *Chaos*, 18:013101, 2008.
- [59] L. Huang, K. Park, Y.-C. Lai, L. Yang, and K. Yang. Abnormal synchronization in complex clustered networks. *Physical Review Letters*, 97:164101, 2006.
- [60] S. Jalan and R.E. Amritkar. Self-organized and driven phase synchronization in coupled maps. *Physical Review Letters*, 90(1):014101, 2003.
- [61] S. Jalan, R.E. Amritkar, and C.-K. Hu. Synchronized clusters in coupled map networks. I. numerical studies. *Physical Review E*, 72:016211, 2005.

- [62] J. Jost and M.P. Joy. Spectral properties and synchronization in coupled map lattices. *Physical Review E*, 65:016201, 2001.
- [63] G. Kane. *Modern Elementary Particle Physics*. Addison-Wesley, 1993.
- [64] K. Kaneko. Period-doubling of kink-antikink patterns, quasiperiodicity in antiferro-like structures and spatial intermittency in coupled logistic lattices. *Progress of Theoretical Physics*, 72(3):480–486, 1984.
- [65] K. Kaneko. Lyapunov analysis and information flow in coupled map lattices. *Physica D*, 23:436–447, 1986.
- [66] K. Kaneko. Pattern dynamics in spatiotemporal chaos. *Physica D*, 34:1–41, 1989.
- [67] K. Kaneko. Towards thermodynamics of spatiotemporal chaos. *Progress of Theoretical Physics Supplement*, 99:263–287, 1989.
- [68] K. Kaneko. Clustering, coding, switching, hierarchical ordering, and control in a network of chaotic elements. *Physica D*, 41:137–172, 1990.
- [69] K. Kaneko. *Theory and applications of coupled map lattices*. John Wiley & Sons, 1993.
- [70] K. Kaneko and I. Tsuda. *Complex Systems: Chaos and Beyond*. Springer, 2000.
- [71] J. Koiller and L.-S. Young. Coupled map networks. *Nonlinearity*, 23:1121–1141, 2010.
- [72] C. Li, C. Xu, W. Sun, J. Xu, and J. Kurths. Outer synchronization of coupled discrete-time networks. *Chaos*, 19:013106, 2009.
- [73] K. Li, M. Small, and X. Fu. Generation of clusters in complex dynamical networks via pinning control. *Journal of Physics A: Mathematical and Theoretical*, 41:505101, 2008.
- [74] P.G. Lind, J.A.C. Gallas, and H.J. Herrmann. Coherence in scale-free networks of chaotic maps. *Physical Review E*, 70:056207, 2004.
- [75] L. Lodata, S. Boccaletti, and V. Latora. Synchronization properties of network motifs. *Europhysics Letters*, 78:28001, 2007.
- [76] W. Lu, F.M. Atay, and J. Jost. Synchronization of discrete-time dynamical networks with time-varying couplings. *SIAM Journal on Mathematical Analysis*, 39(4):1231–1259, 2007.
- [77] W.L. Lu, B. Liu, and T. Chen. Cluster synchronization in networks of distinct groups of maps. *The European Physical Journal B*, 77:257–264, 2010.

Bibliography

- [78] X.B. Lu and B.Z. Qin. Adaptive cluster synchronization in complex dynamical networks. *Physics Letters A*, 373:3650–3658, 2009.
- [79] Z. Ma, Z. Liu, and G. Zhang. A new method to realize cluster synchronization in connected chaotic networks. *Chaos*, 16:023103, 2006.
- [80] M. Maher and C. Beck. Chaotic quantization and the mass spectrum of fermions. *Chaos, Solitons & Fractals*, 37:9–15, 2008.
- [81] S.C. Manrubia and A.S. Mikhailov. Mutual synchronization and clustering in randomly coupled chaotic dynamical networks. *Physical Review E*, 60(2):1579, 1999.
- [82] M. Masujima. *Path Integral Quantization and Stochastic Quantization*. Springer, 2nd edition, 2008.
- [83] A. Mondal, S. Sinha, and J. Kurths. Rapidly switched random links enhance spatiotemporal regularity. *Physical Review E*, 78:066209, 2008.
- [84] K. Mönig. First bounds on the higgs boson from hadron colliders. *Physics*, 3:14, 2010.
- [85] A. Motter. Bounding network spectra for network design. *New Journal of Physics*, 9:182, 2007.
- [86] A. Motter, C. Zhou, and J. Kurths. Network synchronization, diffusion, and the paradox of heterogeneity. *Physical Review E*, 71:016116, 2005.
- [87] M. Namiki. *Stochastic Quantization*. Springer, 1992.
- [88] M.E.J. Newman. The structure and function of complex networks. *SIAM Review*, 45(2):167–256, 2003.
- [89] M.E.J. Newman, C. Moore, and D. Watts. Mean-field solution of the small-world network model. *Physical Review Letters*, 84:3201, 2000.
- [90] T. Nishikawa and A.E. Motter. Maximum performance at minimum cost in network synchronization. *Physica D*, 224:77–89, 2006.
- [91] T. Nishikawa and A.E. Motter. Synchronization is optimal in nondiagonalizable networks. *Physical Review E*, 73:065106(R), 2006.
- [92] T. Nishikawa, A.E. Motter, Y.-C. Lai, and F.C. Hoppensteadt. Heterogeneity in oscillator networks: Are smaller worlds easier to synchronize? *Physical Review Letters*, 91(1):014101, 2003.
- [93] G. Osipov, J. Kurths, and C. Zhou. *Synchronization in Oscillatory Networks*. Springer Series in Synergetics. Springer, 2007.

- [94] E. Ott. *Chaos in dynamical systems*. Cambridge University Press, 1993.
- [95] P. Palaniyandi, P. Muruganandam, and M. Lakshmanan. Desynchronized wave patterns in synchronized chaotic regions of coupled map lattices. *Physical Review E*, 72:037205, 2005.
- [96] L.M. Pecora and T.L. Carroll. Master stability functions for synchronized coupled systems. *Physical Review Letters*, 80:2109–2112, 1998.
- [97] M.E. Peskin and D.V. Schroeder. *An Introduction to Quantum Field Theory*. Perseus Books, 1995.
- [98] A. Pikovsky, M. Rosenblum, and J. Kurths. *Synchronization: A universal concept in nonlinear sciences*. Cambridge University Press, 2001.
- [99] S. Poria, M.D. Shrimali, and S. Sinha. Enhancement of spatiotemporal regularity in an optimal window of random coupling. *Physical Review E*, 78:035201(R), 2008.
- [100] P.C. Rech, M.W. Beims, and J.A.C. Gallas. Naimark-sacker bifurcations in linearly coupled quadratic maps. *Physica A*, 342:351–355, 2004.
- [101] P.C. Rech, M.W. Beims, and J.A.C. Gallas. Generation of quasiperiodic oscillations in pairs of coupled maps. *Chaos, Solitons & Fractals*, 33:1394–1410, 2007.
- [102] M. Schäfer and C. Beck. Discrete symmetries of chaotic strings. *Dynamical Systems*, 25:253, 2010.
- [103] T. Schreiber. Spatio-temporal structure in coupled map lattices: two-point correlations versus mutual information. *Journal of Physics A: Mathematical and General*, 23:L393–L398, 1990.
- [104] H. Shibata. Ks entropy and mean lyapunov exponent for coupled map lattices. *Physica A*, 292:182–192, 2001.
- [105] F. Sorrentino and E. Ott. Network synchronization of groups. *Physical Review E*, 76:056114, 2007.
- [106] S. Strogatz. From kuramoto to crawford: exploring the onset of synchronization in populations of coupled oscillators. *Physica D*, 143:1–20, 2000.
- [107] S. Strogatz. *Sync. The Emerging Science of Spontaneous Order*. Hyperion, 2003.
- [108] J. Sun, E.M. Bollt, and T. Nishikawa. Master stability functions for coupled nearly identical dynamical systems. *Europhysics Letters*, 85:60011, 2009.

Bibliography

- [109] I.G. Szendro, D. Pazó, and M.A. Rodríguez andh J.M. López. Spatiotemporal structure of lyapunov vectors in chaotic coupled-map lattices. *Physical Review E*, 76:025202, 2007.
- [110] J.-P. Uzan. The fundamental constants and their variation: observational and theoretical status. *Reviews of Modern Physics*, 75(2):403, 2003.
- [111] A. Varella Guedes and M. Amorim Savi. Spatiotemporal chaos in coupled logistic maps. *Physica Scripta*, 81:045007, 2010.
- [112] D.B. Vasconcelos, R.L. Viana, S.R. Lopes, A.M. Batista, and S.E. de S.Pinto. Spatial correlations and synchronization in coupled map lattices with long-range interactions. *Physica A*, 343:201–218, 2004.
- [113] K. Wand, X. Fu, and K. Li. Cluster synchronization in community networks with nonidentical nodes. *Chaos*, 19:023106, 2009.
- [114] D.J. Watts and S.H. Strogatz. Collective dynamics of ‘small-world’ networks. *Nature*, 393:440, 1998.
- [115] C. Zhou, A.E. Motter, and J. Kurths. Universality in the synchronization of weighted random networks. *Physical Review Letters*, 96:034101, 2006.

Acknowledgments

Firstly, I want to express my gratitude to my advisor Prof. Dr. Martin Greiner for guidance and support during the years of research which finally led to this thesis.

I also want to thank Prof. Dr. Dr. h.c. mult. Walter Greiner for financial support and his lectures, which kept me in touch with other exciting fields of physics beyond the topics presented in this thesis.

Great thanks are given to the Frankfurt Institute for Advanced Studies for financial support and providing the working and computing infrastructure. The numerical results presented in this thesis could not have been obtained without the super computing infrastructure provided by the Center for Scientific Computing (CSC) in Frankfurt, so I want to thank this institution and their staff for making these resources available to me.

I'd also wish to thank my colleagues Jan Scholz and Dominik Heide for helpful discussions and collaborations. They also provided great support while I was finishing this thesis by proofreading the manuscript, which is highly appreciated. To Jan Scholz I am indebted for the countless times he patiently helped me with all kind of IT-related questions.

To Prof. Dr. Christian Beck I am grateful for fruitful discussions and hospitality during my research stays at the Queen Mary, University of London.

I want to thank all people at the Frankfurt Institute for Advanced Studies for many inspiring discussions and generally making the years as a Ph.D. student at this institute an interesting and enjoyable time.

Last but not least I want to thank my family and friends for their unconditional support and encouragement.

Acknowledgments

Mirko Schäfer

Altenberg 6a
35606 Solms-Oberbiel
✉ schaefer@fias.uni-frankfurt.de

Personal Data

Date of birth 10.01.1980
Place of birth Ehringshausen, Germany
Nationality German

Academic Career

7/2007 - 8/2007 **Research stay**, *Queen Mary, University of London*, Collaboration with Prof. Dr. Beck.

10/2006 - today **Ph.D. student (physics)**, *Frankfurt Institute for Advanced Studies (FIAS), Goethe-Universität Frankfurt am Main*, Ph.D. thesis on "Dynamics of Chaotic Strings"
Supervisor: Prof. Dr. Martin Greiner.

8/2006 **Diploma in physics**, *Justus-Liebig-Universität Gießen*, Average grade: 1.0.

9/2005 - 7/2006 **Diploma thesis title: "Proactive robustness of networks against cascade failures"**, Supervisor: Prof. Dr. Martin Greiner.

7/2005 **Research stay**, *Queen Mary, University of London*, Collaboration with Prof. Dr. Beck.

9/2003 - 7/2004 **Study abroad**, *Universitat Autònoma de Barcelona, Spanien*, Erasmus program.

09/2002 **Vordiplom in physics**, Average grade: 1.1.

10/2000 - 9/2006 **Diploma student in physics**, *Justus-Liebig-Universität Gießen*.

6/1999 **Abitur**, *Goetheschule Wetzlar*, Average grade: 1.5.
specialized courses: Physics, Mathematics

Practical Experiences

- 10/2004 - 7/2005 **Student assistant (theoretical physics)**, *Justus-Liebig-Universität Gießen*.
electrodynamics, statistical physics
- 03/2004 - 05/2004 **Internship**, *Checkpoint Systems*, European Marketing Department, Barcelona, Spain.
- 10/2002 - 7/2003 **Student assistant (theoretical physics)**, *Justus-Liebig-Universität Gießen*.
quantum mechanics, classical mechanics

Further experiences

- 8/2009 **JGW SchülerAkademie, a holiday course for interested and talented pupils**, *Papenburg*, organization of the academy.
- 8/2008 **JGW SchülerAkademie**, *Papenburg*, organization of the academy.
- 5/2008 **Conference of PhD students, Hans-Böckler-Stiftung**, *Springe*, monitoring.
- 8/2007 **JGW SchülerAkademie**, *Papenburg*, organization of the academy.
- 7/2006 **JGW SchülerAkademie**, *Weimar*, lecture class, "Self organization in nature and society".
- 7/2005 **JGW SchülerAkademie**, *Schney*, lecture class, "Complex networks in nature, technology and society".

Scholarships

- 10/2004 - today **e-fellows.net**, online scholarship.
- 2/2003 - 9/2006 **German National Academic Foundation**.

Language skills

- German **native speaker**
- English **fluent**
- Spanish **very good**
- French **good**
- Catalan **basic knowledge**

IT skills

- C, C++
- Mathematica™, Gnuplot
- T_EX, L^AT_EX, Microsoft Office™, Open Office
- Linux, Microsoft Windows™

Publications

- in press Mirko Schäfer, Martin Greiner, “Disordered chaotic strings”, *Chaos, Soliton & Fractals*
- 2010 Mirko Schäfer, Christian Beck, “Discrete symmetries of chaotic strings”, *Dynamical Systems* 25, 253–268
- 2008 Dominik Heide, Mirko Schäfer, Martin Greiner, “Robustness of networks against fluctuation-induced cascading failures”, *Physical Review E* 77, 56103
- 2006 Mirko Schäfer, Jan Scholz, Martin Greiner, “Proactive Robustness Control of Heterogeneously Loaded Networks”, *Physical Review Letters* 96, 108701
- 2006 Sebastian Jost, Mirko Schäfer, Martin Greiner, “Network Perspective of Wind-Power Production”, *Wind Energy – Proceedings of the Euromech Colloquium (Springer, 2006)*

Conferences and seminars

- 5/2010 **Thiele Seminar**, *University of Aarhus, Denmark*, Talk: “Master Stability Functions for two-cluster synchronization on bipartite networks”.
- 12/2008 **BCNet WORKSHOP**, *Barcelona, Spain*, Poster: “Robustness of maximal chaotic behaviour on ring-like coupled map networks”.
- 6/2008 **58th Meeting of Nobel Laureates**, *Lindau*, Participation as a “Young Researcher, Fellow of Siemens”.
- 2/2008 **DPG-Frühjahrstagung**, *Berlin*, Talk: “Synchronization and desynchronization in chaotic map networks”.
- 3/2006 **DPG-Frühjahrstagung**, *Dresden*, Poster: “Proactive Robustness Control of Heterogeneously Loaded Networks”.
- 2/2006 **DYONET**, *Dresden*, Talk: “Proactive Robustness Control of Heterogeneously Loaded Networks”.
- 8/2004 **CNET**, *Aveiro, Portugal*, *Science of Complex Networks: From Biology to the Internet and WWW*.